UNIVERSITY OF CAPE TOWN
IYUNIVESITHI YASEKAPA • UNIVERSITEIT VAN KAAPSTAD

The Effects of Different Degrees of Confinement on the Deformation of Square Plates Subjected to Blast Loading

Carlo Geretto

Thesis presented in fulfilment of the requirements
of the degree of Doctor of Philosophy

Blast Impact and Survivability Research Unit
Department of Mechanical Engineering
University of Cape Town
November 2012

This page has been intentionally left blank.

Declaration

I, Carlo Geretto, hereby:

(a) grant the University of Cape Town free licence to reproduce the above thesis in whole or in part, for the purpose of research;

(b) declare that:

(i) this thesis is my own work, both in concept and execution, and that apart from the normal guidance from my supervisor, I have received no assistance.

(ii) neither the substance nor any part of the above thesis has been submitted in the past, or is being, or is to be submitted for a degree at this University or at any other university.

I am now presenting the thesis for examination for the degree of PhD.

Signed on the 1st November, 2012

.....

Carlo Geretto

This page has been intentionally left blank.

Abstract

This work relates to the effects of the degree of confinement for air blasts only.

The response of a structure subjected to a blast load is dependent on several factors; for instance stand off distance, geometry and mass of explosive, geometry of the structure, medium (air, water, soil) and degree of confinement. Depending on the location of the explosion relative to the surrounding structures different degrees of confinement are obtained. In addition, depending on the degree of confinement the accumulation of high temperature gas products will exert additional loads on the structure. This thesis reports the results of experimental and numerical investigations into the effect of the different degrees of confinement and target plate thickness on the response of square mild steel target plate.

In the experiments, the effects of unconfined, fully vented and fully confined blast loads on the response of square mild steel target plates with different thicknesses (3, 4 and $5mm$) and an exposed area of $200 \times 200mm$ are investigated. The unconfined and fully vented experiments were carried out on a ballistic pendulum whereas the fully confined experiments were carried out on a free standing base. A system was devised and implemented to measure the transient midpoint deflection of the target plates. The mass of explosive and target plate thickness were varied to obtain plate midpoint deformations ranging from one to fourteen target plate thicknesses.

For the numerical simulations, the different degrees of confinement were modelled in LS-DYNA® V971 R6.6220.; a hydrodynamic code that allows for the fluid (blast wave) - structure (target plate) interaction to be simulated. Three dimensional quarter symmetry models were implemented to increase the efficiency of the simulations. The target plates were modelled with shell elements and the material behaviour was defined by the Johnson-Cook material model. The material parameters required for the Johnson-Cook material model were obtained from material characterisation using quasi-static and dynamic test data.

In the experiments, the target plates only exhibited mode I failure (large inelastic failure) characterised by an uniform global dome with the maximum deformation occurring in the centre of the target plate. In general, an increase in the midpoint deflection with an increasing mass of explosive was observed irrespective of degree of confinement or target plate thickness. *The midpoint deflection versus dimensionless damage number for the different degrees of confinement correlated well with published trends. The midpoint deflection determined from transient deflection histories correlated well with final midpoint deflections.*

The numerical models when compared to experiments using the final midpoint deflection and deformed profile of the target plate showed good correlation with the experiments. Consequently a qualitative analysis of the pressure was carried out with respect to the different degrees of confinement. *The numerical predictions for the transient response of the target plate underpredicted the peak midpoint deflection, the amplitude and period of the elastic response after the peak deflection.* A parametric study was carried out to predict the response of 2 and 6mm thick target plates to different blast loads. The results correlated well with predictions based on experimental trends.

It was observed that:

- the impulse generated from a fully confined blast is approximately 4 times greater than an equivalent mass unconfined blast.
- a fully vented blast generates approximately 3 times the impulse to that of an equivalent mass unconfined blast.
- consequently the midpoint deflection increases as the degree of confinement increases.

Acknowledgements

I would like to extend my appreciation and thanks the following people:

First and foremost I would like to thank my PhD supervisor, Prof. G.N. Nurick, for sharing his wealth of knowledge, support, advice and at some points much needed guidance. Thank you for giving me the freedom and confidence to try new things. Prof. Nurick has yet to say 'no' to any of my requests whether it be work or personal which goes to show the character of Prof. Nurick.

Dr. S. Chung Kim Yuen, from the dreaded tutor in my undergraduate studies to one of the best friends one could ask for. Thank you for your immense support, guidance and having the drive to push me to succeed.

I would like to extend my great appreciation to the members of BISRU, especially to my officemates Patrick Smith, Andrew Bowden, Yolande Iyer, Kwame Boachie-Yiadom, Richard Curry and the mighty Erik Pickering, for their friendship, the many topics of discussions and the needed distractions. You have all made my time at BISRU memorable.

Many thanks to Mr. S. Ginsberg for his help and guidance with the design and manufacture of electronic circuits and Mr. G. Newins and all the workshop staff for all the friendly banter and preparing the test specimens.

A special thanks to Dr. L. Schwer for offering his much needed guidance and expertise in LS-DYNA. Thank you for helping me when no one else could.

For the assistance and many interesting conversations from engineering to everyday life, I would like to extend my gratitude to Mr. V. Balden.

The financial assistance of the National Research Foundation (NRF) towards this research is hereby acknowledged. Opinions expressed and conclusions arrived at, are those of the author and are not necessarily to be attributed to the NRF.

To the members of Conbrako, especially Mr. R.G. Child, I cannot thank you enough for all your support throughout the years. You have always kept life interesting and reminded me that nothing is impossible. Thank you for including me in the Conbrako family.

A very special thank you to Dr. J.A. Lines for her understanding, patience, encouragement and love throughout my studies.

Last, but by no means least, my family. To my mother and father who have never really understood what I was doing but always offered support and their love. I extend my sincere gratitude and love. I would also like to thank my two brothers Sandro and Marco Geretto, my sister-in-law Ester Geretto and my nephew Luca Geretto for providing many free meals and supporting me through this PhD; you have made my time in Cape Town memorable.

Contents

List of Figures

2 Literature Review

List of Tables

Glossary

BISRU Blast Impact and Survivability Research Unit

FC Fully Confined Blast

FV Fully Vented Blast

LED Light Emitting Diode

SHPB Split Hopkinson Pressure Bar

UC Unconfined Blast

This page has been intentionally left blank.

Nomenclature

Upper Case Roman

A	Cross-sectional Area
B	Target Plate Breadth
C_o	Speed of Sound in Medium
C_R	Reflective Pressure Coefficient
F	Force
I	Impulse
L	Target Plate Length
P	Pressure
T	Temperature
V_{free}	Free Volume of Container
W	TNT Equivalent Mass
Z	Scaled Distance
E	Elastic or Young's modulus

Lower Case Roman

h	Target Plate Thickness
k	Specific Heat Ratio $\frac{C_p}{C_v}$
l	Length
m	Mass
t	Time
u	Displacement
v	Velocity

Greek

δ	Midpoint Deflection
$\dot{\epsilon}$	Strain Rate
ν	Poisson's ratio
Φ_q	Dimensionless Damage Number for Quadrangular Plates
ρ	Density
σ	Stress
ε	Strain

Superscripts

el	elastic
pl	plastic

Subscripts

exp	Pertaining to the Explosive
melt	Melting
nom	Nominal
norm	Normalised
o	Original or Initial
v	Pertaining to the Vent in Structure
y	Pertaining to Yield of Material

Johnson and Cook Constants

A	Yield Stress
B	Hardening Coefficient
C	Strain Rate Parameter
m	Thermal Parameter
n	Hardening Exponent

Non-essential variables and those quoted only in a review of literature are defined where used.

1 Introduction

1.1 Background and Motivation for the Thesis

The effects of blast loading have been studied for many years to gain a better understanding and obtain characteristics of the blast load [1, 2]. Understanding the loading from a explosion, whether it be accidental or malevolent, allows for systems to be designed and implemented which minimize civilian and military casualties and structural damage [3–5]. Experimental and numerical investigations involving buildings and vehicular transport such as aircraft, buses, motorcars and ships subjected to various types of explosions have been carried out however, many of the investigations remain classified or only published as company or institute reports that never make their way into the public domain [6].

Depending on the environment where the explosion occurs the surrounding structures will be subjected to significantly different blast loads. The UFC 3-340-02 (formerly TM 5-1300) [7] design manual, classifies blast loads into two main categories namely unconfined and confined blast loads. The unconfined explosion category is further subdivided by the height and stand off distance of the detonation point from the target surface whilst the confined explosion category is subdivided by the degree of confinement. Table 1.1 lists the blast loading categories and the subdivisions.

Table 1.1: Blast Loading Categories [7]

Confinement	Category
Unconfined Explosion	1. Free Air Burst 2. Air Burst 3. Surface Burst
Confined Explosion	1. Fully Vented 2. Partially Vented 3. Fully Confined

The available literature is heavily biased to unconfined explosions (free air burst). Nevertheless the effects of confined explosions are gaining interest as applications where the containment of an explosion are critical such as bomb disposal, explosive storage and explosive extruding are becoming more relevant. Confined blast loads are less researched as the complexity of the blast load is high and studying the load is not an easy task. Initial studies into blast confinement were focused on spherical and cylindrical containers (e.g. Baker [8] and Duffey and Mitchell [9]) but recently due to the increased terrorist threats the studies have been broadened to include cuboidal containers (e.g. aircraft luggage containers [10, 11] and bomb disposal vessels [12, 13]).

This thesis aims to address the short fall in the literature by investigating the structural response of cuboidal containers to confined explosions. By excluding different sides of the cuboidal container the effects of different degrees of confinement is studied.

There have been numerous numerical studies carried out in the field of blast loading and blast mitigation, for example Yiannakopoulos [14], Ambrosini *et al.* [15], Duffey *et al.* [16] and Brundage *et al.* [17]. Highly complex full scale simulations are carried out which are validated to laboratory scale experiments. As technology advances and the efficiency of numerical solvers increases the simulations where complex interactions occurs can be modelled in more details. The goal of numerical models is to simulate the effects of a blast load and determine the structures response without performing full scale experiments.

1.2 Thesis Objectives

The aim of this thesis is to address the short fall in the literature by investigating the blast loads in different degrees of confinement on the final and transient response of square mild steel monolithic target plates. In Table 1.1 the blast loading categories are specified. In this thesis the degrees of confinement investigated are,

1. Free Air Burst Blast (hereafter referred to as unconfined blast)
2. Fully Vented Blast
3. Fully Confined Blast

The principle objectives of the thesis are:

(a) determine whether the degree of confinement effects the response of square mild steel target plates.

(b) carry out experiments to assess the performance of the degrees of confinement on the final and transient midpoint deflections.

(c) carry out a material characterisation of the target plates for use in the numerical simulations.

(d) carry out numerical analyses to model the dynamic response of the target plates.

(e) compare the experimental results with the numerical predictions.

(f) draw conclusions and make recommendations for future work.

1.3 Method of Solution

In order to attain the objectives, a series of experiments are carried out in the Blast Impact and Survivability Research Unit (BISRU) blast chamber. The unconfined and fully vented experiments performed on the ballistic pendulum and the fully confined experiments on a free standing heavy base. The locally obtained $3mm$, $4mm$ and $5mm$ thick mild steel target plates used were $300 \times 300mm$ with an exposed blast load area of $200 \times 200mm$. The mass of explosive in each degree of confinement was varied to subject the target plates to different magnitude blast loads.

The numerical analysis was carried out in the hydro-dynamic code LS-DYNA® V971 R6.6220. LS-DYNA is a commercial finite element code widely used to simulate explosive detonation and fluid structure interaction. The numerical predictions of the final midpoint deflections, global deformation profiles and the transient response are compared with the experimental results to validate the numerical model.

Material characterisation was also carried on the mild steel plates to determine material constants used to describe the material behaviour in the numerical simulations. The material constant were obtained from various material tests such as uniaxial tensile tests (quasi-static) and split Hopkinson pressure bar tests (high strain rate).

1.4 Outline of the Thesis

A review of the relevant literature is presented in Chapter 2. The different degrees of confinement and the associated blast loads are described. Several examples of the degrees of confinement are also presented. The reflection of blast waves off reflective surfaces is discussed followed with a brief overview of scaling principles for blast loads.

The configurations and procedures of the experimental investigation together with the theory used to determine the impulse from the swing of the ballistic pendulum are

presented in Chapter 3. The manufacturing details for the fully confined containers and a description of the transient displacement sensors is also described.

Chapter 4 lists the experimental results obtained and observations made. The results are divided into the three degrees of confinement investigated and the transient midpoint deflections.

An analysis of the experimental results is presented in Chapter 5. The effects of target plate thickness and the degrees of confinement are discussed. The effects of the different boundary conditions on the fully confined experiments are also discussed.

Chapter 6 presents the methods and the results obtained from the material characterisation for the different target plate materials. The results from the material characterisation are used to describe material behaviour in the numerical simulations.

Chapter 7 describes the development of the numerical blast models. The results of the numerical simulations are presented in Chapter 8 with a comparison of the final midpoint deflections and the a comparison of the transient midpoint deflections being made.

Conclusions are drawn and recommendations for future work are presented in Chapters 9 and 10 respectively.

This page has been intentionally left blank.

2 Literature Review

The interaction between a blast wave and a variety of structures has been studied for many years and in many different fields of interest such as bomb disposal [9, 13, 18], blast wave mitigation with reference to personal [19, 20], vehicular [11, 21, 22] and structural [7, 23, 24] safety and military munition [7]. This chapter will present a review of the literature on blast loading focusing on the different degrees of confinement investigated and the related effects.

This chapter starts with the characterisation of an explosion followed by a description of unconfined blast loads. Confined blast loads and container geometry will be described followed by blast wave reflections. Lastly scaling principles of blast loads will be discussed.

2.1 Explosions

An explosion is the sudden, rapid and violent release of energy into the surrounding environment [1, 7]. The localised accumulation of energy at the detonation point is abruptly dissipated into the environment in various manners such as light, heat, sound and blast waves. A blast wave is a region of highly compressed air that is characterised by an almost instantaneous increase in pressure from the ambient pressure (P_o) to the peak overpressure (P_s) [7]. The blast wave propagates radially outwards at supersonic speeds. As the blast wave expands into the surrounding environment the velocities and

pressures associated with the blast wave diminish [7]. The pressure history of a blast wave is extremely complex and for practical reasons is simplified for structural analyses. A simplified free air pressure profile of a blast wave passing a point is illustrated in Figure 2.1.

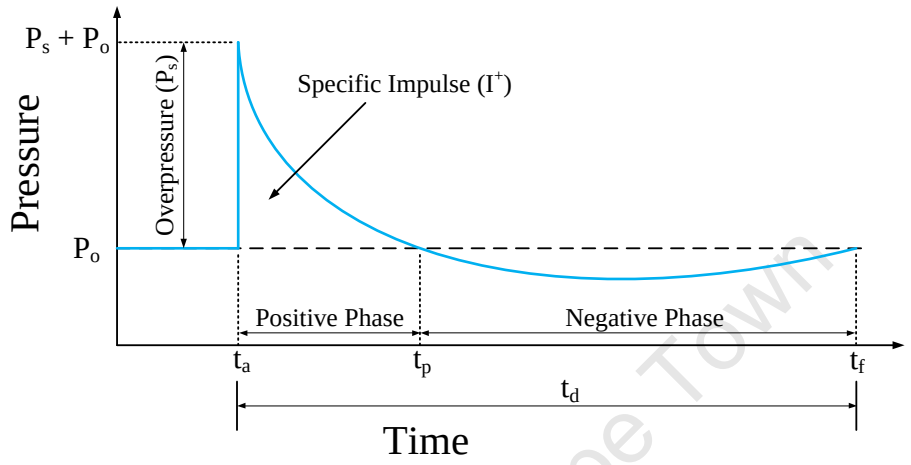

Figure 2.1: Typical Free Air Pressure Profile [1, 7, 20, 25–27]

Prior to the arrival of the blast wave conditions at the point are at ambient conditions. Upon arrival of the blast wave (t_a) there is a near discontinuous pressure 'jump', known as the overpressure (P_s), from atmospheric pressure (P_o) to a peak incident pressure ($P_s + P_o$). As the blast wave expands past the point the pressure decays in a quasi-exponential manner back to atmospheric pressure [1]. At time t_p the shock wave pressure drops below atmospheric pressure, due to the contraction of the over expanded gas in the positive phase and the reversal of particle flow. At time (t_f) the pressure returns to atmospheric pressure as equilibrium is reached. The period from t_a to t_p is known as the positive phase of the blast wave and the period from t_p to t_f is known as the negative phase. The blast duration (t_d) is measured from the arrival time (t_a) to the time the pressure returns to ambient pressure (t_f) [1, 6, 28].

The magnitude of peak overpressure is dependent on the type and mass of the explosive material, the location of the detonation point relative to the point/surface of interest and whether any magnification or reflection occurs prior to interaction with a structure [7, 20].

The blast wave will impose dynamic or/and impulsive loads on structures it encounters [1, 6, 7, 26]. The blast load is considered impulsive if the duration of the loading is substantially shorter than the natural frequency of the structure. This implies the structure has insufficient time to fully respond to the applied load [23, 29–31]. If the blast load is dynamic the structure will respond during the loading phase and the response of the structure is dependent on the loading duration, stiffness and mass of the structure [4, 31]. The classifications of an impulsive, dynamic or quasi-static loading proposed by Baker *et al.* [29] are,

$$\begin{aligned} \text{Impulsive Loading} &\implies \omega t_d < 0.4 \\ \text{Dynamic Loading} &\implies 0.4 \leqslant \omega t_d \leqslant 40 \\ \text{Quasi-static Loading} &\implies \omega t_d > 40 \end{aligned}$$

Where t_d is the duration of the applied load and ω is the natural frequency of vibration of the structure and is calculated as, $\omega = \sqrt{\frac{k}{M}}$, where k and M are the elastic stiffness and lumped mass of the structure respectively [4, 29].

The NORSAK standard[32] classifies the three loading domains as,

$$\begin{aligned} \text{Impulsive Loading} &\implies t_d/T < 0.3 \\ \text{Dynamic Loading} &\implies 0.3 < t_d/T < 3 \\ \text{Quasi-static Loading} &\implies t_d/T > 3 \end{aligned}$$

where T is the fundamental period of the structure.

2.2 Unconfined Blast Loading

2.2.1 Introduction

Unconfined blasts can be divided into three main categories; namely free air burst, air burst and surface burst explosions [7, 20]. The categories are loosely defined by the blast load acting on a structure which is effected by the height of detonation (HOD) and the stand off distance (SOD) [7, 20]. No distinct limit between the categories exists and in some instances the categories may overlap [7, 20].

This section of the report presents a description of a free air burst and brief summaries on air and surface bursts.

2.2.2 Free Air Burst

The blast wave generated from a free air burst propagates radially away from the source and impinges directly on the target surface without prior disruption or amplification due to reflection. This type of loading usually occurs when the explosion occurs at a distance above and adjacent to the target surface [7], as illustrated in Figure 2.2.

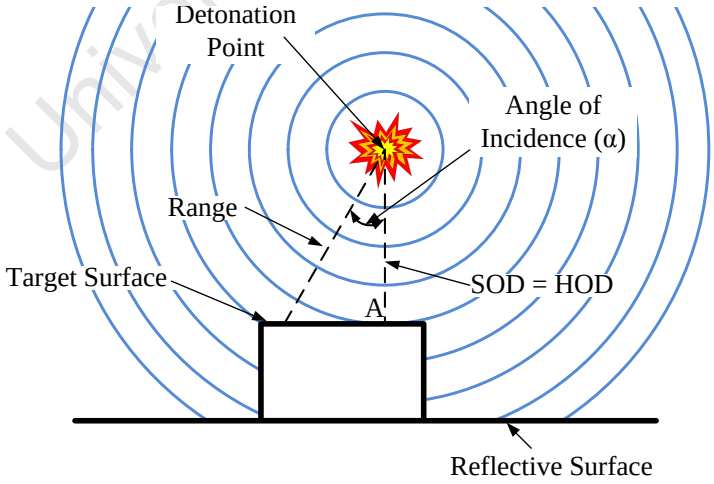

Figure 2.2: Free Air Burst Blast Environment [7, 20]

The incident blast wave propagates radially outwards from the detonation point until it

impacts the target surface where the pressure and impulses associated with the incident wave will be amplified and reflected [7]. Figure 2.3 illustrates the pressure profile at the point labelled A in Figure 2.2, which is a point directly beneath the detonation point on the target surface.

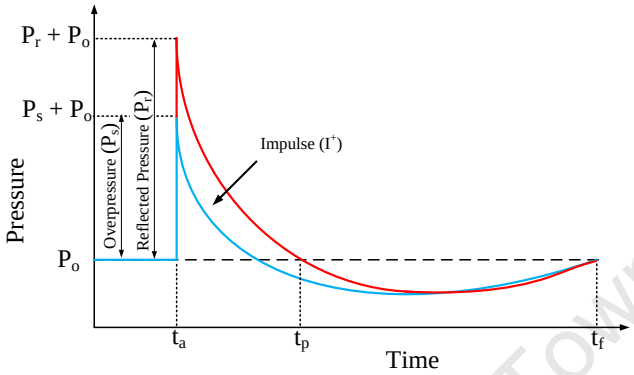

Figure 2.3: Typical Pressure Profiles on Target Surface in a Free Air Burst [1, 7, 20, 25–27]

The pressure acting at point 'A' is termed the maximum normal reflected pressure. The ratio between the maximum normal reflected pressure (P_r) and the incident wave pressure (P_s) is determined from Figure 2.4

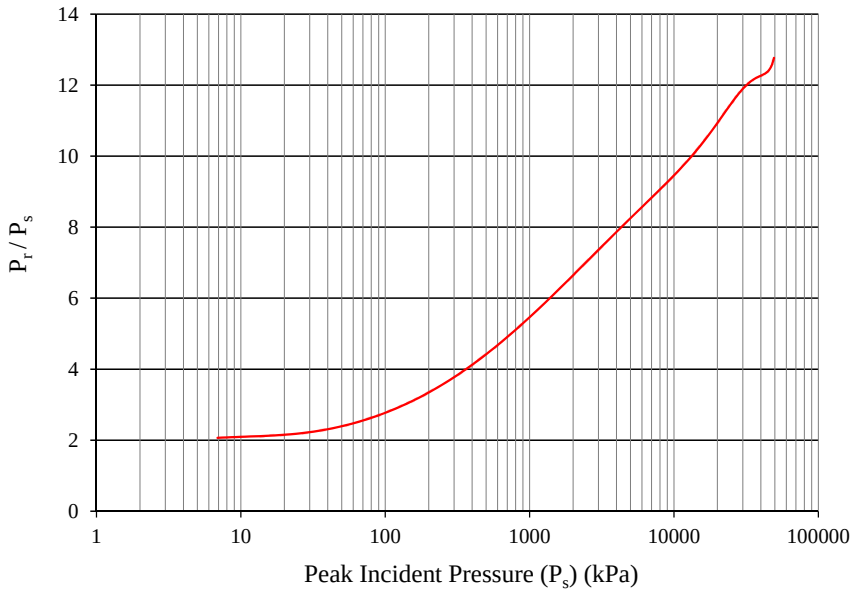

Figure 2.4: Normal Reflected Pressure/Incident Pressure Versus Peak Incident Pressure [7]

The distribution of the load from the explosion is dependent on the magnitude of the

overpressure (P_s), duration of blast load (t_d), the angle of incidence (α), the velocity of the shock wave (v_s) and the stand off distance (SOD) [1, 6, 26]. The peak reflected pressures acting on the target surface vary as a function of the SOD and the angle of incidence. The angle of incidence, illustrated in Figure 2.2, is the angle between a line projected normal to the target surface passing through the detonation point and the detonation point and the line projected from the point of interest through the detonation point. The relationship between the peak reflected pressure, angle of incidence and the scaled SOD ($\frac{SOD}{W^{1/3}}$) is depicted in Figure 2.5. Further details into blast scaling are described in Section 2.5.

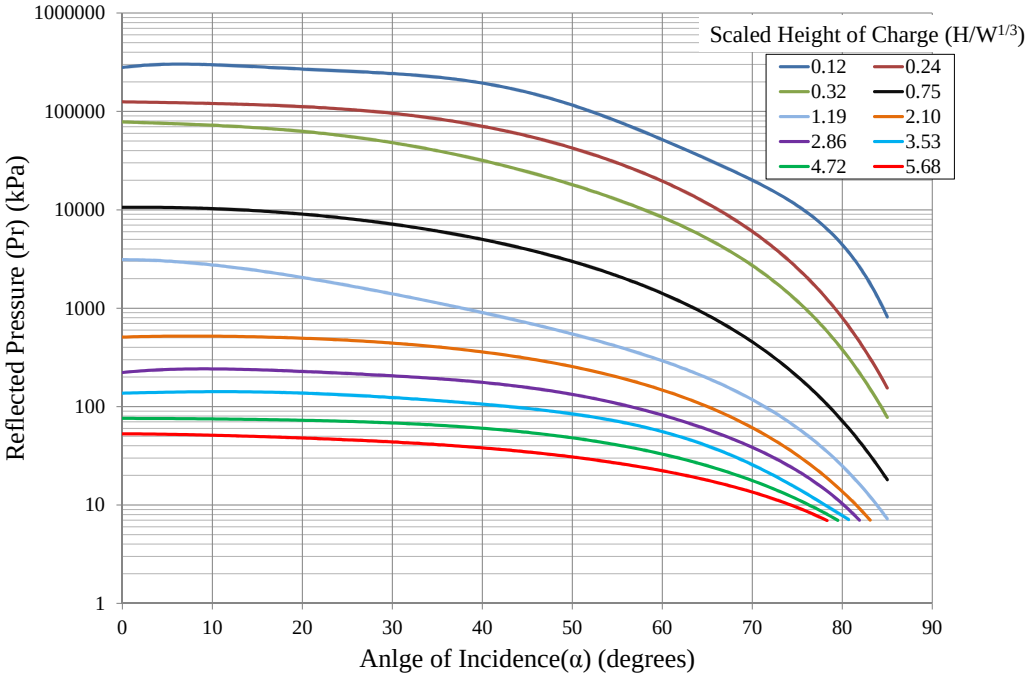

Figure 2.5: Peak Reflected overpressure Versus Angle of Incidence [7]

The positive specific impulse (I^+) of a blast wave is represented as the area under the pressure profile in Figure 2.3 and is calculated with Equation 2.1. Calculations to determine the effect of a blast wave on a structure often neglect the negative phase of the blast wave as the magnitude of the pressure in the positive phase is far greater than that of the negative phase i.e. $P_r >> P^-$ and thus $I^+ >> I^-$ [2, 7].

$$I^{+} = \int_{t_a}^{t_a+t_p} (P_r(t) - P_o)dt \tag{2.1}$$

As stated previously, the pressure profile of a blast wave is extremely complex making it necessary to simplify the profile in order to apply the simplified profile to analytical and numerical models to determine structural response. The Steel Construction Institute [30] observed that for blast loads it is important to accurately represent the impulse rather than the peak overpressure, duration or shape of the blast wave. Figure 2.6 illustrates several simplified pressure load profiles employed to investigate the structural responses to blast loads [23, 30, 31, 33, 34].

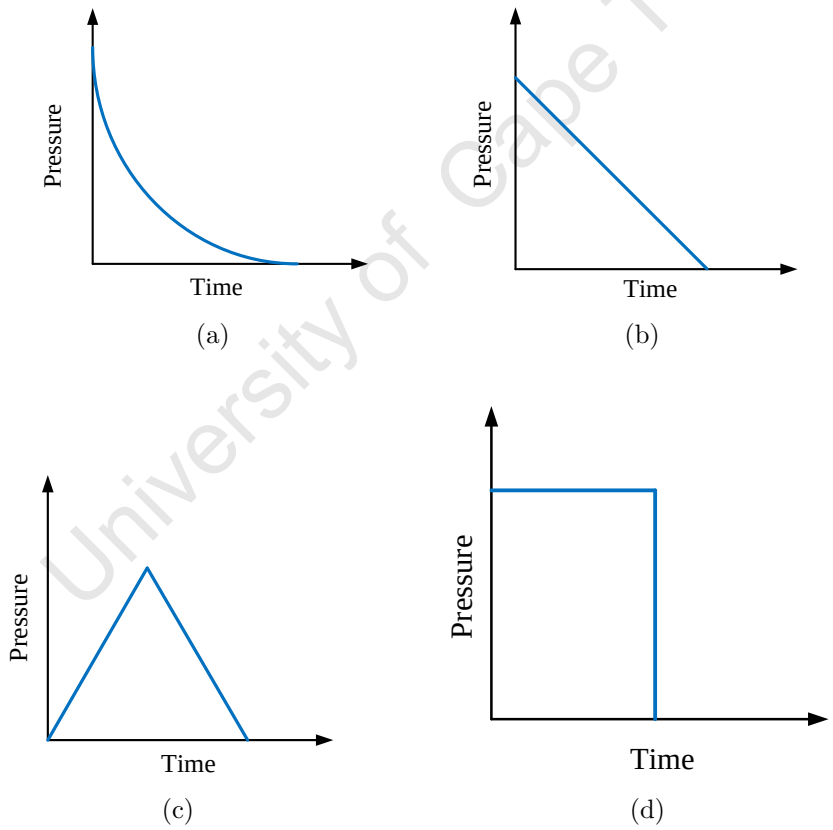

Figure 2.6: Idealised Pressure Load Profiles (a) Exponential Decay Load Pulse, (b) Right Angle Triangular Load Pulse, (c) Triangular Load Pulse, and (d) Rectangular Load Pulse.

Work presented in References [1, 2, 6, 26] present Equations 2.2–2.4 to determine the temperatures (T), pressures (P) and densities (ρ) of a medium on either side of the blast wave.

$$\frac{T_s}{T_o} = \frac{(2kM_s^2 - k + 1)[(k-1)M_s^2 + 2]}{(k+1)^2 M_s^2} = \frac{P_s}{P_o}\left[\frac{(k-1)\frac{P_s}{P_o} + (k+1)}{(k+1)\frac{P_s}{P_o} + (k-1)}\right] \tag{2.2}$$

$$\frac{P_s}{P_o} = 1 + \frac{2k}{k+1}(M_s^2 - 1) \tag{2.3}$$

$$\frac{\rho_s}{\rho_o} = \frac{(k+1)M_s^2}{(k-1)M_s^2 + 2} = \frac{\frac{P_s}{P_o}}{\frac{T_s}{T_o}} \tag{2.4}$$

Subscripts s and o are the conditions behind the shock wave and the ambient conditions in front of the shock wave respectively. Where k is the specific heat ratio($\frac{C_p}{C_v}$), C_o is the speed of sound in surrounding medium, ρ is density, T is temperature. M_s is the mach number which is a scalar variable that relates the speed of the shock wave to the speed of sound(C_o) in the medium it is travelling, see Equation 2.5.

$$M_s = \frac{v_s}{C_o} = \frac{2 + (k-1)M_s^2}{(k+1)M_s^2} = \sqrt{1 + \frac{k+1}{2k}\frac{P_s - P_o}{P_o}} \tag{2.5}$$

2.2.3 Air Burst

An explosion is termed an air burst when the detonation point is at a distance from and above the target surface so that the reflection of the incident wave off the ground occur prior to the incident wave impacting the target surface. As the blast wave propagates along the ground a third wave, termed a Mach stem, is formed [1, 6, 7]. Depending on the height of the Mach stem, which is dependent on the velocity of the incident wave, SOD and HOD the target surface will either be loaded entirely by the Mach stem or a combination of the incident wave and Mach Stem. Further details on air burst loading may be found in References [1, 2, 7, 20, 28, 35]. Figure 2.7 is an illustration of an air burst explosion.

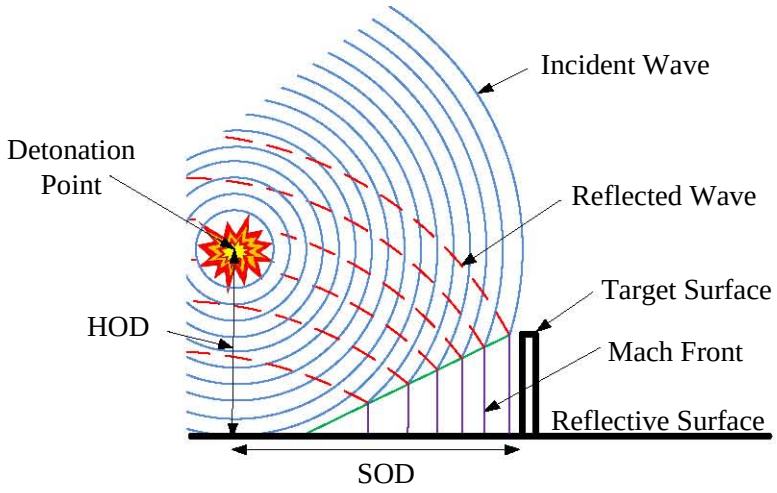

Figure 2.7: Air Burst Blast Environment [2, 7, 20]

2.2.4 Surface Burst

A surface burst occurs when a charge is detonated on or close to a reflective surface [7]. The incident wave is reflected and amplified at the point of detonation, the incident and reflected waves merge to form a single wave that propagates away from the detonation point. The wave generated in a surface burst is similar in nature to a Mach stem but is hemispherical in shape [7]. Figure 2.8 illustrates a surface burst blast environment. The reader is referred to References [1, 7] for further information on surface bursts.

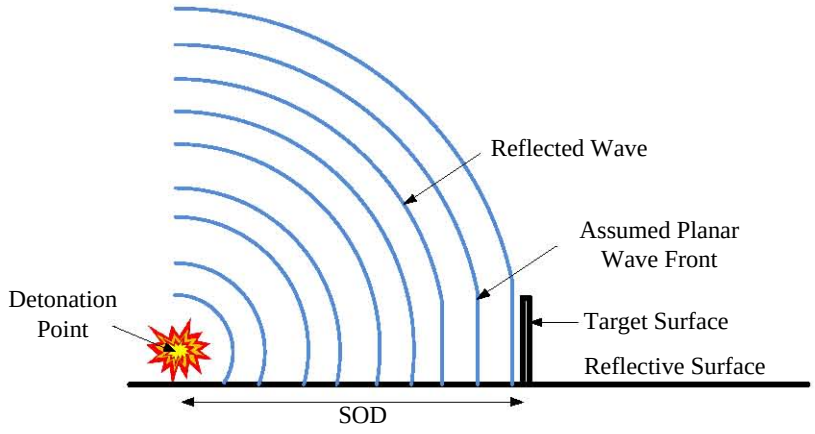

Figure 2.8: Surface Burst Blast Environment [7]

2.2.5 Blast Loading of Monolithic Plates

Extensive experimental studies have been carried out to investigate the large permanent deformation of the circular and quadrangular plates subjected to unconfined blast loads. The response of thin plates with clamped and built-in boundaries subjected to uniform and localised blast loading has been studied for many years. Jones [36] and Nurick and Martin [37, 38] present overviews on the theoretical and experimental results of plates to uniform blast loads. The results reported discuss the effects of target plate geometry (circular, square and quadrangular) on the final midpoint deflection. Numerous studies have been carried out to investigate the effects of boundary conditions [39–41], stand off distances [42, 43], stiffener location and number [44–46] on the deformation of blast loaded target plates.

This section of the report will be primarily focused on uniformly load plates as this type of loading is similar to the loading present in this research. Further details into localised blast loading my be found in References [39, 45, 47–50].

2.2.5.1 Failure Modes

Menkes and Opat [51] observed that for fully clamped beams subjected to increasing uniform blast loads three distinct failure modes existed. Figure 2.9 is a schematic of the initial loading condition and the three failure modes observed by Menkes and Opat [51]. The three failure modes were classified as,

Mode I: large inelastic deformation.

Mode II: large inelastic deformation with tensile tearing at the supports.

Mode III: transverse shear failure at the supports.

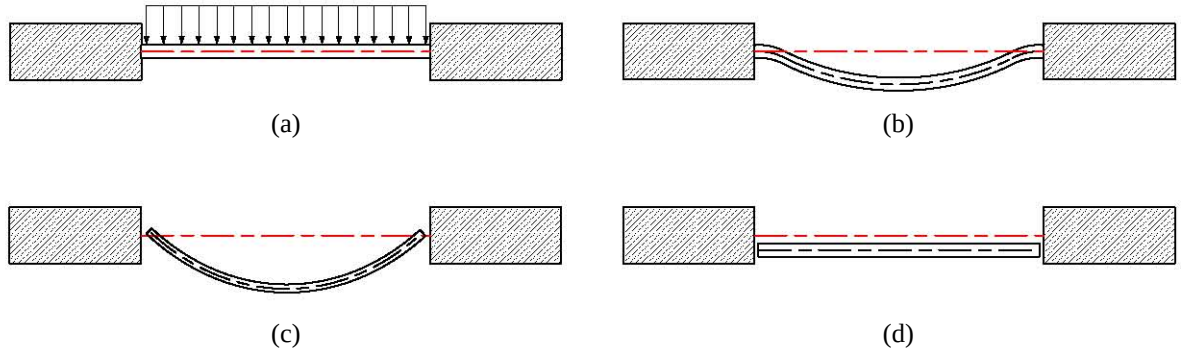

Figure 2.9: Failure Modes of Fully Clamp Beams Subjected to Uniform Blast Loads [51]: (a) Initial Loading Condition, (b) Mode I: large inelastic deformation, (c) Mode II: large inelastic deformation with tensile tearing at the supports and (d) Mode III: transverse shear failure at the supports

Similar failure modes were observed for circular [52] and quadrangular [53] plates subjected to uniform blast loads. Further categories within mode I failure were reported by Nurick *et al.* [41] and were classified as,

Mode I: large inelastic deformation: no necking.

Mode Ia: large inelastic deformation: necking at places on the boundary.

Mode Ib: large inelastic deformation: necking around the entire boundary.

Nurick and Shave [54] identified further division of mode II failure. Nurick and Shave [54] classified Mode II failure modes as,

Mode II*: partial tearing at the boundary.

Mode IIa: complete tearing with increasing midpoint deflection.

Mode IIb: complete tearing with decreasing midpoint deflection.

2.2.5.2 Response Under Uniform Blast Loading

Teeling-Smith and Nurick [52] reported on the response of fully clamped circular mild steel target plates. The mass of explosive was varied to attain a range of final midpoint deformations which spanned the three modes of failure. The final midpoint deflection increased with the increase in the impulse. The increasing midpoint point deflection resulting in thinning of the boundary until partial tearing occurred. Further increases

in the impulse will lead to complete tearing of the target plate; thereafter the midpoint of the target plate decreased with the increase in impulse. Figure 2.10 is a series photographs showing the evolution of the final midpoint deflection of circular plates with the increase of impulse reported by Teeling-Smith and Nurick [52].

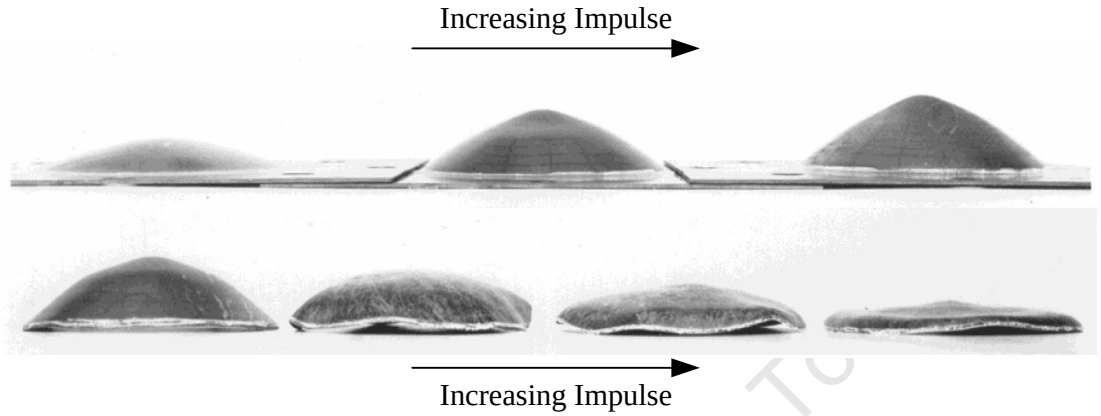

Figure 2.10: Evolution of the Final Midpoint Deflection of Circular Plates with the Increase of Impulse [52]

Olson *et al.* [53] and Nurick and Shave [54] investigated the response of fully clamped square plates subjected to uniform blast loads. The response of square plates subjected to uniform blast loading observed by Olson *et al.* [53] and Nurick and Shave [54] was similar to the response of circular plates reported by Teeling-Smith and Nurick [52]. Olson *et al.* [53] reported that tearing at the boundary started in the middle of the sides and progresses to the corners of the target plate as the impulse is increased. In experiments where the corners were torn out the specimen rotated around the remaining attached corners. "Pulling-in" at the mid-sides of the plates was evident during mode II failure(including initiation). Figure 2.11 is a series of photographs presented by Nurick and Shave [54] illustrating the evolution of the midpoint deflection of square plates with increasing impulse. The deflection increases with increasing impulse until partial tearing at the boundary occurs. Further increasing the impulse advances tearing along the boundary with an increasing midpoint deflection. Upon complete tearing the midpoint deflection decreases with the increasing impulse until complete shear failure occurs at the boundary with little midpoint deflection.

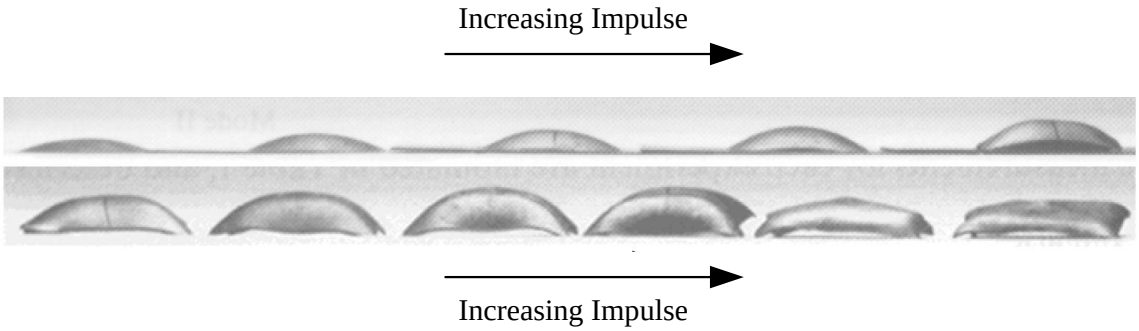

Figure 2.11: Evolution of the Final Midpoint Deflection of Square Plates with the Increase of Impulse [54]

Thomas and Nurick [55] investigated the effects of built-in and fully clamped boundaries on the final midpoint deflection of uniformly loaded circular plates. The built-in plates were manufactured from $20mm$ thick plates with an area of $200 \times 200mm$. A $100mm$ diameter region at the centre of the plate was machined out from both sides resulting in a circular region with an approximate thickness of $1.6mm$. The plates in the fully clamped setup were clamped between two $20mm$ thick clamp frames which had $100mm$ diameter holes machined in the centre of the clamp frames. Figure 2.12 illustrates the different boundary conditions investigated by Thomas and Nurick [55].

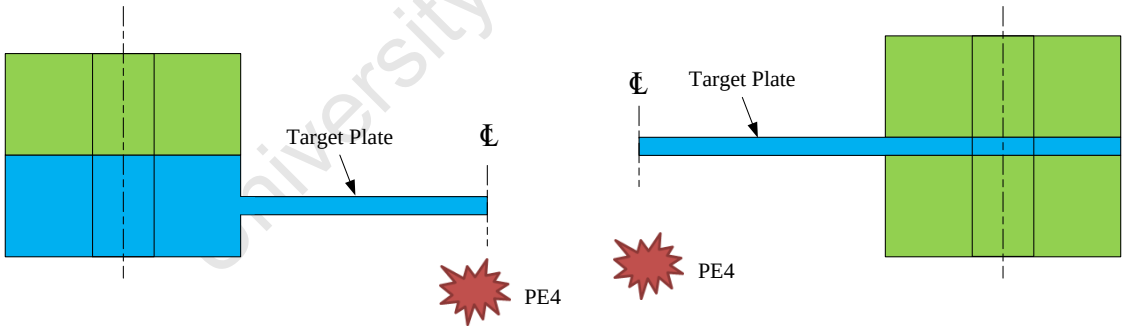

(a) Built-in Target Plate (b) Fully Clamped Target Plate

Figure 2.12: Schematic of Circular Target Plates with Different Boundary Fixations [55]

The results reported by Thomas and Nurick [55] showed that there is little difference between the boundary conditions for mode I failure, however the onset of mode II failure was significantly effected. The built-in boundary decreased the threshold of mode II failure, *i.e.* partial tearing at the boundary was encountered at lower impulses in comparison with the fully clamped boundary. The deformation profile between the two

boundary conditions was also different as the deformation began at the boundary for the built-in boundary whilst the deformation of the fully clamped boundary started under the clamped region. The results presented by Thomas and Nurick [55] emphasise the importance of boundary conditions when assessing tearing and the transition between mode I and II failure.

Nurick *et al.* [41] investigated the effect of the boundary edge conditions of the clamp frame on the onset of thinning and tearing of circular plates subjected to uniform blast loads. Figure 2.13 is a schematic illustrating the different edge conditions investigated by Nurick *et al.* [41]. The edge conditions investigated were a sharp edge, 1.5mm fillet radius and a 3.2mm fillet radius.

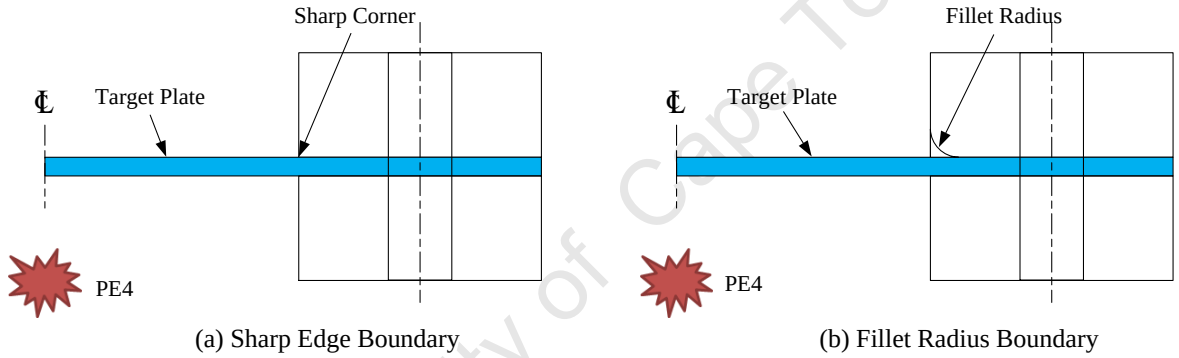

Figure 2.13: Schematic of Sharp and Fillet Radius Boundary Edge Conditions [41]

The necking of the target plate with a sharp edge condition was characterised by a sharp indentation, due to the clamp frame, proceeded by stretching and thinning. The necking observed with the filleted edge condition was distinctly different to the sharp edge condition but was similar to the thinning observed in an uniaxial tensile specimen. Nurick *et al.* [41] also reported that the increase in the fillet radius delayed the onset of tearing which allowed for greater energy absorption resulting in larger midpoint deflection before the onset of tearing. Figure 2.14 is a series of photographs illustrating the thinning at the boundary observed by Nurick *et al.* [41] for the three different boundary conditions.

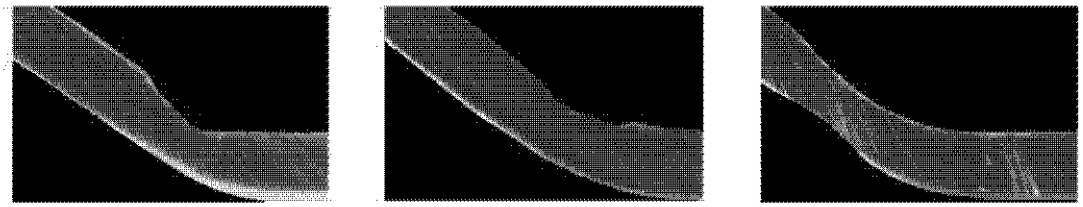

(a) Sharp Edge – 20.19Ns (b) Radius 1.5mm – 20.08Ns (c) Radius 3.2mm – 23.31Ns

Figure 2.14: Photographs Illustrating Thinning of the Target Plate under Different Boundary Edge Conditions [41]

Olson *et al.* [53] implemented NAPSSE (Non-linear Analysis of Plate Structures using Super Elements) [56, 57] to analyse uniformly blast loaded plates. NAPSSE represents the displacement fields by both analytical and polynomial functions to reduce the number of elements required to achieve design level accuracy. Olson *et al.* [53] successfully predicted the maximum deflection and final deformation profile of a uniformly loaded plate with NAPSSE.

Olson *et al.* [53] applied a uniformly distributed square pressure pulse to a quarter symmetric plate model. The duration of the pressure pulse was assumed to be $15\mu s$, which was approximately equal to the explosive burn time. The magnitude of the pressure was calculated such that the applied impulse in the simulation corresponded to experimental values.

Olson *et al.* [53] observed that the inclusion of stain rate effects in the material model had significant effects on the yield stress and the plate response. Strain rate effects were incorporated by scaling the yield stress with the Cowper-Symonds relation [58]. Figure 2.15 is a plot of the predicted dynamic yield stress, strain rate and time to first yield versus impulse. The strain rates were high, ranging from 640 to $3160s^{-1}$ as the impulse increased from 5 to $40Ns$. The corresponding yield stress was also high and ranged from 800 to $900MPa$. The time of occurrence for first yield initially decreased rapidly with increasing impulse but a plateau at high impulses was observed. The time of first yield decreased from 9.5 to $3.5\mu s$ with the increasing impulse.

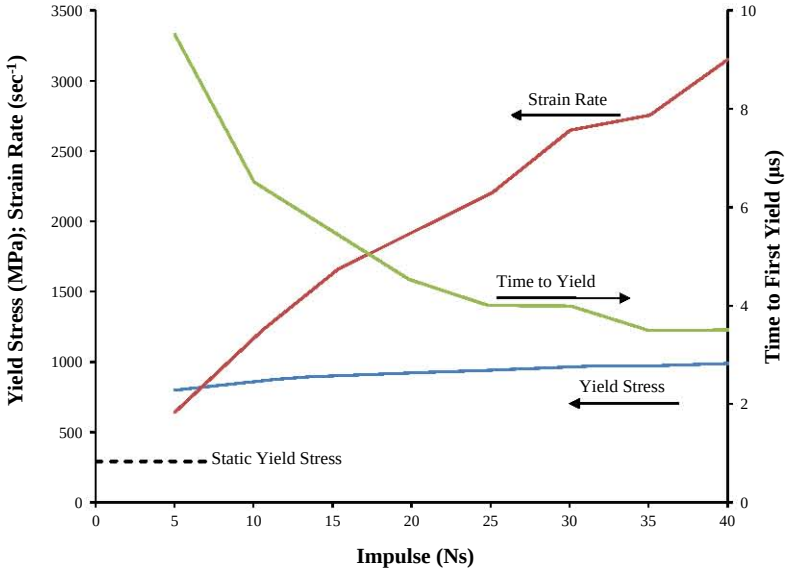

Figure 2.15: Yield Stress, Strain Rate and Time to First Yield versus Impulse [53]

The effects of strain rate inclusion in the material model on the transient midpoint deflection of the plate are illustrated in Figure 2.16. The result illustrated is for a plate subjected to an uniformly applied impulse of $15Ns$. The inclusion of strain rate effects significantly reduced the final midpoint deflection and the associated time of the plate to reach the maximum deflection.

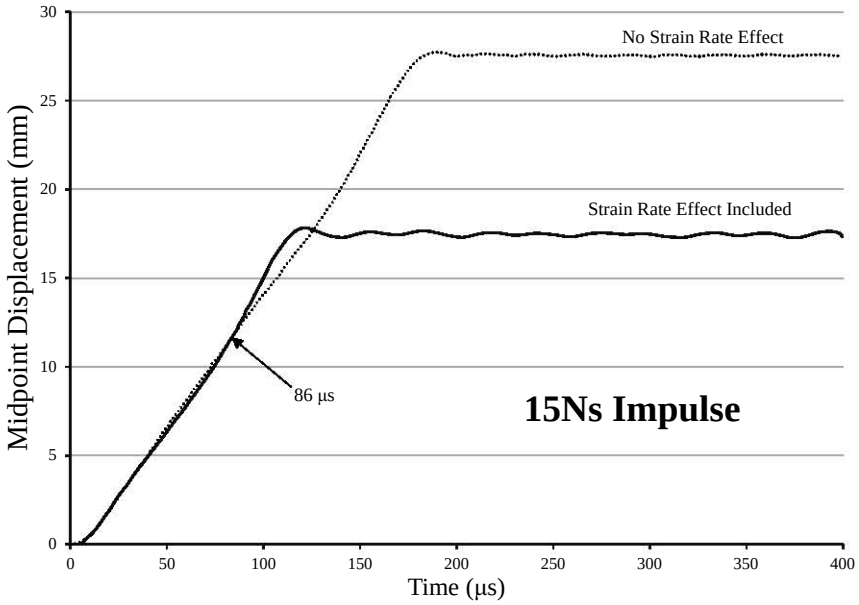

Figure 2.16: Strain Rate Effects on Transient Displacement [53]

Consequently, the transient plate deformation was effected by the inclusion of strain rate effects as shown by the centre line profiles illustrated in Figure 2.17. The centre line profile illustrated in Figure 2.17a corresponds to the point highlighted in Figure 2.16 occurring at $86\mu s$. The midpoint deflections at $86\mu s$ are similar however the deflection distributions are distinctly different. The non-strain rate profile has a steeper slope at the boundary and a longer developed length. Consequently, mode II failure was predicted for the non-strain rate profile whereas, mode I failure was predicted for the strain rate effect profile throughout the response of the plate..

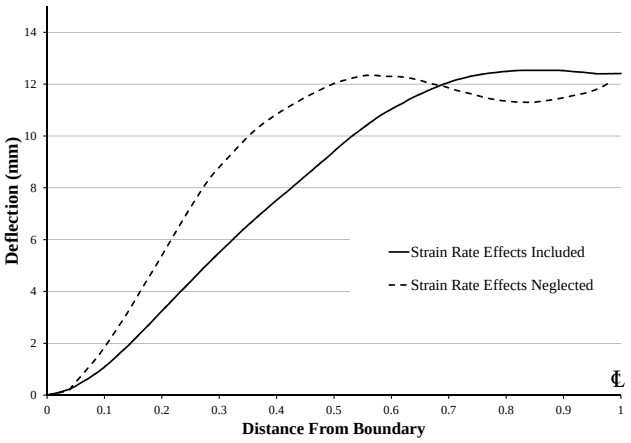

(a) Profile at $86\mu s$

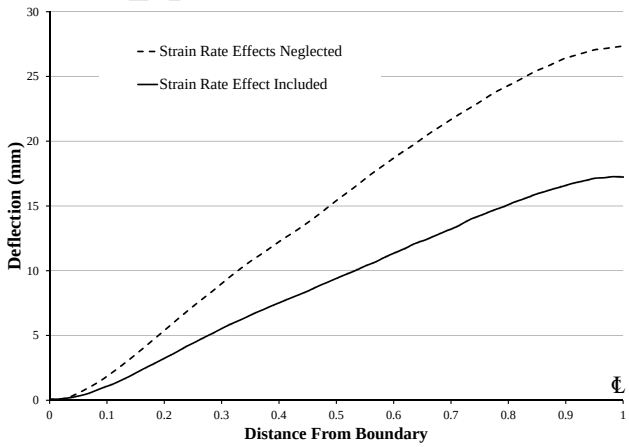

(b) Final Permanent Profile

Figure 2.17: Centre Line Profiles of Square Plates Subjected to an Impulse of $15Ns$ [53]

The transient deformation profiles of a plate subjected to an impulse of $20Ns$ is depicted in Figure 2.18. The central region of the plate in the early stages was essentially flat as would be expected from impulsive theory. As time progressed and the global deformation increased, the flat region decreased in size. Olson *et al.* [53] reported that mode II failure was first encountered at $20Ns$ and was expected to occur at $101\mu s$ where the central displacement was $20mm$. However, if no failure criteria was set(i.e. mode I failure) the maximum deflection of $23.2mm$ would have occurred at $121.5\mu s$.

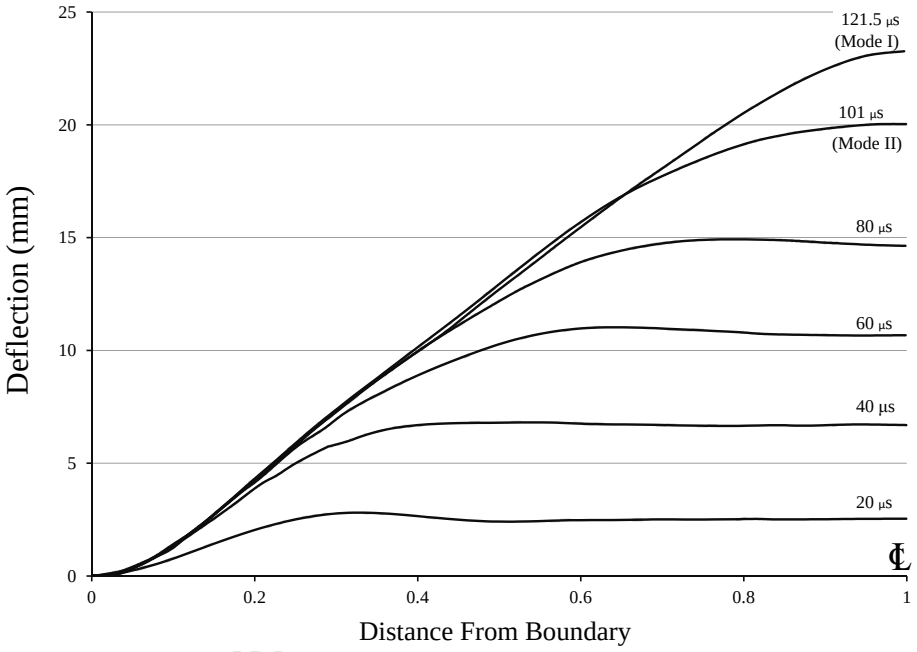

Figure 2.18: Transient Plate Profiles for $20Ns$ Impulsive Load [53]

Olson *et al.* [53] observed that mode II failure occurred at an impulse of $20Ns$ and above. The mode I failure observed exhibited characteristic failure where the final plate deflection increased with the increasing impulse and the plate retained the characteristic deformation profile. Figure 2.19 illustrated the predicted final deformation profiles of the plates subjected to various impulsive loads. For impulses above $20Ns$, where mode II was predicted, the plate profile was taken at the times of first failure in each case. As the impulse increase above $20Ns$ the plate does not have enough time to reach the mode I characteristic shape before tearing occurs. In these cases the central portion of the plate remain relatively flat and deformations were more concentrated at the boundaries.

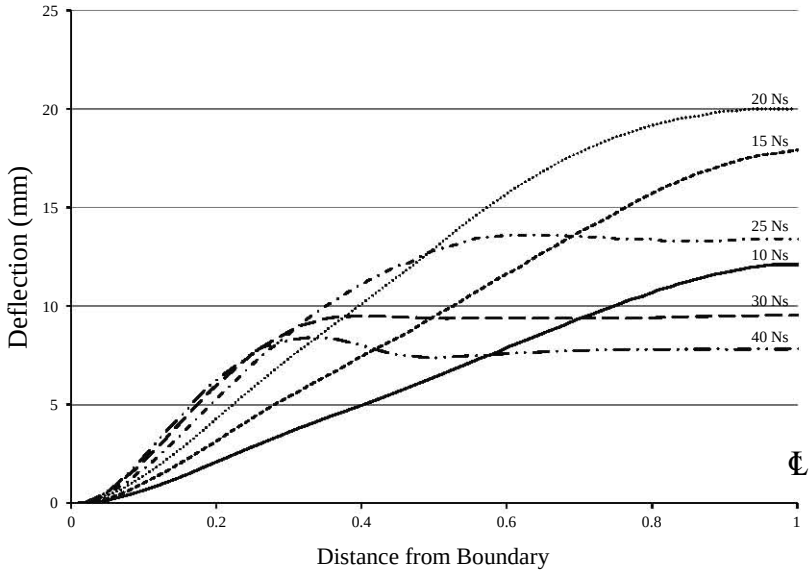

Figure 2.19: Predicted Failure Profiles [53]

Figure 2.20 illustrated the predicted strain distributions, reported by Olson *et al.* [53], along the boundaries of the plate exhibiting mode II failure($I > 20Ns$). It was observed that mode II failure initiated at the centre of each side. For higher impulses the failure would occur simultaneously along the central region of each side. The extent of the failure increased rapidly with the increase in impulse.

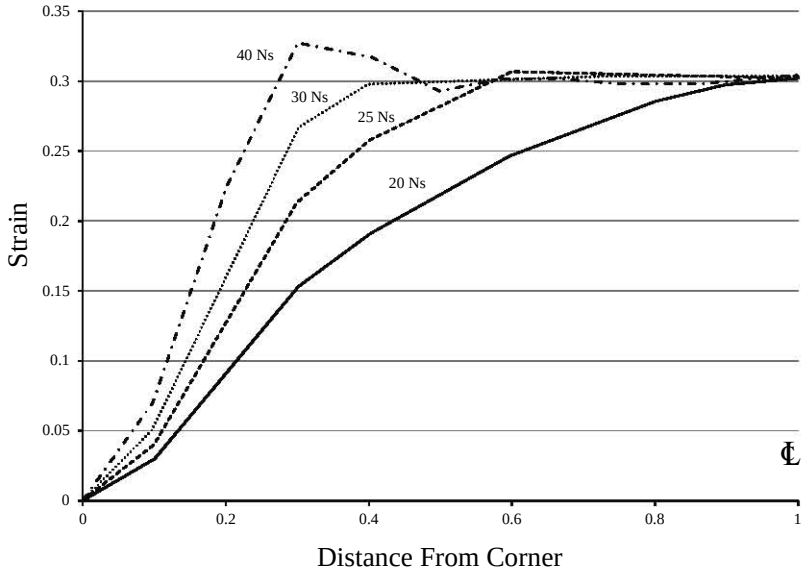

Figure 2.20: Strain Distribution at Mode II Failure [53]

Implementing a high speed streak camera, Zhu [59] recorded transient deformations of specific nodes on the surface of square target plates subjected to an uniform blast load. Experiments were carried out on mild steel and aluminium alloy square and rectangular target plates. A typical deflection history, recorded with the optical techniques, for a point $5mm$ from the midpoint of an aluminium alloy target plate is illustrated in Figure 2.21.

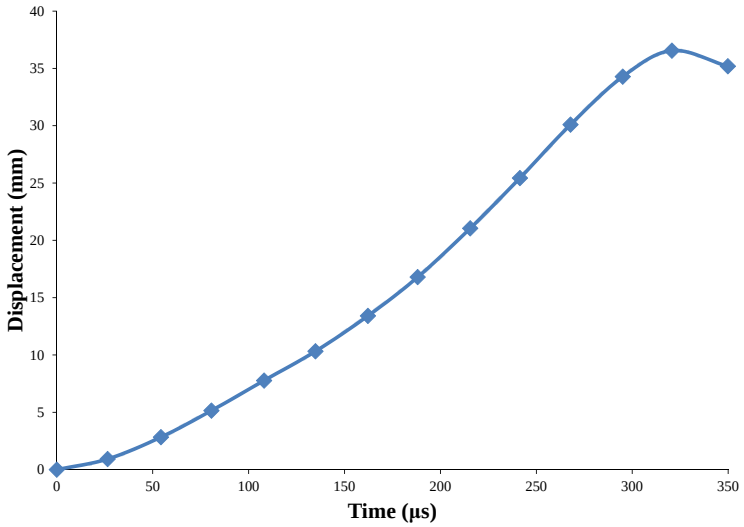

Figure 2.21: Deflection History of a Node $5mm$ from the Midpoint of an Aluminium Alloy Square Plate [59]

Zhu [59] reported similar mode I failure results for mild steel and aluminium alloy square target plates. The deformation of the target plates was characterised by a flat plateau that contracts towards the centre of the target plate as the deflection increases. The final deformation profile had a 'pyramid' shaped profile. Similar deflection histories were observed for rectangular plates however the final deformation shape was 'roof' shaped. The final deformation profiles were similar to the profiles predicted by Jones [36].

Zhu [59] simulated the experiments using the Variational Finite Difference Method which incorporated material elasticity and strain hardening. Figure 2.22 illustrates the numerical results obtained for a square aluminium alloy plate subjected to an uniform blast wave. The numerical simulation results show the contraction of the flat plateau

region of the plate as the deflection increases as well as the formation of plastic hinge which initiate from the corners of the target plate. The final deformation profile of the numerically simulated plate was similar to the deformation profile observed in experimentation.

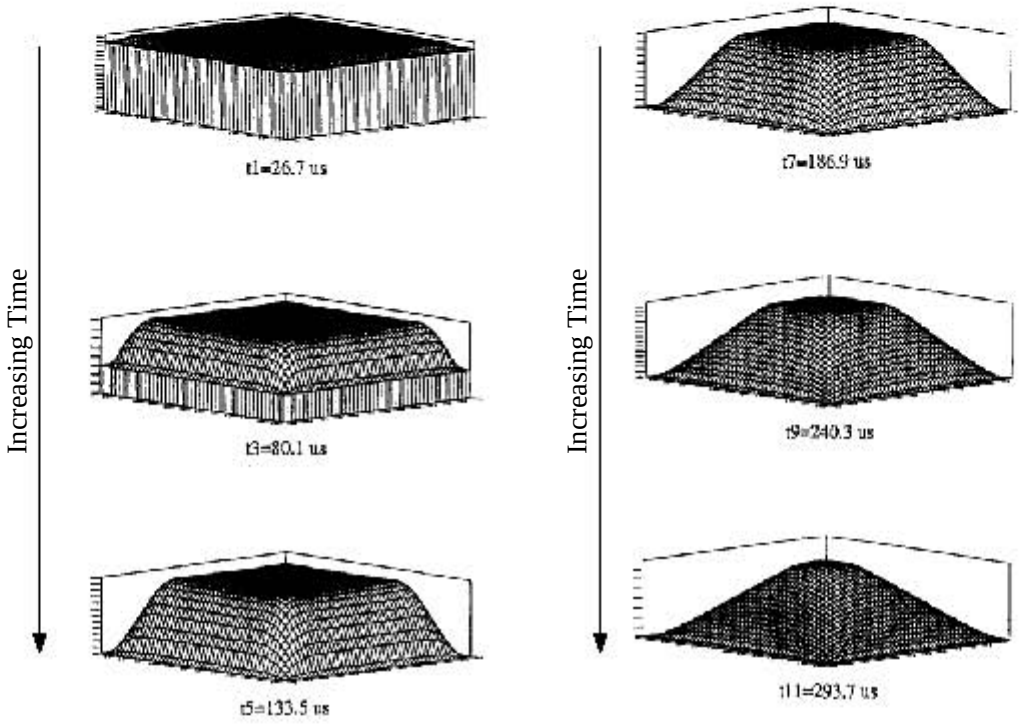

Figure 2.22: Numerically Calculated Transient Deformation Profile of an Aluminium Alloy Square Plate [59]

Figure 2.23 depicts the experimental and numerical transient deformation profiles of a square aluminium target plate at various times. The numerical results showed good agreement with the experimental results.

Balden and Nurick [60] simulated the experiments carried out by Teeling-Smith and Nurick [52] with the finite element code ABAQUS. A uniform blast wave was distributed over the surface of the circular target plate in the form of a square pressure pulse. Figure 2.24 illustrates a equivalent plastic strain contour plot of a target plate subjected to an uniformly distributed $21.69Ns$ impulse. The numerical models predicted final midpoint deflection, mode I failure and the transition between mode I and II failure within acceptable confidence limits.

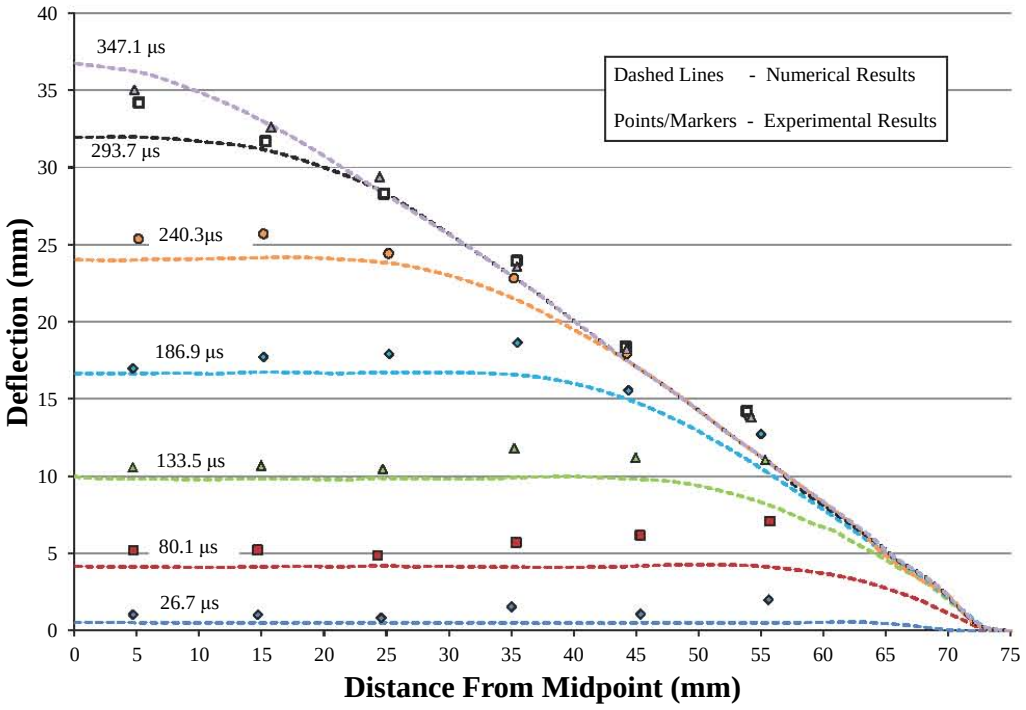

Figure 2.23: Transient Deformation Profile of an Aluminium Alloy Square Plate [59]

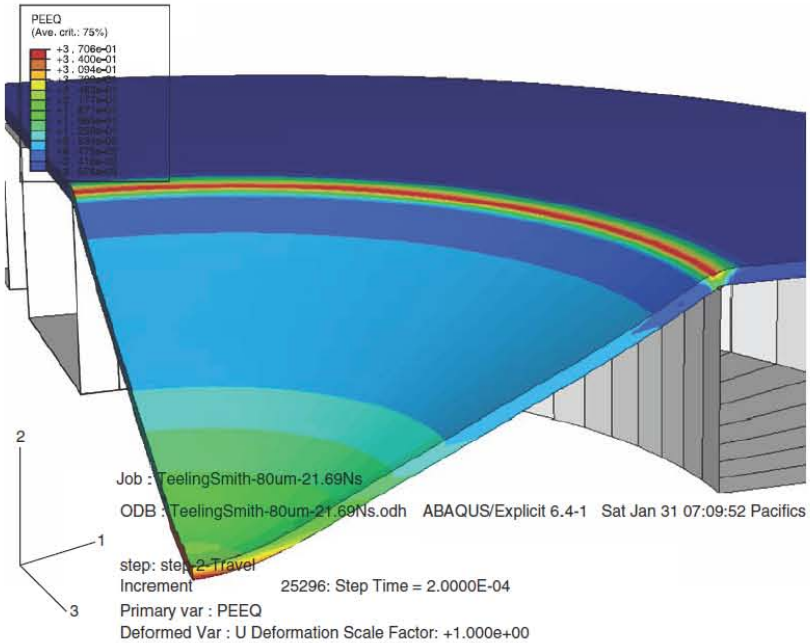

Figure 2.24: Numerical Simulation Results for an Uniform Blast Impulse of $21.69Ns$, Contour Plot of the Equivalent Plastic Strains at $200\mu s$ [60]

Gupta and Nagesh [61] carried out finite element analyses of circular target plates with varying supports subjected to a uniformly distributed square pressure impulsive load. The simulations were carried out with the finite element package ANSYS. The numerical simulations were validated against the experimental results obtained by Nurick *et al.* [41]. Gupta and Nagesh [61] observed that built-in boundaries were less efficient in absorbing shock load in comparison to fully clamped boundary as the fully clamped boundary allows more plastic work to occur before tearing of the target plate. This result concurs with experimental observations reported by Thomas and Nurick [55].

2.2.5.3 Theoretical Predictions

Many theoretical and analytical models have been developed to predict the response of thin fully clamped plates under impulsive loads. The models provide a simple closed form solution which result in sufficiently accurate approximation of plate deformations, deformed profiles, residual strains and response times. The correlation between the model predictions and experimental results have been shown to be favourable. Nurick and Martin [37, 38] published an extensive overview of this field.

Johnson [62] proposed a dimensionless damage number (α) to predict the response of a target plate subjected to ballistic loading. The dimensionless damage number proposed by Johnson [62] is given as,

$$\alpha = \frac{\rho V_o}{\sigma_d} \tag{2.6}$$

where ρ is the density of the material, V_o is the impact velocity and σ_d is the damage stress usually replaced with the yield stress (σ_y).

The damage number report by Johnson [62] does not consider the method of impact, target plate geometry nor boundary conditions. Nurick and Martin [38] introduced several factors to normalise variables such as target plate geometry and load type into

dimensionless groups. Johnson's damage number can be written in terms of impulse as,

$$\alpha = \frac{I^2}{A_L^2 h^2 \rho \sigma_d} = \frac{I_o^2}{h^2 \rho \sigma_d} \tag{2.7}$$

where I is the total impulse, A_L^2 is the load area and I_o is the impulse per unit area

Jones [36] proposed a rigid-plastic theoretical model to predict the dynamic response of impulsively loaded fully clamped quadrangular plates. The model considers the influence of finite displacement on the final dynamic response, membrane and bending force on the permanent ductile deformation and tensile tearing of the plate at the boundaries using the Johansen yield criterion. The model incorporates strain rate effects with the inclusion of the Cowper-Symonds relationship, however the effects of material hardening were not incorporated. Jones [36] implemented the conservation of energy to obtain solutions for the maximum permanent transverse displacement.

Jones [36] defined the dimensionless initial kinetic energy (λ) for an uniformly loaded quadrangular plate as,

$$\lambda = \frac{\mu V_o^2 L^2}{M_o h} \tag{2.8}$$

where V_o is an uniformly distributed velocity, L is the plate half length, h is the thickness of the plate, μ is the mass per unit area and M_o is the fully plastic bending moment per unit area and is calculated as $M_o = \sigma_y h^2/4$, where σ_y is the yield strength of the material.

Jones [36] reported that the maximum transverse displacement (δ_f) of a fully clamped quadrangular plate of length $2L$ and breadth $2B$(see Figure 2.25) subjected to an uniformly distributed velocity (V_o), including strain rate effects, is given by,

$$\frac{\delta_f}{h} = \frac{(3-\xi_o)\{(1+\frac{\Gamma}{n})^{0.5}-1\}}{2\{1+(\xi_o-1)(\xi_o-2)\}} \tag{2.9}$$

where the loading parameter (Γ) is given by,

$$\Gamma = \frac{2\rho V_o^2 L^2 \beta^2}{3\sigma_y h^2}(3-2\xi_o)\left(1-\xi_o+\frac{1}{2-\xi_o}\right) = \frac{1}{6}\lambda\beta^2(3-2\xi_o)\left(1-\xi_o+\frac{1}{2-\xi_o}\right) \quad (2.10)$$

and the geometry parameter (ξ_o) is given by,

$$\xi_o = \beta\{(3+\beta^2)^{0.5}-\beta\} \quad (2.11)$$

and the aspect ratio (β) is given by,

$$\beta = \frac{B}{L} \quad (2.12)$$

and the strain rate enhancement (n) is given by,

$$n = 1+\left(\frac{V_o\delta_f}{3\sqrt{2}D_{cs}B^2}\right)^{\frac{1}{p_{cs}}} \quad (2.13)$$

where ρ is the material density and D_{cs} & p_{cs} are the Cowper-Symonds strain rate coefficients.

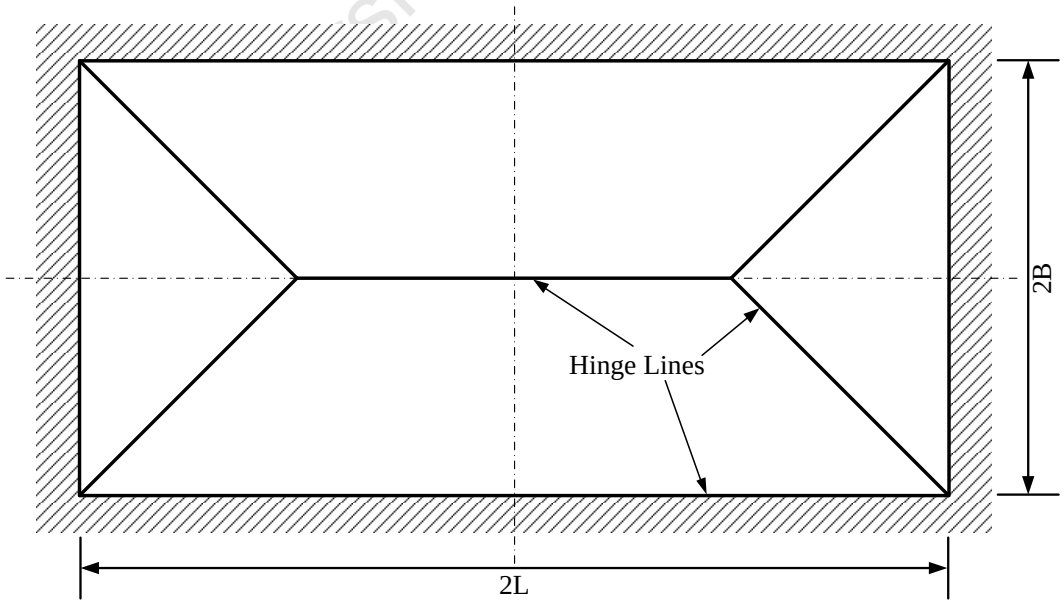

Figure 2.25: Diagram of Plastic Hinge Lines for a Fully Clamped Rectangular Plate Subjected to an Uniformly Distributed Impulsive Load [36]

The theoretical model presented in Equation 2.9 provided reasonable agreement with experimental results in predicting mode I failure response.

Zhao [63] reported a dimensionless number, termed the response number, to study the dynamic plastic response of beams and plates subjected to impulsive loads. The response number was determined by a dimensional reduction of the equations of motion for beams and plates, and was shown to provide suitably accurate solutions for all types of boundary conditions(simply supported, fully clamped etc.) and loading conditions(impulsive, rectangular pressure pulse or dynamic loads). It was also found to describe finite deflections, transverse shear[1], strain rate sensitivity and dynamic tearing.

The response number (Equation 2.14) presented by Zhao [63] for rectangular plates represents three aspects of a structures response: the inertia of the applied loading (ρV_o^2), the resistance of the structure against deformation (σ_y) and the geometry of the structure (L/h).

$$R_n = \frac{\rho V_o^2}{\sigma_y}\left(\frac{L}{h}\right)^2 \tag{2.14}$$

The response number proposed by Zhao [63] can be written in terms of the dimensionless initial kinetic energy (Equation 2.8) reported by Jones [36] and Johnson [62] damage number (Equation 2.6) as,

$$R_n = \frac{\lambda}{4} \qquad\qquad R_n = \alpha\left(\frac{L}{h}\right)^2 \tag{2.15}$$

The deflection-thickness ratio for a fully clamped rectangular plate, given by Jones [36] in Equation 2.9, can be written in terms of the response number as,

$$\frac{\delta}{h} = \frac{(3-\xi_o)\left\{\left[1+\frac{2}{3n}R_n(3-2\xi_o)\left(1-\xi_o+\frac{1}{2-\xi_o}\right)\right]^{1/2}-1\right\}}{2\{1+(\xi_o-1)(\xi_o-2)\}} \tag{2.16}$$

[1]Li and Jones [64] question the ability of the response number to describe transverse shear

Nurick and Martin [37, 38] proposed a dimensionless impulse(Φ), also termed the damage number, to relate the plate geometry, applied impulse and material properties of the plates of different thicknesses. The relationship for circular plates is given by,

$$\Phi_c = \frac{I(1 + \ln(\frac{R}{R_{exp}}))}{\pi R h^2 (\rho \sigma_y)^{0.5}} \tag{2.17}$$

where I is the applied impulse, R is the plate radius, R_{exp} is the load radius, h is the plate thickness, ρ is the plate density and σ_y is the static yield stress of the plate material.

and for quadrangular plates,

$$\Phi_q = \frac{I}{2h^2 (BL\rho\sigma_y)^{0.5}} \tag{2.18}$$

where B and L are the width and length of the plate respectively.

The dimensionless impulse (Φ_q) proposed by Nurick and Martin [37, 38] can be written in terms of the dimensionless initial kinetic energy (λ) proposed by Jones [36] and the response number (R_n) proposed by Zhao [63] as,

$$\Phi_q = \sqrt{\frac{\lambda}{4\beta}} \qquad \text{and} \qquad \Phi_q = \sqrt{\frac{R_n}{\beta}} \tag{2.19}$$

It is important to note that the dimensionless numbers in Equations 2.17 and 2.18 are only valid for mode I failure (no tearing).

Applying a least squares technique to data from several different experimental series, Nurick and Martin [37, 38] established an empirical relationship for the deflection-thickness ratio for circular (Equation 2.20) and quadrangular (Equation 2.21) plates subjected to uniform impulsive loads. The correlation coefficients were 0.974 with 109 data points and 0.984 with 156 data points for the circular and quadrangular equations respectively.

$$\left(\frac{\delta}{h}\right)_c = 0.425\Phi_c + 0.277 \tag{2.20}$$

$$\left(\frac{\delta}{h}\right)_q = 0.471\Phi_q + 0.001 \tag{2.21}$$

Nurick and Martin [37, 38] proposed that if a circular and quadrangular plate are of equal area, thickness and material properties are subjected to impulsive loading the deflection-thickness ratio of any plate can be determined. The ratio of Equation 2.20 and 2.21 is,

$$\frac{\Phi_c}{\Phi_q} = \frac{2}{\pi^{0.5}} = 1.128 \tag{2.22}$$

Substituting Equation 2.22 into Equation 2.20 the following equation is obtained,

$$\frac{\delta}{h} = 0.480\Phi_q + 0.277 \tag{2.23}$$

2.3 Confined Blast Loading

2.3.1 Introduction

A confined blast refers to an explosion that occurs within or close to a structure that limits the propagation of the blast wave [7, 20]. A confined blast results in more damage than the equivalent mass unconfined blast [65]. The damage depends on various geometrical parameters of the confinement vessel and explosive charge such as geometrical dimensions and shape, charge location, size and location of vents/openings as well as explosive characteristics [7, 20, 65]. Typically a confined blast load is comprised of a short duration shock load and a long duration gas pressure load. The shock and gas pressure loads are described as,

Shock Loads

The initial loading on the structure is a series of high magnitude short duration shock loads [35]. The source of the first shock load is the reflection of the incident blast wave off the walls on the structure. Depending on the degree of confinement, the remainder of the shock loads are caused by the re-reflection of the reflected waves within the structure. At each re-reflection the blast wave is attenuated and rapidly decays as the energy of the blast wave dissipates.

Gas Pressures

Depending on the degree of confinement there will be a secondary long-term dynamic load exerted on the walls of the structure [16]. The secondary load is caused by the accumulation of detonation products and subsequent after-burning raises the temperature gases and detonation products within the structure [66, 67]. This phenomenon generates a gas pressure which exerts a long duration load of the walls of the structure. The magnitude of the pressures associated with the dynamic load are smaller than the shock loads however the durations of the gas pressure loading can be significantly longer.

Confined blast loading can be divided into three categories based on the degrees of confinement namely fully vented, partially confined and fully confined [7]. This section of the report starts with a description of the degrees of confinement and the associated blast loads, followed by details of studies performed on different geometric shape confinement structures.

2.3.2 Fully Vented Explosion

A fully vented explosion occurs when the detonation point occurs next to some form of barrier or in a structure that has one or more sides open to the atmosphere [7] as illustrated in Figure 2.26. The build up of gas pressures inside the structure are insignificant in comparison to the shock loads, as the structure is unable to contain the gas pressures [68]. A blast is deemed to be fully vented if the duration of the gas pressure (t_g) is less than the duration of the shock load (t_s) as described in Equation 2.24.

$$t_g < t_s \tag{2.24}$$

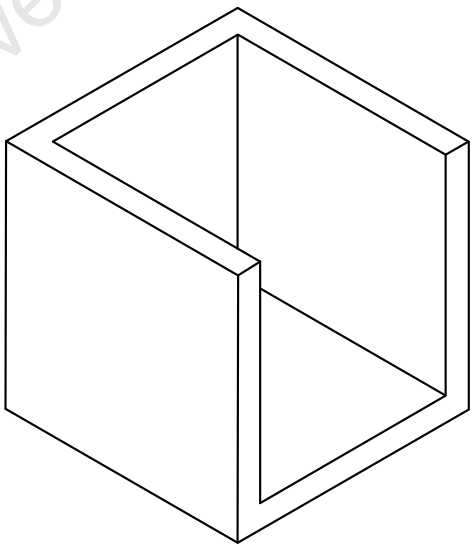

Figure 2.26: Example of a Fully Vented Structure [7]

Keenan and Tancreto [68] presented design criteria for the loading inside fully and partially vented cubicle structures. Keenan and Tancreto [68] defined a fully vented blast when the conditions in Equation 2.24 and 2.25 are satisfied. The conditions in Equation 2.25 provides a conservative criterion which is based on the geometric effects of the structure. It incorporates the initial free volume of the container (V_{free}) and the vented area (A_v). The vent area is defined as the area of the structure which is open to the atmosphere.

$$\frac{A_v}{V_{free}^{\frac{2}{3}}} \geqslant 0.6 \tag{2.25}$$

where A_v is the vent area and V_{free} is the free volume of the container.

Keenan and Tancreto [68] proposed an ideal pressure profile, shown in Figure 2.27, to describe the pressure acting on the wall of a fully vented structure. Values for design load such as peak reflected overpressure (P_r), impulses (I_s) and durations (t_s) for various charge masses are obtained from the technical manuals(e.g. UFC 3-340-02 [7]) and through experimental results presented by Keenan and Tancreto [68].

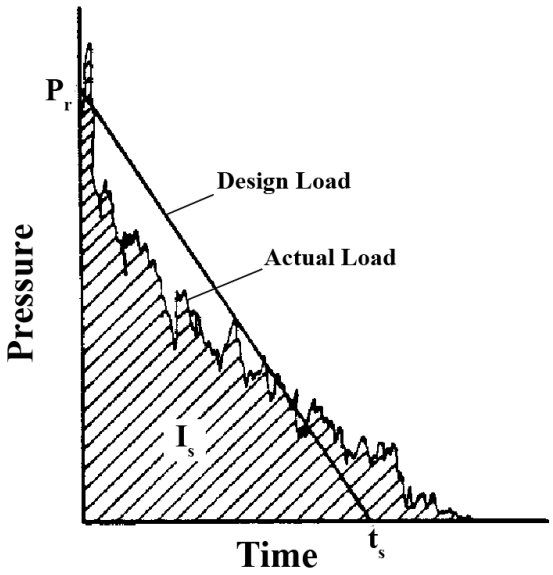

Figure 2.27: Pressure Profile Inside a Fully Vented Cubicle [67, 68]

Consider a charge detonated in a cubicle fully vented structure as shown in Figure 2.28. In the initial stages the blast wave expands until striking the nearest wall of the structure where the blast wave is reflected and amplified [7]. The blast wave is reflected back and forth between the walls and floor of the container. The initial blast wave, reflected waves and products of the explosion escape the structure by passing through the unobstructed openings in the structure [68]. The pressure of the blast wave exiting the structure corresponds to the pressure associated with an unconfined surface blast [68]. The reflected waves, travelling at higher velocities, merge with initial blast wave exiting the structure [68]. The merging of the initial and reflected wave reinforces the blast wave exiting the structure causing the peak overpressure and impulse to increase.

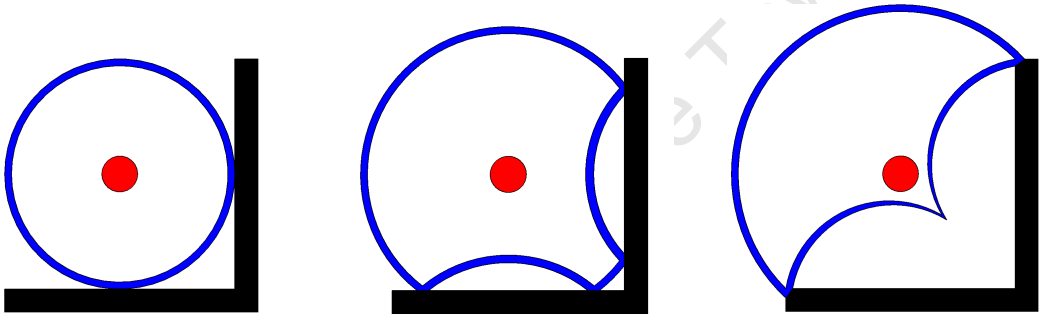

Figure 2.28: Illustration of a Fully Vented Blast Wave Profile

2.3.3 Partially Confined Explosion

The partially vented structure is one that has limited size openings/vents which are open to the atmosphere [7], as illustrated in Figure 2.29. Keenan and Tancreto [68] defined an explosion to be a partially confined explosion when the duration of the gas pressure (t_g) exceeds the duration of the shock load (t_s), $t_g > t_s$. Furthermore Keenan and Tancreto [68] defined a cubicle structure to be partially confined if Equation 2.26 is satisfied.

$$\frac{A_v}{V_{free}^{\frac{2}{3}}} < 0.6 \tag{2.26}$$

where A_v is the vent area and V_{free} is the free volume of the container.

The blast load applied to the structure is a combination of a shock and gas pressure load [7, 68]. In some cases the load generated by the gas pressure can be more damaging than the shock load, depending on the duration of the gas pressure in comparison to the duration of the shock load [68]. The gas pressure is due to the reflected waves, high temperature gas and the accumulation of gaseous products produced by the detonation of the explosive. The duration of the gas pressure is finite and is proportional to the size/area of the vents.

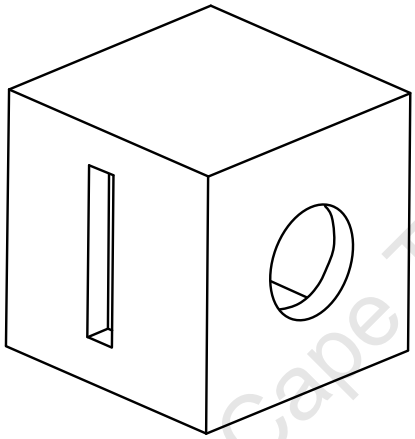

Figure 2.29: Example of a Partially Vented Structure [7]

Consider a cubicle container with vents, as illustrated in Figure 2.29, and satisfies Equation 2.26. The initial blast wave expands and impacts the walls of the container where it is reflected and reinforced. The blast wave reflects back and forth off the walls of the container attenuating with time. The build up of detonation products and high temperature gases creates a gas pressure load on the walls of the structure. As the process continues the pressure from the initial blast wave, reflected wave and gas pressure will escape from the structure through the vent. The venting of the internal pressure will occur until the pressure within the container returns to ambient conditions.

The pressure profile illustrated in Figure 2.30 is a typical partially vented pressure profile. Similar pressure histories have been observed in References [35, 65, 69, 70]. The initial shock load, the repeated shock loads and the decay of the pressure back to ambient conditions are evident from the pressure profile. The gas pressure was determined by fitting a least-squares second order polynomial to the pressure data obtained [65].

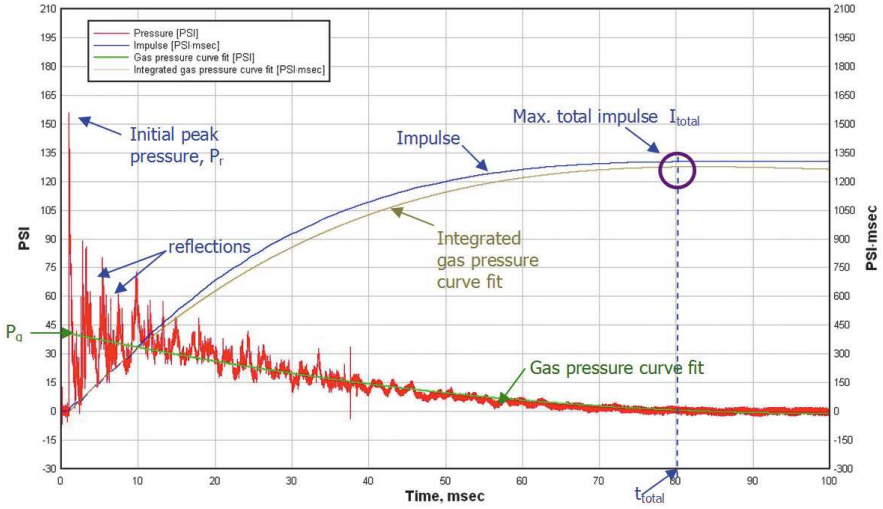

Figure 2.30: Typical Partially Confined Pressure Profile [65]

Weibull [69] carried out experiments to determine the maximum gas pressure in different shaped chambers (spherical, tube and cube) with limited size vents. The results obtained by Weibull [69] are illustrated in Figure 2.31 for various charge masses and shaped chambers. Weibull [69] acknowledges that the fit illustrated in Figure 2.31 is truly empirical and is not founded on any form of theoretical prediction however states that the fit will give an approximation to the peak gas pressure within a structure up to a charge-volume ratio ($\frac{m}{V}$) of $5kg/m^3$.

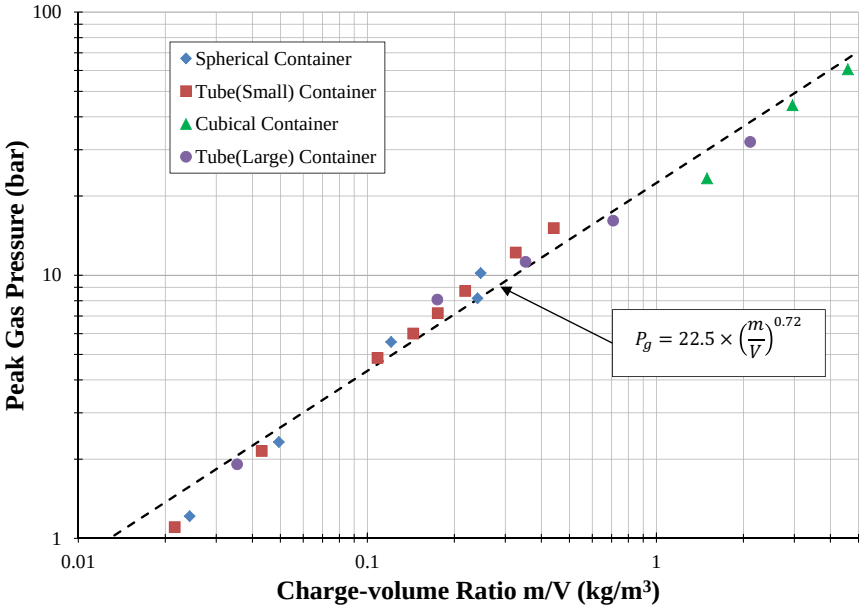

Figure 2.31: Peak Gas Pressure Versus Charge-Volume Ratio [69]

Keenan and Tancreto [68] proposed an simplified pressure load (Figure 2.32) to apply to the walls of a partially confined structure to determine the structural response. The simplified pressure load is comprised of an idealised shock load, similar to the ideal unconfined pressure loads shown in Figure 2.6b, and an ideal gas pressure. Values for design load such as peak reflected overpressure (P_r and P_g), impulses (I_s and I_g) and durations (t_s and t_g) for various charge masses are obtained from the technical manuals (e.g. UFC 3-340-02 [7]).

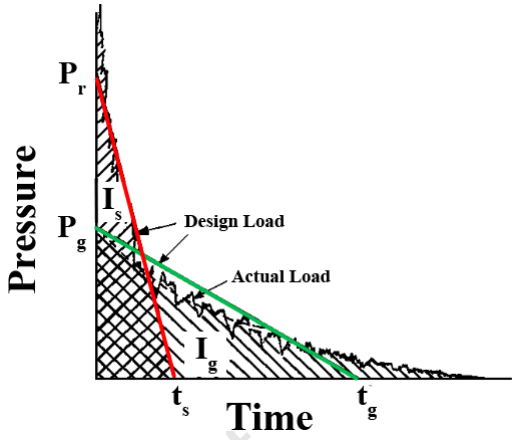

Figure 2.32: Simplified Partially Confined Pressure Profile [68]

Tancreto and Helseth [71] developed a semi-empirical model, *FRANG*, to predict the gas pressure within a structure. The model was based on the simplified partially confined pressure profile and experimental results presented by Beyer [72]. To test the validity of the results from *FRANG* Tancreto and Zehrt [73] carried out an experimental and numerical investigation. The experiments consisted of detonating a charge at the centre of a vented cylindrical vessel. The charge mass and vent area were varied to obtain different gas pressures which were measured with pressure transducers. The experiments were modelled in the finite element package, *AUTODYNE*, where the numerical gas pressure histories were obtained.

A comparison of the experimentally measured gas pressure and the *FRANG* gas pressure are illustrated in Figure 2.33. The results from *FRANG*, *AUTODYNE* and the experiments for gas pressure correlated well, however *FRANG* did not predict the rise time of the gas pressure ($10 - 15ms$).

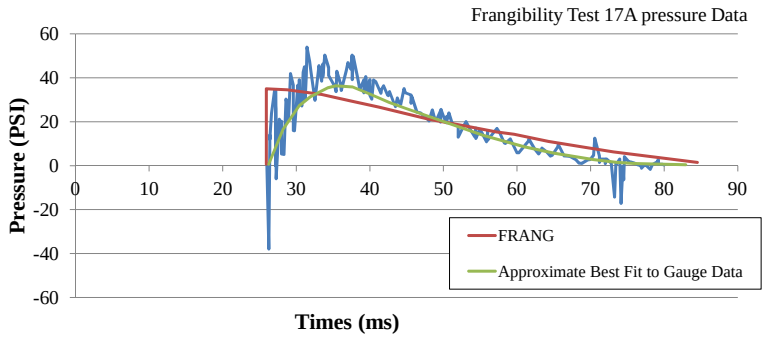

Figure 2.33: Comparison of Experimental and *FRANG* Partially confined Gas Pressure [73]

To incorporate the rise time of the gas pressure Tancreto and Zehrt [73] proposed the pressure profile illustrated in Figure 2.34. Tancreto and Zehrt [73] suggested validated simulations be used to determine the rise time of the gas pressure when the conditions of the experiments are outside the limits of *FRANG*.

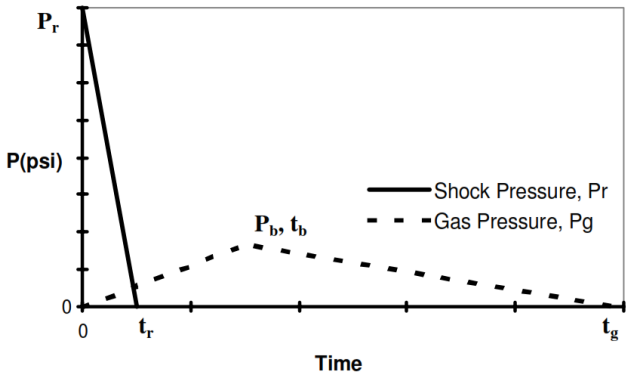

Figure 2.34: Simplified Partially Confined Pressure Profile Including the Effects of Gas Pressure Rise Time [73]

Edri *et al.* [65] carried out experiments to investigate the impulse distribution on the walls of a cubicle blast chamber and the correlation between the values presented in the UFC 3-340-02 technical design manual [7]. The experiments were carried out in a specially made concrete and steel structure with internal dimension of $2.9 \times 2.9 \times 2.7m$ (length $\times$ width $\times$ height). The roof of the structure had a $1.2m$ hole to vent the blast wave and explosive products. Gas pressures were measured at nine locations on one wall of the structure with Kulite HEM-375-2500A pressure transducers. Five experiments were carried out with TNT charges ranging from $0.5 - 4kg$.

The measured gas pressures were consistently 27% below the value predicted by the UFC 3-340-02 manual. Edri *et al.* [65] states, " *A possible explanation to this difference is that the gas pressure is not an unmistakable physical value, as it depends on the type and characteristics of the analysis method decided upon by the analyst.*" The measured total impulse ($Itotal$), the area under the pressure time curve, was also compared to the UFC 3-340-02 values and it was found that on average the predicted total impulse was 97% greater than the measured impulse.

2.3.4 Fully Confined Explosion

Full confinement of an explosion refers to a structure that either totally or near totally confines the effects of the explosion [7, 20]. The internal blast loading within a fully confined structure is extremely complex, thus less investigated [65]. The complexity of the internal loading is due to the repetitive shock loading, long duration pressure loading and interaction of the blast waves at the boundaries and joint interfaces [7, 20, 65].

The repetitive shock loads are generated by the initial blast wave being repeatedly reflected off the interior walls of the structure. The pressure profile in a fully confined cubicle structure with interior dimensions of $2.58ft$ ($\approx 786mm$), subjected to a blast wave from a $0.5lb$ ($\approx 227g$) spherical Pentolite charge, is illustrated in Figure 2.35.

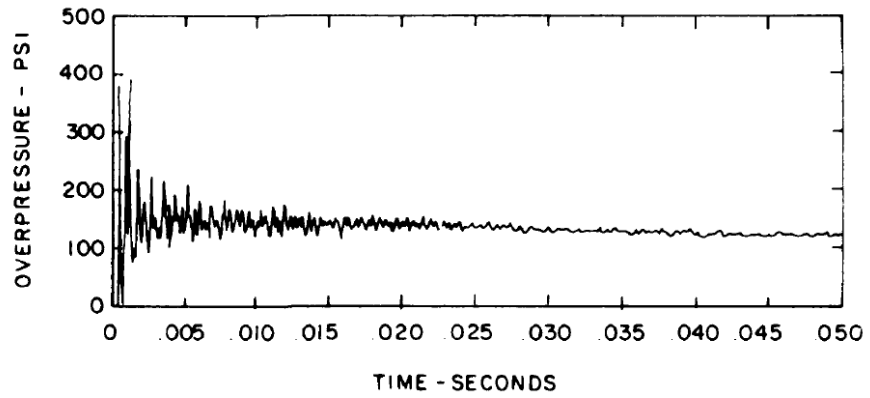

Figure 2.35: Fully Confined Pressure-Time History in a Cubical Structure Subjected to a Blast Wave from a $0.5lb$ ($\approx 227g$) Pentolite Charge [35]

The repetitive shock loads due to the reflection of the initial blast wave are clearly evident in Figure 2.35 [7, 26]. As with a partially confined explosion the gas pressure within the container is due to the build up of detonation product and high temperature gases. As no venting occurs and after a period of time the detonation product and high temperature gases exert a constant static load on the walls of the structure.

The simplified pressure-history proposed by the UFC 3-340-02 [7] technical manual is illustrated in Figure 2.36a. The pressure profile is comprised of a triangular pressure pulse that decays to a constant static overpressure ($P_{residual}$). The manual assumes the magnitude of subsequent shock loads and associated impulses are small and can be neglected. The parameters required to construct the pressure profile are obtained from the various tables and figures in the manual.

Figure 2.36b illustrates the pressure-time history for a fully confined blast load proposed by Baker *et al.* [29]. The profile is comprised of three triangular pressure pulses which represent the repeated shock loading present in the structure. The peak pressure of the pulse is equal to half the peak pressure of the previous pulse. The durations (t_d) of the pulses are equal and is set to be twice the arrival time of the initial shock wave ($t_d = 2 \times t_a$). The profile proposed by Baker *et al.* [29] does not account for residual pressures within the structure. The recommendations presented by Baker *et al.* [29] do not describe how the initial peak pressure (P_{R1}) is determined.

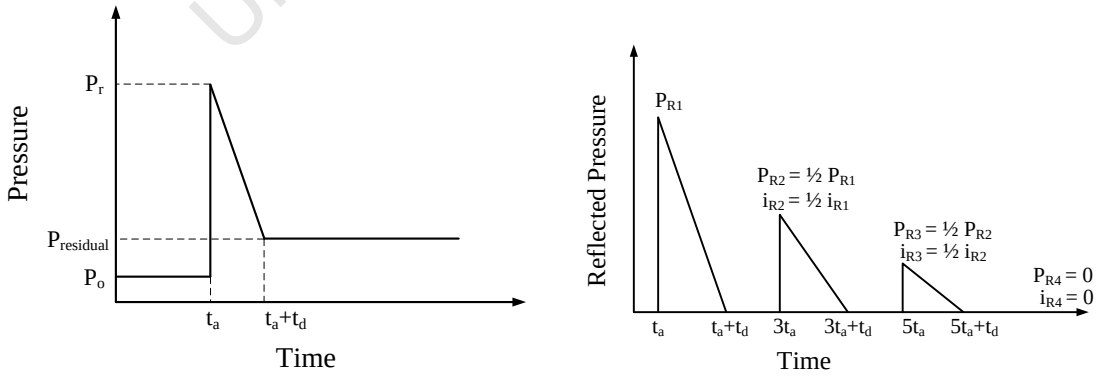

(a) UFC 3-340-02 [7] (b) Baker *et al.* [29]

Figure 2.36: Idealised Fully Confined Pressure Profiles

The pressure profile proposed in the UFC 3-340-02 [7] technical manual is based on the assumption that the pressure is applied uniformly to the entire surface of the structure, which is true for spherical containment vessels. Gregory [74] investigated the distribution of the pressure on the walls of a cylindrical confinement vessel. Figure 2.37 illustrates the pressure distribution on the interior walls. Gregory [74] provided qualitative results illustrating the complex distribution and not quantitative measures to predict the spatial distribution and the variation of the distribution with time. In general the distribution of the pressure increases towards the corners of the container.

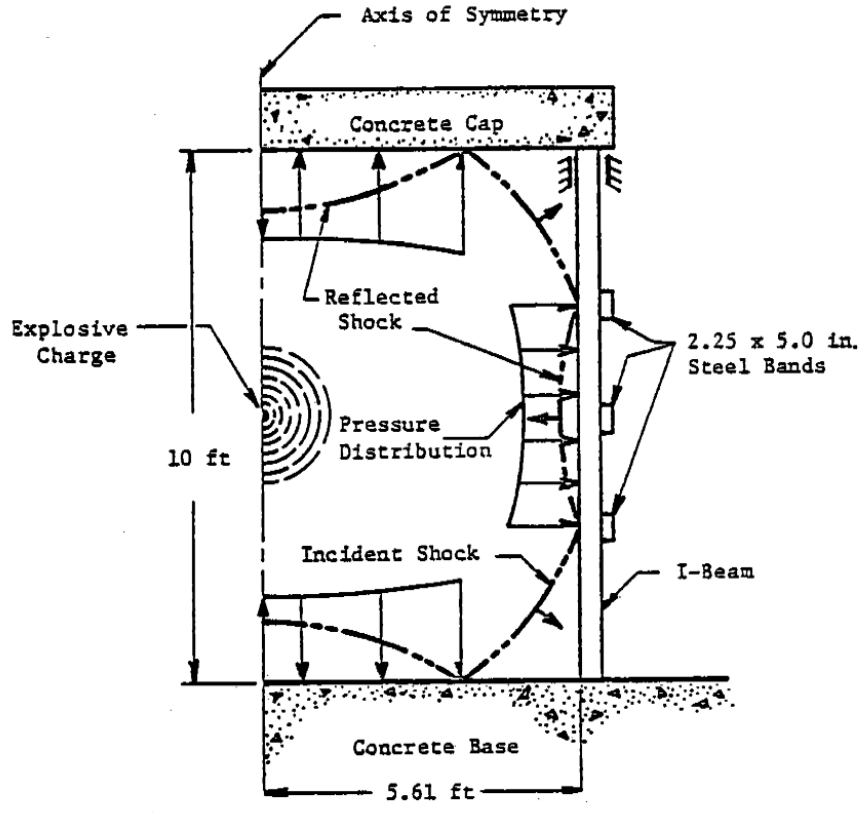

Figure 2.37: Schematic of Shock Wave Reflections on the Interior Walls of a Cylindrical Confinement Vessel [74]

2.3.4.1 Spherical Confinement Vessel

Spherical vessels are the most efficient in terms of absorbing and containing blast waves as there are no edges or vertices where the shock wave focusing can occur [13], hence the most prevalent geometry for explosion containment. A typical spherical confinement vessel is depicted in Figure 2.38.

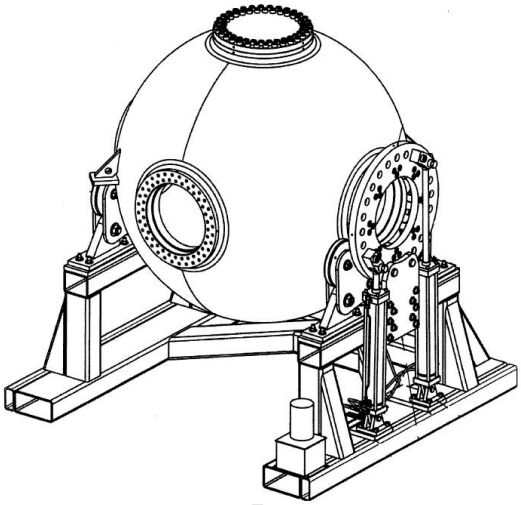

Figure 2.38: Typical Spherical Confinement Vessel [75]

Baker [8] developed the theory to describe the elastic-plastic response of a thin spherical shell subjected to internal blast loading. Baker [8] employed spherical symmetry of the vessel and the load to simplify the analysis. The motion of the shell was described with one dimensional analysis. Applying a triangular pressure profile, Equation 2.27, Baker [8] reported predictions for,

- Elastic response phase (Equation 2.28).
- Plastic response phase
  - neglecting shell thinning and radius change (Equations 2.31 & 2.32).
  - considering shell thinning and radius change (Equation 2.34).

$$p(t) = \begin{cases} P_r(1 - t/t_d) & \text{for } 0 < t \leq t_d \\ 0 & \text{for } t \geq t_d \end{cases} \tag{2.27}$$

Elastic Response Phase [8]

The elastic response of a spherical containment vessel was given as,

$$\delta_r = \begin{cases} K\left(1 - \frac{t}{t_d} - \cos\omega t + \frac{\sin\omega t}{\omega t}\right) & \text{for } 0 < t \leq t_d \\ A\cos\omega(t - t_d) + B\sin\omega(t - t_d) & \text{for } t \geq t_d \end{cases} \tag{2.28}$$

where,

$$\begin{aligned} K &= \frac{P_r}{\omega^2 \rho h} \\ A &= K\left(\frac{\sin\omega t}{\omega t} - \cos\omega t\right) \\ B &= K\left(\sin\omega t + \frac{\cos\omega t_d}{\omega Y} - \frac{1}{\omega t_d}\right) \\ \omega &= \sqrt{\frac{2E}{\rho R^2(1-\nu)}} \end{aligned} \tag{2.29}$$

Where δ_r is the radial displacement, t is the time, t_d is the duration of the triangular pulse, P_r is the peak reflected overpressure, ρ is the density of the material, R is the shell radius, h is the shell thickness, ω is the elastic circular vibration frequency, E is the elastic modulus and ν is Poisson's ratio.

Plastic Response Phase, Neglecting Shell Thinning and Variation in Shell Radius [8]

Equation 2.28 holds true until the onset of yielding (t_y) where the stress in the shell equals the material yield stress (σ_y). The behaviour of the material after yielding was assumed to obey a linear strain hardening law,

$$\sigma = \sigma_y + S(\varepsilon - \varepsilon_y) \tag{2.30}$$

where the subscript y indicates yield values, S is the slope of the plastic portion of the stress-strain curve, ε and σ are the strain and stress in the material respectively.

Neglecting shell thinning and variation in the radius of the spherical shell the plastic response of the shell was given as,

for $t_y \leq t \leq t_d$

$$\begin{aligned}\delta_r =& \delta_{ry}\cos\omega_p(t-t_y) + \dot{\delta}_{ry}\frac{\sin\omega_p(t-t_y)}{\omega_p} - \frac{2(\sigma_y - S\varepsilon_y)}{\rho R\omega_p^2}\left[1-\cos\omega_p(t-t_y)\right]\ldots \\ &+\frac{P}{\rho h\omega_p^2}\Big\{(1-t/t_d)[1-\cos\omega_p(t-t_y)] + \frac{1}{\omega_p t_d}[\sin\omega_p(t-t_y)\ldots \\ &-\omega_p(t-t_y)\cos\omega_p(t-t_y)]\Big\}\end{aligned} \tag{2.31}$$

for $t_y \geq t_d$

$$\delta_r = \delta_{ry}\cos\omega_p(t-t_y) + \dot{\delta}_{ry}\frac{\sin\omega_p(t-t_p)}{\omega_p} - \frac{2(\sigma_y - S\varepsilon_y)}{\rho R\omega_p^2}\left[1-\cos\omega_p(t-t_y)\right] \tag{2.32}$$

where the plastic circular vibration frequency is,

$$\omega_p = \sqrt{\frac{2S}{\rho R^2}} \tag{2.33}$$

where δ_{ry} is the radial displacement at time of yielding, $\dot{\delta}_{ry}$ is the radial velocity at time of yielding and t_y is the time to first yield.

Plastic Response Phase, Considering Shell Thinning and Variation in Shell Radius [8]

Baker [8] further developed the theory to include response of a spherical shell which included the effects of shell thinning and variation in the shell. Baker [8] assumed the material was incompressible during plastic deformation ($hR^2 = h_o R_0^2$, where subscript 'o' represents initial conditions). Linear strain hardening was assumed for the material. The response of the spherical shell was given by Equation 2.34.

for $t_y \leq t \leq t_d$

$$\frac{d^2R}{dt^2} + \frac{C_1}{R} + C_2 = C_3 R^2 p(t) \tag{2.34}$$

where,

$$\begin{aligned} C_1 &= \tfrac{2[\sigma_y - S(1+\varepsilon_y)]}{\rho} \\ C_2 &= \tfrac{2S}{\rho R_o} \\ C_3 &= \tfrac{1}{\rho R_o^2 h_o} \end{aligned} \tag{2.35}$$

Equation 2.34 is a non-linear and solved with numerical methods to determine the plastic response considering thinning and variation on the shell radius.

Baker *et al.* [76] further developed the analytical model to include the residual pressures present in the spherical vessel after an explosion occurred. Baker *et al.* [76] modified the applied pressure profile to,

$$p(t) = \begin{cases} P_r(1 - \frac{t}{t_d}) & \text{for } 0 < t \leq t_{static} \\ P_{static} & \text{for } t \geq t_{static} \end{cases} \tag{2.36}$$

where

$$t_d = \frac{2I_r}{P_r} \qquad \text{and} \qquad t_{static} = t_d \left(1 - \frac{P_{static}}{P_r}\right)$$

P_r is the peak reflected overpressure, t_d is the equivalent time duration, I_r is the reflected impulse and t_{static} is the time at which the decaying pressure equals the static overpressure,P_{static}.

The solution for the elastic radial displacement and the maximum strain for a spherical shell subjected to an impulsive load is given in Equation 2.37 [77]. The load was deemed impulsive if the duration (t_d) was very short and much smaller than the vessels natural frequency ($t_d << \omega$).

$$\delta_r = \frac{I}{\rho h \omega} \sin \omega t \qquad \varepsilon_{max} = \frac{I}{h\sqrt{\rho}\sqrt{\frac{2E}{1-\nu}}} \tag{2.37}$$

Duffey *et al.* [77] further presents an analytical formula (Equation 2.38) to determine the elastic strain history.

$$\varepsilon(t) = \frac{I}{h\sqrt{\rho}\sqrt{\frac{2E}{1-\nu}}} f(\omega t, \omega \Delta T) \tag{2.38}$$

where

$$f(\omega t, \omega \Delta T) = \tfrac{1}{\omega \Delta t}(1 - \cos \omega t) \qquad \text{for } 0 \leq t \leq \Delta T$$

$$f(\omega \Delta T) = \tfrac{1}{\omega \Delta t}(\cos \omega (t - \Delta T) - \cos \omega t) \quad \text{for } t > \Delta T$$

Duffey *et al.* [77] compares theoretical predictions for the elastic strain history (Equation 2.38) and the experimentally measured strains. The experiments consisted of detonating a PBX-9404 spherical charge (diameter $25.4mm$) centrally within a spherical vessel (diameter of $325mm$; wall thickness of $6.35mm$). The strain was measured at several locations with strain gauges. Figure 2.39 illustrates the results of the predicted and measured strains.

The predicted initial peak strain was on average 20% higher than the strain gauge measurements. The remainder of the response could not be compared as motion of the shell was affected by two dimensional effects.

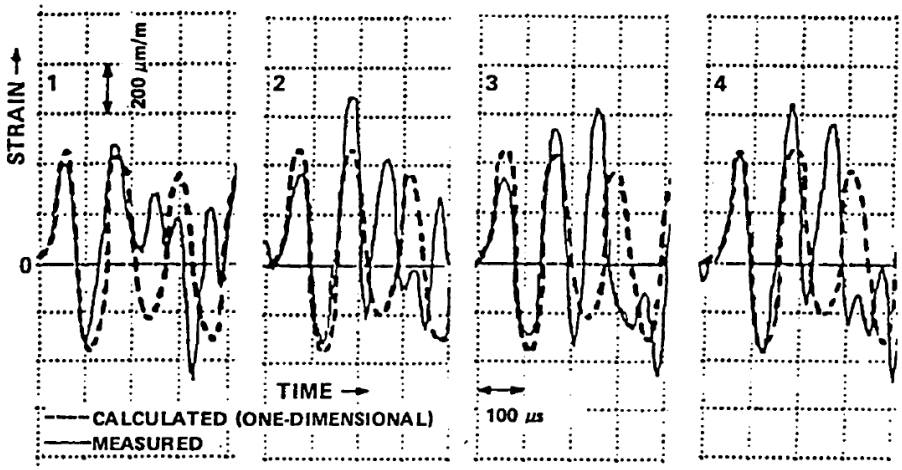

Figure 2.39: Comparison of Experimental and Calculated Strain [77]

Auslender and Combescure [78] presented an analytical solution for the elastic (Equation 2.41) and plastic (Equation 2.42) response of a hollow sphere. The thickness (h) of the hollow sphere was greater than 5% of the inner radius (R_i) preventing the use of shell theory and less than 20% of the inner radius which enabled the formulation of an important assumption for the analytical solution. The sphere material was characterised as an elastic-plastic material with isotropic linear elasticity and with isotropic work hardening in the plastic regime. The isotropic work hardening relation was given by,

$$\sigma_{eq} = \sigma_y + k\varepsilon_{eq}^p \tag{2.39}$$

where σ_{eq} is the equivalent stress, σ_y is the yield stress, k is the plastic hardening parameter and ε_{eq}^p is the total equivalent plastic strain.

The hollow sphere was subjected to an uniformly distributed pressure pulse of the form,

$$P(t) = P_r e^{-\frac{t}{t_d}} \tag{2.40}$$

where P_r is the peak reflected overpressure, t is the time and t_d is the duration of the pressure pulse.

The radial stress was assumed to be a linear decreasing function through the thickness of the sphere (the maximum stress occurring on inner surface) and that inertia effects generated by the dynamic load do not influence the radial stress. Based on these assumptions the elastic deflection was presented as,

$$\delta(r,t) = \frac{\Psi}{1+\alpha^2}[e^{-\frac{t}{t_d}} - \cos(\omega_o t) + \alpha\sin(\omega_o p)] \tag{2.41}$$

where

$$\begin{aligned} \omega_o^2 &= \tfrac{12\lambda\mu+8\mu^2}{\rho r^2(\lambda+2\mu)} \\ \alpha &= \tfrac{1}{\omega_o t_d} \\ \Psi &= \tfrac{1}{\omega_o^2}\tfrac{P}{\rho(R_o-R_i)}\left(1+\tfrac{4\mu(r-R_o)}{r(\lambda+2\mu)}\right) \end{aligned}$$

ω_o is the elastic cyclic frequency, λ & μ are the Lamé coefficients, R_i & R_o are the inner and outer radii respectively and r is the point of interest within the hollow sphere thickness.

The plastic phase radial deflection, neglecting elastic strains in work hardening law, proposed by Auslender and Combescure [78] was given as,

$$\delta_p(r,\tau) = A\cos(\omega_p(\tau+t_y)) + B\sin(\omega_p(\tau+t_y)) + \frac{Xe^{-(\tau+t_y)/t_d}}{1+\Upsilon^2} - \frac{\sigma_y r}{2k} \tag{2.42}$$

where

$$\begin{aligned}
\omega_p &= \tfrac{2\pi}{t_p} = \tfrac{1}{r}\sqrt{\tfrac{4k}{\rho}} \\
X &= \tfrac{P_r e^{-t_y/t}}{\rho(R_o-R_i)\omega_p^2} \\
\Upsilon &= \tfrac{t_p^2}{4\pi^2 t_d^2} \\
A &= \delta(r) - \tfrac{X}{1+\Upsilon^2} + \tfrac{\sigma_y r}{2k} \\
B &= \tfrac{\dot{\delta}_o(r)}{\omega_p} + \tfrac{\Upsilon X}{1+\Upsilon^2} \\
\tau &= t - t_y
\end{aligned}$$

t_y is the time of first yield, t_p is the plastic period of the shell, σ_y is the yield stress of the material, k is the work hardening parameter, $\delta(r)$ and $\dot{\delta}_o(r)$ are the final elastic displacements and velocities.

Auslender and Combescure [78] compared the predicted results to finite element simulations. Figure 2.40 illustrates the comparison between predicted and numerical results. Both results are in good agreement, however the shift in the numerical results are artificially created by the finite element calculation to process the discontinuity in the loading function [78].

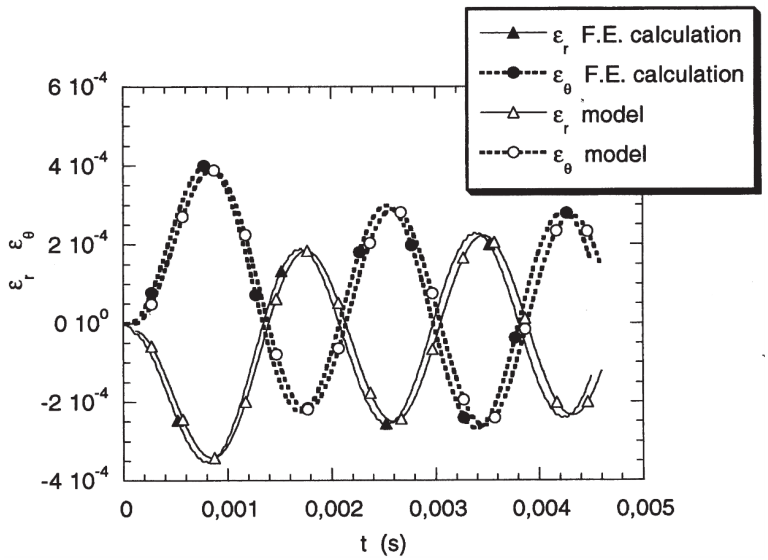

Figure 2.40: Experimental and Analytical Results Comparison for the Elastic Response of a Hollow Sphere [78]

White *et al.* [79] carried out a series of experiments to investigate the elastic response of a spherical vessel. The vessel was of diameter of $137mm$ and wall thickness of $2.54mm$. The mass of Pentolite detonated within the container was varied to obtain different magnitude loading. Experimental results were compared to the analytical approach presented by Baker *et al.* [76]. The experimental and predicted results are illustrated in Figure 2.41.

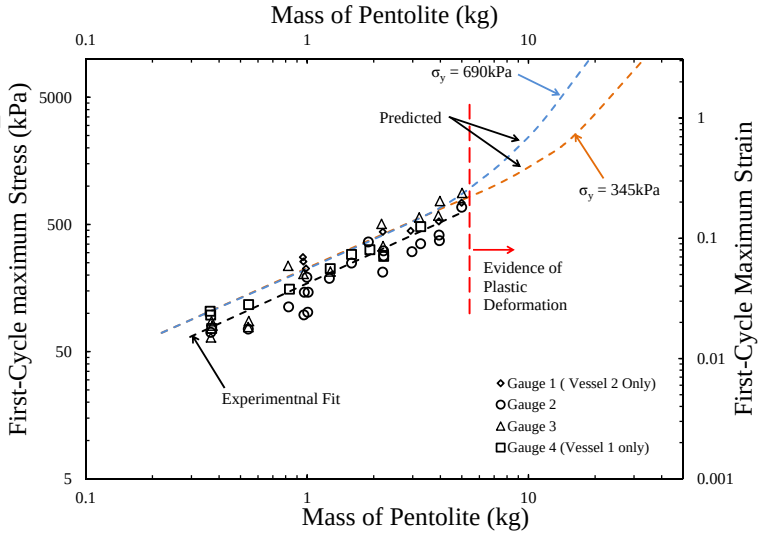

Figure 2.41: Experimental and Analytical Results Comparison for the Elastic Response of a Spherical Containment Vessel [79]

Typically the predicted stresses were on average 24% greater than the measured stresses, however all the results fell in the 90% confidence envelope. The difference between the results was attributed to the blast wave data for the analytical model. Full density Pentolite was used to generate the blast wave data for the analytical model however low-bulk-density Pentolite was used in the experiments which produced a weaker blast wave and hence less stress in the container [79].

Buzukov [80, 81] presented the first results that exhibited the phenomenon of strain growth in the vessel [82]. Strain growth is where the maximum elastic response of a vessel occurs after the initial response of the vessel [16, 83]. Figure 2.42 depicts strain growth in a cylindrical vessel, the maximum strain occurs at approximately $4ms$ after the initial peak. Strain growth has serious implications on the design of explosive chambers with respects to the fatigue life of the vessel. The strain growth phenomenon does not form part of this investigation and the reader is referred for further details on strain growth to References [82–85] for cylindrical vessels and References [16, 75, 85–89] for spherical vessels.

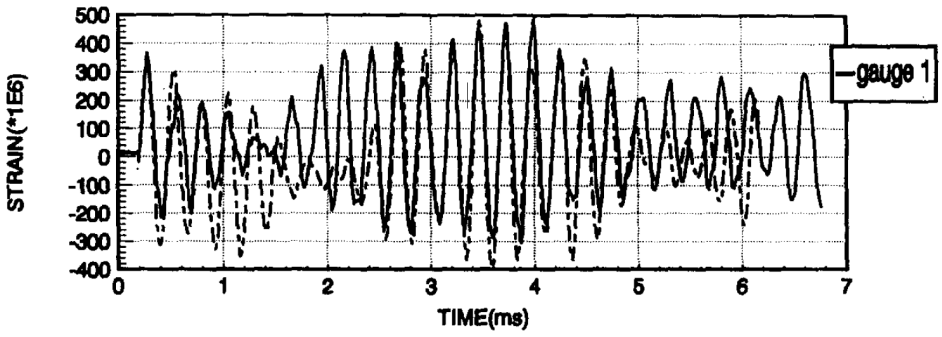

Figure 2.42: Strain History of Explosively Loaded Cylinder Exhibiting Strain Growth [84]

To improve the energy absorption characteristics of bomb disposal vessels White *et al.* [79] compared the response of elastic (multiple use) and elastic-plastic (single use) spherical containment vessels. White *et al.* [79] reported that elastic-plastic vessels can absorb from 25-1200 times more energy, with a weight reduction of 5-35 times in comparison to an elastic vessel of equal radii, explosive charge and material. Further details on design considerations, failure criteria and numerical modelling of spherical confinement vessels can be found in References [16, 90–97].

2.3.4.2 Cylindrical Confinement Vessel

A right-circular cylindrical structure is probably the most common shape of containment vessel due to ease of manufacture, the convenience of the shape and relative efficiency of absorbing internal blast loads [9].

Proctor [98] observed the near rupture deformation pattern in air or water filled right-circular stainless steel cylinders subjected to internal blast loading never exceeds a length of four radii and that the maximum radial deformation occurred nearest the mid-plane of the charge. Figure 2.43 illustrates the deformation pattern of air or water filled right-circular stainless steel cylindrical vessels where the maximum radial deformation occurs within the 'four' radii bounds.

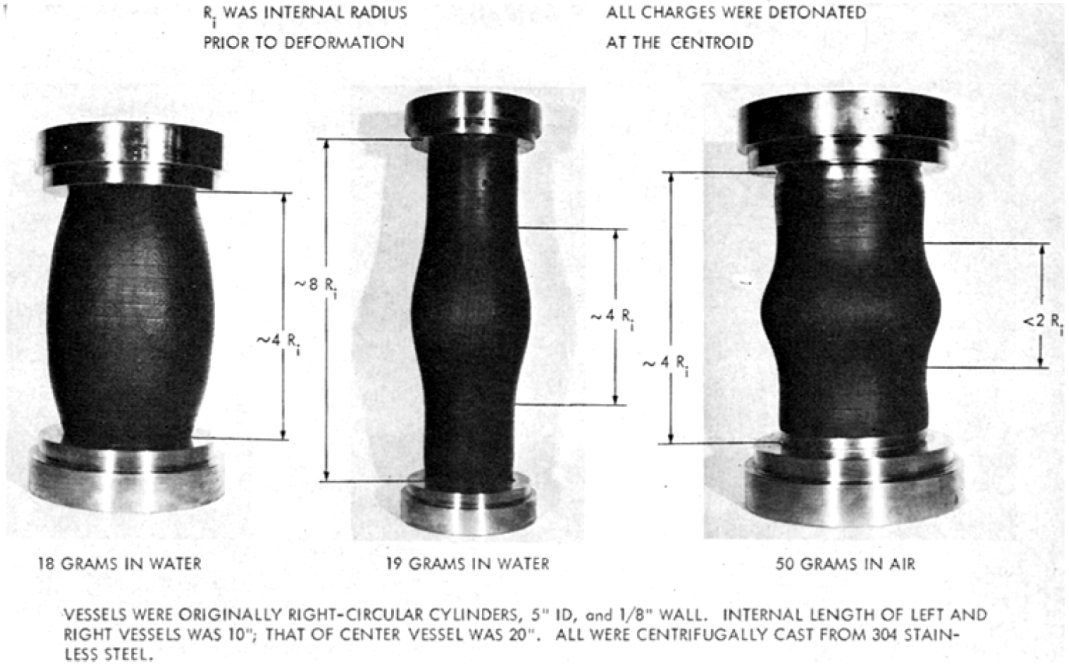

Figure 2.43: Deformation Pattern Observed on Air and Water Filled Cylinders [98]

Proctor [98] proposed Equation 2.43 which is the explosion-containment equation for water filled cylinders. The equation predicts the maximum charge mass ($(\overline{W}_R)_{max}$) a vessel can withstand before rupture, termed marginal containment [98].

$$(\overline{W}_R)_{max} = \left[\frac{\rho^{0.85}\varepsilon_u(2\sigma_y + \sigma_u + \sigma_u\varepsilon_u)(5.32 + 0.183R_i/h)(R_o^2 - R_i^2)^{1.85}}{10^6(1.47 + 0.0373R_i/h_o)^{0.15}R_i^{0.15}}\right]^{0.811} \tag{2.43}$$

where ρ is the density of the vessel material, ε_u is the ultimate tensile strain of the vessel material, σ_y is the yield stress of the vessel material, σ_u is the ultimate stress of the vessel material, R_i is the inner radius of the vessel, h is the vessel wall thickness and R_o is the outer radius of the vessel.

The relationships proposed by Proctor [98] cannot predict the magnitude of the radial displacement for a certain charge mass nor predict the bulge shape or strain distribution as a function of the axial length [9].

Duffey and Mitchell [9] and Benham and Duffey [99] investigated the response of mild steel air filled cylindrical containers with open and closed ends subjected to internal blast loading respectively. The work of Duffey and Mitchell [9] focused on the radial strain as a function of the axial length, whereas Benham and Duffey [99] focused on the peak radial deflection and hence circumferential strain and not the final deformed shape of the cylindrical vessel. Figure 2.44 illustrates the geometries of the cylinders implemented by Duffey and Mitchell [9] and Benham and Duffey [99].

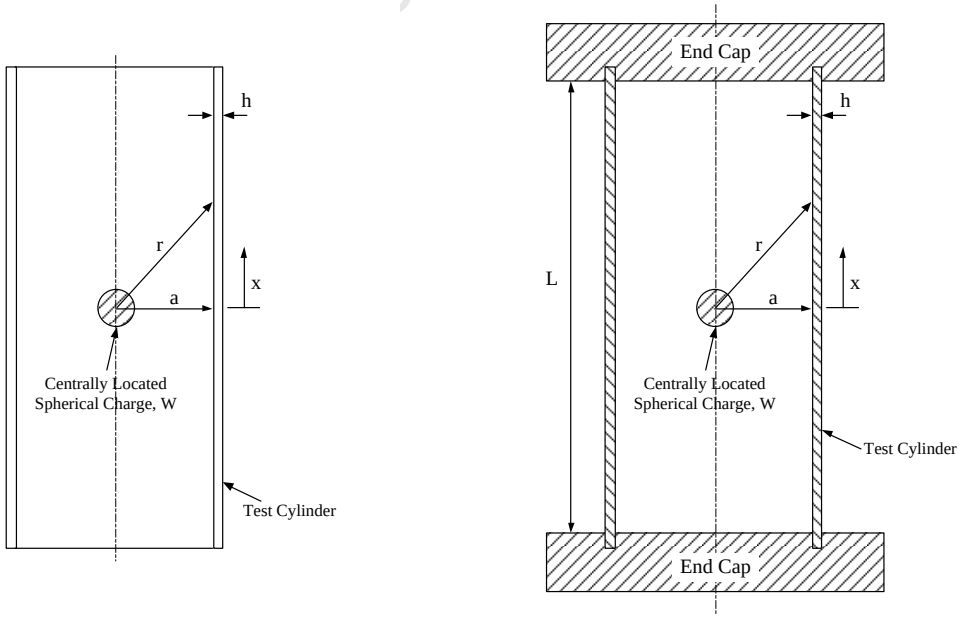

(a) Open Cylindrical Vessel [9] (b) Closed Cylindrical Vessel [99]

Figure 2.44: Schematic of Cylindrical Vessel Geometry

Duffey and Mitchell [9] proposed Equation 2.44 to determine the radial strain as a function of the radial length in a cylinder with open ends (Figure 2.44a) subjected to a purely impulsive load. Equation 2.44 was obtained by utilizing axisymmetry, assuming the shell wall was sufficiently thin so that wave propagation thought the thickness could be neglected and the fact that the ends of the cylinder were open eliminating the axial inertial effects (no axial stress). Equation 2.44 also incorporates rigid-linearly strain hardening material with strain rate sensitivity.

$$\varepsilon(x) = \frac{I_{eff}^2(x)}{2\rho h^2 \sigma_y \left[1 + \left(\frac{I_{eff}(x)}{\rho h R D}\right)^{\frac{1}{p}}\right]} \tag{2.44}$$

Where I_{eff} is the effective reflective impulse and was calculated with Equation 2.45, ρ is the density of the vessel material, h is the wall thickness, σ_y is the yield stress, R is the cylinder radius and D, p are strain rate sensitivity constants.

$$I_{eff} = (I_{nr} - I_{so})\frac{R}{(R^2 - x^2)} + I_{so} \tag{2.45}$$

where x is the axial distance along the cylinder (shown in Figure 2.44), I_{so} and I_{nr} are the side on and resultant impulse respectively and are calculated with Equations 2.46 and 2.47 respectively.

$$\frac{I_{so}}{P_o^{\frac{2}{3}} W^{\frac{1}{3}}} = \frac{0.06333}{P_o^{\frac{1}{3}} Z} - \frac{0.06289}{(P_o^{\frac{1}{3}} Z)^2} \qquad \text{for } 2.38 \leq P_o^{\frac{1}{3}} Z \leq 68 \tag{2.46}$$

$$\frac{I_{nr}}{P_o^{\frac{2}{3}} W^{\frac{1}{3}}} = \frac{0.1204}{P_o^{\frac{1}{3}} Z} + \frac{0.1384}{(P_o^{\frac{1}{3}} Z)^2} + \frac{0.003708}{(P_o^{\frac{1}{3}} Z)^3} \qquad \text{for } 0.1096 \leq P_o^{\frac{1}{3}} Z \leq 23.8 \tag{2.47}$$

where P_o is the ambient pressure, W is the explosive mass, Z is the scaled distance ($Z = (x^2 + R^2)/W^{1/3}$). The constants in Equations 2.46 and 2.47 are based on empirical data for Pentolite explosive.

Figure 2.45 presents the theoretical and experimental peak strain results obtained for mild and stainless steel cylinders. The two experimental readings were measured on either side of the maximum deformation to illustrate the symmetry of the deformation. In the case of the mild steel results (Figure 2.45a) the predicted peak strain was lower than the experimental values, this was attributed to the strain rate sensitivity model used for the predictions [9]. However reasonable predictions were obtained for the maximum strain. The predictions for stainless steel (Figure 2.45b) ignored strain rate effects of the material. However an extreme strain hardening model was implemented. The predictions and experimental results were in close agreement along the axial length of the cylinder.

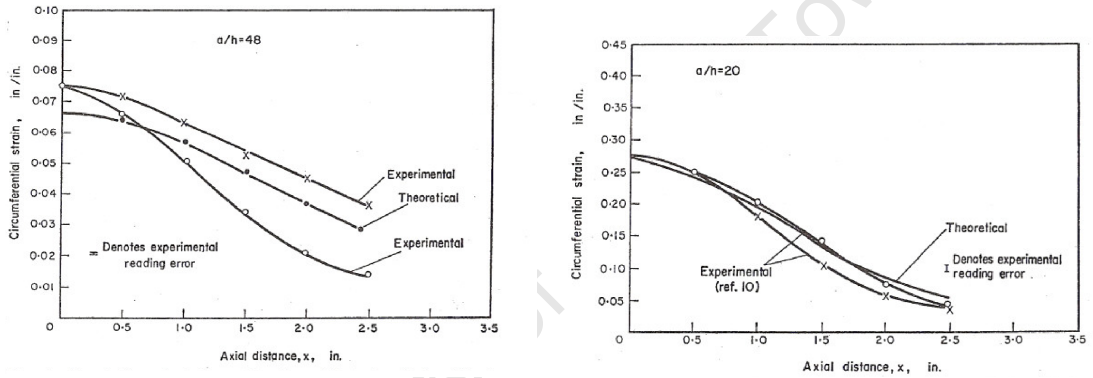

(a) (b)

Figure 2.45: Circumferential Strain Versus Axial distance Results for Cylinders with Open Ends Subjected to an Internal Blast Load [9] (a) 50g of Pentolite in Mild Steel Vessel and (b) 50g of Pentolite in Stainless Steel Vessel.

Benham and Duffey [99] proposed Equation 2.48 to predict the radial displacement of a cylinder where the length is greater than twice the radius($L > 2R$). The axial stress and axial bending moment were both neglected from the model to simplify the solutions.

$$\frac{d^2\delta_r}{dt^2} + \frac{\lambda\sigma_y^D}{\rho R^2}w + \frac{\sigma_y^D}{\rho R} = \frac{I_o}{\rho h}\delta(t) + \frac{P_o}{\rho h}U(t-T)exp[-\alpha(t-T)] \tag{2.48}$$

Where δ_r is the radial displacement, T is the delay time between the impulsive and long-term pressure, $U(t-T)$ is the heaviside step function, $\delta(t)$ is the delta function,

α is the pressure decay constant, h is the wall thickness, σ_y is the yield stress, R is the cylinder radius, ρ is the mass density, λ is the strain hardening parameter, I_o is the initial specific impulse and P_o is the magnitude of the equilibrium pressure which was calculated as,

$$P_o = \frac{CW}{V} \tag{2.49}$$

where W is the mass of explosive, V is the empty volume of the cylinder and C is the explosive constant ($3000 ft^3 psi/lb$ ($\approx 1.3 m^3 MPa/kg$) for common solid secondary explosive [99]).

The pressure loading applied to the inside walls of the cylindrical container was described in Equation 2.50 and shown graphical in Figure 2.46.

$$p(t) = I_n r\delta(t) + P_o U(t-T)e^{-\alpha(t-T)} \tag{2.50}$$

where I_{nr} is the specific impulse and was determined from Equation 2.47 , T is the delay between the initial impulse and the application of the long term pressure, P_o is the magnitude of the equilibrium pressure and α is the pressure decay constant.

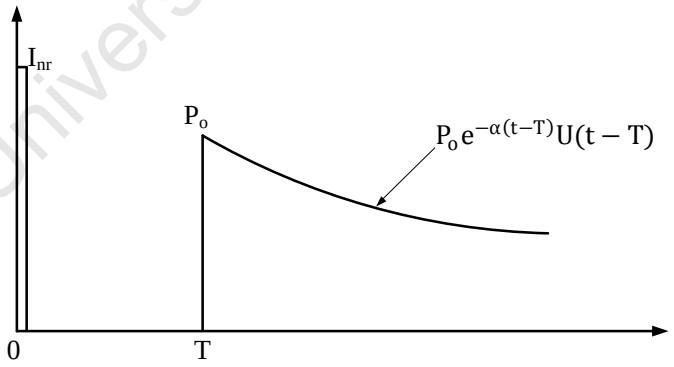

Figure 2.46: Assumed Pressure Profile Applied to Inner Walls of a Cylindrical Container [99]

Two theoretical bounds on the final maximum deformation exist for Equation 2.48. The lower bound was given by considering a constant yield stress and the cylinder was open-ended. The upper bound is given by a dynamic yield stress in a closed ended cylinder. The upper bound solution was obtain by numerically solving Equation 2.48.

The solution for the lower bound is given by,

$$\delta_r(t) = \frac{\mu}{\beta^{\frac{1}{2}}} \sin \beta^{\frac{1}{2}} t - \frac{\gamma}{\beta}(1 - \cos \beta^{\frac{1}{2}} t) + \ldots$$
$$\zeta U(t-T) \left(\frac{exp[-\alpha(t-T)]}{\alpha^2 + \beta} + \frac{\sin(\beta^{\frac{1}{2}}(t-T) - \xi)}{\beta^{\frac{1}{2}}(\alpha^2+\beta)^{\frac{1}{2}}} \right) \tag{2.51}$$

Where

$$\beta = \frac{\lambda \sigma_y^D}{\rho R^2} \qquad \gamma = \frac{\sigma_y^D}{\rho R} \qquad \mu = \frac{I_{nr}}{\rho h}$$

$$\zeta = \frac{P_o}{\rho h} \qquad \xi = \tan^{-1}\left(\frac{\beta^{\frac{1}{2}}}{\alpha}\right)$$

Figure 2.47 illustrates the experimental and predicted results presented by Benham and Duffey [99]. The maximum radial deformation was normalised by the material yield stress.

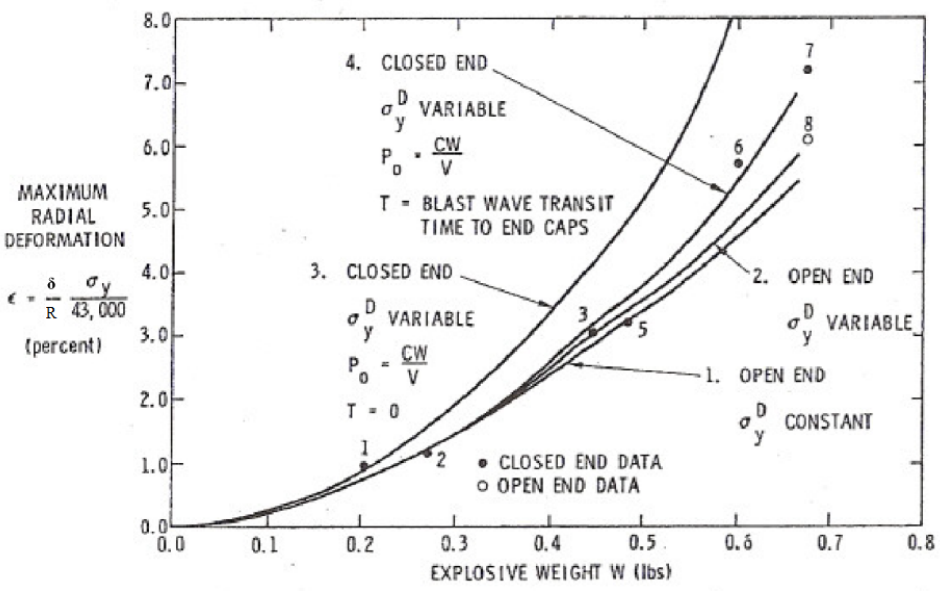

Figure 2.47: Theoretical Predictions and Experimental Results for Internal Blast Loading of Cylindrical Containers [99]

The four predicted curves shown in Figure 2.47 correspond to:

Curve 1 - a closed form solution to Equation 2.48 assuming the ends of the cylinders are open (i.e. $P_o = 0$) and the yield stress is held constant. The closed form solution is given in Equation 2.51. This solution generates the lower bound prediction limit.

Curve 2 - a numerical solution to Equation 2.48, where the yield stress is variable and the cylinder is assumed open.

Curve 3 - a numerical solution to Equation 2.48 for a closed cylinder, in which strain rate variations of the yield stress are included and the static internal pressure generated by the explosion is applied a T=0. This solution generates the upper bound prediction limit.

Curve 4 - Similar to Curve 3 but static internal pressure is applied at the delayed time T, which is the time between the initial impulse load and the application of the quasi-static pressure.

The experimental results fall within bounds (upper bound - curve 3, lower bound - curve 1) of the predictions [99]. The good correlation between experimental and curve 4 supported the use a delay between the impulsive and equilibrium load to predict the final maximum radial deformation. Benham and Duffey [99] presented Equation 2.52 to determine the type of loading which governed radial deformation.

$$\bar{\eta} = \eta \left(\frac{t_{max} - T}{t_{max}} \right) \qquad \text{where } \bar{\eta} = 0 \text{ for } T > t_{max} \tag{2.52}$$

where $\bar{\eta}$ is the effective internal pressure ratio, η is the ratio of the equilibrium pressure(Equation 2.49) to the static burst pressure of the cylinder($h/R \times \sigma_{UTS}$), t_{max} is the time taken to reach the peak deflection and T is the delay between the impulsive load and the equilibrium pressure.

Benham and Duffey [99] observed, both theoretically and experimentally, that for R/h of 20 and a 21-inch long cylinder the load can be categorised by,

$$\begin{aligned} \text{Purely Impulsive:} \quad & 0 < \bar{\eta} < 0.3 \\ \text{Impulsive and long term pressure:} \quad & 0.3 < \bar{\eta} < 0.8 \end{aligned}$$

For $0.8 < \bar{\eta} < 1$ unpredictably large deformation occurs and if $\bar{\eta} > 1$ bursting of the cylinder may occur. The value of $\bar{\eta}$ can be easily calculated for a given design to determine whether the loading will be purely impulsive, a combination of impulsive and pressure loading or the cylinder may burst [99].

The dynamic plastic response of a short cylindrical shell subjected to different idealised pressure pulses (rectangular, exponential decay and triangular) was presented by Li and Jones [100]. The transverse shear force, circumferential membrane force and the longitudinal bending moment were retained in the model. Li and Jones [100] also reported that the boundary conditions placed on the ends of the cylindrical shell influence the final permanent transverse displacement.

Martineau *et al.* [101] carried out two experiments to provide experimental data for validation of numerical codes. The cylindrical shells, in the experiments, were subjected to internal blast loads which caused radial expansion at strain rates in the order of $10^{-4}s^{-1}$. The cylindrical shells characterised by the wall thickness ($2.54mm$ and $5.08mm$) were fabricated from 101 OFE[2] copper and had internal diameter of $102.06mm$ and a length of $406.4mm$. A solid circular cylinder of PBX-9501 high explosive, which extended the length of the cylinder, was located centrally within the cylinder and detonated from one of the ends of the cylinder. Figure 2.48 is a series of photographs, obtained from the high speed camera, illustrating the transient deformation of the $2.54mm$ thick cylindrical shell.

[2]OFE - Oxygen-Free-Electronic

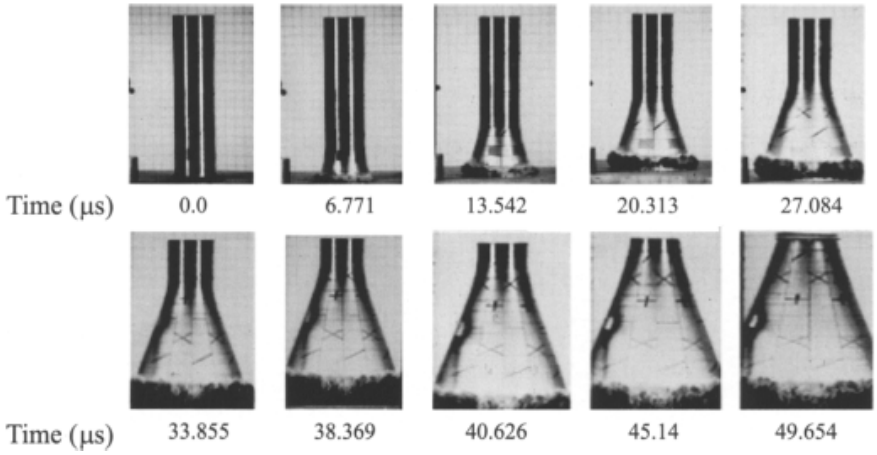

Figure 2.48: High Speed Camera Footage of Explosively Loaded Thin Cylindrical Shell [101]

Martineau *et al.* [101] also carried out an experiment to illustrate the instabilities in the copper sample before fragmentation occurred. The experiment consisted of detonating an axially aligned slug of C4 explosive (diameter - 12.7mm, length - 76.2mm) in a 304.8mm long OFE copper cylinder with a 2.54mm inner diameter and a wall thickness of 6.35mm. Figure 2.49a illustrates the results obtained from the experiment. The arrows in Figure 2.49a highlight the location of several visible instabilities on the outer surface of the cylinder. Figure 2.49b is a photomicrograph of the micro-structure of the cylinder at one of the visible instabilities. It was evident that large ductile deformation had occurred from the elongated grains and that instabilities develop on both the inner and outer surfaces.

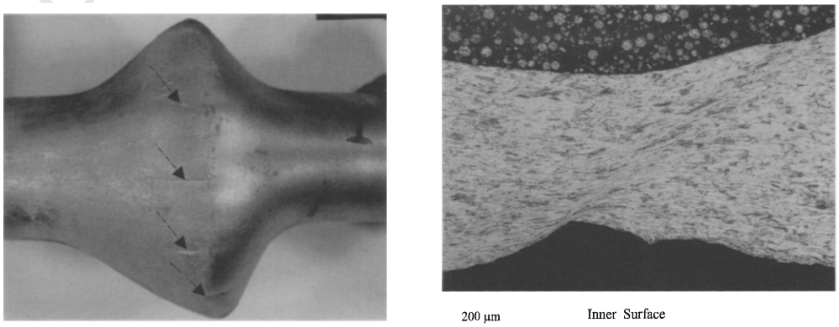

(a) (b)

Figure 2.49: Results of Explosively Loaded OFE Copper Cylindrical Shells [101] (a)Bulged Cylinder from C4 Experiment, (b) Shear Band in Cylinder Wall from C4 Experiment.

Held [102] proposed an empirical relationship (Equation 2.53) between the radius of a steel tube (R) and the degree of damage (η). A relatively small bulge was declared as 10% damage, partially tearing as 40% damage and substantial petalling as 80% damage [102]. Examples of the degrees of damage are illustrated in Figure 2.50.

$$R = 0.447 \times \eta^{-0.291} \times W^{0.58} \times (10^3 \times h)^{-0.5} \tag{2.53}$$

where R is the inner radius of the tube, η is the degree of damage, W is the charge mass and h is the tube wall thickness.

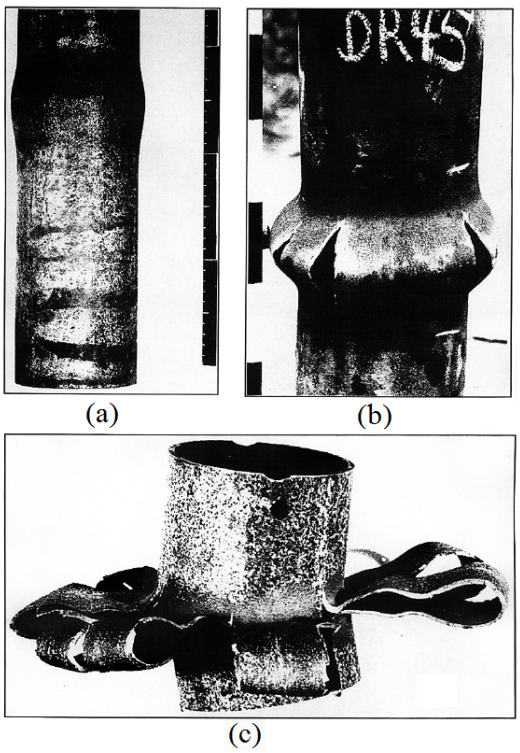

Figure 2.50: Examples of Degrees of Damage (η) [101]: (a) 10%, (b) 40% and (c) 80%

A extensive history on explosion containment vessels was presented by Zheng *et al.* [103]. Zheng *et al.* [103] discussed multiple-use, single-use, single-layered, multi-layered, metallic and composite containment vessels and their applications through the years. Zheng *et al.* [103] also present the key concepts and methods for the design of containment vessels such as scale effects, failure modes and failure criteria. Further details of composite containment vessels can be found in References [104–106].

2.3.4.3 Cuboidal Confinement Vessel

Research into explosion confinement cuboidal containers has been carried out with much research in recent years, especially in the aviation sector where the luggage containers may be approximated as cubic containers. Many investigations have been carried out, however the results have been classified or only published as company or institute reports and never made public [6, 10, 11].

Yiannakopoulos [107, 108] and Yiannakopoulos and Kiernan [109] carried out several experiments to determine the optimal mounting techniques for pressure transducers and accelerometers to the walls of a thin walled cuboidal containers subjected to internal blasts respectively. The explosive charge, Pentolite, was located and detonated centrally within an $1 \times 1 \times 1m$ mild steel cube container having a wall thickness of $5mm$.

Yiannakopoulos [107] investigated the optimal accelerometer and mounting technique for measuring the acceleration of the midpoint of a deforming side wall of a cuboidal container. The accelerometers and pressure transducers were mounted near the midpoints of the walls of the containers. Table 2.1 lists the experimental configurations implemented.

Table 2.1: Accelerometer and Mounts Implemented by Yiannakopoulos [107]

Wall	Label	Accelerometer	Label	Pressure Transducer
1	A1	Endevco 7255A-01/adaptor, 50,000g range	P1	PCB 109A
2	A2	Endevco 7270AM6/adaptor, 60,000g range	P2	PCB 109A
3	A3	Endevco 7270A-20K /cap/bromo-butyl pads	P3	PCB 109A
4	A4	Endevco 7270A-20K/cap/PRC-1422 polysulphide pads	P4	PCB 109A

The measured pressures and accelerations from two experiments (Events 1 & 2) are illustrated into Figure 2.51. Both experiments were carried out with a Pentolite charge mass of $250g$. The recording of the pressure histories was not successful due to faulty inserts resulting in the transducer being ejected from the mounts [107]. However, the arrival time of the blast wave was recorded and was useful in estimating the peak reflected overpressure. Both the raw and smoothed (software generated $40kHz$ low pass filter) acceleration signals are depicted in Figure 2.51.

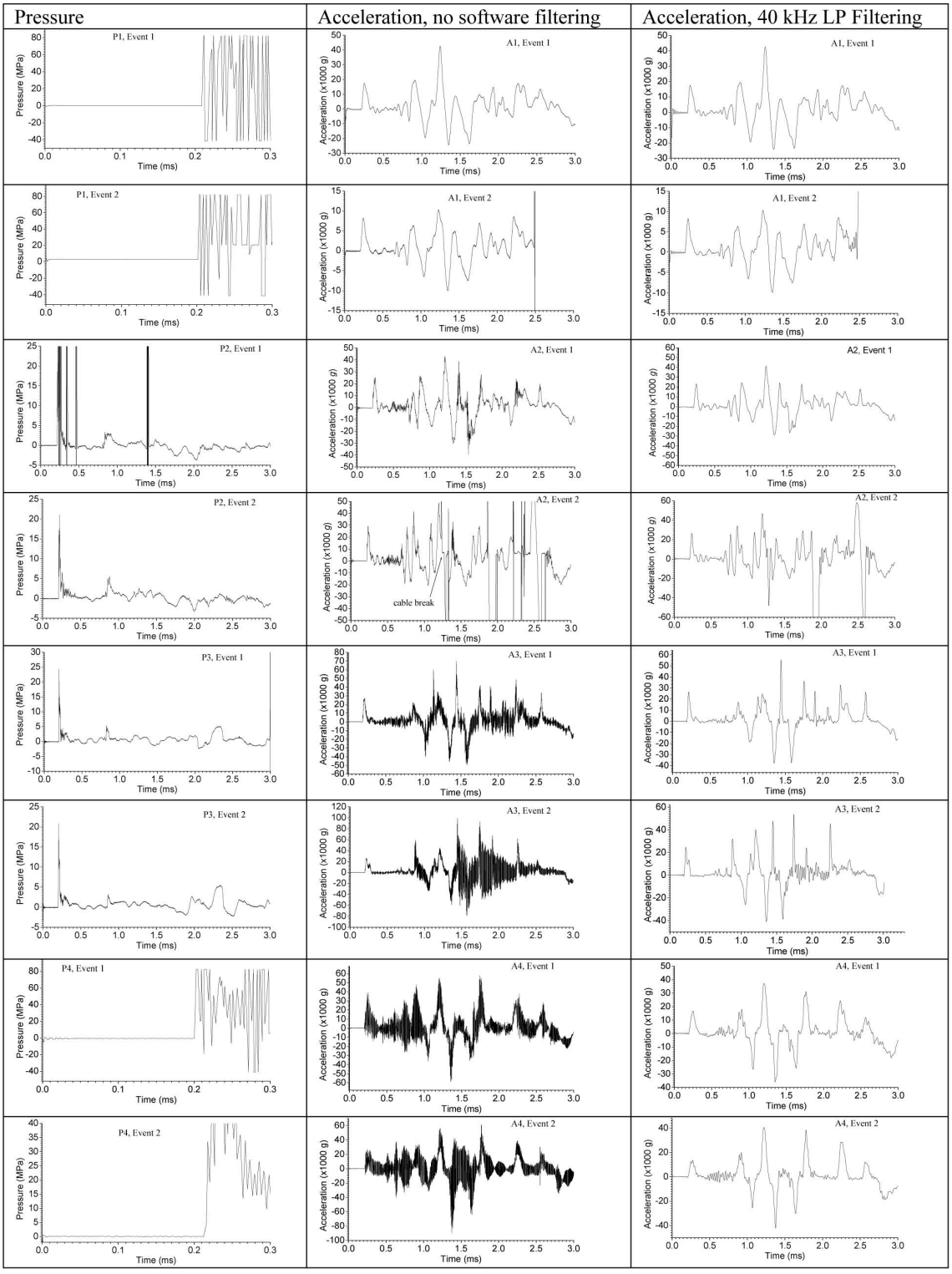

Figure 2.51: Pressure and Acceleration Results for a $250g$ Pentolite Charge Detonation Within a $1m^3$ Mild Steel Cuboidal Container [107]

In several experiments the cable failure due to cable whipping was observed, see Figure 2.51 – A1 Event 2 and A2 Event 2. The velocities and the displacements of the different accelerometers is depicted in Figure 2.52. The velocity and displacement were obtained from integrating the acceleration signal. Figures 2.51 and 2.52 show that there is good agreement between all the different mounting assemblies. The mounting technique A3 (Endevco 7270A-20K /cap/bromo-butyl pads) provided the most consistent results between the two experiments.

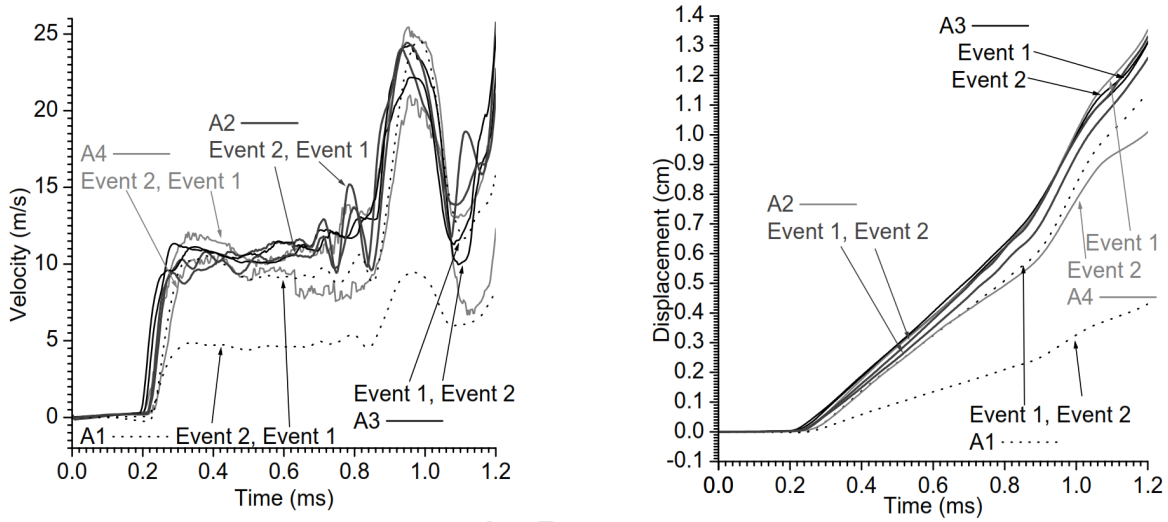

Figure 2.52: Velocity and Displacement Results Obtained from Integrating Acceleration Signal [107]

Yiannakopoulos and Kiernan [109] carried out further experimentation to determine optimal pressure transducer mounts for thin metal cuboidal containers. The experimental setup was similar to Yiannakopoulos [107] however the mass of explosive increased to $1kg$ and the pressures were measured at several locations to investigate the effects of blast wave enchantment at the different interaction interfaces. Yiannakopoulos and Kiernan [109] also carried full scale experiments in the magazine and missile storage rooms aboard a decommissioned ship. However these results are omitted from this report.

Figure 2.53 illustrates the location of the pressure transducers monitored by Yiannakopoulos and Kiernan [109]. The pressure transducers were PCB-109A piezoelectric type with a ceramic coating to protect the sensor from the effects of the detonation

flash and impact due to shrapnel from the detonator casing.

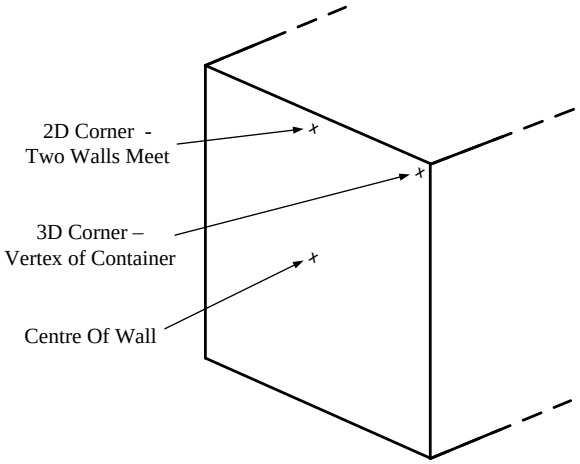

Figure 2.53: Locations of Pressure Transducers on $1m^3$ Steel Cubic Container [109]

The pressure histories for a $1kg$ charge of Pentolite explosive are illustrated in Figure 2.54. The difference in the pressure histories is clearly evident. The pressure history at the 2D corner (Figure 2.54b) has lower peak overpressure in comparison to the midpoint peak overpressure, however the duration of the blast load is significantly longer. The peak overpressure and durations of the blast load at the 3D corner (Figure 2.54c) are greater than both the midpoint and 2D corner suggesting the greatest loads occur at the corners of a cuboidal container.

To validate the simulations Yiannakopoulos [14] carried out two experiments where $250g$ of Pentolite explosive was centrally located and detonated within a $1m^3$ cubicle container having a wall thickness of $5mm$. The pressures and accelerations at the midpoint were recorded for the first $3ms$ and the displacement was measured with streak photography. The experiments were also filmed with a high speed camera. The mounting techniques for the pressure transducer and accelerometers were presented by Yiannakopoulos and Kiernan [109] and Yiannakopoulos [107] respectively.

Figure 2.55 is a series of photographs, recorded by a high speed camera, illustrating the detonation sequence and the resulting deformation of a cubicle container subjected to an internal blast load. The fireball generated by the detonation of the explosive is seen escaping the container at $1ms$ [14]. Large plastic deformation is evident from $2.5ms$

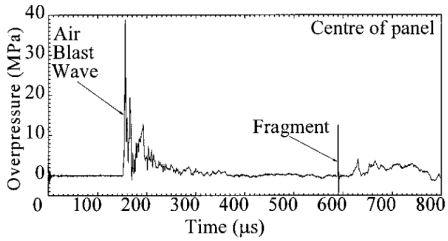

(a) Overpressure At Centre of Wall

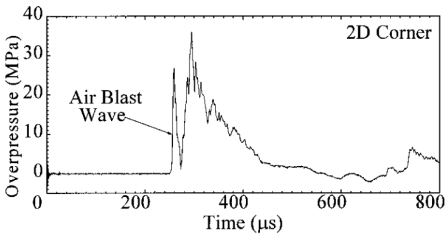

(b) Overpressure Near 2D Corner

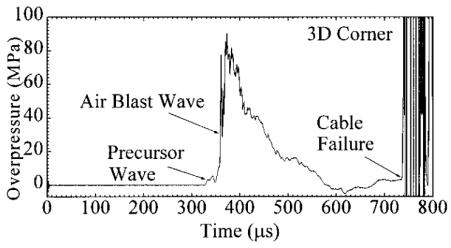

(c) Overpressure Near 3D Corner

Figure 2.54: Pressure History Measured for a $1kg$ Pentolite Charge Detonated in a $1m^3$ Cubic Container [109]

and, though not clear in Figure 2.55, rupture of one on the walls occurs at $20ms$.

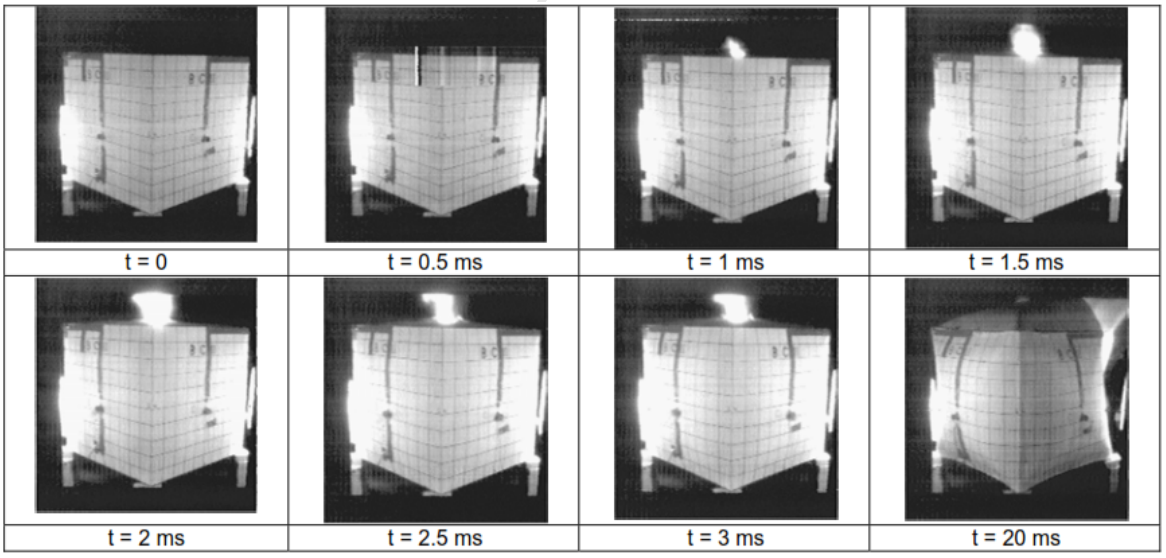

Figure 2.55: High Speed Camera Footage Illustrating Detonation Sequence and Deformation of Cuboidal Container Subjected to Internal Blast Loading [14]

The pressure and acceleration histories obtained from one side wall for both experiments are illustrated in Figure 2.56. A summary of the experimental results are listed in Table 2.2.

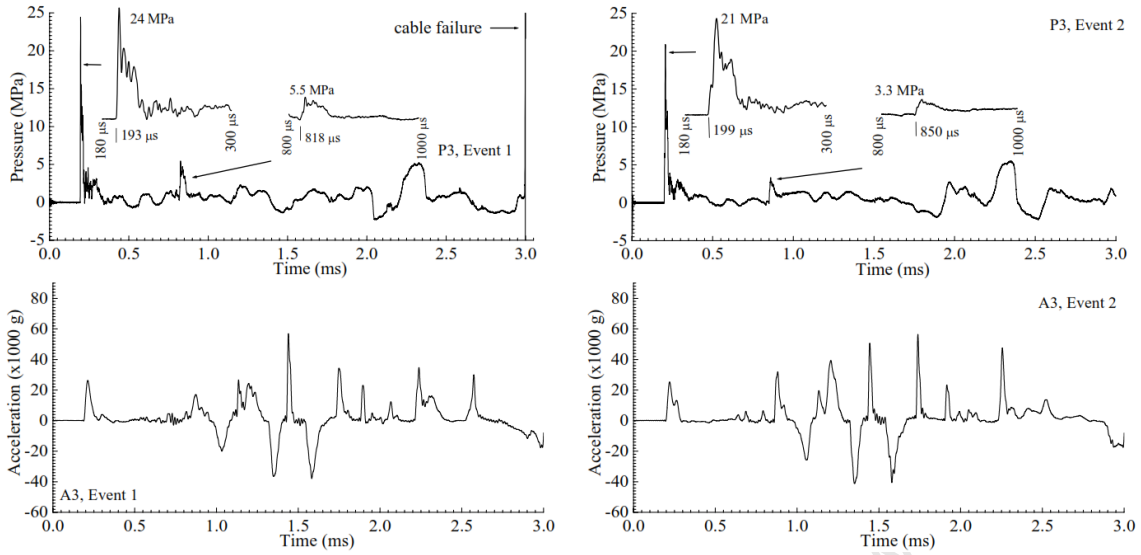

Figure 2.56: Pressure and Acceleration Histories for Steel Container with a 250g Pentolite Charge [14]

Table 2.2: Summary of Experimental Results For Validation of Finite Element Model [14]

Experiment	Peak Reflected Pressure (MPa)	Arrival Time (μs)	Specific Impulse (kPa.s)	Peak Acceleration (g)	Final Displacement from Acceleration Signal at 1440μs (cm)	Final Displacement from Streak Photography at 1330μs (cm)
1	24	193	0.56	26300	1.95	2.1
2	21	199	0.41	25300	1.96	NA

Yiannakopoulos [14] present different finite element modelling techniques to simulate internal air blast loading inside a steel cubicle. The finite element modelling techniques evaluated in the first series of simulations are,

1. Lagrangian (LAG) with default hourglass control. The air, explosive and wall utilise Lagrangian mesh.

2. Lagrangian with Flanagan-Belytschko stiffness hourglass control (HLAG), similar to LAG.

3. Arbitrary-Lagrangian-Eulerian (ALE), both the air and explosive are re-meshed at each time step.

4. Arbitrary-Lagrangian-Eulerian with hourglass control (HALE) where the explosive has hourglass control and the air is re-meshed at each time step.

5. Eulerian (EUL) both the explosive and air are modelled with Eulerian elements and the wall with Lagrangian elements.

6. Eulerian with a constrained Lagrangian plate (EULC) in which the wall of the container are embedded in the air and move through the air-explosive mesh.

The models in the first series of simulations had identical mesh sizes, illustrated in Figure 2.57.

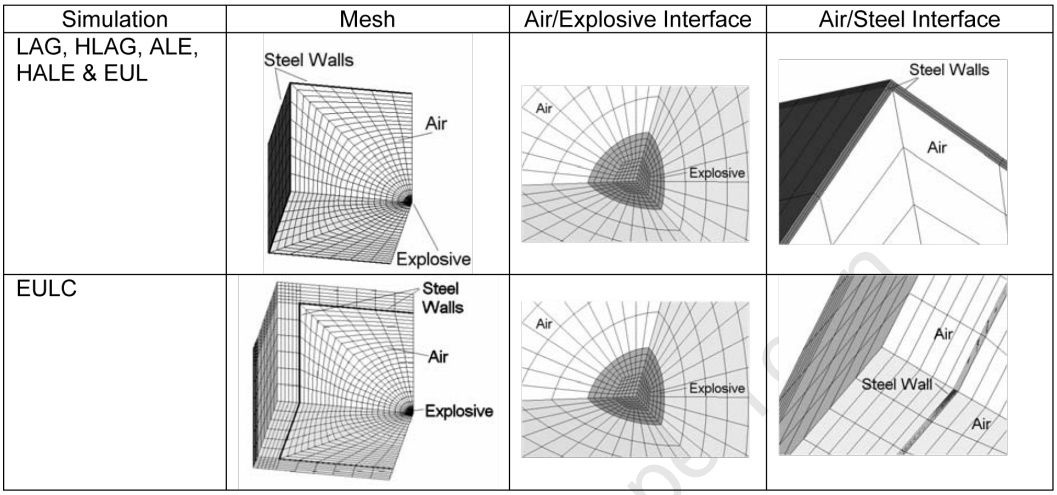

Figure 2.57: Meshed Models for the Simulations of a Cubic Containment Vessel [14]

The finite element package LS-DYNA3D was used to model the various techniques. One eighth symmetric models were implemented to simulate the experiments which were meshed with 8 node brick elements. The termination time of the first series of simulations was set to $1400\mu s$ which was sufficient to capture the reflection of the initial blast wave [14]. The results of the various techniques are illustrated in Figure 2.58.

Both the LAG and HLAG solutions provided results that were comparable to the experiments, however in both cases the mesh distortion (bowtie elements) was severe and explosive elements jetted through the structure. In the case of the HLAG the simulation terminated with an error at $1080\mu s$. The ALE simulation resolved the mesh distortion but boomerang elements did appear and drastically slowed the simulation. The ALE simulations was manually terminated at $310\mu s$ due to the increased runtime occurred from the boomerang elements.

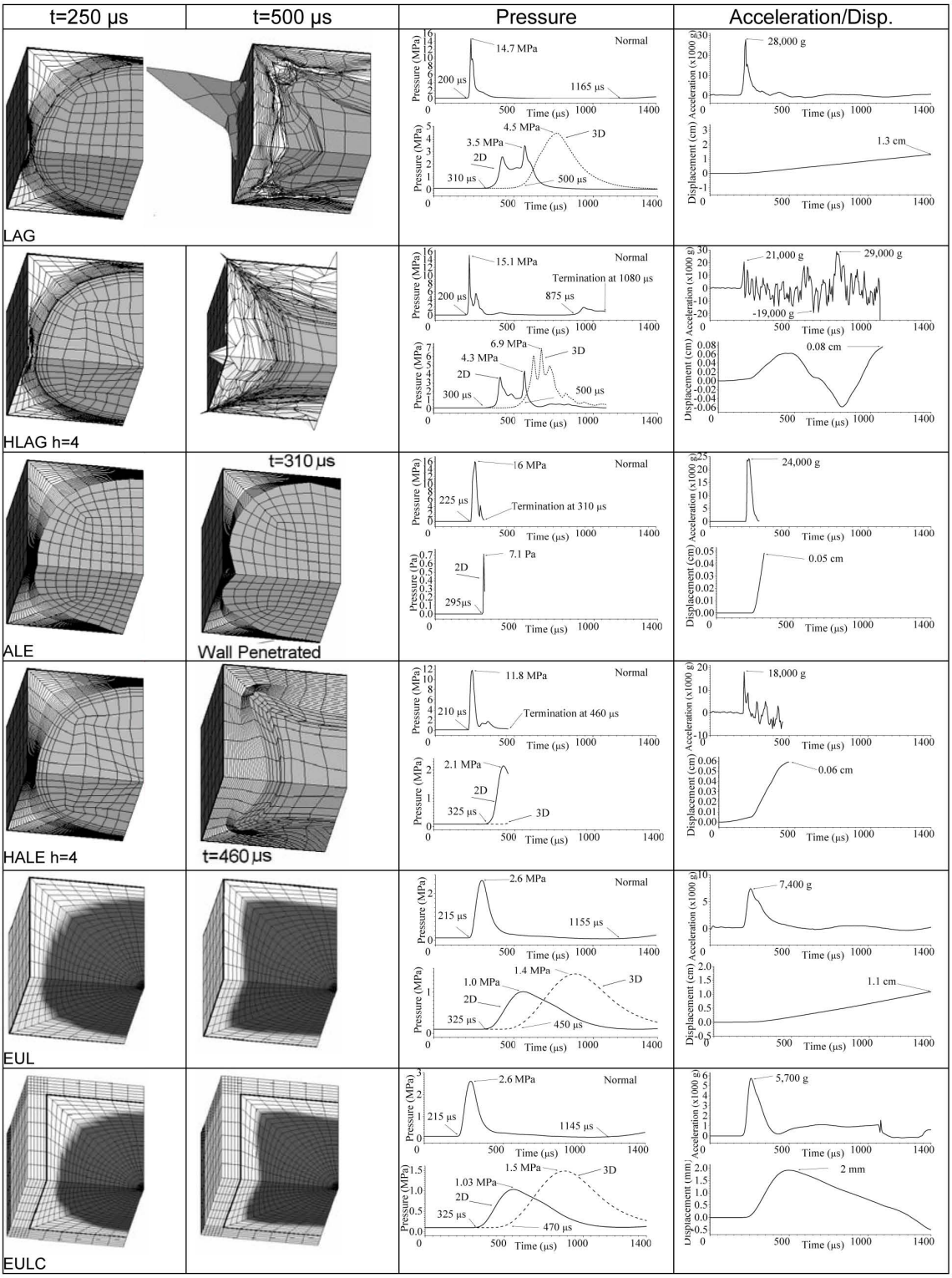

Figure 2.58: Finite Element Results For Different Numerical Formulations – Series One [14]

The HALE simulation ran to $460\mu s$ before boomerang elements appeared and the simulation was halted. The EUL and EULC simulation ran to the predetermined termination time, however the peak pressures, resulting impulses and accelerations were low in comparison to the experiments. The lower results were expected due to the abrupt mesh change at the explosive/air interface [14].

The second series of simulations extended the termination time of the most successful simulations from series one (EUL and HLAG) to $3ms$. HLAG was replaced with HALE as the run time of HLAG could not be extended due to severe mesh distortion. The models were meshed with finer mesh, termed HALEHI and EULHI, to improve stability and investigate the effect of mesh size on the peak pressures. An additional model was included in which the air/explosive was made up of uniform cube Eulerian elements (EULCUBE). The results for the seconds series of simulations is depicted in Figure 2.59.

The HALE simulation terminated early ($945\mu s$) due to the presence of boomerang elements which induced oscillation in both the acceleration and displacement. HALEHI simulation produced the highest peak pressure and impulses, however the simulation terminated at $570\mu s$. The air and explosive meshes were deleted from both the HALE and HALEHI simulations at the termination times and were restarted and set to a $3ms$ runtime . The oscillations in the accelerations and displacements of the wall continued throughout the simulation.

The EULHI simulation which went to the termination time and produced a slightly higher pressure than the EUL simulation. The EULCUBE simulation resulted in a higher pressure than the EULHI simulation and a better correlation to the experimental acceleration. The results from the EUL, EULHI and EULCUBE simulations illustrated the effects of mesh size on the simulations results.

From the results of the simulations Yiannakopoulos [14] states that Eulerian formulation provides close correlation to experimental results however a very fine mesh is required to capture the blast wave and hence is computationally expensive.

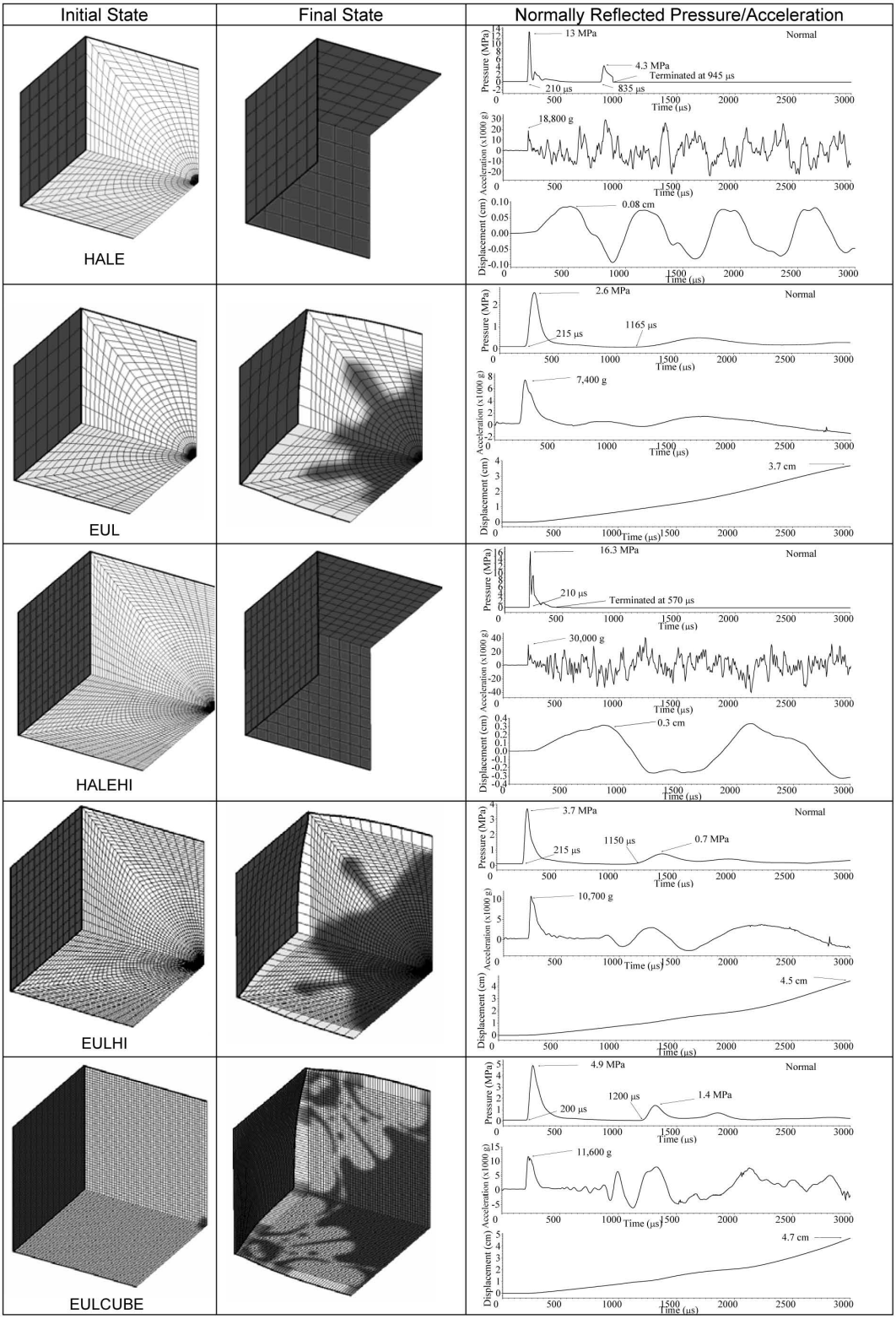

Figure 2.59: Finite Element Results For Different Numerical Formulations – Series Two [14]

A comparison between experimental results and numerical results for the response of a rectangular container to internal blast loading was carried out by Brundage *et al.* [17]. The experiments consisted of detonating a cylindrical charge at the centre of an instrumented rectangular container, illustrated in Figure 2.60. The container was manufactured from $3/16in$ ($\approx 4.8mm$) thick A36 steel. The plates were butt welded together and the joints reinforced with steel angles.

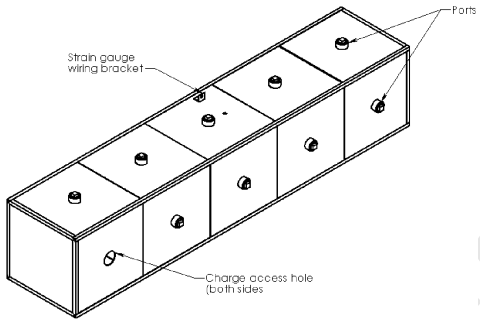

Figure 2.60: Rectangular Container [17]

Brundage *et al.* [17] modelled the experiments with a shock physics code (CTH) to predict the blast loading and a structural dynamics code (PRONTO3D) to predict the structural response of the container. Figure 2.61 compares the predicted(CTH) and experimental pressure histories at two gauge locations. The exact position of where the pressure gauges were located was not specified. The predicted results were in good agreement with the experimental results. The pressure transducer in Figure 2.61a failed after the second reflection of the blast wave.

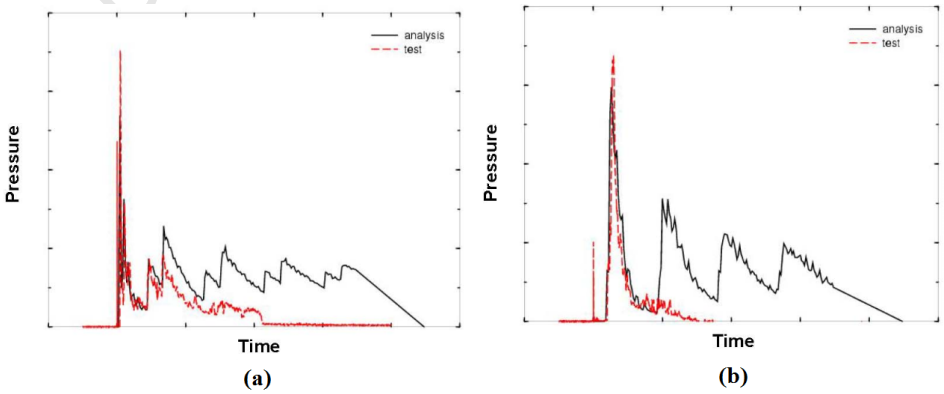

Figure 2.61: Comparison of Predicted and Experimental Pressure Histories in Rectangular Containers [17]

The CTH pressure profiles were applied to the structural elements in PRONTO3D. In the simulation it was assumed that the blast loading was complete before the vessel responded. Figure 2.62 illustrates the numerical and experimental deformed shape of the rectangular container. The final deformation shapes and displacements of both the predicted and experimental were similar and the deformation, almost cylindrical, were also similar. The deformation shape of the square end plate exhibited similar deformation profiles to work presented by [54].

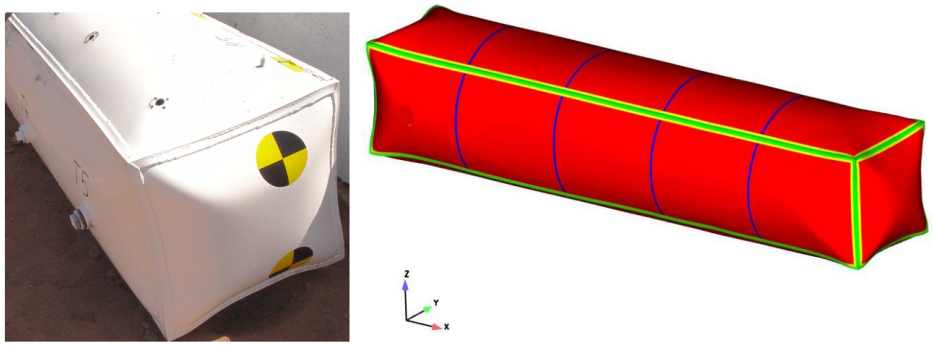

Figure 2.62: Numerical and Experimental Deformation of Rectangular Container [17]

Figure 2.63 is a comparison between the strain predicted by PRONTO3D and the experimental results. The predicted strain is slightly under-predicted but within acceptable limits.

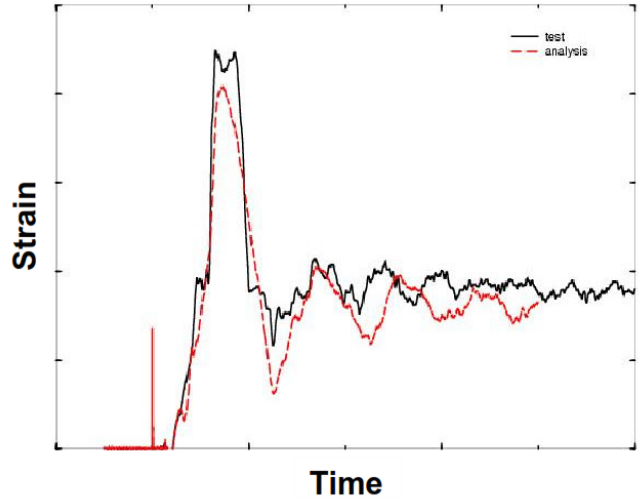

Figure 2.63: Comparison Between Predicted and Experimental Strain Measurements [17]

Hoffman and Wilson [12], Klein *et al.* [13] proposed two different designs for bomb disposal containers. The aim of both design was to reduce the current mass and size of typical bomb disposal containers. The container proposed by Hoffman and Wilson [12], illustrated in Figure 2.64, was capable of containing a five pound TNT equivalent blast and was capable of transit through the standard doors ($36in$ ($\approx 914mm$) wide) and elevators. The interior of the bomb disposal container was lined with a foam core to attenuate the effects of the blast wave. The prototype passed a test of $5lb$ ($\approx 2.3kg$) of C4 high explosive which was above the design specification. Consequently, the container has entered service at Hartsfield-Jackson Atlanta International Airport, Georgia[12].

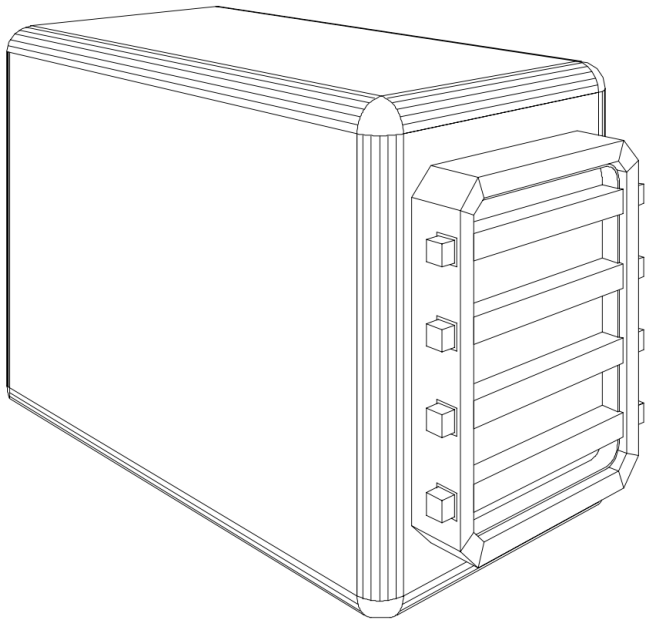

Figure 2.64: Low Cost Bomb Disposal Container [12]

Klein *et al.* [13] presented experimental results for internal blast loading of composite bomb disposal containers. The containers were designed to be light enough for two able people to lift and move, the proposed mass of the containers was $55lb$ ($\approx 25kg$). The vessel was designed to confine the effects of a $1lb$ ($\approx 0.45kg$) black powder equivalent explosion. The first container tested was manufactured from KEVLAR fabric impregnated with an epoxy resin. In the initial test the KEVLAR containers exhibited no damage from a $0.5lb$ ($\approx 0.23kg$) black powder charge, however the container was completely destroyed when subjected to a $1lb$ charge mass. Several modification were

made to the initial design such as the curing process, SPECTRA fabric replaced the KEVLAR fabric and door opening was made smaller. A photograph of the SPECTRA container is shown in Figure 2.65.

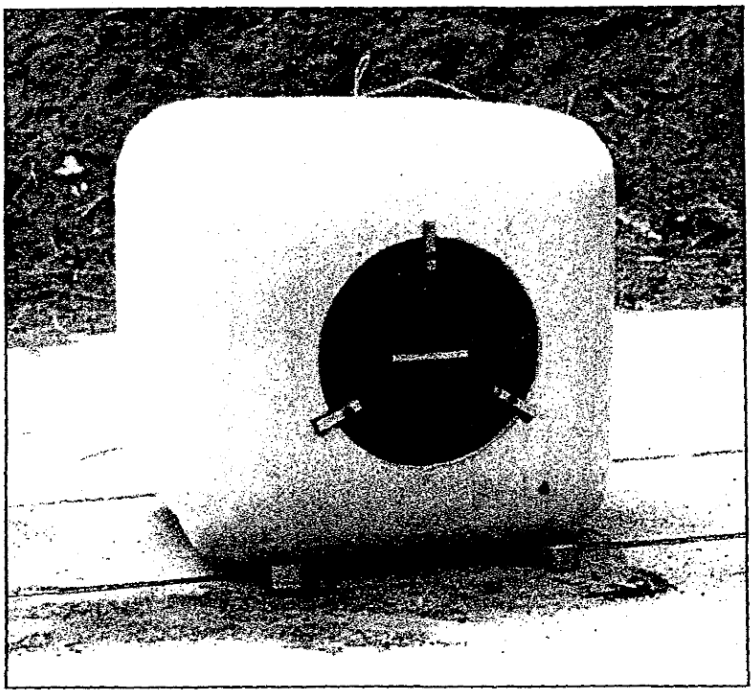

Figure 2.65: Composite Bomb Disposal Vessel [13]

The SPECTRA container was tested with a charge mass of $0.75lb$ ($\approx 0.34kg$) of black powder. After testing the container was relatively undamaged, however small burn holes were found on closer inspection and the interior of the container was charred. No further testing was reported by Klein *et al.* [13] on the SPECTRA container. Klein *et al.* [13] acknowledge that further improvements such as thermal liner to prevent burn through of the material, making the global shape of the container more spherical and lining the container with an energy absorbing material are required to meet the initial specifications.

The Aircraft Hardening Program was initiated to investigate techniques to mitigate the effects of explosion on civil transport aircraft [11]. The mitigation techniques investigated included hardened luggage containers, protective fuselage liners, increasing stand off distance between explosive device and the fuselage skin of the aircraft and the

use of novel high strength materials to manufacture the fuselage and skin of the aircraft [10, 11, 110]. This section will focus on the hardening of luggage containers as they can be approximated as cuboidal containers, see Figure 2.66 for dimensions for the most commonly used commercial luggage container (LD-3) [10].

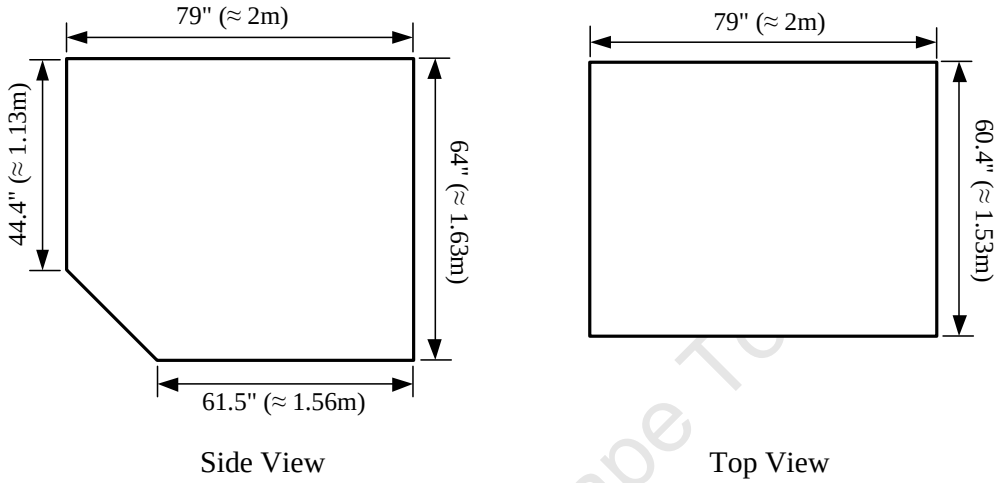

Figure 2.66: Dimensions of LD-3 Luggage Container [10]

The hardening of luggage containers present an interim solution for explosion containment aboard an aircraft. Factors such as cost, durability, maintenance, tare weight were considered to insure container feasibility [10, 110]. During the research eight different hardened luggage containers were tested. Each container had a different technique to mitigate the blast load, some of the techniques investigated were increasing wall thickness, partial venting, employing high strength or composite materials and honeycomb sandwich panels. For further details into the design techniques refer to Reference [10]. The results of the tests were evaluated on the tare weight of the container versus the explosive charge mass contained. Figure 2.67 depicts the results obtain from testing the eight different design techniques.

Based on the results an explosion could be effectively mitigated by high strength, high ductility or KEVLAR-like materials and the mass of the container would be less than the current containers employed by the airlines [10]. The airlines have been slow to introduce blast resistant luggage containers due to the cost of the containers [10].

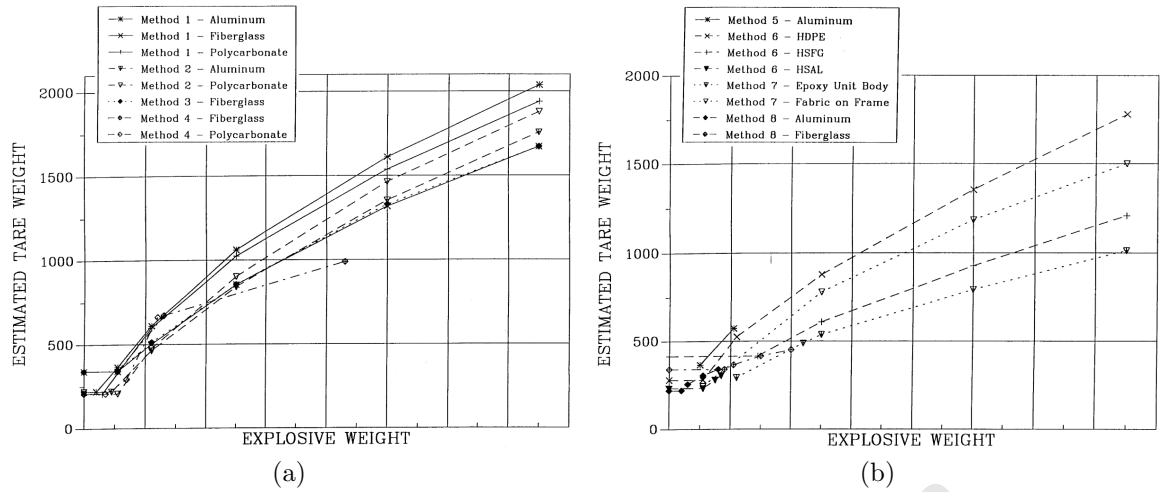

Figure 2.67: Estimated Tare Weight Versus Explosive Weight for Different Material Luggage Containers [10]

2.4 Blast Wave Reflection

When a shock wave travelling through a medium encounters another medium it experiences a reflection [6]. Reflection of blast waves is broken into 2 categories namely regular reflection and irregular/mach reflection. Regular reflection is comprised of two shock waves; the incident and reflected wave whilst a mach reflection is made up of an incident and reflected waves and a mach stem [6]. Regular reflection can further be broken down into normal and oblique reflection. Figure 2.68 illustrates the regular and mach reflected waves.

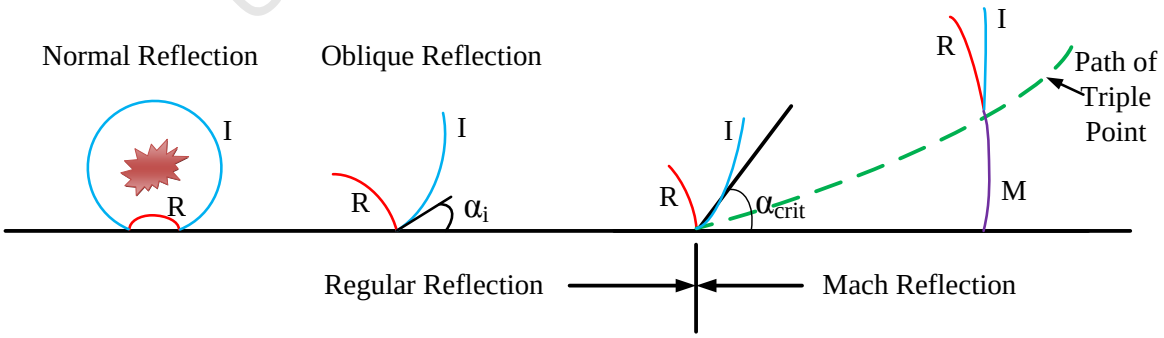

Figure 2.68: Diagram of Reflected Waves [26]

2.4.1 Normal Reflected Waves

A normal reflection occurs when a shock wave interacts with a surface at 0° i.e. head on and is reflected back to the the source. Figure 2.69 shows four stages of a shock wave propagating away from the source. Stages labelled t_1 and t_2 show the shock wave propagating away from the detonation point before any interactions have taken place. In stage t_3 the shock wave has collided with the reflective surface and has been reflected. The last stage (t_4) shows the the reflected shock wave travelling back to the detonation point as the incident waves travels away from it.

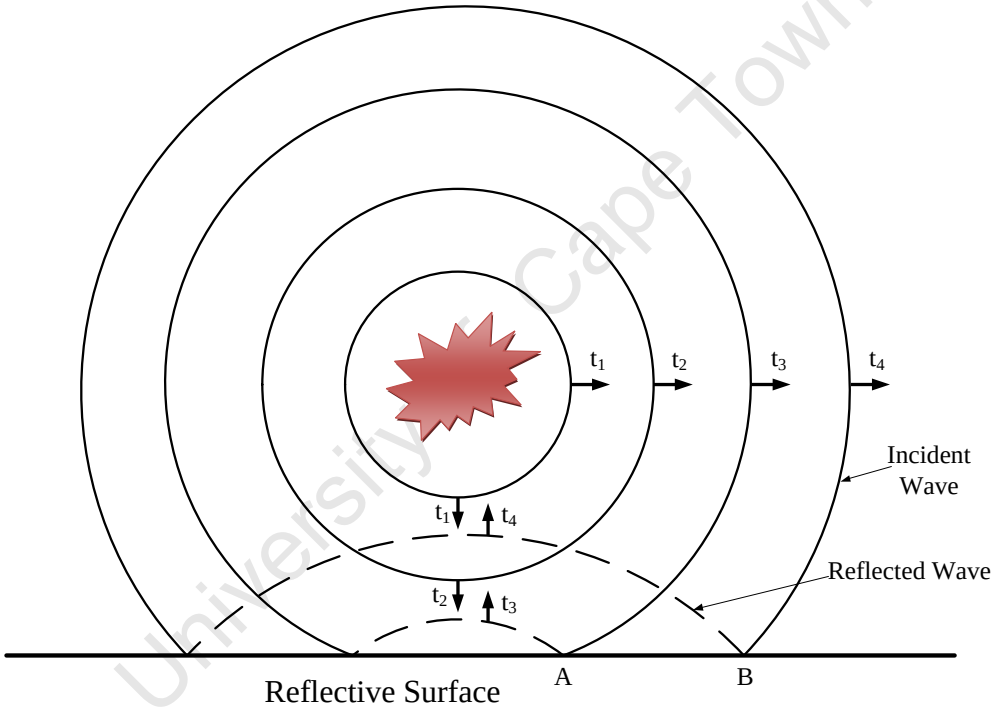

Figure 2.69: Normal Reflected Waves [2]

The normal reflected overpressure can be calculated using either Equation 2.54 [1] or 2.55 [26]. The ratio of reflected pressure to the incident pressure is known as the reflection coefficient (C_R). Equation 2.54 shows that if the shock wave is travelling just above the speed of sound in the medium i.e. $M_x \approx 1$ the reflection coefficient is approximately two however if the speed of the shock wave is great i.e. $M_x \gg 1$ the reflection coefficient will be eight [1]. The same magnification can be calculated from

Equation 2.55 when the incident pressure is very high or low [26]. Due to the effects of gas dissociation and particle ionisation of air particles near to the explosion, reflection coefficients of 20 or more have been recorded [2, 26].

$$C_R = \frac{P_r}{P_s} = \frac{8M_x^2 + 4}{M_x^2 + 5} \tag{2.54}$$

$$C_R = \frac{P_r}{P_s} = 2\left(\frac{7P_o + 4P_s}{7P_o + P_s}\right) \tag{2.55}$$

Where P_r is the reflected pressure, P_o is the ambient pressure, P_s is the overpressure and M_x is the Mach number.

2.4.2 Oblique Reflections

As the angle of incidence increases from 0° i.e propagates away from the source, an oblique reflection of the shock wave occurs. Figure 2.70 is a schematic of a oblique reflection where α_i is the angle of incidence and α_r is the angle of reflection. The arrows shown on the waves indicate the direction of the wave propagation.

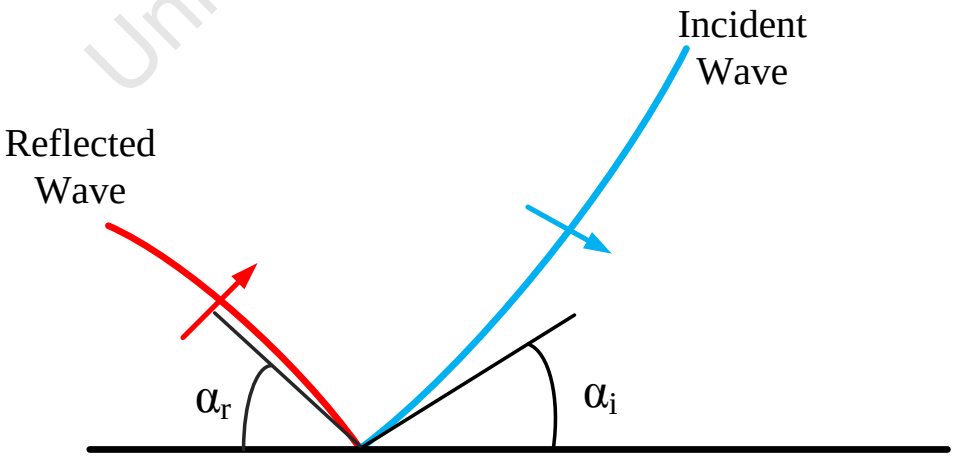

Figure 2.70: Schematic of Oblique Reflection [1]

Oblique reflected waves have the following properties:

1. At some value of α_i the magnitude of the reflected pressure is greater than that of the normal reflection. For a blast wave travelling through air the angle ranges from 40° to 50° [1, 2, 26].

2. The angle of reflection increases as the angle of incidence increase [2, 26].

3. For a given incident pressure there is some value of α_i that the reflected pressure is a minimum [2, 26].

4. There is a critical angle (α_{crit}) of incidence where a transition from oblique to mach reflection occurs. At angles greater than α_{crit} mach reflection will occur [2, 26].

Figure 2.71 shows the reflection coefficient versus the angle of incidence for shock waves travelling through air at various overpressures.

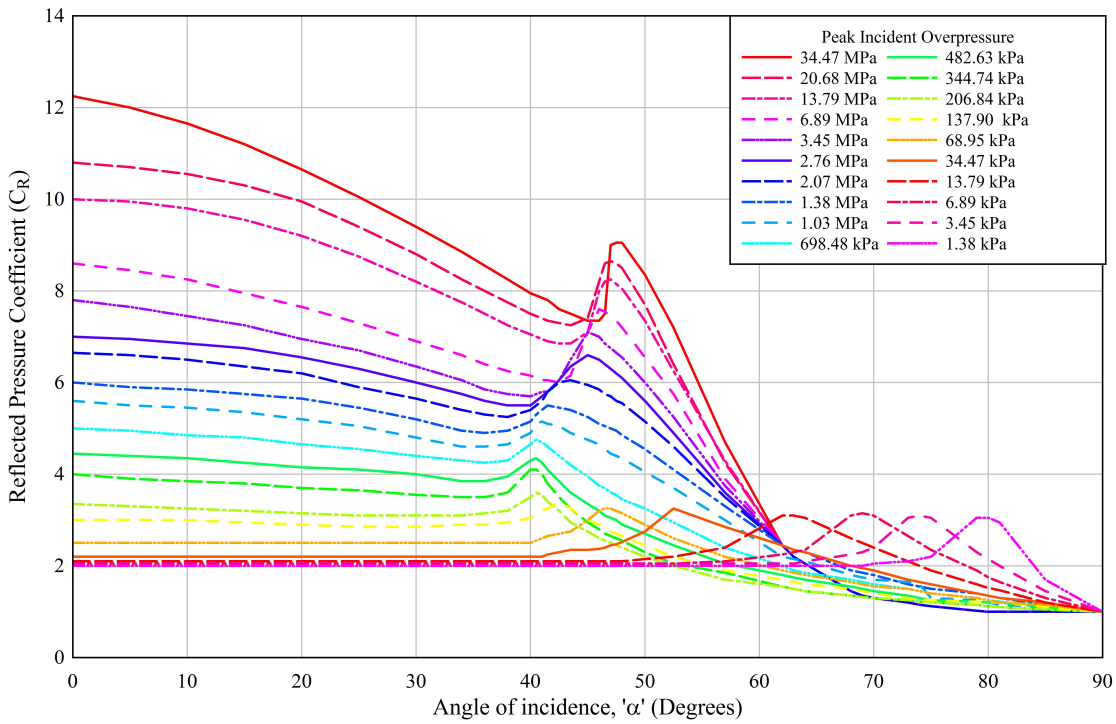

Figure 2.71: Reflective Coefficient at Various Overpressure and Angles of Incidence [7, 26]

2.4.3 Mach Reflection

When the angle of incidence reaches a critical value, α_{crit}, which is dependent on the overpressure and the mach number of the shock wave a mach reflection occurs [26]. At this point the reflected wave and the incident wave coalesce to form a third shock front called the mach stem [2]. The mach stem is named after Ernst Mach who published the first paper on this phenomenon as reported by Ben-Dor [111]. The point where the three waves merge is known as the triple point. Figure 2.72 illustrates the components of a mach reflection. As the mach stem travels away from the source it grows in height.

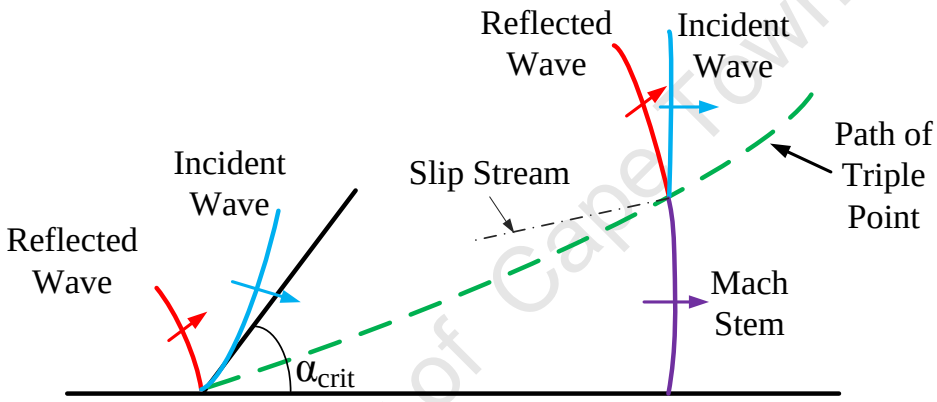

Figure 2.72: Schematic of Mach Reflection [1]

Figures 2.72 and 2.73 illustrates the path of the triple point as the mach stem grows. A slip stream forms behind the triple point as it propagates away. A slip is a region where the densities and velocities of the air particle differ but the pressure in this region is the same [2, 26].

The mach stem grows rapidly and tends to engulf the two-shock system above it. The magnitude of the pressures in the mach stem are greater than that in the incident wave for a given horizontal distance [2].

Ben-Dor [111] further divided mach reflection into 12 categories with the possibility of further divisions. The details of the categories have been omitted; the reader is referred to Reference [111] for the further classification of mach reflection.

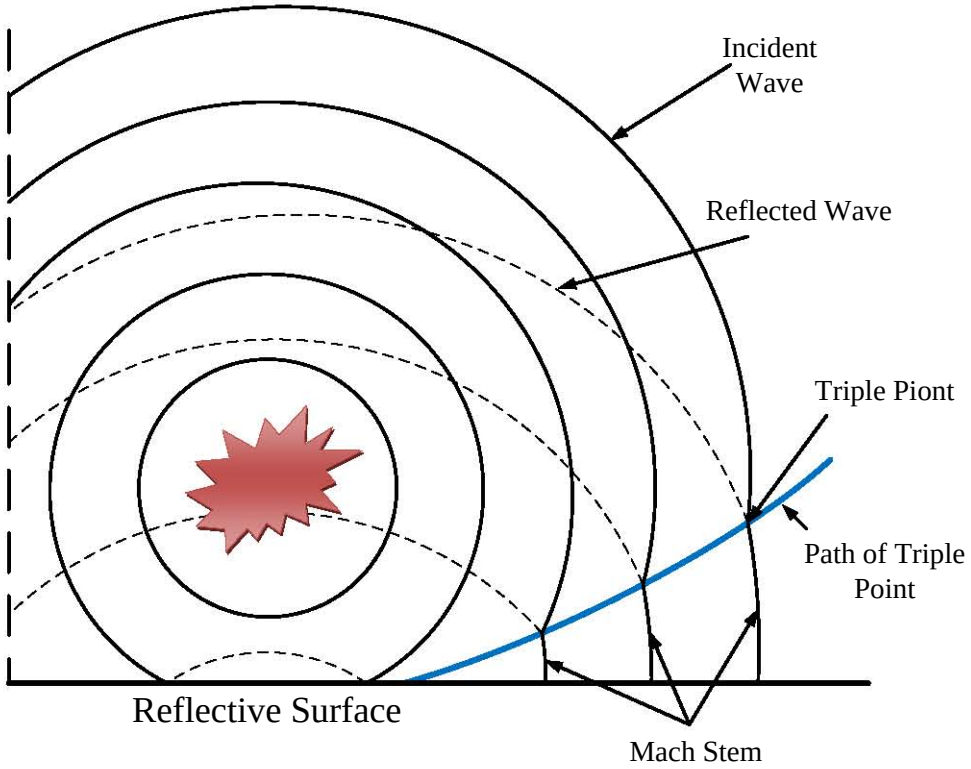

Figure 2.73: Reflected Waves [2]

2.5 Scaling Principles

Full-scale experiments can be costly in terms of price, preparation and measurement [112]. Consequently, it is desirable to scale down the experiments. Scaling principles for blast loads are based on the fundamentals of geometrical similarity [1]. Scaling enables the prediction of full scale response of a structure subjected to a blast wave based on test data obtained from scaled down, geometrically similar experiments [1, 36, 113].

The most common form of blast scaling is the Hopkinson-Cranz or 'cube-root' scaling law [1, 113]. The scaling law was first formulated by Hopkinson [114] and independently by Cranz [115]. A formal definition for this principle can be quoted from Baker *et al.* [29] as: "*Self-similar blast waves are produced at identical scaled distances when two explosive charges of similar geometry and of the same explosive but of different sizes are detonated in the same atmosphere.*"

Hopkinson-Cranz scaling law is based the geometric similarities between the two charge masses, W_1 and W_2. The masses are directly proportional to the cube of the diameter of the explosive [26], as shown in Equation 2.56.

$$\begin{aligned} W_1 &\propto d_1^3 \\ W_2 &\propto d_2^3 \\ \therefore \quad \frac{W_1}{W_2} &= \left(\frac{d_1}{d_2}\right)^3 \\ \therefore \quad \frac{d_1}{d_2} &= \left(\frac{W_1}{W_2}\right)^{\frac{1}{3}} \end{aligned} \tag{2.56}$$

The ratio of explosive diameters is written as $\lambda = \frac{d_1}{d_2}$ [26]. For the overpressure at a certain point to be the same for the two explosives with the a diameter ratio of λ, the ratio of distances between the point and the explosives must therefore also be λ [26], as depicted in Figure 2.74.

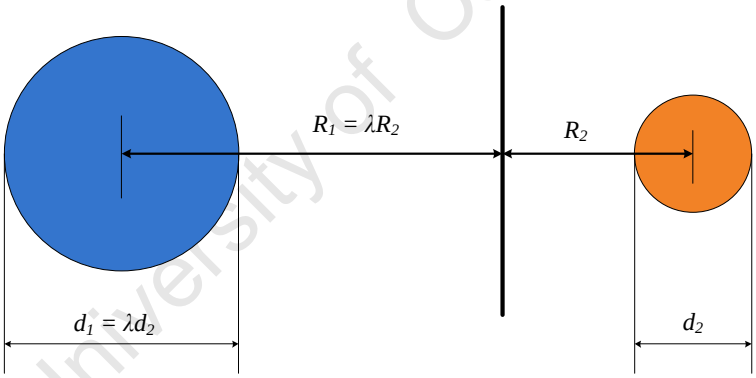

Figure 2.74: Basis of Hopkinson-Cranz Scaling [26]

Hence the following relationship between the stand off distance and the mass of the explosive is given by,

$$\frac{R_1}{R_2} = \left(\frac{W_1}{W_2}\right)^{\frac{1}{3}} \Rightarrow \frac{R_1}{W_1^{\frac{1}{3}}} = \frac{R_2}{W_2^{\frac{1}{3}}} = Z \tag{2.57}$$

Z is known as the scaled distance and is used as a constant of proportionality [26]. This equation is widely used and accepted but it is only valid for spherical charges and for $Z > 0.16 m/kg^{1/3}$ [113, 116].

2.5.1 Scaling of a Blast Wave

Brode [26] developed Equations 2.58 and 2.59 to predict the overpressure of a blast wave in the near field ($P_s > 10bar$) and medium to far field ($0.1 < P_s < 10bar$).

Near Field

$$P_s = \frac{6.7}{Z^3} + 1 \quad bar \tag{2.58}$$

Medium to Far Field

$$P_s = \frac{0.975}{Z} + \frac{1.455}{Z^2} + \frac{5.85}{Z^3} - 0.019 \quad bar \tag{2.59}$$

Henrych [26] proposed three equations (Equations 2.60-2.62), similar to Brode's equations, where the categories were classified by the scaled distance (Z).

For $0.05 \leq Z < 0.3m/kg^{1/3}$

$$P_s = \frac{14.072}{Z} + \frac{5.54}{Z^2} - \frac{0.357}{Z^3} + \frac{0.00625}{Z^4} \quad bar \tag{2.60}$$

For $0.3 \leq Z \leq 1m/kg^{1/3}$

$$P_s = \frac{6.194}{Z} - \frac{0.326}{Z^2} + \frac{2.132}{Z^3} \quad bar \tag{2.61}$$

For $1 \leq Z \leq 10m/kg^{1/3}$

$$P_s = \frac{0.662}{Z} + \frac{4.05}{Z^2} + \frac{3.288}{Z^3} \quad bar \tag{2.62}$$

Kinney and Graham [1] proposed Equations 2.63 and 2.64 to determine the peak overpressure and the blast duration respectively.

Overpressure Equation

$$\frac{P_s}{P_o} = \frac{808(1 + (\frac{Z}{4.5})^2)}{\sqrt{1 + (\frac{Z}{0.048})^2}\sqrt{1 + (\frac{Z}{0.32})^2}\sqrt{1 + (\frac{Z}{1.35})^2}} \tag{2.63}$$

Blast Duration Equation

$$\frac{t_d}{W^{1/3}} = \frac{980\left[1 + (\frac{Z}{0.54})^{10}\right]}{\left[1 + (\frac{Z}{0.02})^3\right]\left[1 + (\frac{Z}{0.74})^6\right]\sqrt{1 + (\frac{Z}{6.9})^2}} \tag{2.64}$$

This page has been intentionally left blank.

3 Experimental Details and Procedures

Three series of experiments were designed and performed to assess three different degrees of confinement of a blast load. The performance of the degrees of confinement were evaluated on the transient and final midpoint deflection of square monolithic mild steel target plates. The degrees of confinement are referred to as:

Series 1: Unconfined Blast

Series 2: Fully Vented Blast

Series 3: Fully Confined Blast

The blast load was generated by the detonation of a spherically shaped charge of plastic explosive (PE4) placed in the geometric centre of the target plate at a constant stand off distance of $100mm$. The explosive characteristics of PE4 are nearly identical to C4 plastic explosive, the difference being the type and proportion of plasticizer[1]. Table 3.1 lists some properties of PE4.

Table 3.1: Properties of PE4 Explosive [117, 118]

Detonation velocity	8193 m/s
Density	1603kg/m^3
TNT Equivalence	130%

[1]PE4 - 88% RDX, 11% Lithium Grease - Plasticizer, 1% Penta-erythritol dioleate [117]
C4 - 91% RDX, 2.1% Polyisobutylene - Plasticizer, 1.6% Motor Oil, 5.3% 2-ethylhexyl sebacate [118]

Different charge masses were detonated to achieve varying blast loads that would result in plate deformations ranging from one to fourteen plate thicknesses. Furthermore three different target plate thicknesses (3, 4 and 5mm) were tested. The 3 and 4mm thick plates were fabricated from locally manufactured commercial grade mild steel whilst the 5mm thick plate was fabricated from grade 300WA steel. All the target plates and containers in a thickness series were made from the same batch of steel to ensure that there is material consistency throughout a thickness series.

3.1 Ballistic Pendulum

The unconfined and fully vented experiments were performed on the ballistic pendulum in the Blast Survivability and Impact Research Unit (BISRU) blast chamber. The ballistic pendulum, as implemented in many other studies to determine the impulse transferred to a target plate as a result of a blast load [40, 43–46, 54, 119–123], consisted of an I-beam suspended in air by four spring steel cables, test rig and counter balancing masses. The impulse witnessed by the target plate was determined from the amplitude of the swing of the ballistic pendulum.

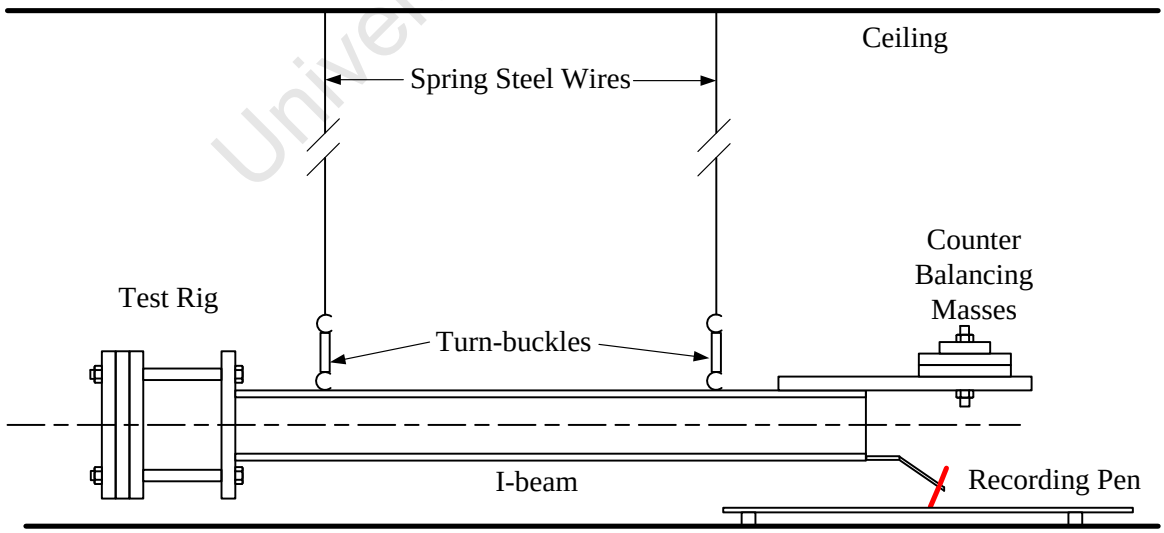

Figure 3.1: Schematic of Ballistic Pendulum

3.1.1 Ballistic Pendulum Theory

The ballistic pendulum was treated as a simple pendulum where the rotational inertia of the pendulum and the mass of the connecting cables were ignored. Figure 3.2 illustrates a diagram of a simple pendulum. Simple pendulum theory requires that the amplitude (θ) (See Figure 3.2) of the pendulum satisfy $sin\theta \approx \theta$ and that the pendulum undergoes only two dimensional motion. The amplitude of the pendulum was controlled by adjusting the total mass of the pendulum whilst the pendulum was balanced in all directions in order to maintain its orientation and keep the motion two dimensional.

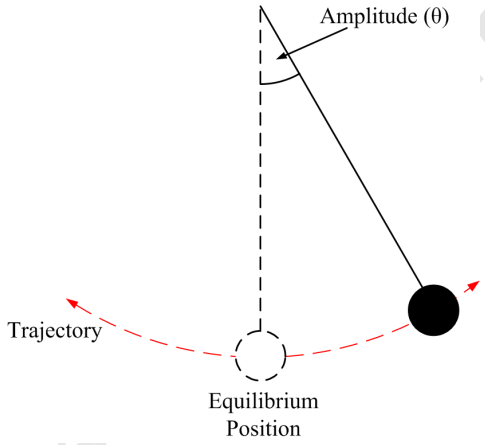

Figure 3.2: Illustration of Simple Pendulum

The linearised equation of motion, assuming viscous damping, for a simple pendulum is expressed as,

$$\ddot{x} + 2\beta\dot{x} + \omega_n^2 x = 0 \tag{3.1}$$

where

$$\beta = \frac{C}{2m_p} \qquad \text{and} \qquad \omega_n = \frac{2\pi}{T}$$

where C is the damping coefficient, m_p is the total mass of the pendulum and T is the natural period of the pendulums motion.

The solution to Equation 3.1 is given by:

$$x(t) = \frac{(e^{-\beta t})\dot{x}_o sin(\omega_d t)}{\omega_d} \tag{3.2}$$

where $\dot{x}$ is the initial velocity of the pendulum and ω_d is calculated using

$$\omega_d = \sqrt{\omega_n^2 - \beta^2} \tag{3.3}$$

The maximum positive displacement (x_1) of the pendulum occurs at $t = \frac{T}{4}$ and the minimum negative displacement (x_2) occurs at $t = \frac{3T}{4}$, substituting these values into Equation 3.2 gives,

$$x_1 = \frac{\dot{x}_o T}{2\pi} e^{\frac{-1}{4}\beta T} \tag{3.4}$$

$$\tag{3.5}$$

$$x_2 = \frac{\dot{x}_o T}{2\pi} e^{\frac{-3}{4}\beta T} \tag{3.6}$$

β is determined by dividing x_1 by x_2 and solving for β.

$$\beta = \frac{2}{T} ln \frac{x_1}{x_2} \tag{3.7}$$

The initial velocity ($\dot{x}_o$) of the pendulum is determined by re-arranging Equation 3.4 to give

$$\dot{x}_o = \frac{2\pi}{T} x_1 e^{\frac{1}{4}\beta T} \tag{3.8}$$

The impulse transferred to the pendulum can now be calculated as

$$I = m_p \dot{x}_o \tag{3.9}$$

Consider Figure 3.3, the horizontal distances measured by the pen (ΔR and ΔL) are not the same as the actual horizontal distance moved by the pendulum (x_1 and x_2). The difference between these readings must be taken into account.

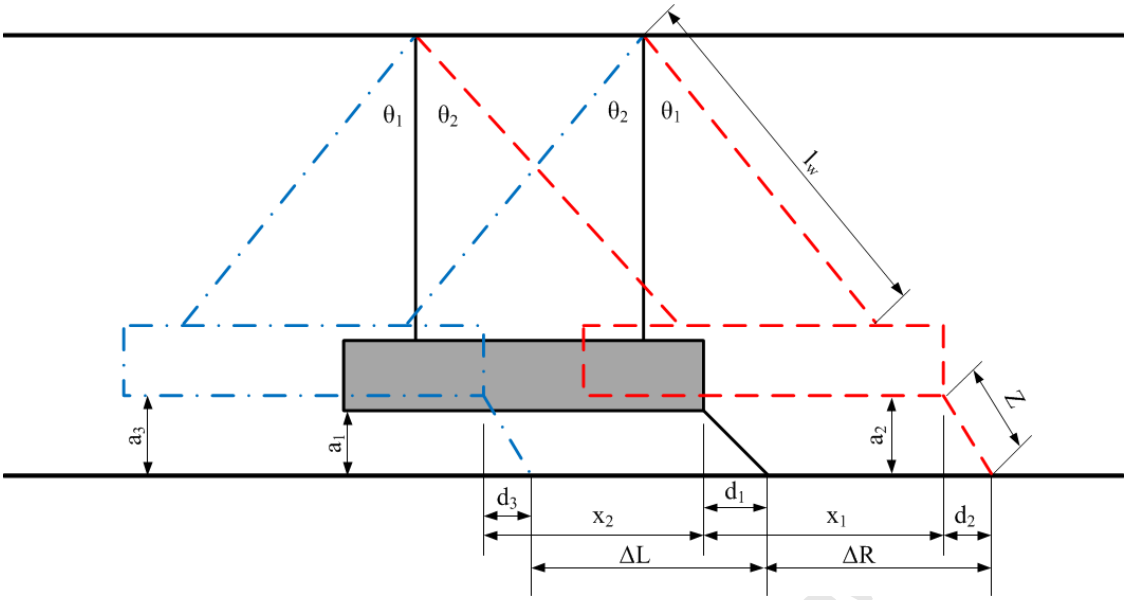

Figure 3.3: Schematic of the Pendulum Geometry and Motion

The measurable quantities in Figure 3.3 are the wire length (l_w), the initial distance of the pendulum above the ground (a_1), the length of the pen (Z) and the maximum forward and backward stroke of the pendulum (ΔR and ΔL). At rest the difference between the ends of the pen and the pendulum can be calculated using simple trigonometry. The difference (d_1) is given by,

$$d_1 = \sqrt{Z^2 - a_1^2}$$

Similarly the difference between the end of the pendulum and the pen at the maximum forward stroke is given by,

$$d_2 = \sqrt{Z^2 - a_2^2}$$

where

$$a_2 = l_w(1 - cos\theta_1) + a_1$$

The difference between the end of the pendulum and the pen at the maximum backward stroke is given by,

$$d_3 = \sqrt{Z^2 - a_3^2}$$

where

$$a_3 = l_w(1 - cos\theta_2) + a_1$$

From Figure 3.3, x_1 and x_2 may be determined from simple trigonometry as,

$$x_1 = l_w sin\theta_1 \tag{3.10}$$

and

$$x_2 = l_w sin\theta_2 \tag{3.11}$$

The measurable distances ΔR and ΔL may be written as,

$$\Delta R = x_1 - d_1 + d_2 = l_w sin\theta_1 - \sqrt{Z^2 - a_1^2} + \sqrt{Z^2 - (l_w(1 - cos\theta_1) + a_1)^2} \tag{3.12}$$

and

$$\Delta L = x_2 + d_1 - d_3 = l_w sin\theta_2 + \sqrt{Z^2 - a_1^2} - \sqrt{Z^2 - (l_w(1 - cos\theta_2) + a_1)^2} \tag{3.13}$$

Before the impulse could be determined the measurable constants, a, l_w, z and T, were determined. The period of the pendulum (T) was taken as the average over ten oscillations. Then applying Newton's method to Equations 3.12 and 3.13 the values of θ_1 and θ_2 were determined. The values of x_1 and x_2 were then calculated by substituting the values θ_1 and θ_2 into Equations 3.10 and 3.11 respectively. The values of x_1 and x_2 were then substituted into Equation 3.7 to determine β. The initial velocity of the pendulum was then determined from Equation 3.8. Knowing the total mass of the pendulum and its initial velocity the impulse transferred to the pendulum (Equation 3.9) from the explosion was calculated.

Table 3.2 lists the constants required to calculate the impulse transferred to the target plate. The mass of the pendulum was increased during the experimentation in order to reduce the horizontal travel of the pendulum and hence reduce the amplitude of the pendulum to ensure simple pendulum theory is still applicable. The period of the pendulum (T) was taken as the average period over 10 oscillations.

Table 3.2: Pendulum Constants

Unconfined Experiments					
Experiment Number	Mass of Pendulum (kg)	a (m)	l_w (m)	z (m)	T (s)
3mm Plates Test 1	135.67	0.156	2.945	0.204	3.38
3mm Plates Test 2-5	134.01	0.156	2.945	0.204	3.38
3mm Plates Test 6-10	214.27	0.156	2.945	0.204	3.38
3mm Plates Test 11	306.30	0.156	2.945	0.204	3.38
4mm Plates Test 1-11	292.67	0.156	2.947	0.212	3.38
5mm Plates Test 1-10	296.60	0.156	2.947	0.212	3.38
5mm Plates Test 11-12	306.30	0.156	2.947	0.212	3.38
Fully Vented Experiments					
Experiment Number	Mass of Pendulum (kg)	a (m)	l_w (m)	z (m)	T (s)
3mm Plates Test 1-5	387.98	0.153	2.945	0.212	3.38
3mm Plates Test 6-10	451.48	0.153	2.945	0.212	3.38
3mm Plates Test 11-13	451.09	0.153	2.945	0.212	3.38
4mm Plates Test 1-6	452.30	0.153	2.945	0.212	3.38
4mm Plates Test 7-9	451.09	0.153	2.945	0.212	3.38
5mm Plates Test 1	242.18	0.150	2.945	0.2045	3.38
5mm Plates Test 2-3	321.39	0.150	2.945	0.2045	3.38
5mm Plates Test 4-10	451.09	0.152	2.945	0.212	3.38

3.1.2 Ballistic Pendulum Setup

For reliable impulse measurements the ballistic pendulum was balanced such that the mass of the test rig, which included the clamp frames, target plate, nuts, bolts, steel shroud and spacers located at one end of the I-beam, was counter balanced by additional masses at the other end of the I-beam. The ballistic pendulum was balanced with a machinist spirit level and adjustments made with the turn-buckles connecting the pendulum to the steel cables. This procedure ensures equal tensions in the four spring steel cables and that the swing of the pendulum acts through the centroid of the ballistic pendulum.

3.2 Series 1 - Unconfined Blast

The unconfined blast loading refers to free air bursts where an explosive charge, standing in free air, was detonated at a constant stand off distance from the target plate. The resulting blast wave impinges directly onto the target plate, without any prior amplification or reflection, and subjects the target plate to a high magnitude short duration impulsive pressure load. Figure 3.4 illustrates a schematic of the unconfined blast loading configuration. Unconfined blast experiments were carried out to create a baseline to compare the effects of the degrees of confinement.

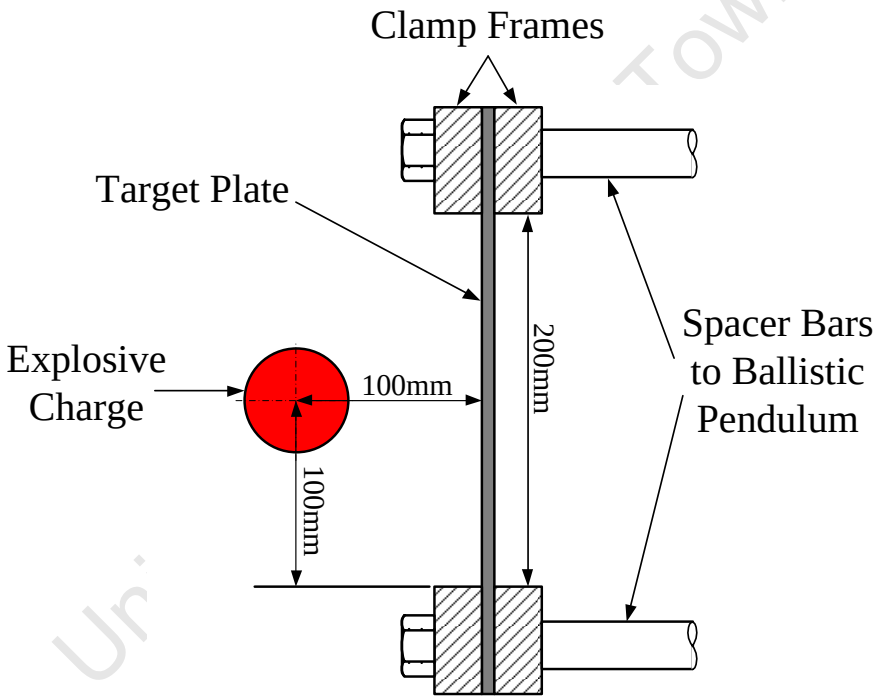

Figure 3.4: Unconfined Blast Configuration (Cross-sectional View)

3.2.1 Unconfined Ballistic Pendulum Setup

A photograph of the ballistic pendulum setup for the unconfined blasts is shown in Figure 3.5. The target plate ($300 \times 300mm$) was clamped and bolted between two $12mm$ thick clamp frames which were then attached to the ballistic pendulum. The

area of the target plate exposed to the blast load was $200 \times 200mm$ after the plates had been clamped. The region behind the target plate was enclosed in a steel shroud to protect the transient displacement sensors from the blast wave and eliminates any effects the flash from the detonation process may have on the sensors. Further details on the transient displacement sensors will be discussed in Section 3.6

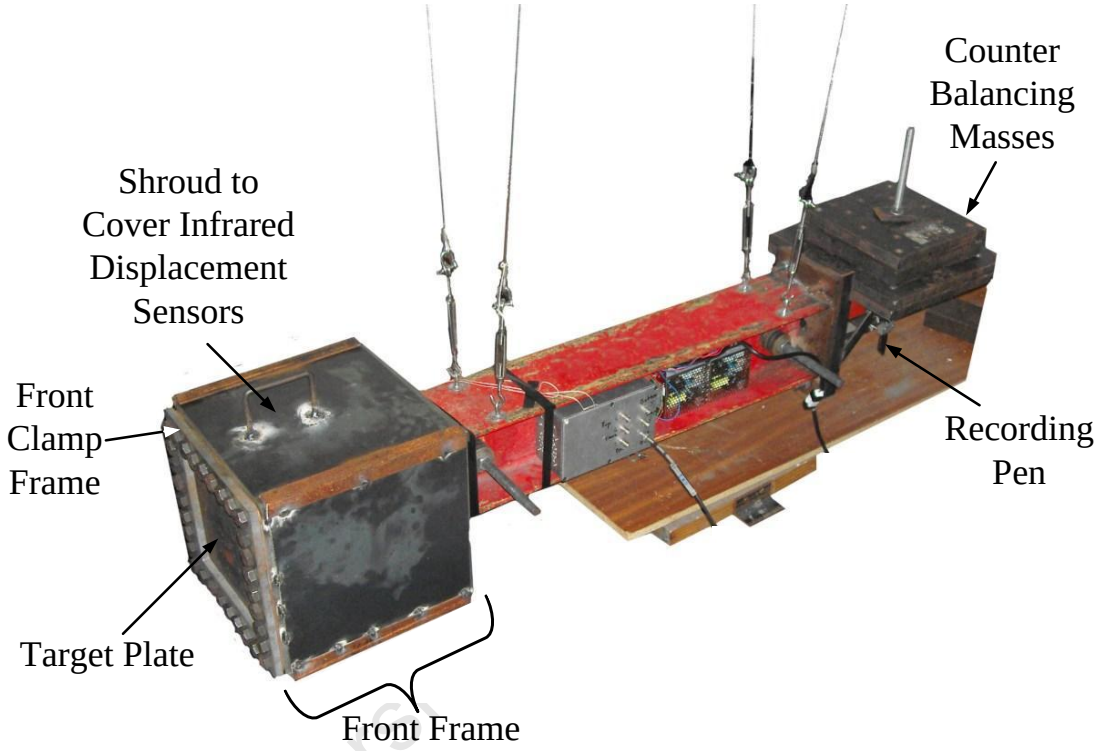

Figure 3.5: Photograph of the Pendulum Setup for Unconfined Experiments

The accurate vertical positioning of the explosive charge with respect to the target plate was ensured with specially cut polystyrene columns, as depicted in Figure 3.6. While polystyrene columns may have an effect on the response of the target plates it was assumed to burn on detonation and had no quantifiable effect [26]. No experiments were carried out to investigate the effects of the polystyrene columns. A spacer ensured the horizontal positioning and stand off distance ($100mm$) remained constant and at the correct distances.

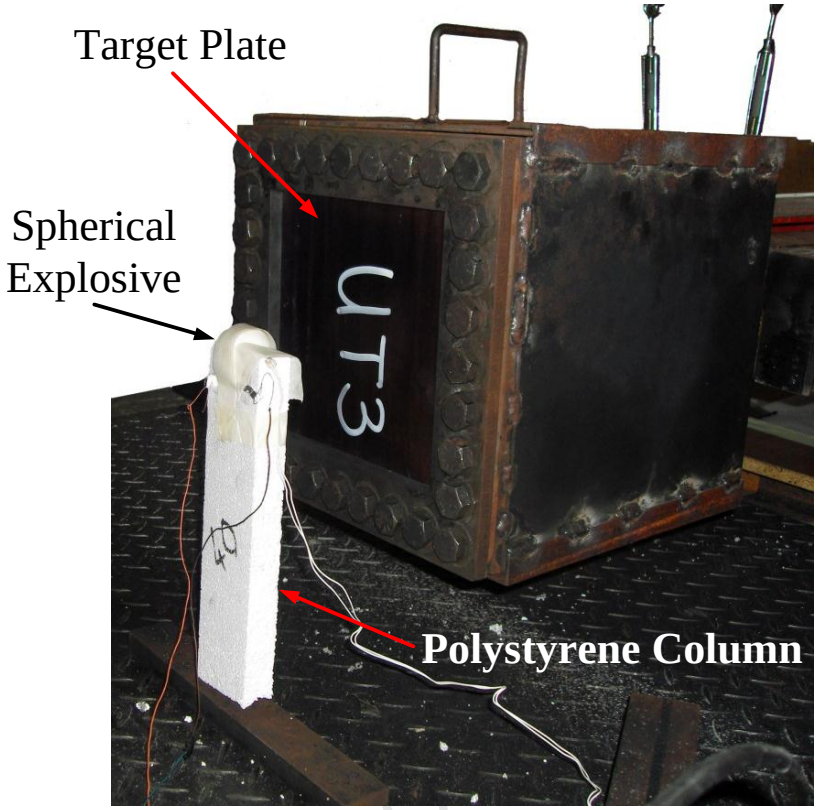

Figure 3.6: Positioning of Explosive in Unconfined Experimentation

3.3 Series 2 - Fully Vented Blast

Experiments carried out in series 2 investigated the response of target plates subjected to a fully vented blast load. The blast load was generated by detonating an explosive charge in the geometric centre of a cuboidal structure with one side open to the atmosphere *i.e.* a five sided cuboidal structure. The venting property, defined in Equation 3.14, of the experiments carried out in series 2 was greater than one, hence satisfying the criteria proposed by Keenan and Tancreto [68] for a container to provide a fully vented blast load.

$$\frac{A_v}{V_{free}^{2/3}} \geqslant 0.6 \tag{3.14}$$

where A_v is the vent area and V_{free} is the free volume of the structure which is the total volume of the container minus the volume of any objects within the container.

The blast load in this scenario is comprised of several high magnitude short duration impulsive loads due to the multiple reflection of the shock wave within the structure [7, 68]. The dynamic load due to the build up of high temperature gases and accumulation of the detonation products could be neglected due to rapid venting [7, 67, 68].

The deformable target plate was located opposite the venting area of the cuboidal structure. The remaining side walls were made from $10mm$ thick mild steel plates for insignificant or no plastic deformation. Figure 3.7 shows a schematic of the fully vented blast load setup on the ballistic pendulum.

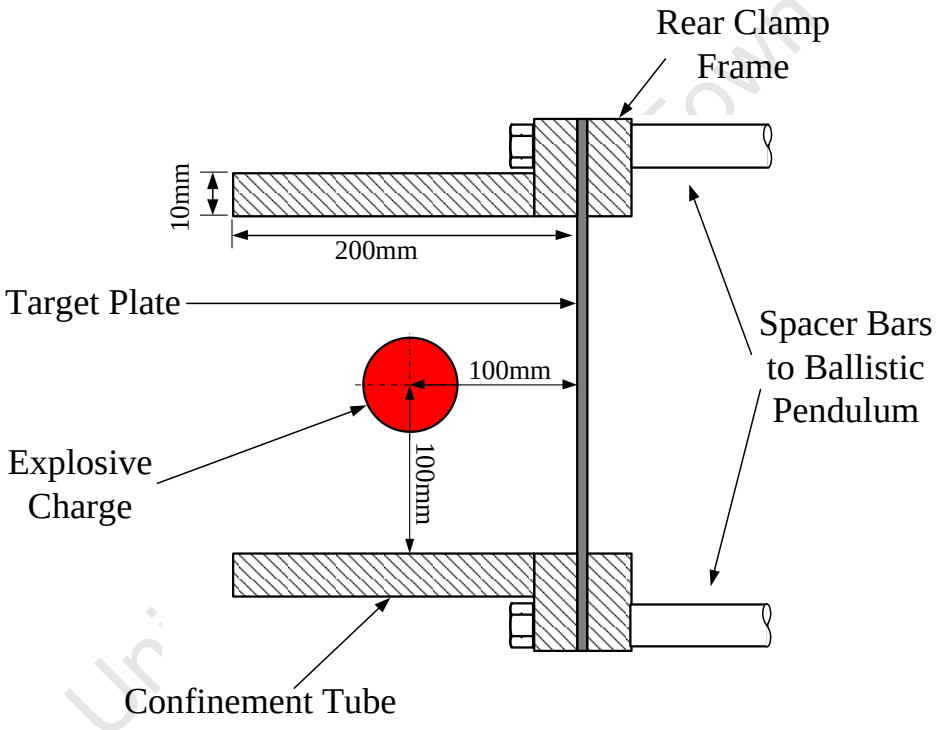

Figure 3.7: Schematic of Fully Vented Blast Configuration (Cross-sectional View)

3.3.1 Fully Vented Ballistic Pendulum Setup

The fully vented experiments were also performed on the ballistic pendulum, similar setup as the unconfined experiments. The front clamp frame in the unconfined experimental setup was replaced with a confinement tube which was a $10mm$ thick $200mm$ long flanged square steel tube, as depicted in Figure 3.7 and in a photograph of

the fully vented pendulum setup in Figure 3.8 . Extra mass was added to the pendulum for the fully vented experiments to reduce the horizontal travel of the pendulum as the impulse transferred to the pendulum was expected to be greater than that of the unconfined experiments.

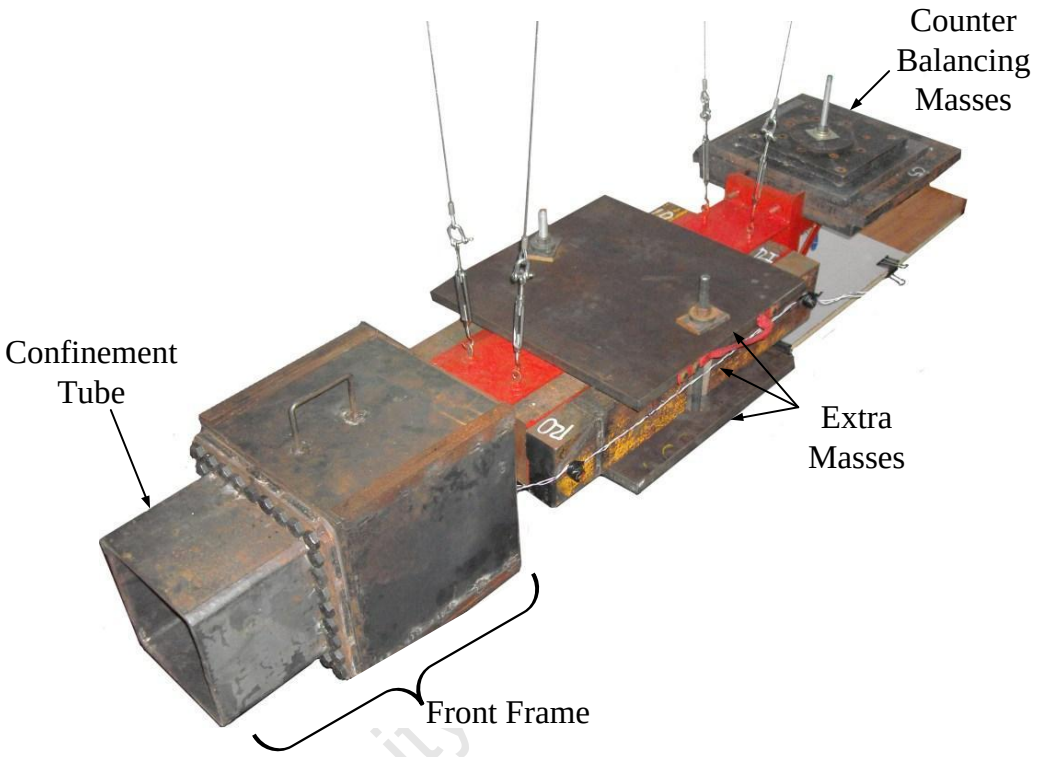

Figure 3.8: Photograph of Pendulum Setup for Fully Vented Experiments

The spherical charge was accurately located in the centre of the confinement tube (*i.e.* 100*mm* from any surface) with a polystyrene column. The polystyrene column positioned the charge at the correct stand off distance and vertical height. The horizontal location of the explosive charge was accurately set with a spacer block. The polystyrene column was fixed to the confinement tube with double sided tape. The profile of the polystyrene column is illustrated in Figure 3.9a and the location of the explosive charge within the confinement tube is depicted in Figure 3.9b.

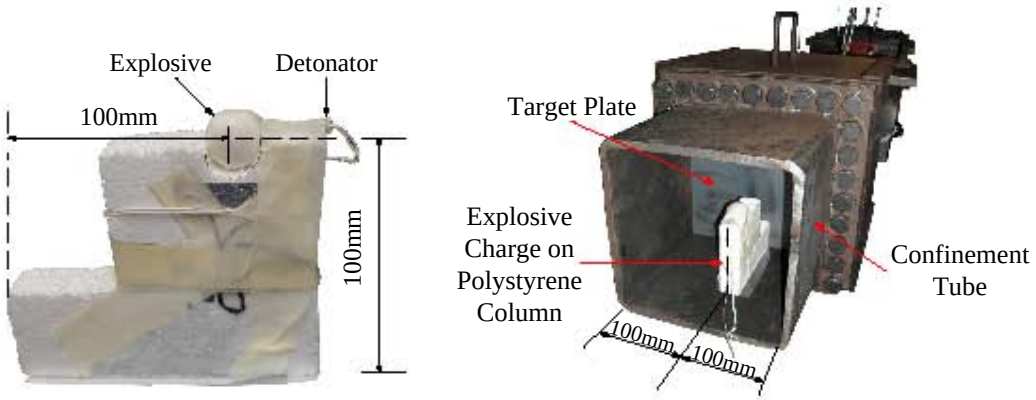

(a) Stand Off Distance and Vertical Position of Explosive charge on Polystyrene Column

(b) Location of Explosive Charge in the Confinement Tube

Figure 3.9: Photograph of the Positioning of Explosive in Fully Vented Experiments

3.4 Series 3 - Fully Contained Blast

The effects of a fully confined blast load were investigated in series 3. An explosive charge was detonated at the geometric centre of a sealed cuboidal container which confined the blast wave and all the explosive products within the container. The container would be subjected to two distinct loads namely an impulsive load and a dynamic gas pressure load. The impulsive load comprised of several high intensity short duration pressure loads due to the repeated reflection of the blast wave within the container. The containers would also be subjected to a long duration lesser magnitude load, compared to the impulsive load, due to the build up and accumulation of high temperature gases and detonation products [7, 67].

The containers were constructed with six deformable sides, as illustrated in Figure 3.10. The deflection results for the top target plates were compared to the results obtained from the unconfined and fully vented blast experiments as the same boundary conditions were present. The deflection results for the side and bottom target plates were compared to the top target plate deflections to investigate the symmetry of the deformation and the influence of different boundary conditions.

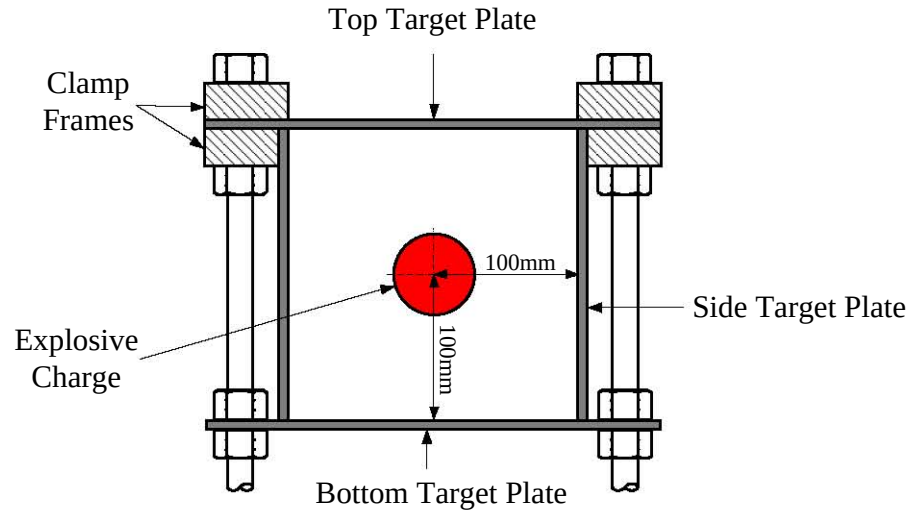

Figure 3.10: Fully Confined Blast Configuration (Cross-sectional View)

The ballistic pendulum was not implemented in this series of experiments because there would be an equilibrium of forces exerted on the container from the blast load. Consequently the tests were performed on a free standing heavy base.

3.4.1 Design and Manufacturing

The container for the fully confined blast had internal dimensions $200 \times 200 \times 200mm$ as depicted in Figure 3.11. The sides and bottom plates were welded together to form the bottom portion of the container and the top plate acted as the lid to the container.

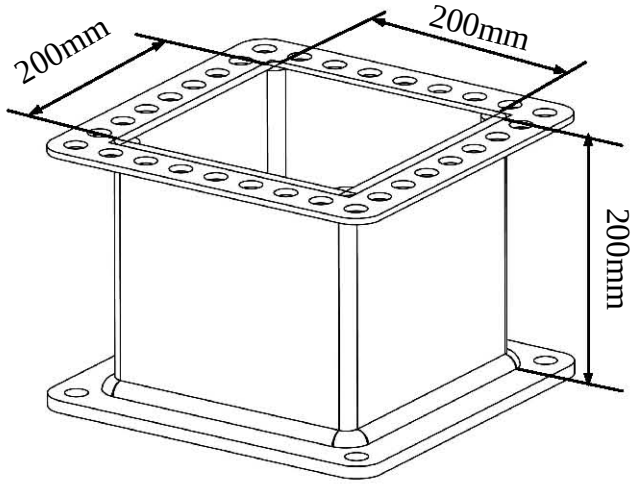

Figure 3.11: Schematic of Internal Dimensions of Containers

A manufacturing jig and several G-clamps (alternatively C-clamps), as depicted in Figure 3.12, were utilized during the welding process to ensure the accuracy of the internal dimensions of the containers and limited the amount of buckling/warping due to the added heat from the welding process. The jig also made the manufacturing process less complicated and time consuming.

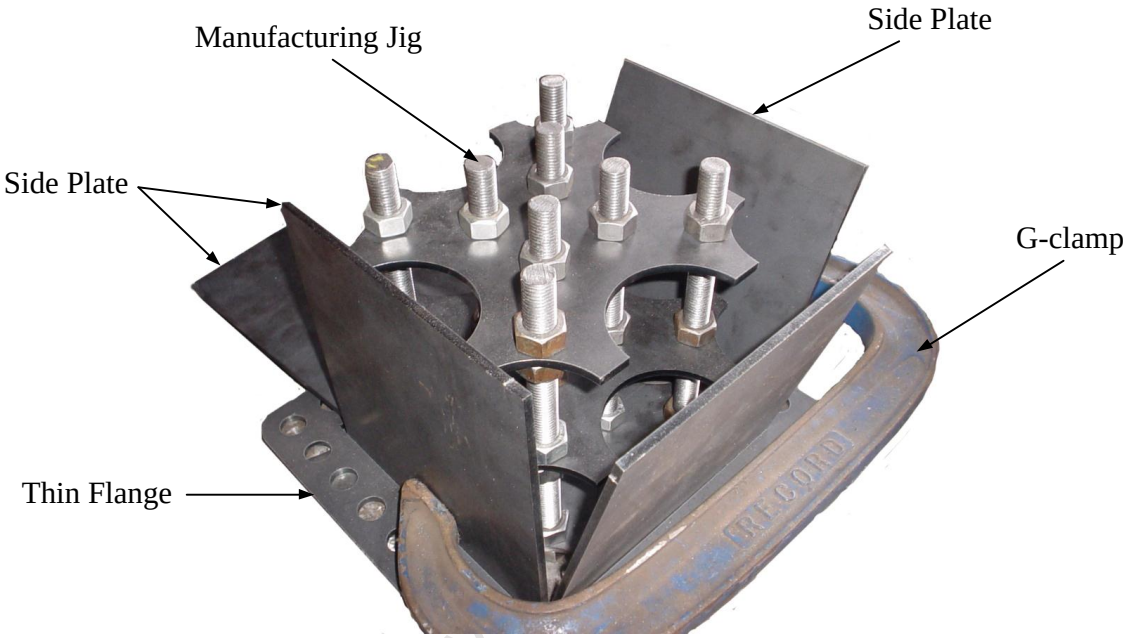

Figure 3.12: Photograph of Manufacturing Jig

The side and bottom plates were welded together with fillet welds from both the interior and the exterior to form the body of the container. The thin flange was welded with a single fillet weld to the body of the container. Figure 3.13 illustrates the location of the fillet welds on the body of the container. After the completion of the welding, the containers were heat treated to remove the residual stress in the containers induced by the welding process. The heat treatment consists of preheating the containers to 400°C for 1 hour then heating to 600°C for 3 hours and left to cool in ambient conditions.

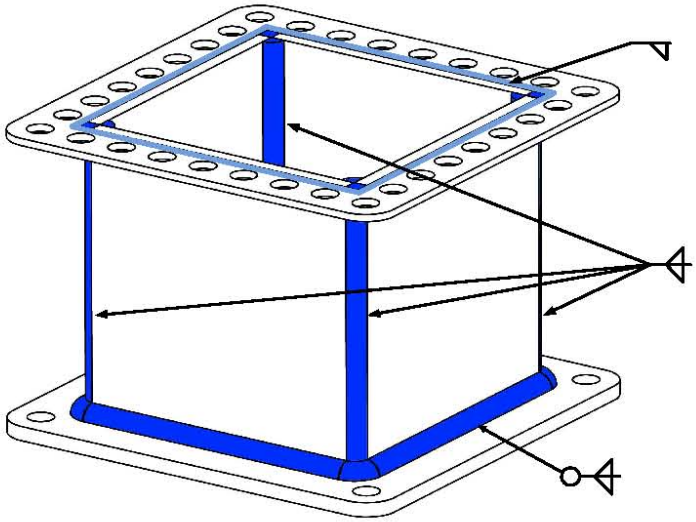

Figure 3.13: Location of Fillet Welds on Fully Confined Container

3.4.2 Fully Contained Blast Experimental Setup

Prior to testing two pairs of two entry holes (⌀1.6mm) were drilled into opposing faces in the bottom corner of the container to fit the detonator and trigger cables. The location and size of the holes were assumed to have little or no influence of the response of the containers to the blast load. The photograph in Figure 3.14 illustrates the location of the entry holes (highlighted in the circles) and the placement of the explosive charge.

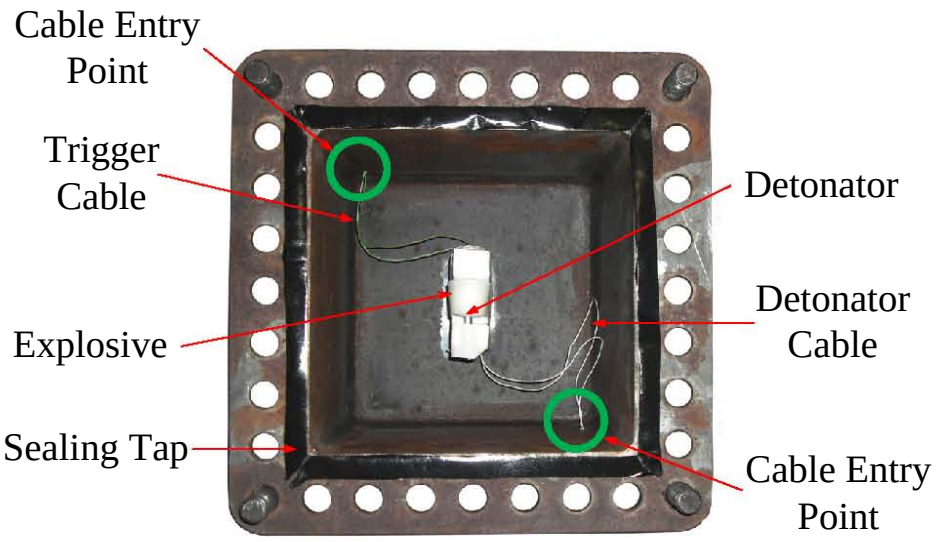

Figure 3.14: Explosive Placement and Cable Entry

The container was then secured to a heavy base plate with four $M16$ threaded bars and nuts at an elevated position eliminating any possible contact between the deforming bottom plate of the container and the base plate. When the container was correctly positioned and locked into place the explosive charge was positioned on top of a piece of polystyrene (see Figure 3.15) located in the centre of the container as depicted in Figure 3.14. Double sided tape secured the polystyrene column to the bottom plate.

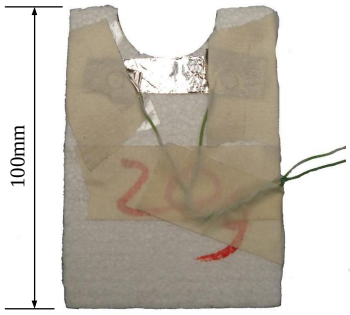

Figure 3.15: Polystyrene Column in Fully Confined Experimentation

Sealing tape, illustrated in Figure 3.14, was applied to the rim of the container to provide an air tight seal between the container and the top plate. The top plate and the clamp frames were bolted to the containers to create a fully confined blast scenario. The experimental setup for a fully confined blast (with the charge inside the container) is depicted in Figure 3.16.

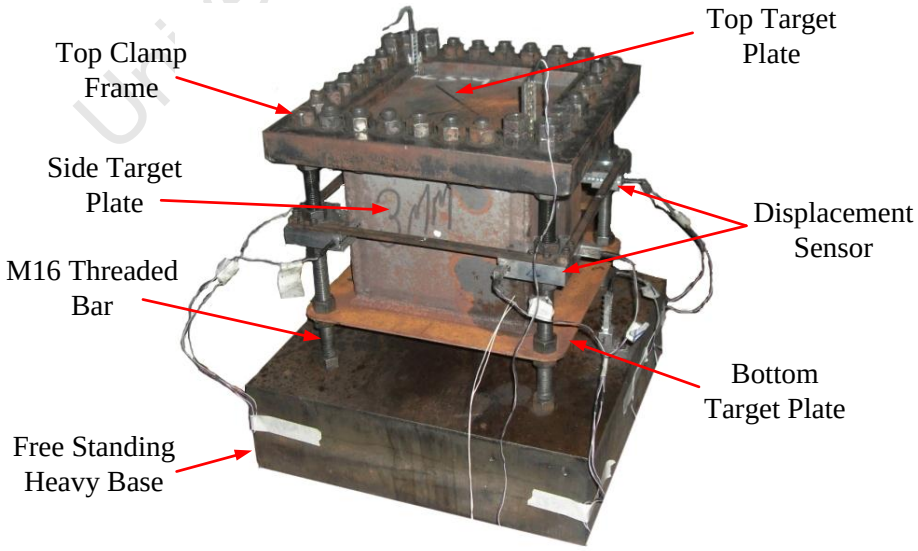

Figure 3.16: Photograph of Fully Confined Experimental Setup

3.5 The Effect of Different Exposed Areas

The ballistic pendulum measures the impulse transfer from the blast wave to the test rig in the direction perpendicular to the exposed area of the target plate. The impulse transfer was dependent on several factors such as charge mass, charge geometry, stand off distance and specimen geometry [122].

The exposed area, in the direction of the impulse transfer, of the unconfined test rig was $300 \times 300mm$ whilst the exposed area of the fully vented test rig was $200 \times 200mm$. The measured impulse in the unconfined blast experiments was the total impulse transferred to the entire exposed area of the test rig not, as in the fully vented blast experiments, to the exposed area of the target plate and hence a comparison of the impulses between the two experimental setups was not possible. Figure 3.17 is a schematic of the unconfined test rig(labelled a in Figure 3.17) and the fully vented test rig(labelled b in Figure 3.17) illustrating the different exposed areas of the test rigs.

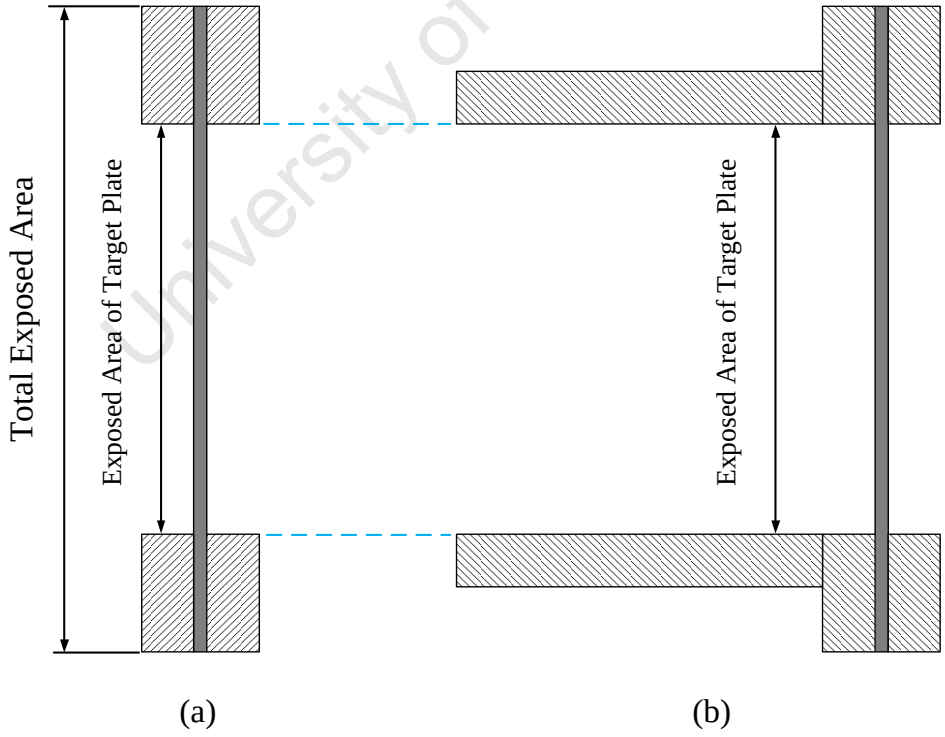

Figure 3.17: Exposed Area Mismatch Between Unconfined and Fully Vented Experiments (Cross-sectional View)

A series of experiments was carried out to assess the effect of the area mismatch between the unconfined and fully vented test rigs and to determine the percentage of the total impulse measured in the unconfined experiments transferred to the exposed area of the target plates. A $20mm$ thick steel plate, assumed to be rigid, with exposed area of $200 \times 200mm$ was attached to the ballistic pendulum. The rigid plate was offset by $200mm$ from the body of the ballistic pendulum to minimise the impulse transfer to the ballistic pendulum body. The exposed area of the rigid plate represented the area of the target plate exposed to the blast wave. Figure 3.18 is a photograph of the rigid plate setup on the ballistic pendulum.

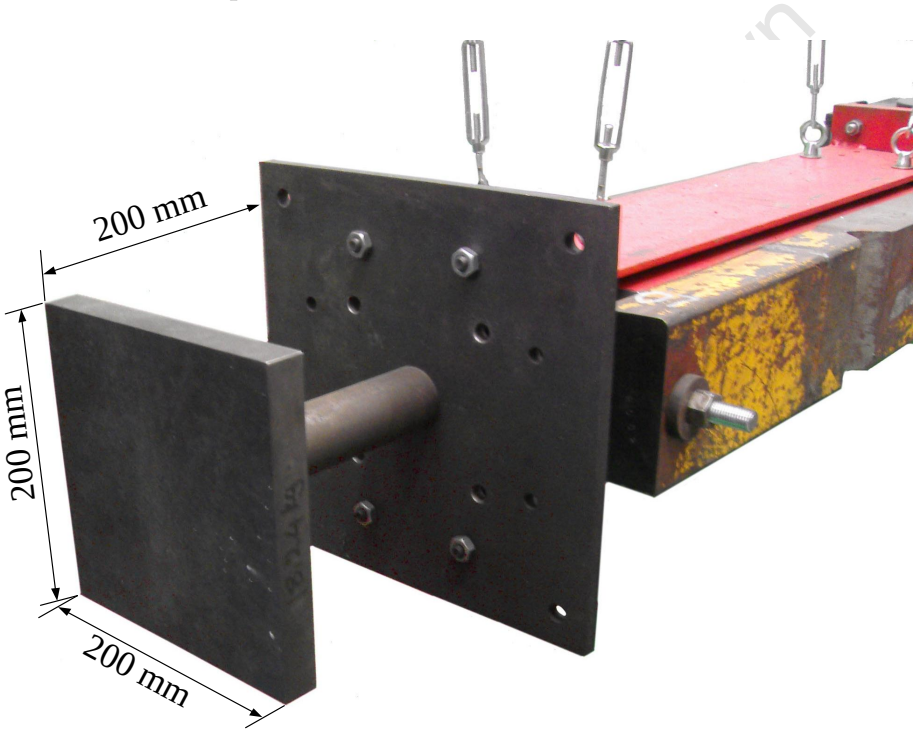

Figure 3.18: Photograph of Rigid Plate Experimental Setup

The setup of the explosive charges was identical to that of the unconfined blast experiments(see Section 3.2.1). Comparing the impulse measurements from the unconfined blast experiments and the rigid plate experiments the impulse transferred to the exposed area of the target plate, as a percentage of the total impulse, could be deduced.

3.6 Transient Displacement Measurement

The transient deflection of the target plate was measured with infrared opposed mode photosensors. Other methods of measuring the transient displacement were considered and are presented in Appendix A. The design and circuitry of the infrared photosensors is also presented in Appendix A Section A.3. The data acquisition equipment recorded the electrical output signal from the photosensors for $150ms$ at a sampling rate of $500kHz$ which was deemed sufficient to capture the response of the target plate.

3.6.1 Description and Location of Photosensor

The layout and design of the sensors was similar to the method presented by Nurick [121]. The sensor was comprised of an infrared light emitting diode (LED) array and an infrared photodiode array positioned directly opposite each other and secured to the clamp frames. Figures 3.19a and 3.19b are photographs of the infrared LED and photodiode arrays respectively.

(a) (b)

Figure 3.19: Photosensor in Clamp Frame, (a) Infrared LED Array, (b) Photodiode Array

The infrared LED array was comprised of high powered infrared LEDs which generated a curtain of light parallel to the target plate and over the midpoint of the target plate. The photodiode array produced an electrical signal dependent on the intensity of infrared light over the array. The plate deformation blocked a percentage of the light curtain reaching the photodiodes and hence decreasing the intensity of the light received by the photodiode array. This change in intensity resulted in an equivalent change in the electrical signal from the sensor which was related to the midpoint deflection of the target plate.

The infrared LED and photodiode arrays were located and mounted in two opposing slots machined in the clamp frames, the slots were also aligned with the midpoint of the plate. The photosensors were fixed in place with two $M3$ bolts.

The sensors in the unconfined and fully vented experiments were located at the midpoint of the opposite inner edges of the rear clamp frame, ensuring the path of curtain of light was over the midpoint of the target plate. Figure 3.20 illustrates the location of the photosensor in the unconfined and fully vented experiments.

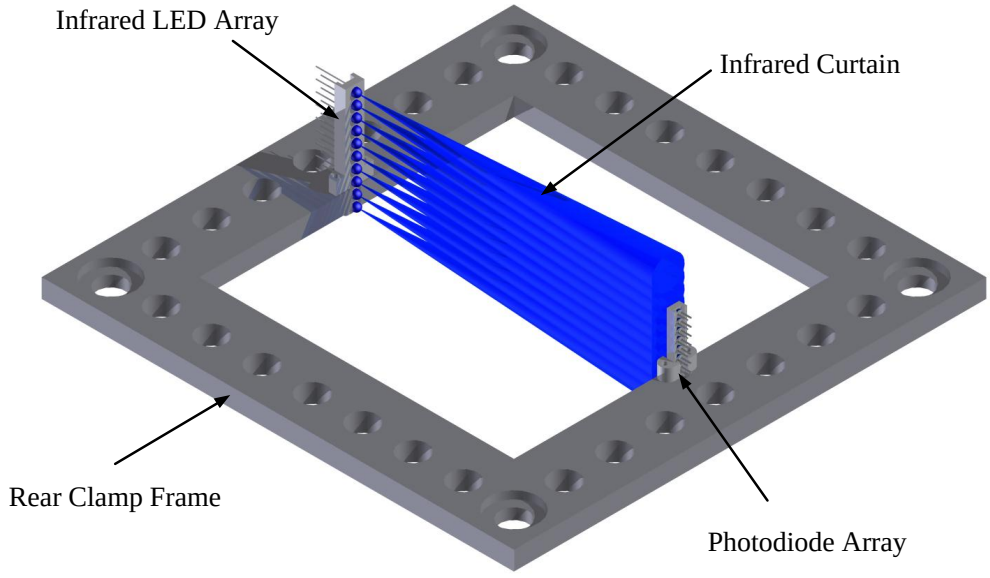

Figure 3.20: Illustration of Light Curtain Emitted from LED Array and the Location of Photosensors for Unconfined and Fully Vented Experiments

All six sides of the cuboidal container in the fully confined blast experiments were measured. The photosensors measuring the sides and bottom plate deflection were mounted and fixed to the heavy mounting frame and aligned with the midpoint of the edges of the relative target plate. The photosensor measuring the top plate deformation were located in opposite corners of the top clamp frame. Figure 3.21 illustrates the location of the photosensors location and their respective light curtains.

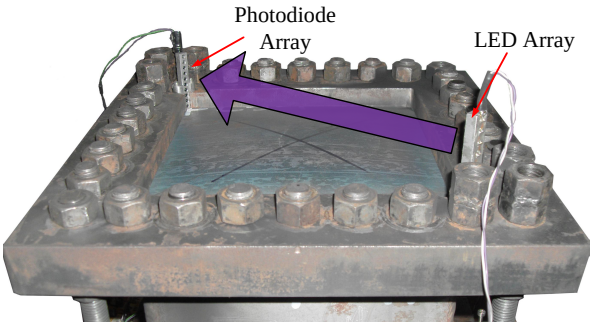

(a) Top Plate Light Sensor

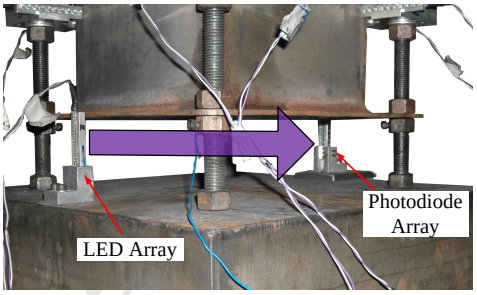

(b) Bottom Plate Sensor

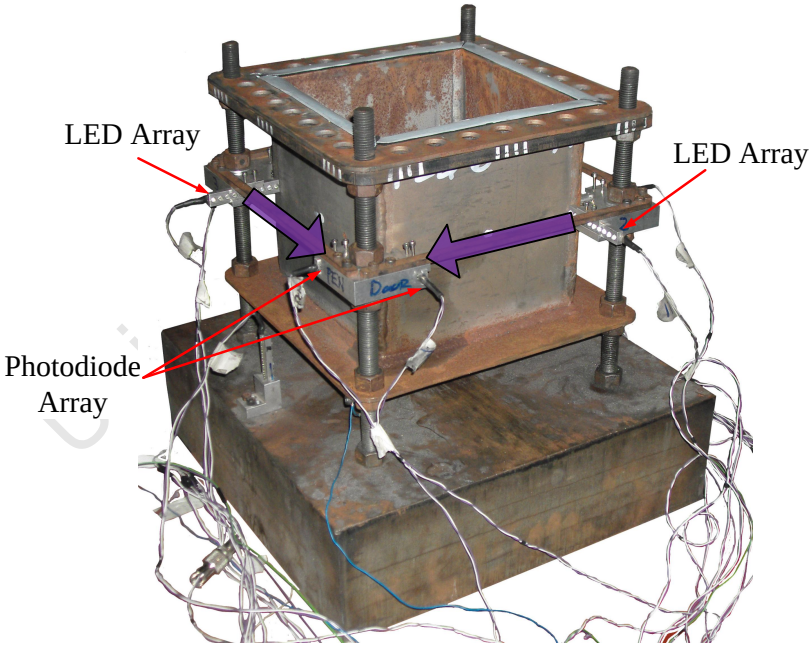

(c) Side Plate Light Sensors - Only Two Sides Shown for Clarity

Figure 3.21: Location of Infrared Sensors - Fully Confined Experiments

3.6.2 Calibration of Photosensors

In the unconfined and fully vented blast experiments a calibration factor was determined before every testing period or when one of the photosensor arrays broke and was replaced. In the fully confined blast experiments a calibration test was carried out after every fully confined test as the entire assembly was disassembled and then reassembled for the next test. Prior to the calibration test the sensors were switch on and left for forty minutes to reach their normal operating temperature, thereafter the calibration test was carried out. The calibration test entailed measuring and recording voltage levels at several known displacements. Figure 3.22 illustrates results from several calibration tests. It must be noted that sensors are only valid for midpoint deflection greater than $4mm$.

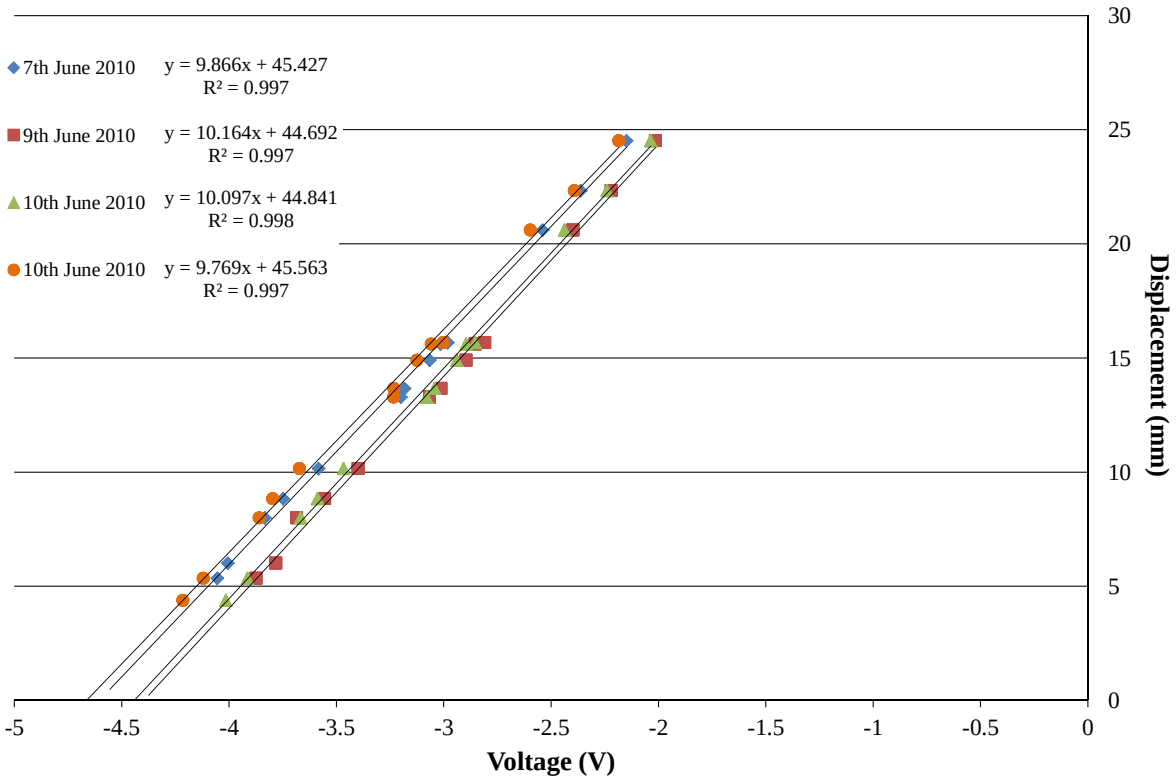

Figure 3.22: Calibration Curves For $3mm$ Unconfined Experiments

3.6.3 Trigger Circuit

A trigger signal which initiated the recording of data from the photosensors was generated at the time of detonation of the explosive charge. The triggering mechanism was a thin strip of aluminium foil attached to the polystyrene column as close to the explosive charge as possible. The strip of foil was connected to a circuit which generated the trigger signal when an open circuit occurred *i.e.* when the strip of foil tore. The blast wave generated from the detonation of the explosive charge tore the strip of foil generating the trigger signal. The position of the tin foil strip on a polystyrene column for a fully vented experiment is depicted in Figure 3.23.

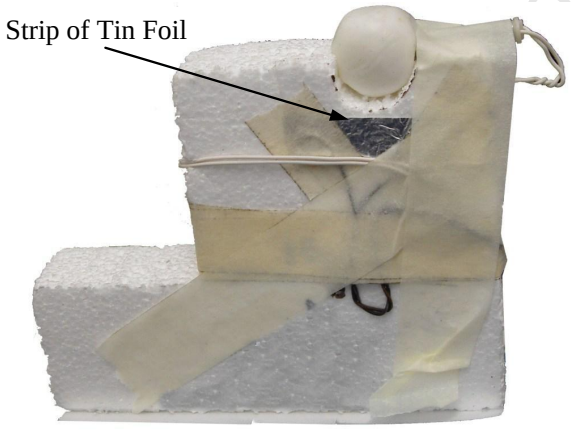

Figure 3.23: Position of Tin Foil Strip on a Fully Vented Experiment Polystyrene Column

4 Experimental Results

Ninety four experiments were carried out to investigate the effects of the degree of confinement and target plate thickness on the response of square steel plates subjected to blast loading.

The experimental results are presented in the following sections,

1. Unconfined blast loaded plates.
2. Fully vented blast loaded plates.
3. Fully confined blast loaded plates.
4. Transient midpoint deflections.

This chapter presents observations made on examining the target plates post testing, experimental readings including all measured and some calculated values.

The experiments were numbered according to the degree of confinement, target plate thickness, the sequence in which performed and the mass of explosive. The degrees of confinement were abbreviated to,

Unconfined Blast - UC; Partially Vented - FV; Fully Confined - FC

For example, an experiment numbered FV-3-10-60g refers to a fully vented blast; 3mm thick target plate; the tenth experiment in the 3mm thick target plate fully vented series; charge mass of 60g.

4.1 Unconfined Blast Loaded Plates

A total of 34 tests (11 off $3mm$, 11 off $4mm$ and 12 off $5mm$ thick target plates) were carried out to investigate the effect of unconfined blast loads on final midpoint deflection. Results obtained for the 3, 4 and $5mm$ thick target plates subjected to unconfined blast loads are presented in Table 4.1.

Table 4.1: Unconfined Midpoint Deformation Results

Test Number	Nominal Thickness(mm)	Charge Mass (g)	Total Area Impulse(Ns)	Exposed Area Impulse(Ns)	Deflection (mm)
3mm Plate					
UC-3-1	3.1	10	10.5	7.0	0.0
UC-3-2	3.1	30	29.5	19.5	5.3
UC-3-3	3.1	40	43.1	28.5	8.0
UC-3-4	3.1	50	52.6	34.7	10.2
UC-3-5	3.1	50	48.7	32.2	8.8
UC-3-6	3.1	60	61.7	40.8	13.7
UC-3-7	3.2	60	60.5	40.0	13.3
UC-3-8	3.1	70	72.7	48.1	15.7
UC-3-9	3.1	70	67.4	44.5	15.6
UC-3-10	3.1	70	67.8	44.8	14.9
UC-3-11	2.8	30	28.6	18.9	7.7
4mm Plate					
UC-4-1	4.1	30	33.2	21.9	2.0
UC-4-2	4.0	30	33.2	21.9	2.1
UC-4-3	4.0	40	40.6	26.8	4.4
UC-4-4	4.0	40	42.8	28.3	4.2
UC-4-5	4.0	50	49.6	32.8	6.9
UC-4-6	4.0	50	54.3	35.9	9.2
UC-4-7	4.0	60	53.2	35.1	8.4
UC-4-8	4.0	60	62.6	41.4	8.7
UC-4-9	4.0	70	64.8	42.8	12.3
UC-4-10	4.0	70	69.1	45.7	10.4
UC-4-11	4.1	50	48.8	32.2	7.7
5mm Plate					
UC-5-1	5.1	20	24.1	15.9	0.7
UC-5-2	5.1	40	41.2	27.2	0.7
UC-5-3	5.1	10	11.8	7.8	0.2
UC-5-4	5.1	15	18.3	12.1	0.2
UC-5-5	5.1	50	52.9	35.0	1.5
UC-5-6	5.1	20	22.6	14.9	0.2
UC-5-7	5.1	50	51.2	33.8	1.8
UC-5-8	5.1	50	49.6	32.8	1.4
UC-5-9	5.1	70	74.5	49.2	4.5
UC-5-10	5.1	70	69.7	46.0	5.5
UC-5-11	5.1	60	54.2	35.8	6.5
UC-5-12	5.1	60	53.9	35.6	6.2

Figures 4.1, 4.2 and 4.3 are photographs of the cross section deformation profiles of a selection of 3, 4 and 5mm thick target plates subjected to different unconfined blast loads respectively. As expected, the midpoint deflection increases with an increase in the mass of explosive.

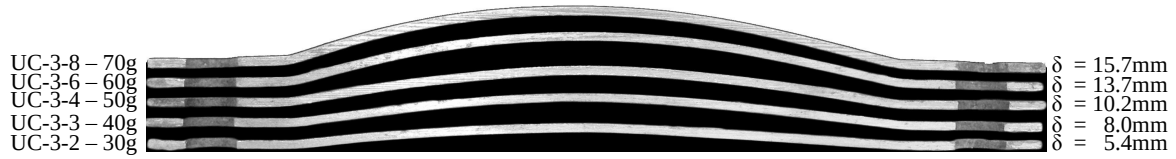

Figure 4.1: Photograph of the Cross Sectional Deformation Profiles of a Sample of 3mm Thick Target Plates Subjected to Unconfined Blast Loads

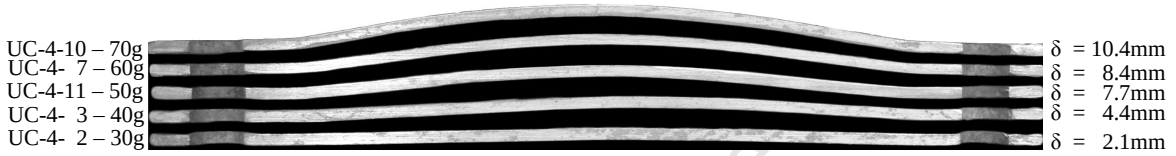

Figure 4.2: Photograph of the Cross Sectional Deformation Profiles of a Sample of 4mm Thick Target Plates Subjected to Unconfined Blast Loads

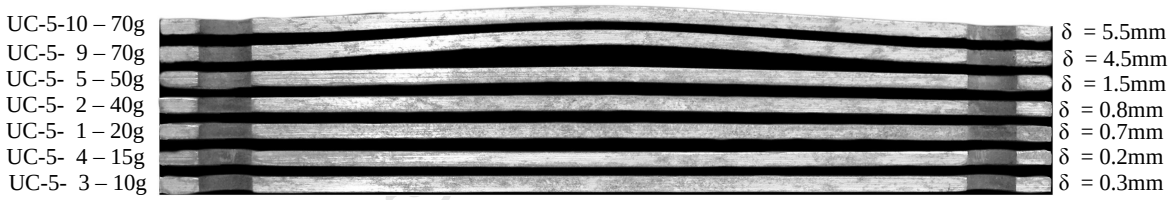

Figure 4.3: Photograph of the Cross Sectional Deformation Profiles of a Sample of 5mm Thick Target Plates Subjected to Unconfined Blast Loads

Large inelastic deformation (Mode I) was observed for the 3 and 4mm target plates. The 5mm target plates exhibited small inelastic deflection, in some cases the deflection was not distinguishable from the target plate surface. Limitations on the charge mass detonated[1] within the blast chamber prevented any higher inelastic deformations being obtained. **As the midpoint deflections obtained for the 5mm target plates were not representative of large inelastic deformation, the midpoint deflections results were not considered for subsequent analyses but included here for completeness.**

[1]Maximum allowable charge mass is 70g.

The deformation profile of the target plates was characterised by an uniform global dome with the maximum deformation occurring in the centre of the target plate. Typical of the response of quadrangular plates subjected to uniform air blast loading as reported by References [54, 59].

Plastic hinges were observed in the 3 and $4mm$ thick target plates subjected to large charge masses. The plastic hinges extended from the corners to the centre of the target plate at an angle of 45°. Predominantly the deformation profiles were symmetrical however asymmetrical deformations did occur. In cases where asymmetrical deformation profile was evident the maximum and midpoint deflections were within 5%.

4.1.1 Comparison of Measured and Target Plate Impulse Measurements

Table 4.1 lists two impulse measurements namely the total area and the exposed area impulse. The total area impulse refers to the impulse determined from the amplitude of the swing of the ballistic pendulum in the unconfined experiments. The exposed area impulse refers to the impulse transferred to the exposed area of the target plate.

For a comparison between the other degrees of confinement, which have an exposed area of $200 \times 200mm$, the total area impulse in the unconfined experiments needs to be adjusted to account for the area mismatch between the total area and the exposed area of the target plate which affects the impulse measurement [122]. The experimental rig in the unconfined experimental setup had an total area of $300 \times 300mm$ whilst the exposed area of the target plate was $200 \times 200mm$, as illustrated in Figure 4.4.

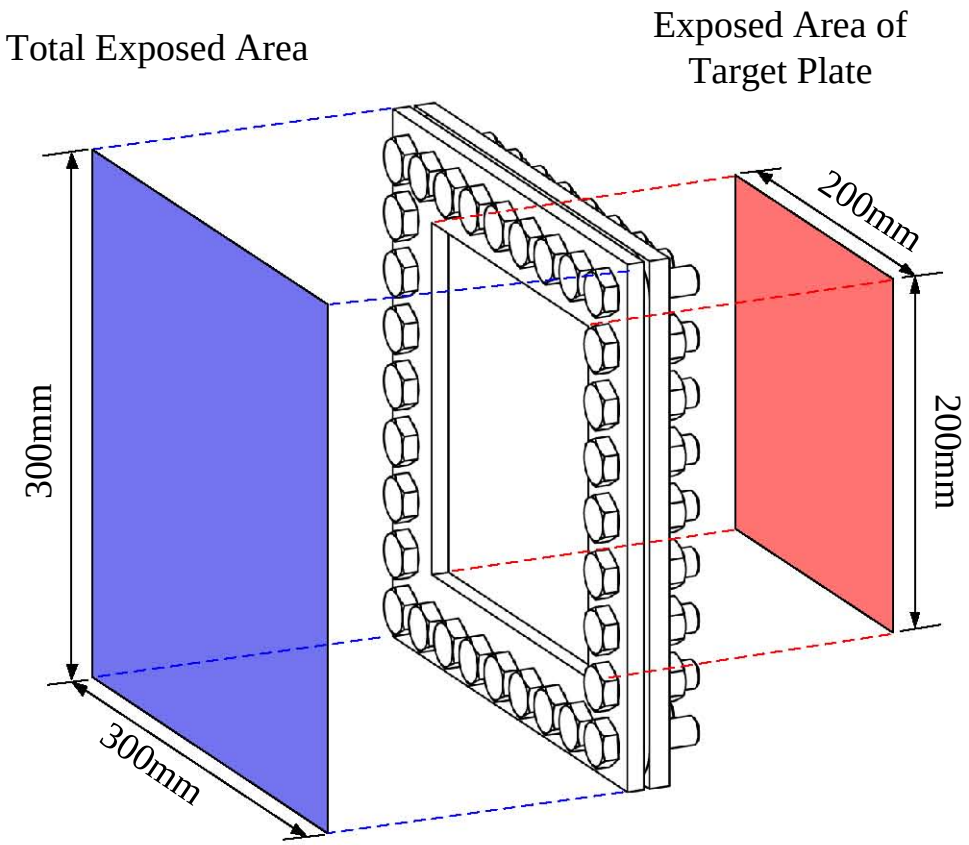

Figure 4.4: Schematic of Unconfined Experimental Rig Illustrating the Total and Target Plate Exposed Areas

A series of experiments, described in Section 3.5, was carried out to determine the percentage of the total impulse transferred to the exposed area of the target plate. In the experiments a rigid target plate with the same area as the exposed area of the target plate in the unconfined setup ($200 \times 200mm$) was subjected to varying magnitude unconfined blast loads. The impulse results from the rigid plate and the unconfined experiments are illustrated in Figure 4.5.

As expected, the reduction in exposed area resulted in the decrease of impulse for the same charge mass. Comparing the impulse measurements in the range of $30 - 70g$ of explosive, assuming reflections of the blast wave off the clamp frame in the unconfined setup were negligible, it was found that approximately 66% of the measured impulse in the unconfined experiments was transferred to the exposed area of the target plate.

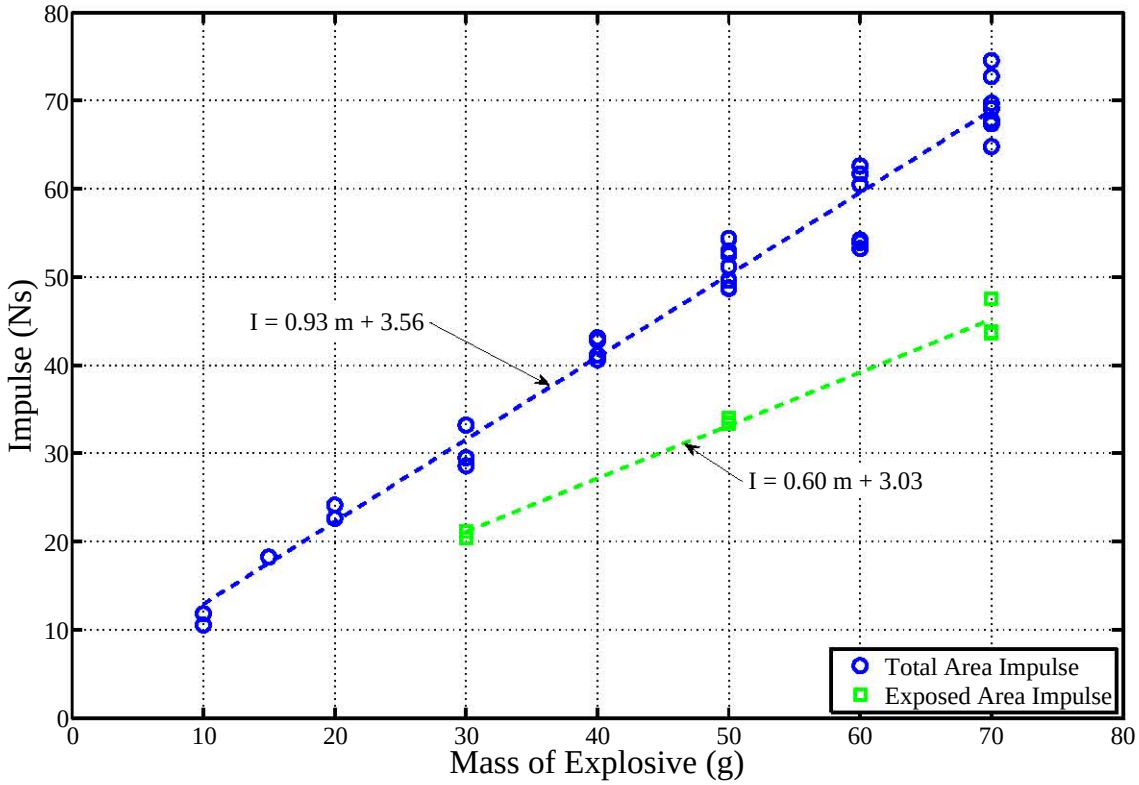

Figure 4.5: Impulse Versus Mass of Explosive Illustrating Reduction in Measured Impulse with Reduction in Exposed Area

The percentage transfer of the impulse indicates that the blast load was not uniform and was concentrated towards the centre of the target plate. If the blast load was uniform the impulse transferred to the exposed area of the target plate, as a percentage, would be equal to the ratio of areas ($\frac{A_{exposed}}{A_{total}} = 44.4\%$).

For subsequent analyses when comparing the impulse, the exposed area impulse, calculated with Equation 4.1, was implemented.

$$I_{target\,plate} = I_{measured\,UC} \times 66\% \tag{4.1}$$

4.2 Fully Vented Blast Loaded Plates

A total of 32 experiments (13 off $3mm$, 9 off $4mm$ and 10 off $5mm$ thick target plates) were carried out to investigate the effects of a fully vented blast loads on the final midpoint deflections of square target plates. Table 4.2 lists the results obtained from the fully vented blast load experiments.

Table 4.2: Fully Vented Midpoint Deformation Results

Test Number	Nominal Thickness (mm)	Charge Mass (g)	Impulse (Ns)	Deflection (mm)
3mm Plate				
FV-3-1	2.7	10	26.1	2.9
FV-3-2	2.8	10	26.2	2.8
FV-3-3	2.7	30	65.9	16.4
FV-3-4	2.8	30	65.6	15.7
FV-3-5	2.8	40	87.5	22.0
FV-3-6	2.7	40	84.2	22.6
FV-3-7	2.8	20	45.1	10.9
FV-3-8	2.8	40	76.6	22.9
FV-3-9	2.8	40	82.1	22.7
FV-3-10	2.8	20	44.8	11.2
FV-3-11	2.7	60	119.7	34.1
FV-3-12	2.8	50	104.4	30.7
FV-3-13	2.8	60	118.6	35.3
4mm Plate				
FV-4-1	4.0	20	44.2	6.8
FV-4-2	4.1	30	64.7	11.2
FV-4-3	4.1	30	64.5	11.0
FV-4-4	4.1	40	85.2	14.9
FV-4-5	4.1	40	84.1	15.1
FV-4-6	4.1	50	103.9	19.1
FV-4-7	4.1	50	103.7	20.5
FV-4-8	4.1	60	119.3	25.3
FV-4-9	4.1	60	121.6	25.6
5mm Plate				
FV-5-1	5.1	30	66.5	6.5
FV-5-2	5.1	30	66.0	6.9
FV-5-3	5.1	50	105.8	14.4
FV-5-4	5.2	20	45.5	4.0
FV-5-5	5.1	20	46.5	4.3
FV-5-6	5.1	40	84.8	12.2
FV-5-7	5.1	40	85.1	13.2
FV-5-8	5.2	50	105.1	17.3
FV-5-9	5.2	60	118.4	20.2
FV-5-10	5.1	60	122.2	18.6

Figure 4.6, 4.7 and 4.8 are photographs of the cross section deformation profiles of a selection of 3, 4 and 5mm thick target plates subjected to different fully vented blast loads respectively.

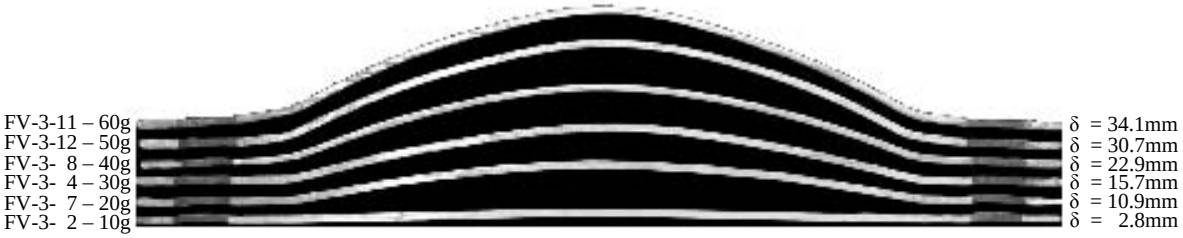

Figure 4.6: Photograph of the Cross Sectional Deformation Profiles of a Sample of 3mm Thick Target Plates Subjected to Fully Vented Blast Loads

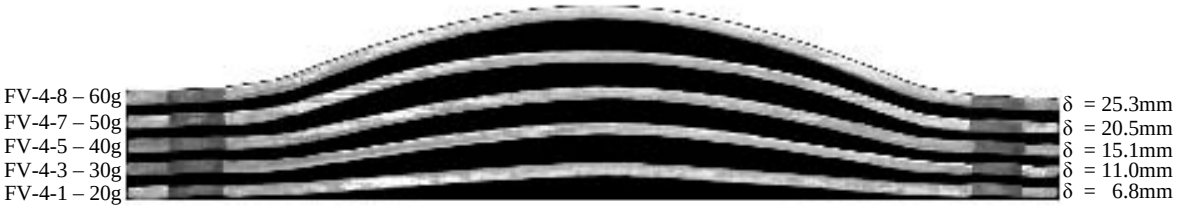

Figure 4.7: Photograph of the Cross Sectional Deformation Profiles of a Sample of 4mm Thick Target Plates Subjected to Fully Vented Blast Loads

Figure 4.8: Photograph of the Cross Sectional Deformation Profiles of a Sample of 5mm Thick Target Plates Subjected to Fully Vented Blast Loads

As expected, the midpoint deflections increases with an increase in the mass of explosive. The resulting midpoint deflections from a fully vented blast load were also greater than the equivalent mass unconfined blast load. The deformation profile was characterised by a global dome with the maximum deflection occurring at the centre of the target plate. Plastic hinges, extended from the corners to the centre of the target plate, were more visible due to larger, final midpoint deformations.

Mode I failure, large inelastic deformation, was observed in all fully vented experiments. Pull-in at the boundary was observed in the 3mm thick target plate at charge masses of 60g.

4.3 Fully Confined Blast Loaded Plates

A total of 18 experiments (8 off $3mm$, 10 off $4mm$ and 10 off $5mm$ thick target plates) were carried out to investigate the effects of a fully confined blast load. The results are presented in two sections namely top target plate and container deflections. Container deflections refer to the deflections of the sides and bottom target plate which make up the containers. Figure 4.9 is a photograph of a fully confined experimental setup illustrating the container target plates. The container deflections were measured to investigate the symmetry of the blast load and determine the effect of different boundary conditions of the final midpoint deflection. Table 4.3 lists the deflection results for the top target plates and the containers for the three different target plate thicknesses.

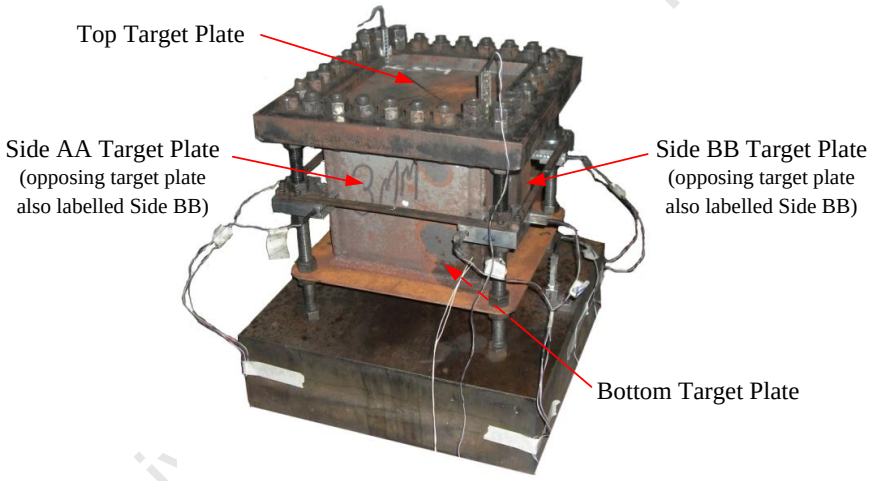

Figure 4.9: Classification of Target Plate Designation on a Fully Confined Container

Table 4.3: Fully Confined Midpoint Deformation Results

Test Number	Nominal Thickness (mm)	Charge Mass (g)	Target Plate Deflection(mm)			
			Top	Bottom	Side AA	Side BB
3mm Plate						
FC-3-1	3.4	20	16.3	13.5	16.0	16.0
FC-3-2	3.4	20	15.7	14.0	15.1	14.4
FC-3-3	3.4	30	23.3	18.4	21.1	20.9
FC-3-4	3.5	30	21.8	18.0	21.0	20.1
FC-3-5	3.4	40	27.5	22.3	23.8	24.6
FC-3-6	3.3	50	34.6	26.7	27.3	27.4
FC-3-7	3.4	60	39.8	31.8	29.5	29.9
FC-3-8	3.4	70	43.3	35.5	33.2	34.1

Continued on next page

Table 4.3 – continued from previous page

Test Number	Nominal Thickness (mm)	Charge Mass (g)	Target Plate Deflection(mm)			
			Top	Bottom	Side AA	Side BB
4mm Plate						
FC-4-1	4.0	20	11.6	11.4	13.5	13.5
FC-4-2	4.1	30	19.2	15.6	17.5	17.7
FC-4-3	4.0	40	24.4	18.6	21.4	20.8
FC-4-4	4.1	40	25.6	18.7	21.7	20.2
FC-4-5	4.1	30	19.7	16.4	18.4	18.9
FC-4-6	4.1	20	13.0	11.1	13.1	13.2
FC-4-7	4.0	50	31.9	24.8	24.9	24.7
FC-4-8	4.1	50	31.0	23.6	25.5	25.2
FC-4-9	4.0	60	37.0	27.6	27.6	27.1
FC-4-10	4.1	70	40.1	32.5	32.0	31.0
5mm Plate						
FC-5-1	5.1	20	8.9	7.9	7.4	7.3
FC-5-2	5.1	20	9.3	8.2	7.6	7.4
FC-5-3	5.1	30	13.9	11.8	11.7	12.0
FC-5-4	5.1	30	13.7	12.5	12.5	12.2
FC-5-5	5.1	40	17.8	14.5	15.8	15.5
FC-5-6	5.1	40	18.4	15.5	15.9	16.0
FC-5-7	5.1	50	21.9	17.1	18.9	18.2
FC-5-8	5.1	50	21.1	17.5	18.5	18.5
FC-5-9	5.1	60	25.4	20.8	21.4	20.2
FC-5-10	5.1	70	29.2	24.1	22.9	23.3

The deflection of opposing side target plates was assumed to be equal and symmetrical due the symmetry of the loading. The midpoint deflection of the side target plate was calculated half the difference between the deformed and the initial measured midpoint dimensions.

Side AA refers to the opposing target plates with the cable entry holes whilst side BB refers to the side target plates without any holes. The cable entry holes were assumed to have negligible effects on the deformation of the side target plates as the entry holes were very small ($\varnothing 1.6mm$). The identification of side AA and BB are highlighted in Figure 4.10 .

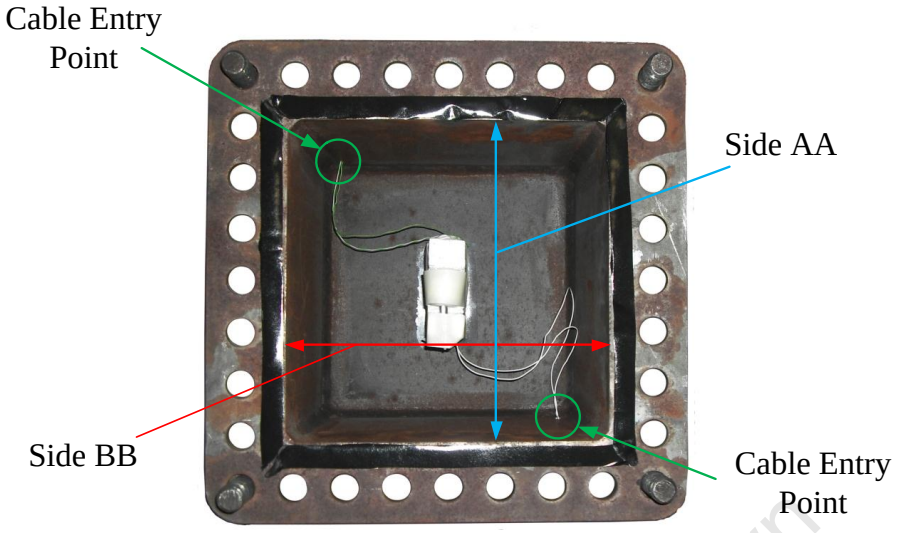

Figure 4.10: Identification of Side AA and BB on Fully Confined Container

4.3.1 Top Target Plate Deflections

Figures 4.11, 4.12 and 4.13 are photographs showing the cross section deformation profiles of a selection of top target plates subjected to different magnitude fully confined blast loads. As expected, the midpoint deflection increases with an increase in the mass of explosive detonated. For an equivalent mass of explosive , the midpoint deflection in the fully confined blast loaded target plates were generally greater then the measured midpoint deflection for the unconfined and fully vented blast loaded target plates.

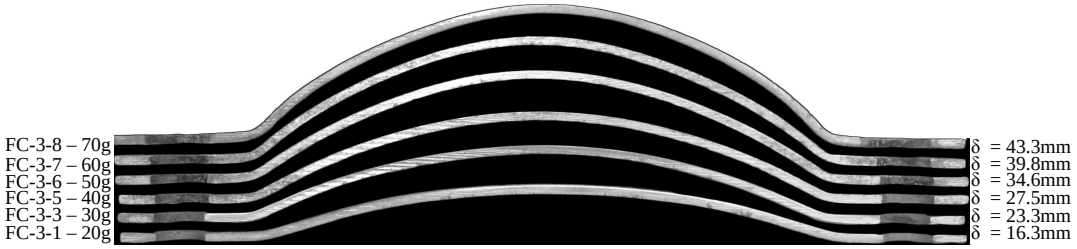

Figure 4.11: Photograph of the Cross Sectional Deformation Profiles of a Sample of 3mm Thick Target Plates Subjected to Fully Confined Blast Loads

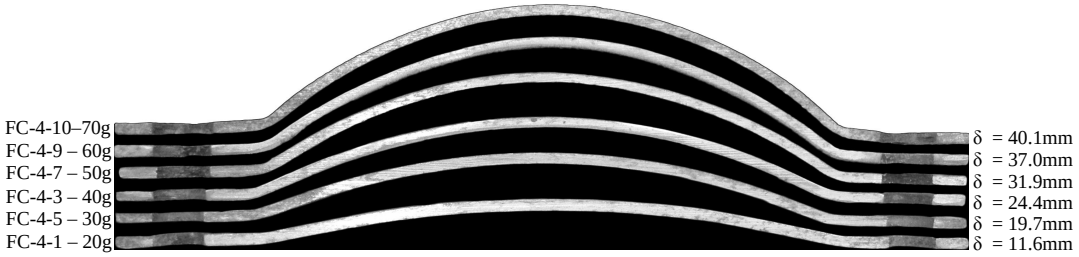

Figure 4.12: Photograph of the Cross Sectional Deformation Profiles of a Sample of $4mm$ Thick Target Plates Subjected to Fully Confined Blast Loads

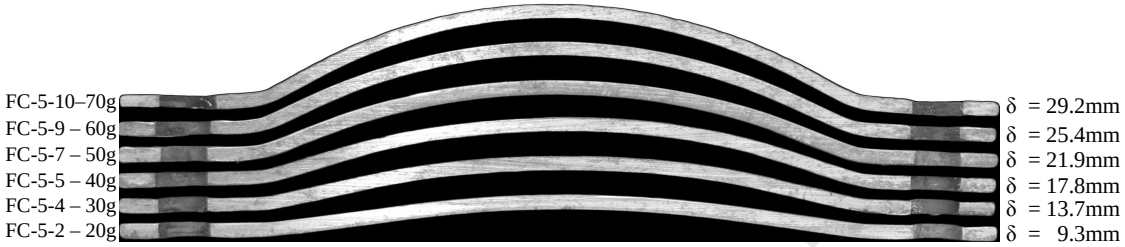

Figure 4.13: Photograph of the Cross Sectional Deformation Profiles of a Sample of $5mm$ Thick Target Plates Subjected to Fully Confined Blast Loads

The target plate deformation profile exhibited a global dome deformation profile with the maximum deformation occurring at the centre of the target plate. Pronounced plastic hinges on the top target plates which extended from the corner to the centre of the top target plates were observed. Severe pull-in at the boundaries was observed on the 3 and $4mm$ top target plates at large charge masses.

In experiments where large midpoint deflections were measured and severe pull-in observed, the target plate was 'scarred' at the boundary due to the interaction between the deforming top target plate and the top clamp frame. No significant thinning at the boundary was observed when the target plate exhibited scarring. Figure 4.14 is a photograph depicting the pull-in observed on the $3mm$ thick top target plate subjected to a blast load generated by the detonation of $70g$ of explosive. The plastic hinges and the scarring on the top target plate are highlighted in Figure 4.14.

All top target plates displayed Mode I failure, large inelastic deformation. The 3 and $4mm$ top target plates exhibited significant boundary effects, pull-in and scarring, at larger charge masses. The fully clamped top target plate permitted significant pull-in at

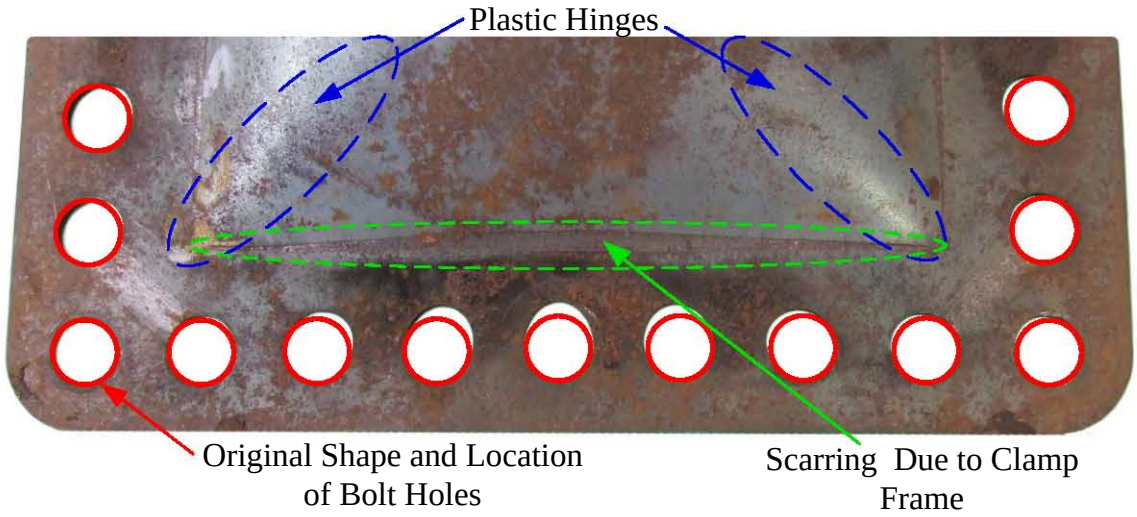

Figure 4.14: Photograph of Pull-in Observed on 3mm Top Target Plate Subjected to a 70g Blast Load

the boundaries, allowing greater midpoint deflections. The effects of the fully clamped boundary in comparison to the welded ('built-in') boundary agree with the results reported by Thomas and Nurick [55]. Further discussions on the effects of boundary conditions will be presented in Section 5.4.

4.3.2 Container Deflections

Photographs of the cross section through the 3, 4 and 5mm thick containers subjected to fully confined blast loads are illustrated in Figures 4.15, 4.16 and 4.17 respectively, showing the increasing deformation profile of the container walls. At the larger masses (50 to 70g) of explosive the final deformed shaped was observed to be approximately spherical.

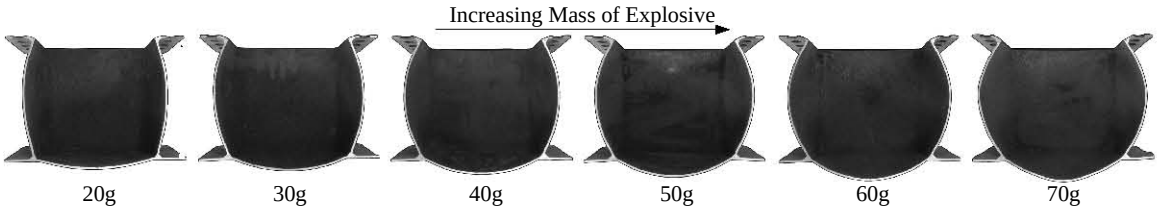

Figure 4.15: Photographs of the Cross Sections Through the 3mm Containers

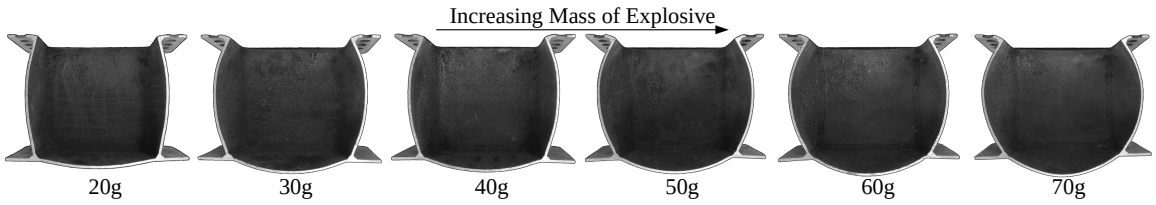

Figure 4.16: Photographs of the Cross Sections Through the $4mm$ Containers

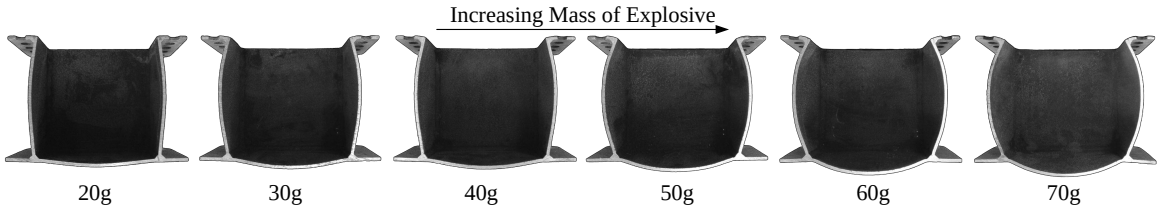

Figure 4.17: Photographs of the Cross Sections Through the $5mm$ Containers

Figures 4.18, 4.19 and 4.20 illustrate the superimposition of the deformation profiles of the fully confined containers at several charge masses showing the increasing deformation profile with increasing mass of explosive. As expected, the midpoint deflections of the walls of the container increases with an increase in mass of explosive. Similarly to the top target plates reported in Section 4.3.1, Mode I failure was observed on the walls of the containers.

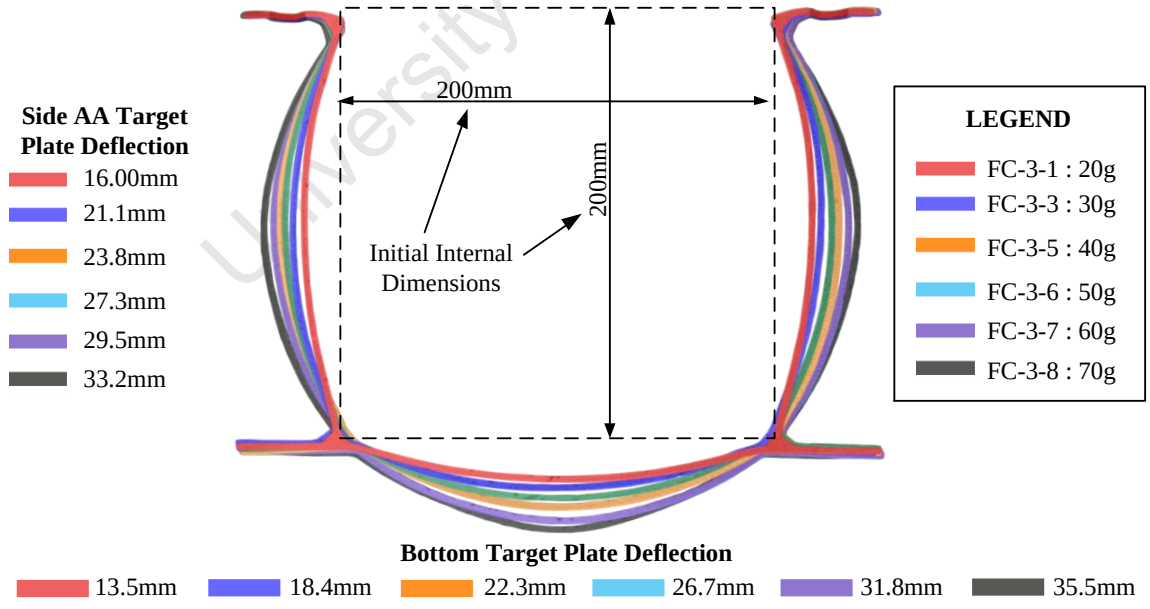

Figure 4.18: Superimposed Cross Section Deformation Profiles of the $3mm$ Thick Fully Confined Containers

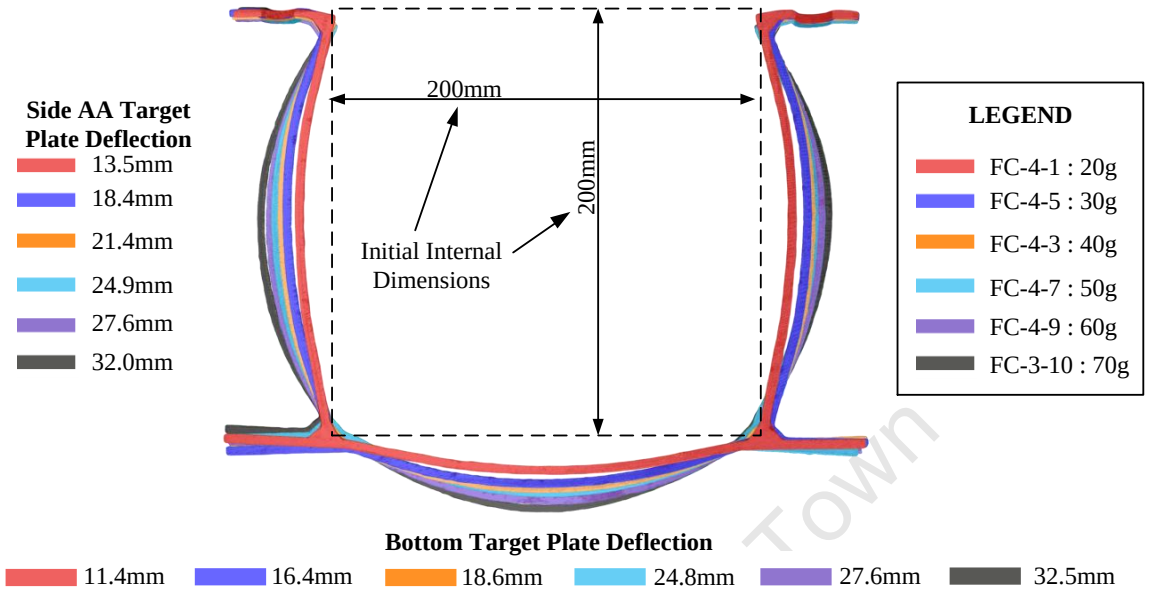

Figure 4.19: Superimposed Cross Section Deformation Profiles of the $4mm$ Thick Fully Confined Containers

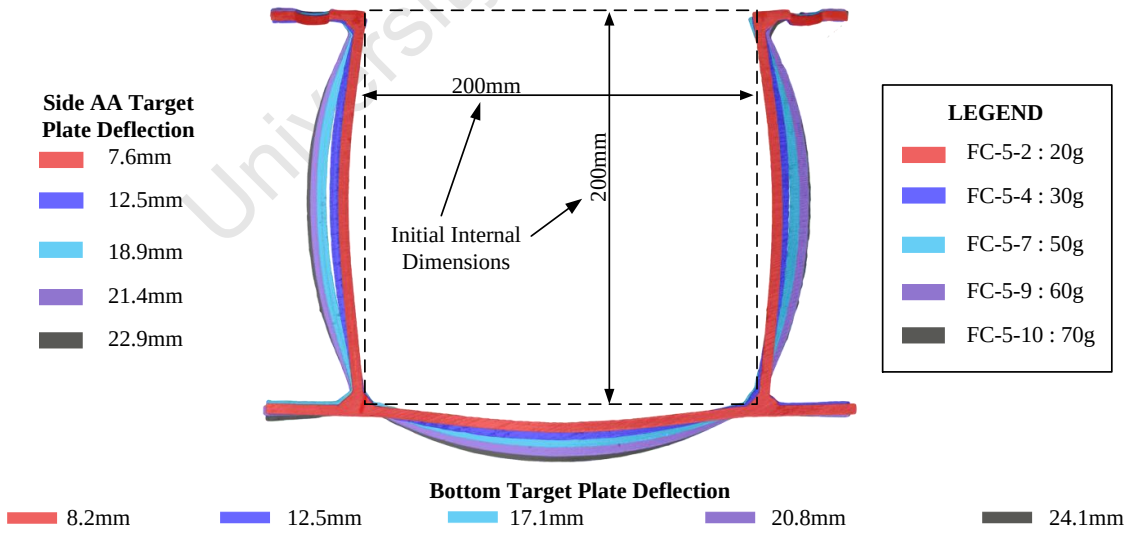

Figure 4.20: Superimposed Cross Section Deformation Profiles of the $5mm$ Thick Fully Confined Containers

The deformation of the container walls resulted in large deformations at the boundaries of the target plates, identified visual and illustrated in Figure 4.21. These boundaries are referred to as Point A, B and C in Figure 4.21.

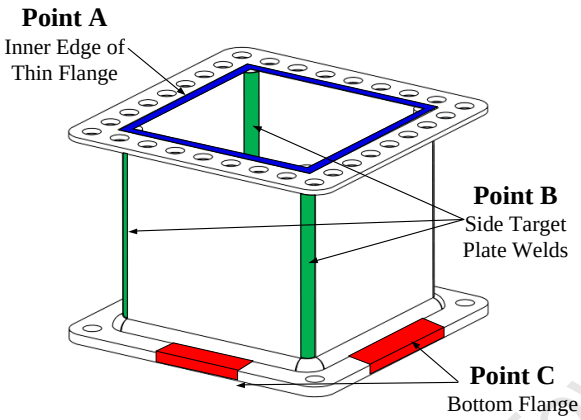

Figure 4.21: Schematic of Fully Confined Container – Highlighting Locations of Significant Boundary Deformation

The inner edge of the thin flange, labelled 'Point A' in Figure 4.21, deformed in towards the bottom target plate. Figure 4.22 illustrates two cross section views of the containers showing the deformation of the inner edge of the thin flange. The maximum deformation occurred at the centre of the thin flange (line AA in Figure 4.22) and decreased towards the corners. The magnitude of the deformation increases with an increase of the mass of explosive and decreases with an increase in target plate thickness. Figure 4.22 also illustrates the cross sectional deformation profiles of the $3mm$ thick containers subjected to different masses of explosive, showing the increase in the deformation with an increase of mass of explosive and that the deformation of the inner edge of the thin flange pivoted about the inner top edge of the bottom clamp frame.

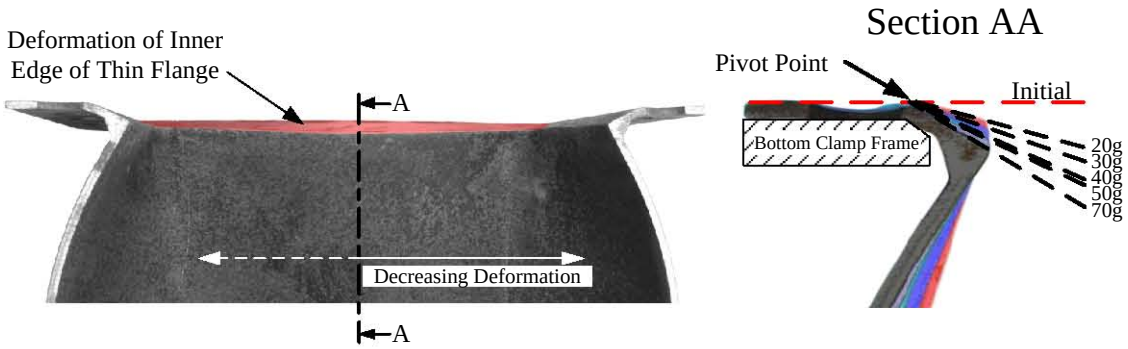

Figure 4.22: Deformation of Inner Thin Flange Observed in $3mm$ Thick Containers

The welded edges of the side target plates, labelled 'Point B' in Figure 4.21, underwent large inelastic deformations. The outward deformation of the side target plates resulted in the inward deformation of the welded edges. In all cases the welded edges deformed towards the centre of the containers. Similar deformation of the welded edges of rectangular steel container were observed by Brundage *et al.* [17]. As expected, the magnitude of the welded edge deformation increases with an increase in charge mass and decreased with the target plate thickness. Figure 4.23 is a series of photographs depicting the welded edges and the increasing pull in of the edge for the $3mm$ containers.

Warping of the bottom flange was also observed in the central region of the bottom flange, labelled 'Point C' in Figure 4.21. The warping of the bottom flange can be attributed to the large inelastic deformation of the bottom target plate pulling the material at the boundary inwards. The severity of the warping increases with an increasing of mass of explosive and decreases with the increase in target plate thickness. Figure 4.24 is a series of photographs illustrating warping bottom flange and the increasing severity of the warping as the charge mass increases.

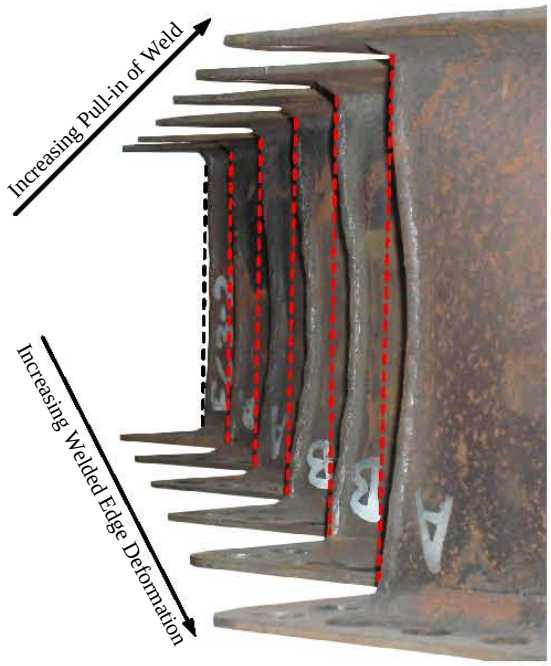

Figure 4.23: Photograph of Welded Edge Pull-in Observed in 3mm Containers

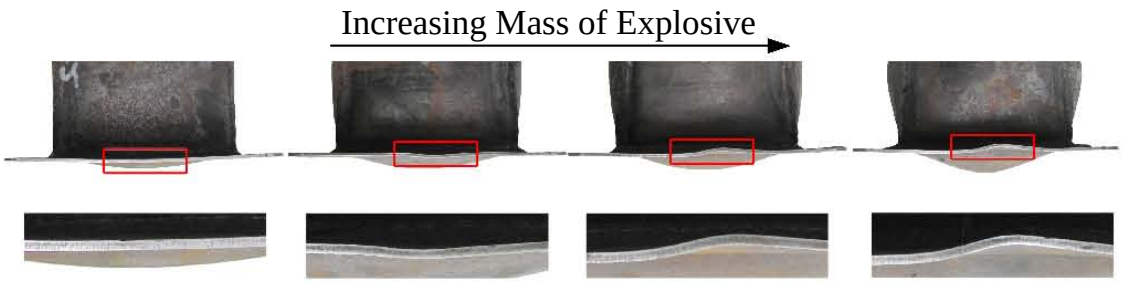

Figure 4.24: Photographs of 3mm Bottom Target Plate Flanges Illustrating Increase in Warping with Increased Explosive Loads

4.4 Transient Midpoint Deflections

The transient response of the target plates in all the experiments was measured with infrared photosensors. Figure 4.25 illustrates an example of a deflection history recorded with the infrared photosensors and the smoothed deflection history. The data was smoothed to reduce the effects of noise and voltage spikes present in the signal. The noise present on the signal was attributed to environmental sources and component assembly. Voltage spikes could have been generated by the electromagnetic pulse generated by the detonation of high explosives or from cable whipping [124].

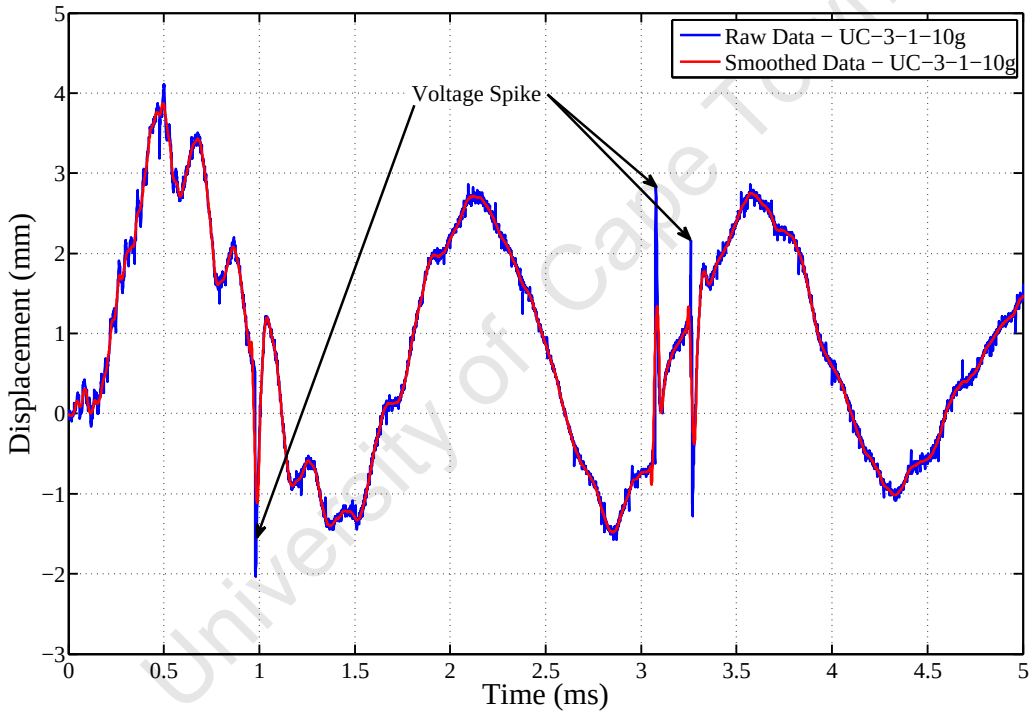

Figure 4.25: Smoothing Function Applied to Raw Data

Figure 4.26 is typical midpoint deflection history recorded of an unconfined blast loaded plate. The midpoint deflection history was characterised by an initial rapid increase in the deflection to peak transient midpoint deflection, thereafter damped elastic oscillations occur leading to the final midpoint deflection. Similar deflection histories have been observed for the response of circular [125] and quadrangular [59, 126] target plates subjected to blast loading.

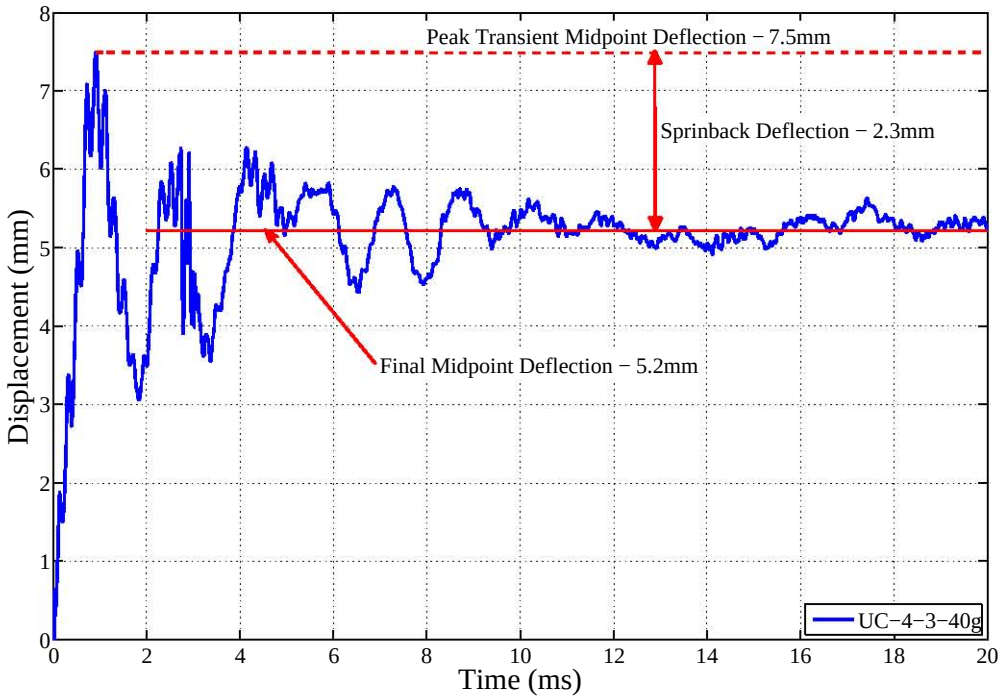

Figure 4.26: Typical Measured Transient Response for $3mm$ Unconfined Blast Load Target Plates

The midpoint deflection from the deflection histories was taken as the average deflection from 2 to $10ms$ and was termed the transient midpoint deflection. The deflection histories where the effects of smoke were evident the midpoint deflection was taken as the average deflection between the peak deflection and the point where significant effects of smoke were encountered. The peak midpoint deflection was taken as the maximum deflection observed after the initial rapid increase of the midpoint deflection. The springback deflection was taken as the difference between the peak and final transient midpoint deflection. Figure 4.26 illustrates the transient midpoint, peak and springback deflection for experiment UC-4-3-40g.

The peak midpoint deflection, transient final midpoint deflection and springback deflections are listed in Tables 4.4, 4.5 and 4.6 for the 3, 4 and $5mm$ thick target plates respectively. Tables 4.4, 4.5 and 4.6 also list the figure numbers for the respective midpoint deflection histories which are presented in Appendix D. **Note the $5mm$ thick target plate subjected to unconfined blast loads are included in the transient analysis.**

Table 4.4: Transient Midpoint Deflection Results for $3mm$ Thick Target Plates

Unconfined Blast Load					
Test Number	Mass of Explosive (g)	Figure Number	Peak Midpoint Deflection (mm)	Transient Midpoint Deflection (mm)	Springback Deflection (mm)
UC-3-1	10	D.1	3.9	0.6	3.3
UC-3-2	30	Failure	*NA*	*NA*	*NA*
UC-3-3	40	D.1	9.0	4.3	4.7
UC-3-4	50	D.2	17.2	10.9	6.4
UC-3-5	50	D.2	14.3	10.4	3.9
UC-3-6	60	D.3	23.8	15.0	8.9
UC-3-7	60	D.3	21.9	16.7	5.2
UC-3-8	70	D.4	26.5	16.3	10.2
UC-3-9	70	D.4	26.4	16.7	9.7
UC-3-10	70	D.4	25.7	13.1	12.6
UC-3-11	30	No Data	*NA*	*NA*	*NA*
Fully Vented Blast Load					
Test Number	Mass of Explosive (g)	Figure Number	Peak Midpoint Deflection (mm)	Transient Midpoint Deflection (mm)	Springback Deflection (mm)
FV-3-1	10	D.12	5.3	0.8	4.6
FV-3-2	10	D.12	5.4	1.5	3.9
FV-3-3	30	D.12	18.7	16.5	2.2
FV-3-4	30	Failure	*NA*	*NA*	*NA*
FV-3-5	40	Failure	*NA*	*NA*	*NA*
FV-3-6	40	Failure	*NA*	*NA*	*NA*
FV-3-7	20	No Data	*NA*	*NA*	*NA*
FV-3-8	40	No Data	*NA*	*NA*	*NA*
FV-3-9	40	Failure	*NA*	*NA*	*NA*
FV-3-10	20	D.12	13.4	11.4	2.0
FV-3-11	60	Failure	*NA*	*NA*	*NA*
FV-3-12	50	Failure	*NA*	*NA*	*NA*
FV-3-13	60	No Data	*NA*	*NA*	*NA*
Fully Confined Blast Load					
Test Number	Mass of Explosive (g)	Figure Number	Peak Midpoint Deflection (mm)	Transient Midpoint Deflection (mm)	Springback Deflection (mm)
FC-3-1	20	D.18	23.3	18.5	4.8
FC-3-2	20	D.18	19.4	16.7	2.8
FC-3-3	30	D.18	22.8	20.8	2.0
FC-3-4	30	No Data	*NA*	*NA*	*NA*
FC-3-5	40	No Data	*NA*	*NA*	*NA*
FC-3-6	50	D.18	39.4	36.0	4.0
FC-3-7	60	D.18	40.3	37.7	2.6
FC-3-8	70	D.18	45.2	42.8	2.3

Table 4.5: Transient Midpoint Deflection Results for $4mm$ Thick Target Plates

Unconfined Blast Load					
Test Number	Mass of Explosive (g)	Figure Number	Peak Midpoint Deflection (mm)	Transient Midpoint Deflection (mm)	Springback Deflection (mm)
UC-4-1	30	D.5	5.3	1.4	3.9
UC-4-2	30	D.5	4.5	2.1	2.4
UC-4-3	40	D.6	7.5	5.2	2.3
UC-4-4	40	Failed	*NA*	*NA*	*NA*
UC-4-5	50	D.7	11.2	5.0	6.2
UC-4-6	50	No Data	*NA*	*NA*	*NA*
UC-4-7	60	No Data	*NA*	*NA*	*NA*
UC-4-8	60	D.8	12.0	6.8	5.3
UC-4-9	70	D.8	16.0	6.5	9.5
UC-4-10	70	Failure	*NA*	*NA*	*NA*
UC-4-11	50	D.7	11.5	6.7	4.9
Fully Vented Blast Load					
Test Number	Mass of Explosive (g)	Figure Number	Peak Midpoint Deflection (mm)	Transient Midpoint Deflection (mm)	Springback Deflection (mm)
FV-4-1	20	D.13	9.8	7.7	2.1
FV-4-2	30	D.13	14.7	9.8	4.9
FV-4-3	30	D.13	13.3	9.6	3.7
FV-4-4	40	D.14	17.3	15.0	2.3
FV-4-5	40	D.14	17.8	14.8	3.0
FV-4-6	50	D.14	20.6	17.7	2.9
FV-4-7	50	D.14	26.9	22.4	4.5
FV-4-8	60	No Data	*NA*	*NA*	*NA*
FV-4-9	60	No Data	*NA*	*NA*	*NA*
Fully Confined Blast Load					
Test Number	Mass of Explosive (g)	Figure Number	Peak Midpoint Deflection (mm)	Transient Midpoint Deflection (mm)	Springback Deflection (mm)
FC-4-1	20	No Data	*NA*	*NA*	*NA*
FC-4-2	30	No Data	*NA*	*NA*	*NA*
FC-4-3	40	No Data	*NA*	*NA*	*NA*
FC-4-4	40	Failure	*NA*	*NA*	*NA*
FC-4-5	30	D.19	25.0	22.9	2.1
FC-4-6	20	D.19	16.0	13.3	2.7
FC-4-7	50	D.19	34.4	30.7	3.8
FC-4-8	50	D.19	34.1	29.3	4.8
FC-4-9	60	D.19	38.6	36.4	2.2
FC-4-10	70	D.19	40.8	38.5	2.4

Table 4.6: Transient Midpoint Deflection Results for $5mm$ Thick Target Plates

Unconfined Blast Load					
Test Number	Mass of Explosive (g)	Figure Number	Peak Midpoint Deflection (mm)	Transient Midpoint Deflection (mm)	Springback Deflection (mm)
UC-5-1	20	D.9	3.8	1.6	2.1
UC-5-2	40	D.10	7.1	1.5	5.6
UC-5-3	10	D.9	2.5	0.5	2.0
UC-5-4	15	D.9	3.9	0.9	3.0
UC-5-5	50	Failed	*NA*	*NA*	*NA*
UC-5-6	20	Failed	*NA*	*NA*	*NA*
UC-5-7	50	D.10	22.4	4.0	18.4
UC-5-8	50	D.10	12.4	6.8	5.6
UC-5-9	70	Failed	*NA*	*NA*	*NA*
UC-5-10	70	D.11	9.9	4.4	5.5
UC-5-11	70	No Data	*NA*	*NA*	*NA*
UC-5-12	60	No Data	*NA*	*NA*	*NA*
Fully Vented Blast Load					
Test Number	Mass of Explosive (g)	Figure Number	Peak Midpoint Deflection (mm)	Transient Midpoint Deflection (mm)	Springback Deflection (mm)
FV-5-1	30	No Data	*NA*	NA	NA
FV-5-2	30	D.15	12.5	6.6	5.9
FV-5-3	50	D.17	21.5	16.5	5.1
FV-5-4	20	D.15	7.6	3.6	4.0
FV-5-5	20	D.15	9.6	7.2	2.4
FV-5-6	40	D.16	16.0	10.0	6.1
FV-5-7	40	D.16	20.4	11.0	5.1
FV-5-8	50	D.17	15.4	17.3	3.1
FV-5-9	60	D.17	17.1	13.3	2.1
FV-5-10	60	Failure	*NA*	*NA*	*NA*
Fully Confined Blast Load					
Test Number	Mass of Explosive (g)	Figure Number	Peak Midpoint Deflection (mm)	Transient Midpoint Deflection (mm)	Springback Deflection (mm)
FC-5-1	20	D.20	13.8	10.3	3.5
FC-5-2	20	D.20	11.2	8.0	3.1
FC-5-3	30	D.21	19.9	15.6	4.4
FC-5-4	30	D.21	19.8	17.3	2.5
FC-5-5	40	D.22	22.9	17.6	5.3
FC-5-6	40	D.22	28.9	22.4	6.5
FC-5-7	50	D.23	24.7	19.0	5.7
FC-5-8	50	D.23	25.8	20.2	5.6
FC-5-9	60	D.24	31.4	25.7	5.7
FC-5-10	70	Failed	*NA*	*NA*	*NA*

As expected, the peak and final midpoint deflections observed from the deflection histories increased with the increase of charge mass. The elastic response of the plate after the peak midpoint deflection decreased with an increase in final midpoint deflection. Figure 4.27 shows the reduction in the elastic response as the midpoint deflection increases.

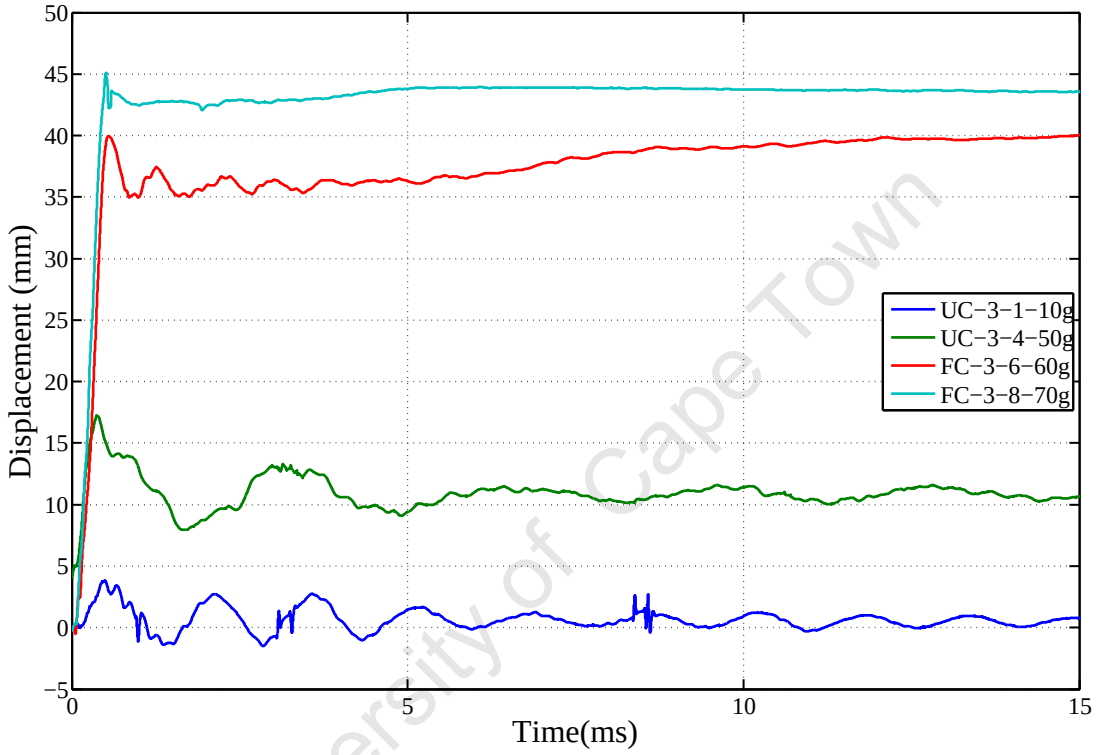

Figure 4.27: Graph Illustrating the Reduction of the Elastic Response As the Midpoint Deflection Increased

In several experiments cable whipping caused the connection between the sensor and the cable to fail. High acceleration forces generated from the blast load and the inertia of the cable create a whipping effect on the cable which tore the cable away from the sensor. Cable whipping of sensors and failure of the cable have been observed on sensors in blast loaded cubicles [14, 109, 124]. Figure 4.28 is a photograph illustrating a failed connection between the cable and the sensor due to cable whipping. As a result, in some experiments partial or no transient data was obtained.

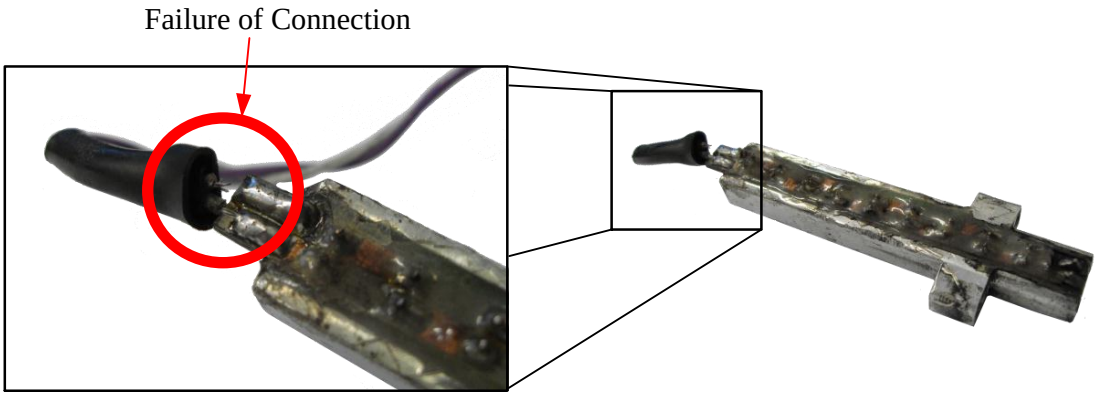

Figure 4.28: Photograph of Failed Photosensor

Figure 4.29 is a transient response of a target plate subject to an unconfined blast load where the sensor partially failed during the experiment(one of the cables tore off infrared diode array) and the initial failure point is also highlighted. After the initial failure of the cable at approximately $2ms$, intermittent contact between the photosensor and the cable occurred and resulted in several voltage spikes which are evident in Figure 4.29

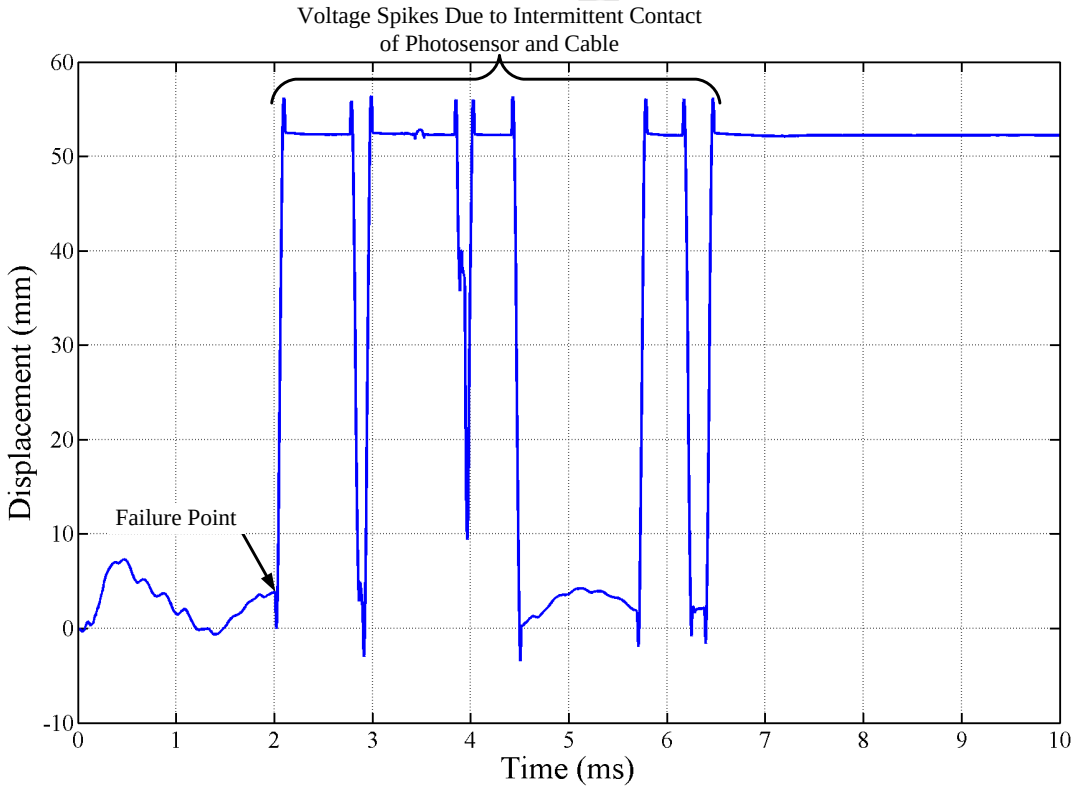

Figure 4.29: Transient Response of a Target Plate where the Sensor Failed

Several deflection histories presented unexpected behaviour where the deflection rapidly dropped below zero for a period of time then increased rapidly and/or the displacement drifts upwards after a period of time. This type of behaviour was predominantly present in the fully confined blast load experiments, however several fully vented blast load experiments exhibited the same behaviour. Figure 4.30 depicts several deflection histories where the unexpected behaviour can clearly be observed.

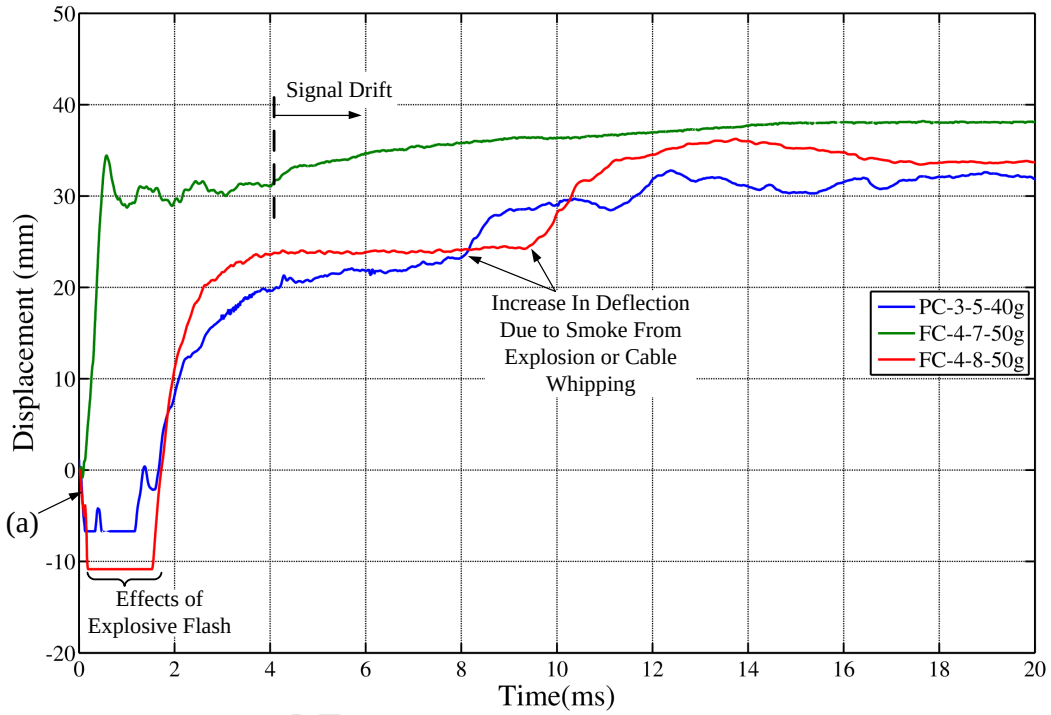

Figure 4.30: Effects of Flash And Smoke on Deflection History

Due to the relative time of the initial decrease in the deflection history and the behaviour of the electronic circuitry the rapid decrease in the deflection history (labelled (a) in Figure 4.30) was attributed to the flash from the explosion. The flash from the explosion saturates the photodiode array which causes the output voltage to drop to the lower limit of the data acquisition device. After the flash from the explosion the sensor recovers; however, detonation products venting through the clamped region of the target plate affects the sensors. The detonation products, mainly soot from burnt polystyrene and burnt explosive, interfered with the infrared curtain resulting in the signal drift upwards.

Figure 4.31 is a series of photographs illustrating a fully confined blast load experiment. The flash from the detonation can be seen in the photograph at $33ms$. After the flash from the detonation smoke can be seen venting from the two pairs of cable entry holes and the clamped region of the container. The build up of soot on the sensor after experiment FC-5-6-40g was carried out is illustrated in Figure 4.32.

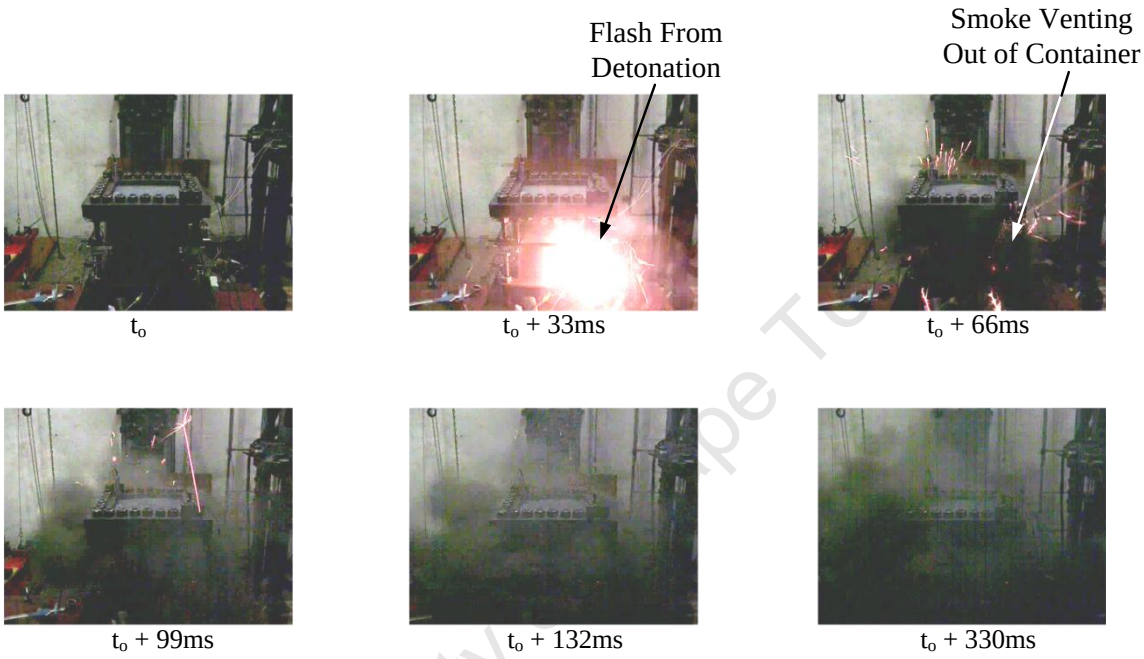

Figure 4.31: Series of Photographs Illustrating the Explosive Flash and Venting of Explosive Products from a Fully Confined Container Undergoing Blast Loading

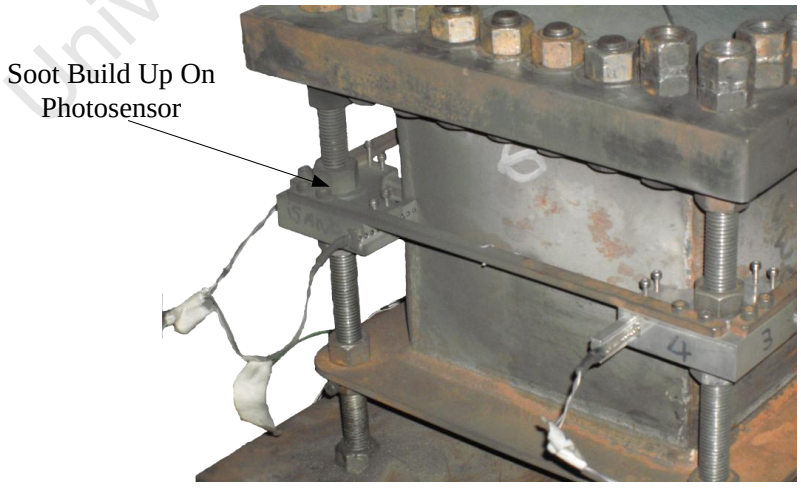

Figure 4.32: Photograph of Soot Build Up on Photosensor After an Experiment

Deflections histories where the flash from the explosion and detonation products had an severe effect were excluded from further analysis. The deflection histories of the sides and bottom target plates in the fully confined experiments were excluded as the results were severely effected by the venting of smoke from the containers.

5 Analysis of Experimental Results

5.1 Relationship Between Explosive Mass and Impulse

The impulse transfer to the target plate versus the mass of explosive for the unconfined and fully vented experiments are plotted in Figure 5.1. A general trend of increasing impulse with the increasing mass of of explosive for both the unconfined and fully vented blast were observed. It is evident from the graph that as the degree of confinement increases the impulse transferred to the target plate increases. Figure 5.1 also shows the repeatability of the tests.

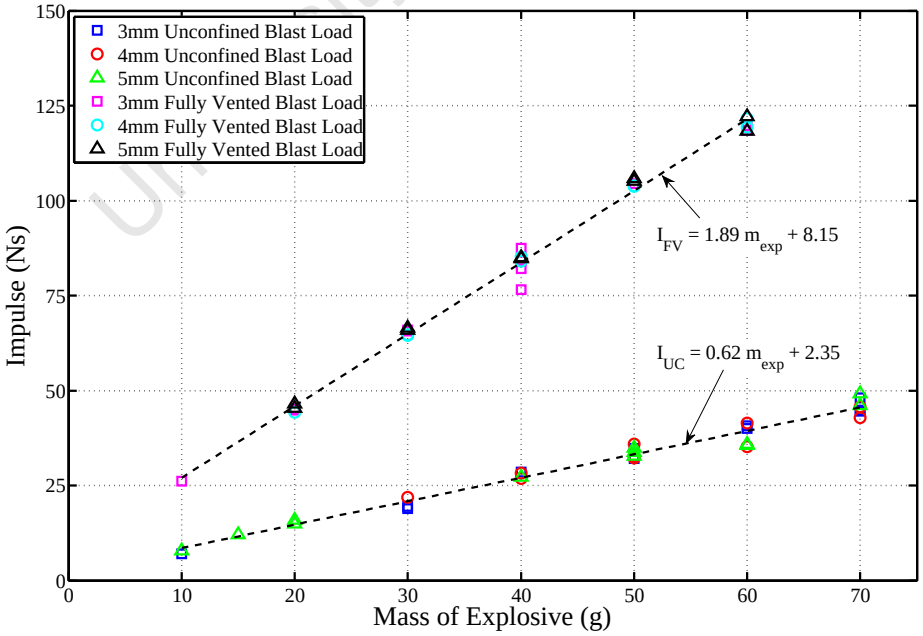

Figure 5.1: Graph of Impulse Versus Mass of Explosive

Least square fits (Equations 5.1 and 5.2) correlate well with data with correlation coefficient of 0.987, where the number of data points were 34 for the unconfined experiments and 0.997, where the number of data points were 32 for the fully vented experiments . The mass of explosive ranges from 10 to 70g for the unconfined blast loads and 10 to 60g for the fully vented blast loads. The results also show the repeatability of the unconfined and fully vented experiments.

$$I_{UC} = 0.62m_{exp} + 2.35 \tag{5.1}$$

$$I_{FV} = 1.89m_{exp} + 8.15 \tag{5.2}$$

Comparing the impulse values obtained from Equations 5.1 and 5.2 in the range of 10 to 60g of explosive a ratio of the impulse from a fully vented blast and an unconfined blast was computed and the result presented in Equation 5.3. The calculations of the respective impulses and the ratio of impulses are presented in Appendix E Table E.1.

$$I_{FV} = 3.1 \times I_{UC} \tag{5.3}$$

Based on this set of experiments, the impulse generated in a fully vented blast is approximately 3 times greater than the equivalent mass unconfined blast, as given by Equation 5.3.

5.2 The Effects of Plate Thickness on the Final Midpoint Deflection

The effect of target plate thickness on the final midpoint deflection was investigated by testing different plate thicknesses (3, 4 and 5mm thick) at each degree of confinement. The top target plates in the fully confined were compared to the unconfined and fully vented target plates as the target plates had similar fully clamped boundary conditions. A comparison of the deformation of the top, side and bottom target plates of the fully confined container are presented in Section 5.4.

Figure 5.2 shows a series of superimposed half cross section deformation profiles of target plates, grouped in mass of explosive and degree of confinement, of the different thickness target plates. Target plates of different thicknesses were superimposed to qualitatively examine the effects of target plate thickness on the final midpoint deflection. It can be observed from Figure 5.2, that the midpoint deflection increases with an increase of mass of explosive and decreases with an increase in plate thickness. This behaviour was expected and similar behaviour has been observed for quadrangular plate subjected to localised [39, 45, 48] and uniform blast loading [46, 59].

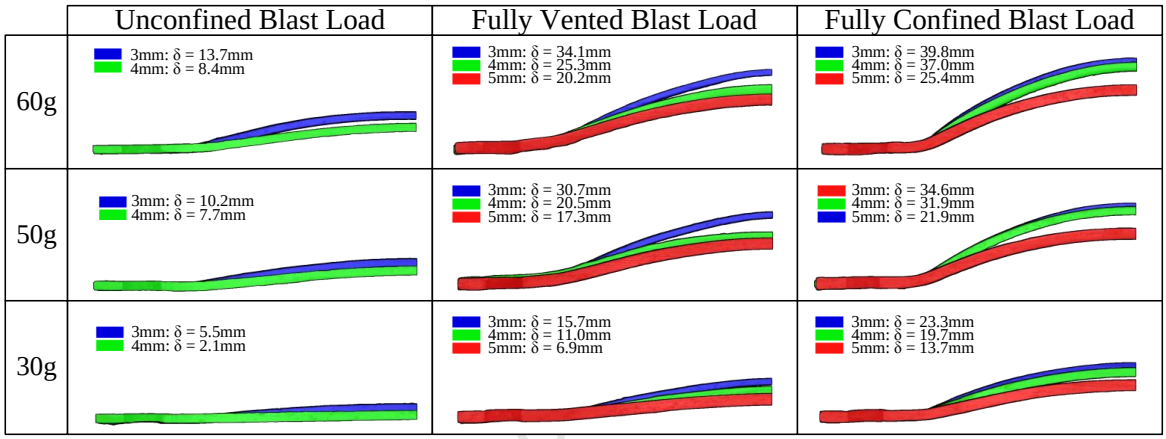

Figure 5.2: Half Cross Section Deformation Profiles of Different Thickness Target Plates Subjected to Different Blast Loads

To account for small variations in target plate thicknesses between the degrees of confinement, particularly the in the $3mm$ thick target plate series[1], the midpoint deflections were normalised by the ratio of respective target plate thickness (h) and the nominal plate thickness (h_{nom}). Normalising the midpoint deflections by the nominal target plate thickness allows results to be compared on a common scale allowing underlying characteristics to be observed. The normalised midpoint deflection (δ^{norm}) was calculated as,

$$\delta^{norm} = \delta_{measured} \times \frac{h}{h_{nom}} \tag{5.4}$$

[1]The $3mm$ thick material was affirmed to be from the same batch of steel even though the thicknesses were different and out of rolling tolerances ($\pm 0.2mm$ [127]) [128]

Results of the normalised final midpoint deflections versus the mass of explosive for the unconfined, fully vented and fully confined experiments are presented in Figures 5.3, 5.4 and 5.5 respectively. Trends of the normalised midpoint deflection and the mass of explosive were obtained with a least square fit. The corresponding equations are displayed on Figures 5.3, 5.4 and 5.5. Experimental midpoint deflections less than one nominal plate thickness were excluded from the fitting procedure as the deflections were within experimental variation (for instance for a $3mm$ thick target plate, if the final midpoint deflection was measured to be $2mm$ the result was discarded). The trends are based on the data presented and no speculation is made for the response outside the range tested.

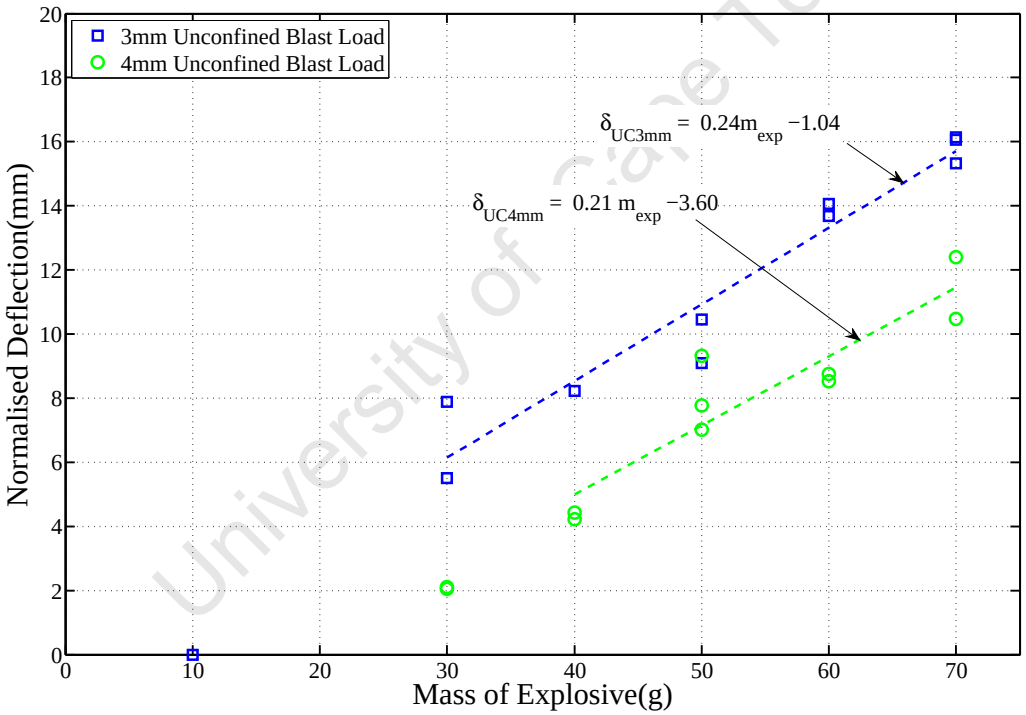

Figure 5.3: Normalised Deflection Versus Mass of Explosive - Unconfined Blast

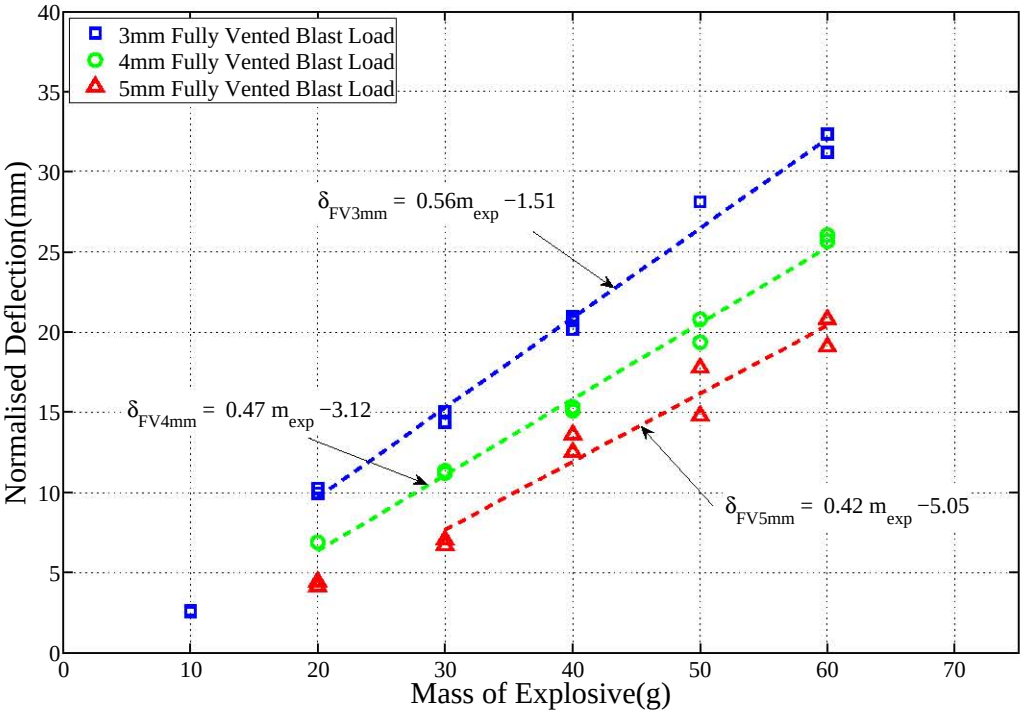

Figure 5.4: Normalised Deflection Versus Mass of Explosive - Fully Vented

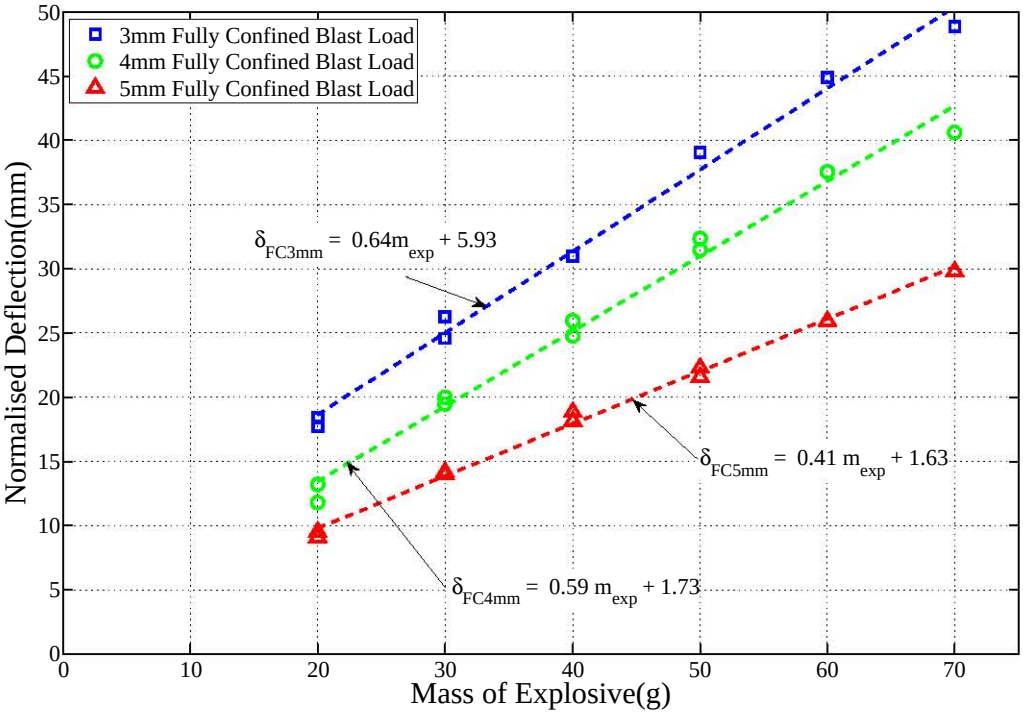

Figure 5.5: Normalised Deflection Versus Mass of Explosive - Fully Confined

Based on experiments carried out on plates subjected to air blast loads, Nurick and Martin [37, 38] presented a dimensionless damage number (Φ_q) for the response of a quadrangular plate subjected to an uniform blast load (see Section 2.2.5.3). The theoretical response of quadrangular plates proposed by Nurick and Martin [37, 38] is based on an uniform blast load and as shown in Section 4.1.1 the blast load experienced in the experiments is not uniform. However, it is the closest approximation to the load experience by the target plates in the different degrees of confinement.

Nurick and Martin [37, 38] reported the dimensionless damage number as,

$$\Phi_q = \frac{I}{2h^2(BL\rho\sigma_y)^{0.5}} \tag{5.5}$$

where I is the applied impulse, h is the target plate thickness, B is the length of the target plate, L is the length of the target plate, ρ is the density of the target plate material and σ_y is the static yield stress of the target plate material.

The empirical relationship between the midpoint deflection-thickness ratio ($\frac{\delta}{h}$) and the dimensionless damage number was reported as,

$$\frac{\delta}{h} = 0.48 \times \Phi_q \tag{5.6}$$

For two target plates made from the same material with equal exposed area but with different thicknesses, h_1 and h_2, subjected to identical blast loads (I), Equations 5.5 and 5.6 for the two target plates can be written as Equations 5.7 and 5.8 respectively.

$$\Phi_{q1} = \frac{I}{2h_1^2(B_1L_1\rho_1\sigma_{y1})^{0.5}} \tag{5.7a}$$

$$\frac{\delta_1}{h_1} = 0.48 \times \Phi_{q1} \tag{5.7b}$$

$$\Phi_{q2} = \frac{I}{2h_2^2(B_2L_2\rho_2\sigma_{y2})^{0.5}} \tag{5.8a}$$

$$\frac{\delta_2}{h_2} = 0.48 \times \Phi_{q2} \tag{5.8b}$$

The ratio of dimensionless damage numbers, Equations 5.7a and 5.8a, can be written as,

$$\frac{\Phi_{q1}}{\Phi_{q2}} = \frac{h_2^2}{h_1^2} \tag{5.9}$$

and the ratio of Equations 5.7b and 5.8b for the two target plates is given as,

$$\frac{\delta_1 h_2}{\delta_2 h_1} = \frac{\Phi_{q1}}{\Phi_{q2}} \tag{5.10}$$

Equating Equation 5.9 and 5.10, and re-arranging results in,

$$\frac{\delta_1}{\delta_2} = \frac{h_2}{h_1} \tag{5.11}$$

Equation 5.11 states that the midpoint deflection ratio between two different thickness plates subjected to identical blasts is inversely proportional to the ratio of the plate thicknesses. Re-arranging Equation 5.11 to Equation 5.12, results in a scaling formula where the midpoint deflection of a target plate can be scaled to the corresponding target plate of different thickness by the inverse of the thickness ratio of the target plates.

$$\delta_1 = \delta_2 \times \frac{h_2}{h_1} \tag{5.12}$$

To determine the validity of Equation 5.12, the midpoint deflections of the 4 and $5mm$ thick target plates in the respective degrees of confinement were scaled to $3mm$ thick target plate midpoint using with Equations 5.13 and 5.14 respectively. The scaled results are illustrated in Figures 5.6, 5.7 and 5.8.

$$\text{4mm Scaled to 3mm} \Rightarrow \quad \delta_{4mm}^{scaled} = \delta_{4mm}^{norm} \times \frac{h_{4mm}}{h_{scaled}} = \delta_{4mm}^{norm} \times \frac{4}{3} \tag{5.13}$$

$$\text{5mm Scaled to 3mm} \Rightarrow \quad \delta_{5mm}^{scaled} = \delta_{5mm}^{norm} \times \frac{h_{5mm}}{h_{scaled}} = \delta_{5mm}^{norm} \times \frac{5}{3} \tag{5.14}$$

After scaling the midpoint deflection the $4mm$ and $5mm$ thick target plates the majority of the scaled midpoint deflections fall within the 90% confidence envelope ($\pm 3mm$) of the $3mm$ thick target plate (Note:± 1 target plate thickness is an accepted confidence envelope [129, 130]). This suggests that Equation 5.11 is valid and is independent of the degree of confinement.

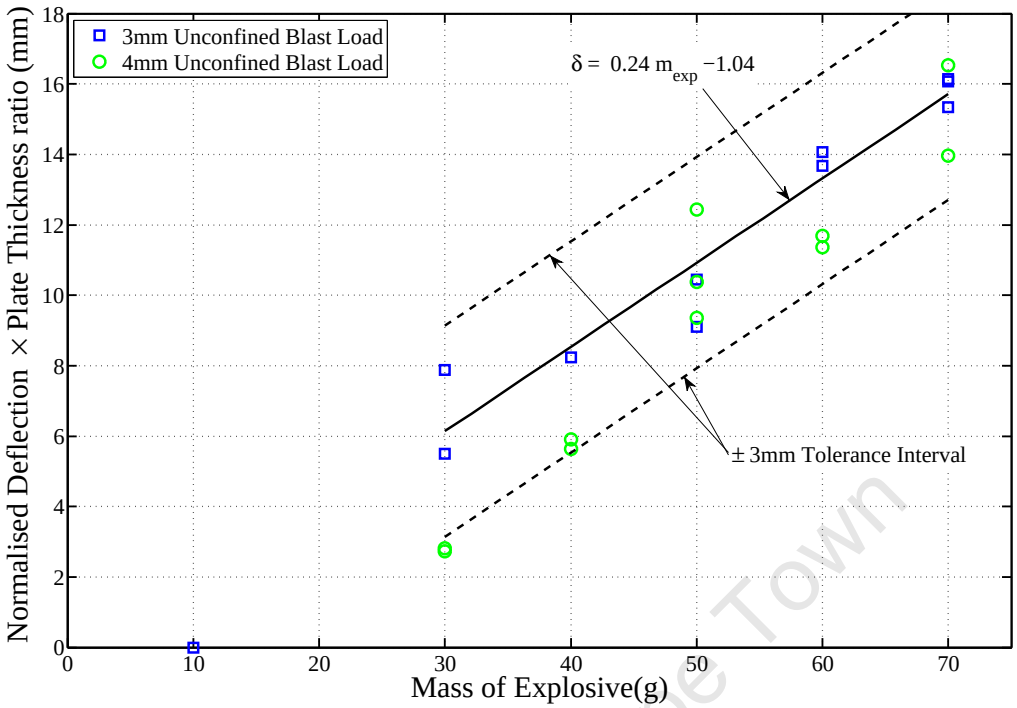

Figure 5.6: Scaled Normalised Midpoint Deflection Versus Mass of Explosive - Unconfined

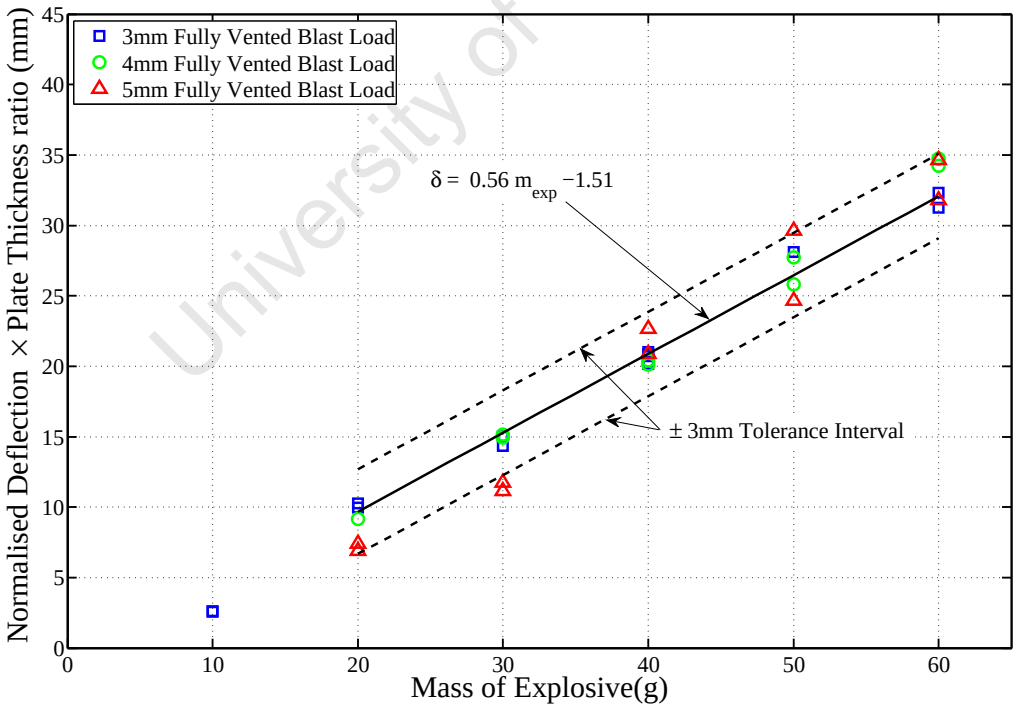

Figure 5.7: Scaled Normalised Midpoint Deflection Versus Mass of Explosive - Fully vented

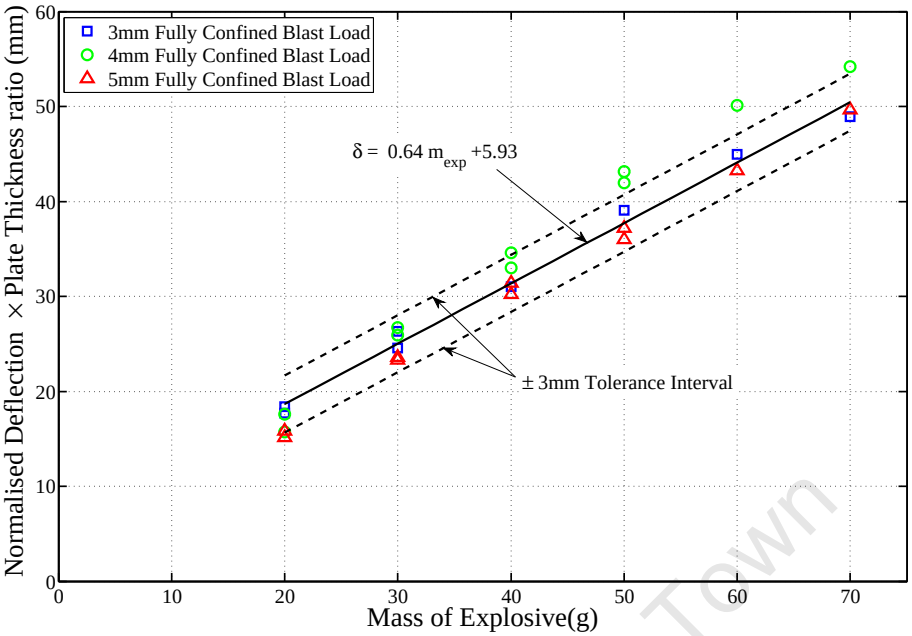

Figure 5.8: Scaled Normalised Midpoint Deflection Versus Mass of Explosive - Fully Confined

The actual midpoint deflection ratios were calculated, from the trend line equations illustrated in Figures 5.3, 5.4 and 5.5, as the average ratio between trend data over the range of 20 to 60g of explosive. The trend data and ratios of midpoint deflections (Equation 5.15) are computed and presented in Appendix E (Tables E.2, E.3 and E.4).

$$R_{34} = \frac{\delta^{norm}_{3mm}}{\delta^{norm}_{4mm}} \qquad R_{45} = \frac{\delta^{norm}_{4mm}}{\delta^{norm}_{5mm}} \qquad R_{35} = \frac{\delta^{norm}_{3mm}}{\delta^{norm}_{5mm}} \tag{5.15}$$

The actual midpoint deflection and the theoretical midpoint deflection ratios are listed in Table 5.1. The difference in the measured and theoretical midpoint deflection ratios are within experimental variation ($< 10\%$). This again suggest that Equation 5.12 can be used to scale midpoint deflections of different thickness plates by the inverse of the target plate thickness.

Table 5.1: Measured and Theoretical Midpoint Deflection Ratios

Midpoint Deflection Ratio	Measured Midpoint Deflection Ratio	Theoretical Midpoint Deflection Ratio	Percentage Difference
R_{34}	0.73	0.75	2.92
R_{45}	0.74	0.80	7.76
R_{35}	0.57	0.60	4.86

5.3 The Effects of Different Degrees of Confinement

The effect of different degrees of confinement on the midpoint deflection was investigated by a comparison of midpoint deflections within the same thickness series.

Figure 5.9 shows a series of superimposed half cross-sectional deformation profiles of target plates, grouped in mass of explosive and target plate thickness, subjected to different blast loads, for a qualitative comparison to analyse the effects of the degree of confinement on the final midpoint deflection. It is clearly evident from Figure 5.9 that the deformations of the target plates increases as the degree of confinement is increased.

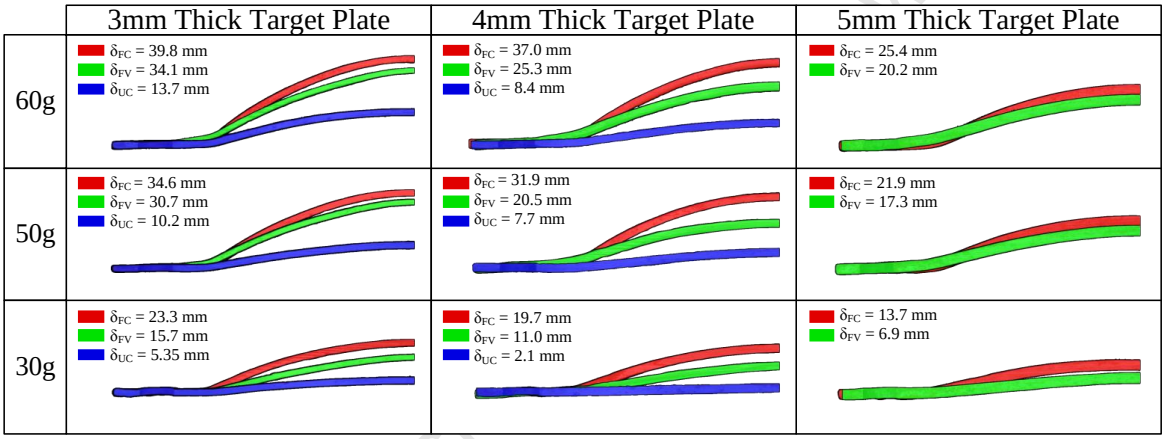

Figure 5.9: Half Cross Section Deformation Profiles of Target Plates Subjected to Different Blast Loads

Figures 5.10, 5.11 and 5.12 illustrate the normalised midpoint deflections versus the mass of explosive for each target plate thickness series. The results show the increase in midpoint deflections with the increase in the degree of confinement, confirm the observation made from Figure 5.9. The results suggests that for the same mass of explosive the damage increases as the degree of confinement increases, probably as a result of pressure build up.

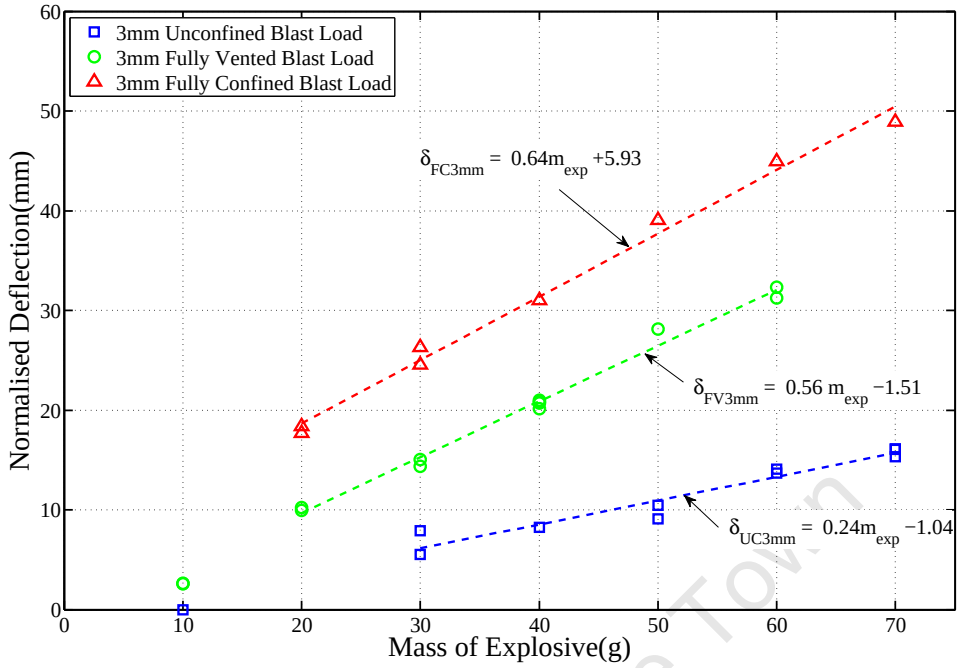

Figure 5.10: Deflection Versus Mass of Explosive - 3*mm* Thick Target Plates

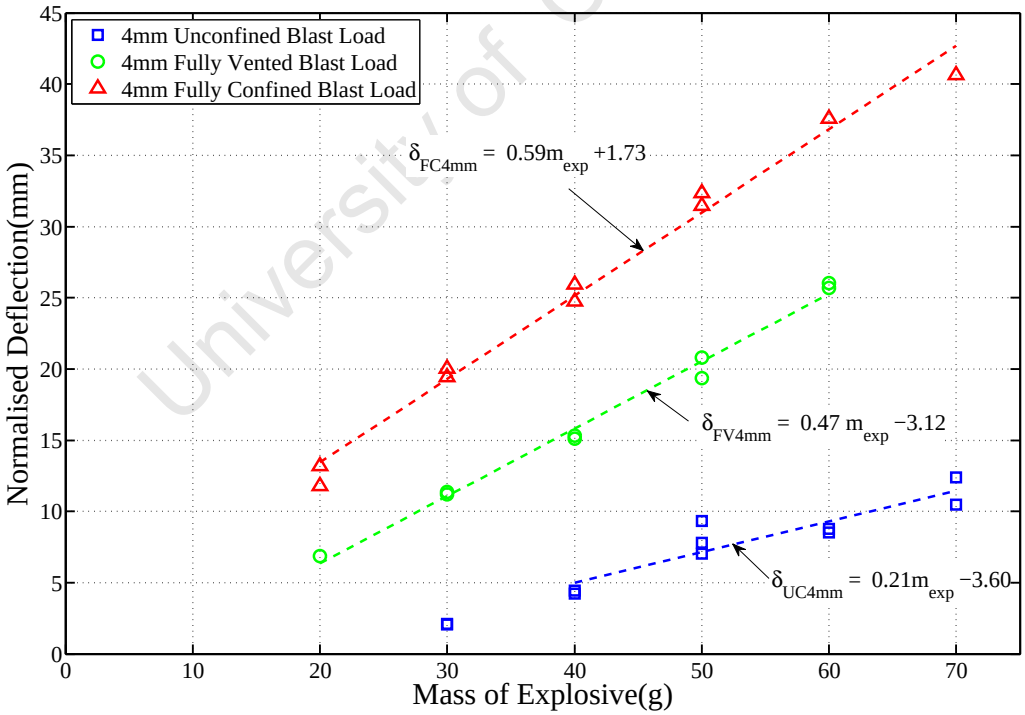

Figure 5.11: Deflection Versus Mass of Explosive - 4*mm* Thick Target Plates

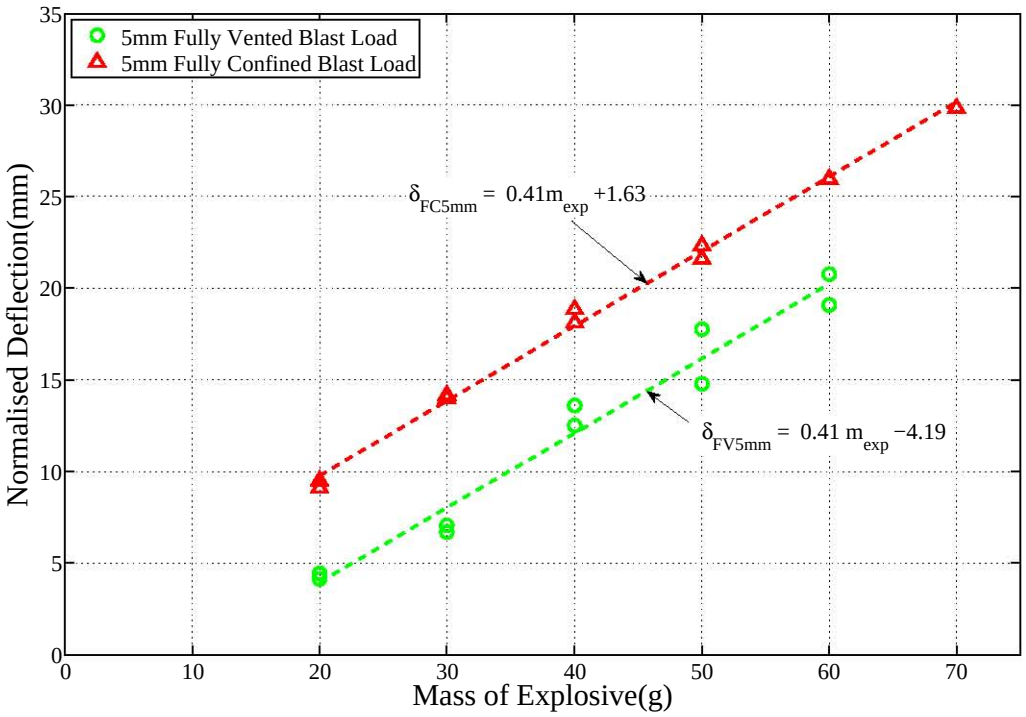

Figure 5.12: Deflection Versus Mass of Explosive - 5mm Thick Target Plates

The magnitude of the blast load was expected to differ in each degree of confinement. Without pressure histories it is difficult to quantify whether the increase load is due to a greater shock or gas pressure load (see Section 2.3.1 for definitions of shock and gas pressure loads).

To quantify the difference in blast loads the theoretical predictions proposed by Nurick and Martin [37, 38] (Equations 5.5 and 5.6, see Section 2.2.5.3) were implemented. For two identical target plates subjected to different blast loads, I_{UC} and I_{PC}, the dimensionless damage number and the deflection-thickness ratio for the target plates are given by,

$$\Phi_{qUC} = \frac{I_{UC}}{2h^2(BL\rho\sigma_y)^{0.5}} \qquad (5.16a)$$

$$\frac{\delta_{UC}}{h} = 0.48 \times \Phi_{q1UC} \qquad (5.16b)$$

$$\Phi_{qFV} = \frac{I_{FV}}{2h^2(BL\rho\sigma_y)^{0.5}} \qquad (5.17a)$$

$$\frac{\delta_{FV}}{h} = 0.48 \times \Phi_{qFV} \qquad (5.17b)$$

Dividing 5.17b by 5.16b gives,

$$\frac{\delta_{FV}}{\delta_{UC}} = \frac{\Phi_{qFV}}{\Phi_{qUC}} \tag{5.18}$$

As the two target plates are identical the ratio of the dimensionless damage numbers $(\frac{\Phi_{qFV}}{\Phi_{qUC}})$ is,

$$\frac{\Phi_{qFV}}{\Phi_{qUC}} = \frac{I_{FV}}{I_{UC}} \tag{5.19}$$

Equating Equation 5.18 and 5.19 gives the midpoint deflection ratio of a fully vented and an unconfined blast as,

$$\frac{\delta_{FV}}{\delta_{UC}} = \frac{I_{FV}}{I_{UC}} \tag{5.20}$$

Similarly, the midpoint deflection ratio between a fully confined and an unconfined blast and a fully confined and a fully vented blast are,

$$\frac{\delta_{FC}}{\delta_{UC}} = \frac{I_{FC}}{I_{UC}} \tag{5.21}$$

$$\frac{\delta_{FC}}{\delta_{FV}} = \frac{I_{FC}}{I_{FV}} \tag{5.22}$$

From trend data, over a range of 20 to 60g of explosive, the average midpoint deflection ratios between the degree of confinement were calculated. The computation of the trend data and the midpoint deflection ratio are presented in Appendix E in Table E.5. Equations 5.23, 5.24 and 5.25 list the midpoint deflection ratios obtained from the trend data from Figures 5.10, 5.11 and 5.12.

$$\frac{\delta_{FV}}{\delta_{UC}} = \frac{I_{FV}}{I_{UC}} = 2.69 \tag{5.23}$$

$$\frac{\delta_{FC}}{\delta_{UC}} = \frac{I_{FC}}{I_{UC}} = 4.13 \tag{5.24}$$

$$\frac{\delta_{FC}}{\delta_{FV}} = \frac{I_{FC}}{I_{FV}} = 1.62 \tag{5.25}$$

Equations 5.23, 5.24 and 5.25 suggest that the midpoint deflection ratio is directly proportional to the ratio of impulses between the degrees of confinement. Substituting the impulse with respects to mass of explosive relationship for an unconfined blast, $I_{UC} = 0.62 \times m + 2.35$ determined in Section 5.1 (Equation 5.3), into Equations 5.23 and 5.24, predictions for the impulse in a fully vented and fully confined blast can be made. Performing the substitutions the predicted impulses for fully vented and fully confined blasts are given as,

$$I_{FV} = 2.71 \times I_{UC} = 2.69 \times (0.62 \times m_{exp} + 2.35) = 1.66 \times m_{exp} + 6.31 \quad (5.26)$$

$$I_{FC} = 4.18 \times I_{UC} = 4.13 \times (0.62 \times m_{exp} + 2.35) = 2.55 \times m_{exp} + 9.71 \quad (5.27)$$

Figure 5.13 is the impulse versus mass of explosive graph presented in Section 5.1 (Figure 5.1) with the calculated impulses (Equations 5.26 and 5.27) plotted on the graph.

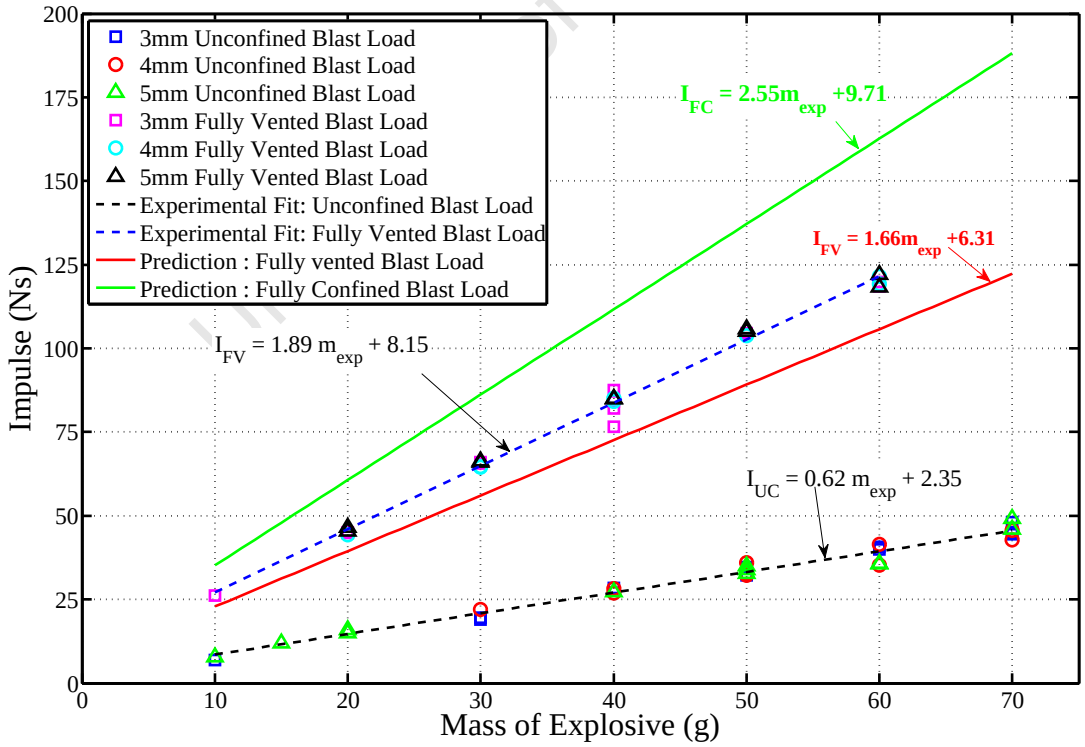

Figure 5.13: Graph of Impulse Versus Mass of Explosive

The results show that the calculated fully vented impulse underpredicts the actual fully vented impulse by 13%. The calculated impulses are acceptable as the values are on the lower limit of experimental uncertainty. The underprediction could be due to the dimensionless damage number proposed by Nurick and Martin [37, 38] (Equations 5.5 and 5.6) being based on a uniformly distributed impulse load whereas the load in the experiments was not uniform as discussed in Section 4.1.1.

The relationship given in Equation 5.24 suggests that the fully confined blast load is equivalent to approximately 4 times the blast load generated in a equivalent mass unconfined blast.

5.3.1 Relationship Between Midpoint Deflection and Impulse

The impulse in the unconfined and fully vented experiments was obtained from the swing of the ballistic pendulum and the results listed in Tables 4.1 and 4.2 respectively. The ballistic pendulum was not implemented in the fully confined experiments because an equilibrium of forces exerted on the container from the blast would result in no swing of the pendulum hence no measurement could be made with the ballistic pendulum. The impulse in the fully confined experiments was calculated using Equation 5.27 obtained in Section 5.3. Table 5.2 lists the calculated fully confined impulses for the mass of explosives investigated.

Table 5.2: Calculated Fully Confined Impulses

Mass of Explosive (g)	Calculated Impulse (Ns)
20	61.4
30	87.1
40	112.9
50	138.7
60	164.5
70	190.2

The normalised deflection versus impulse for the 3, 4 and 5mm thick target plates are plotted in Figures 5.14, 5.15 and 5.16. As expected, the deflection increases with increasing impulse. The calculated and measured results fall within the 90% confidence interval (±1 target plate thickness).

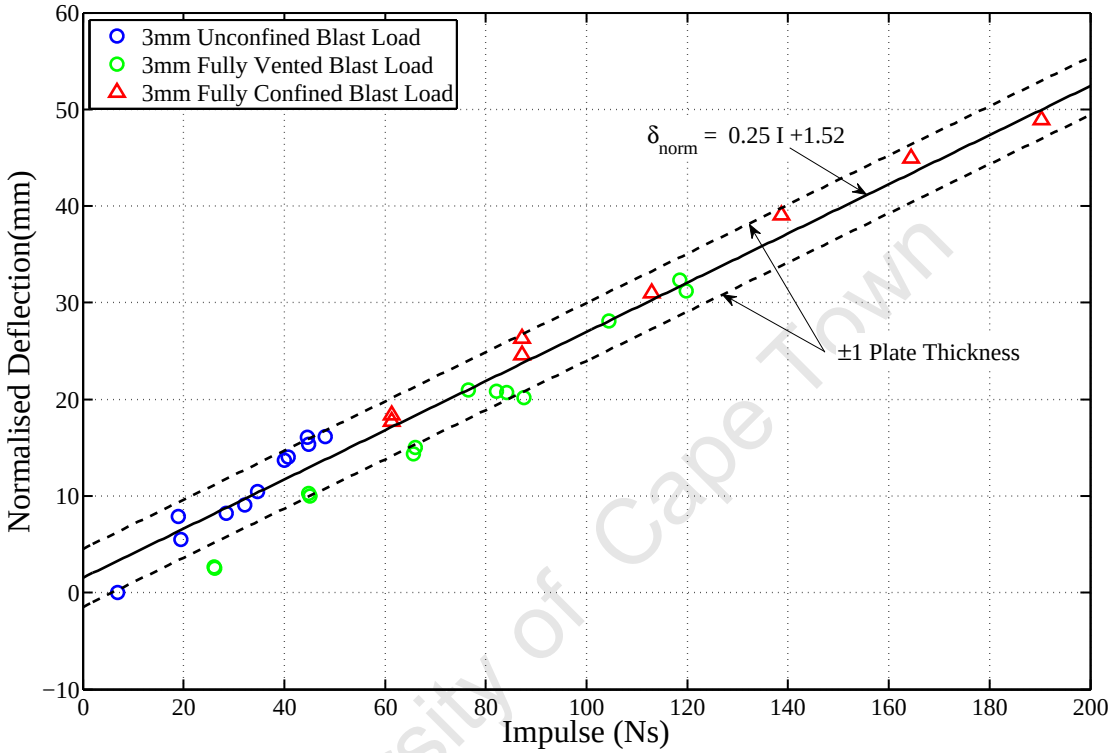

Figure 5.14: Deflection Versus Impulse - 3mm Thick Target Plates

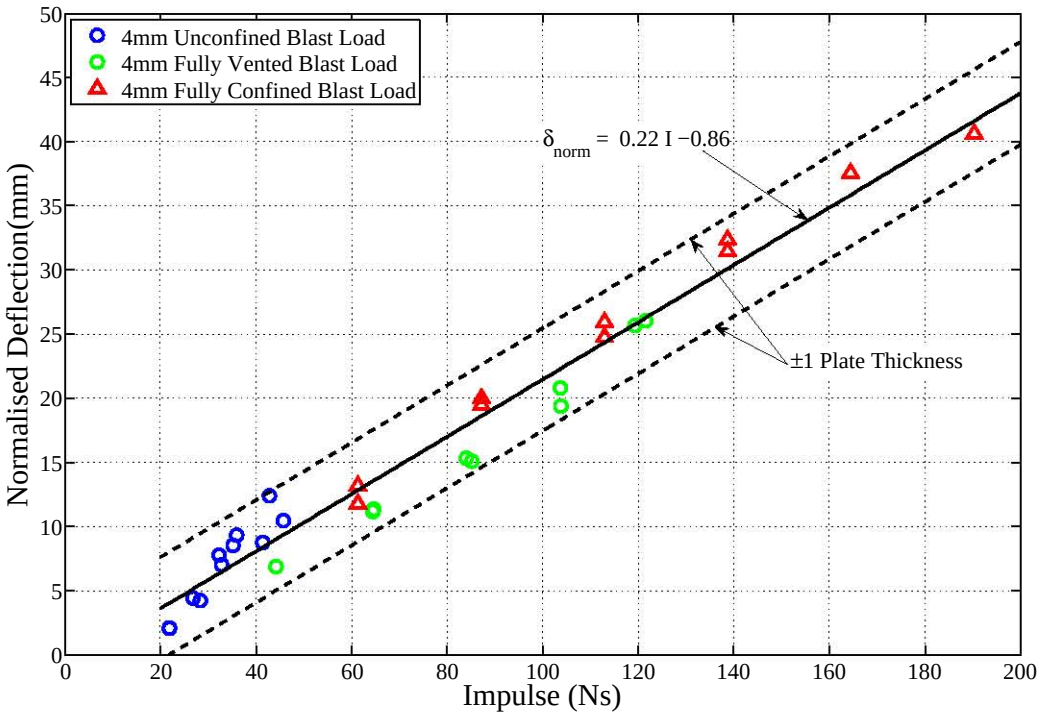

Figure 5.15: Deflection Versus Impulse - $4mm$ Thick Target Plates

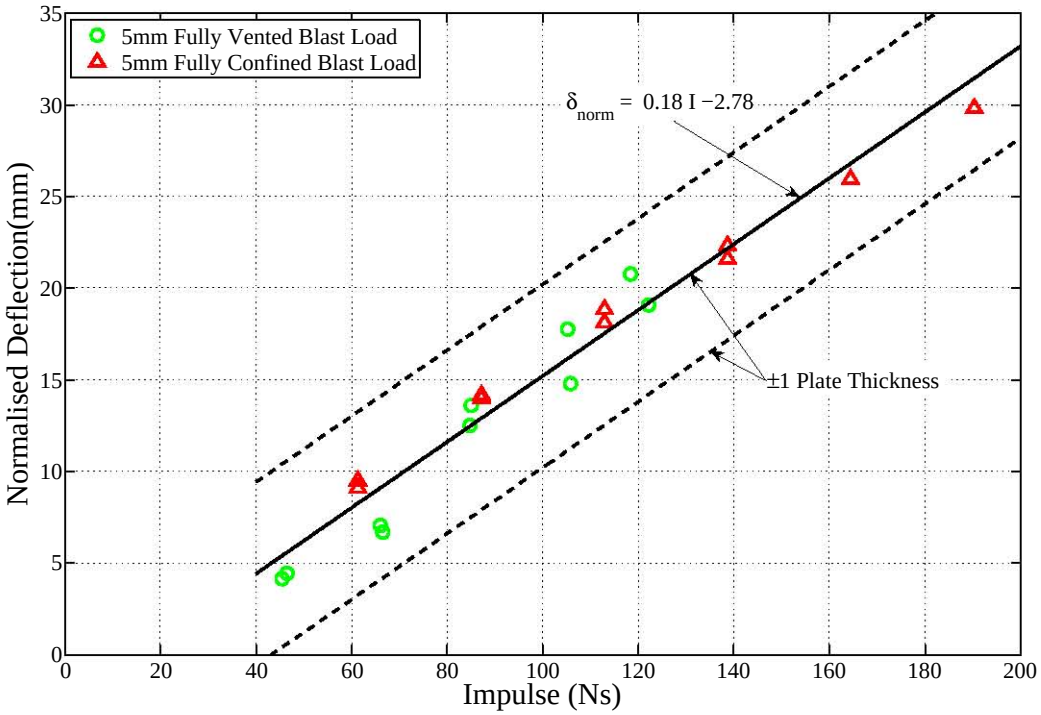

Figure 5.16: Deflection Versus Impulse - $5mm$ Thick Target Plates

Figure 5.17 was obtained from scaling the midpoint deflections of the 4 and 5mm thick target plates by the inverse of the target plate thickness ratio (Equations 5.13 and 5.14 respectively) to the equivalent 3mm thick target plate. The results correlate well with the 3mm thick target plate trend with the majority of the data falling within the $\pm 3mm$ confidence envelope.

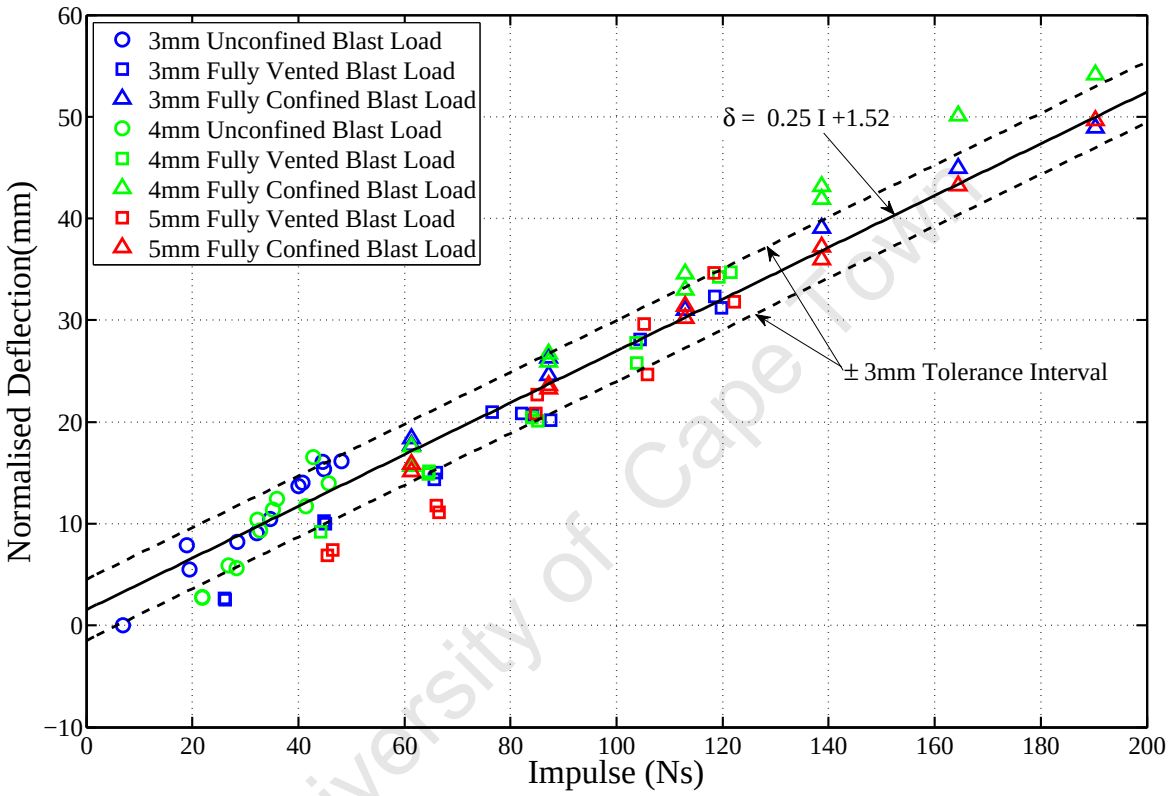

Figure 5.17: Deflection Versus Impulse - Results Scaled by Plate Thickness Ratio

5.3.2 Relationship Between Midpoint Deflection-Thickness Ratio and Dimensionless Damage Number

The normalised midpoint deflection-thickness ratio versus dimensionless damage numbers for all the experiments are illustrated in Figure 5.18. The overall results are consistent with the published trends [37, 38]. The fully confined results, which are calculated with Equation 5.27, correlate well with the published trend with only one data point falling outside the confidence envelope.

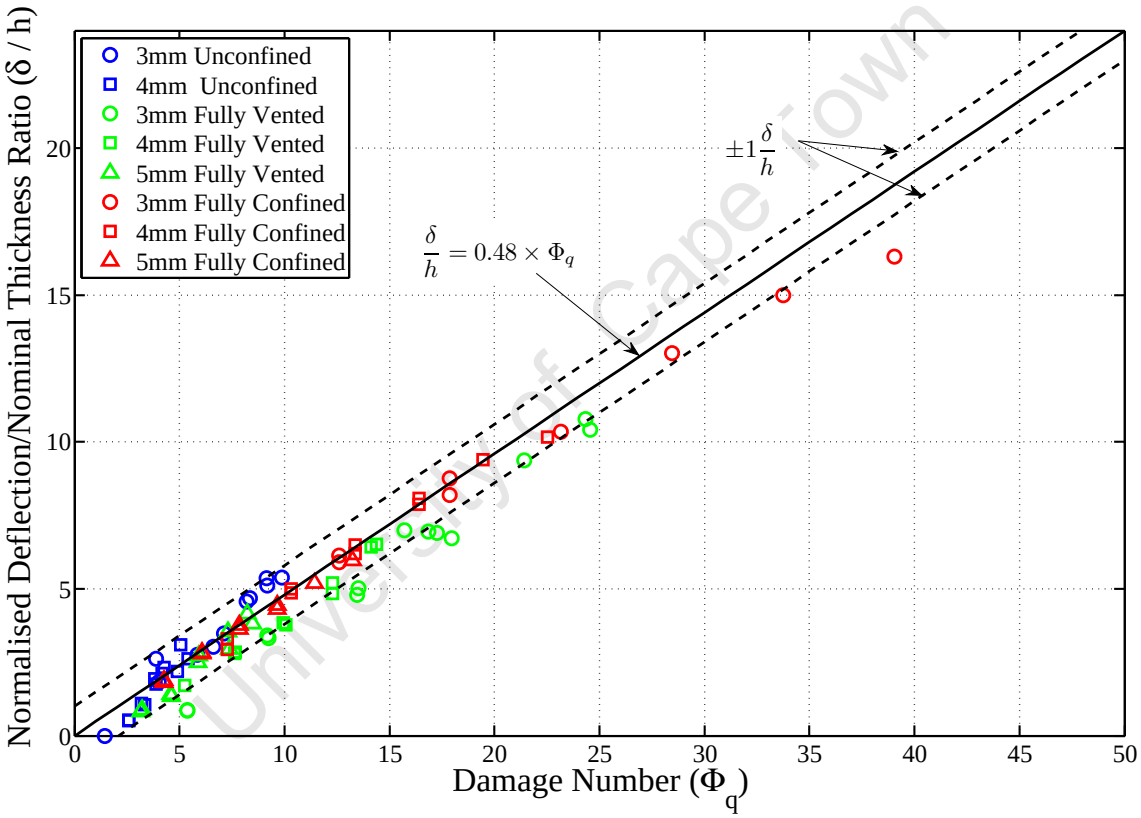

Figure 5.18: Normalised Deflection/Nominal Thickness Ratio Versus Damage Number

5.3.3 Prediction of Final Midpoint Deflections

Based on the results obtained in Section 5.3.2 a set of midpoint deflection prediction formulae, which took the form of the deflection-thickness ratio (Equation 5.6) proposed by Nurick and Martin [37, 38], for the different degrees of confinement were determined. Performing the appropriate substitutions the predicted midpoint deflections for the three degrees of confinement are given by Equations 5.28, 5.29 and 5.30. The impulse relationships for unconfined and fully vented blasts were the experimentally obtained relationships whilst the fully confined blast impulse relationship was taken as Equation 5.27 determined in Section 5.3.

$$\delta_{UC} = 0.48 \times \frac{I_{UC}}{2 \times h \times \sqrt{BL\rho\sigma_y]}} = 0.48 \times \frac{(0.62 \times m_{exp} + 2.35)}{2 \times h \times \sqrt{BL\rho\sigma_y]}} \tag{5.28}$$

$$\delta_{FV} = 0.48 \times \frac{I_{FV}}{2 \times h \times \sqrt{BL\rho\sigma_y]}} = 0.48 \times \frac{(1.89 \times m_{exp} + 8.15)}{2 \times h \times \sqrt{BL\rho\sigma_y]}} \tag{5.29}$$

$$\delta_{FC} = 0.48 \times \frac{I_{FC}}{2 \times h \times \sqrt{BL\rho\sigma_y]}} = 0.48 \times \frac{(2.58 \times m_{exp} + 9.82)}{2 \times h \times \sqrt{BL\rho\sigma_y]}} \tag{5.30}$$

where δ_x is the predicted midpoint deflection, m_{exp} is the mass of explosive and h is the thickness of the target plate in question.

The predicted and experimental normalised midpoint deflections are compared for the 3, 4 and $5mm$ thick target plates in Figures 5.19, 5.20 and 5.21 respectively. The physical parameters (ρ and σ_y) were obtained from Chapter 6 for the respective target plate thicknesses. The predicted midpoint deflections for an unconfined and a fully confined blast correlate well with the experimental results. The prediction of the fully vented blast midpoint deflections are over predicted.

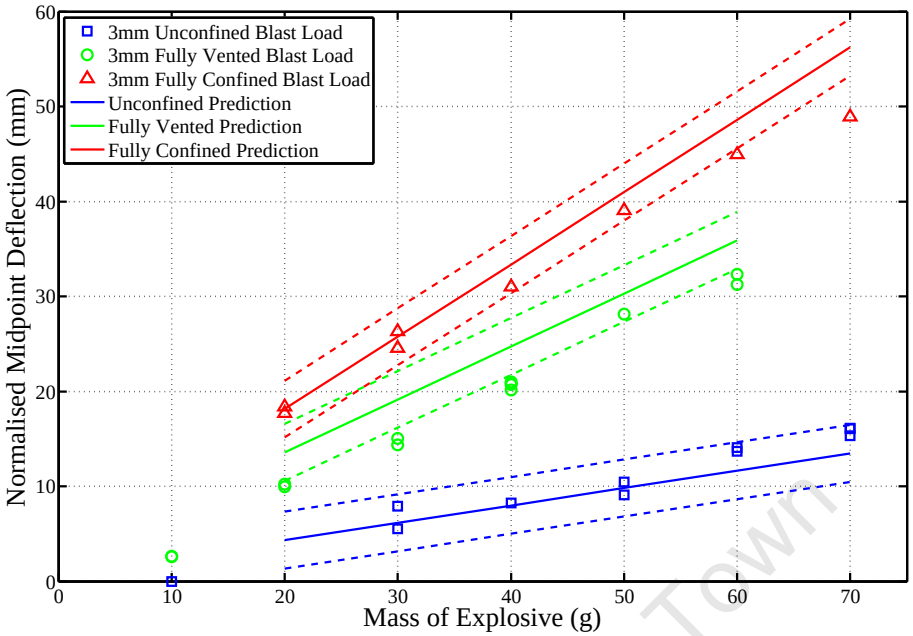

Figure 5.19: Comparison of Predicted and Experimental Normalised Midpoint Deflections for $3mm$ Thick Target Plates. Note: $\pm 3mm$ confidence envelopes have been plotted as dashed lines.

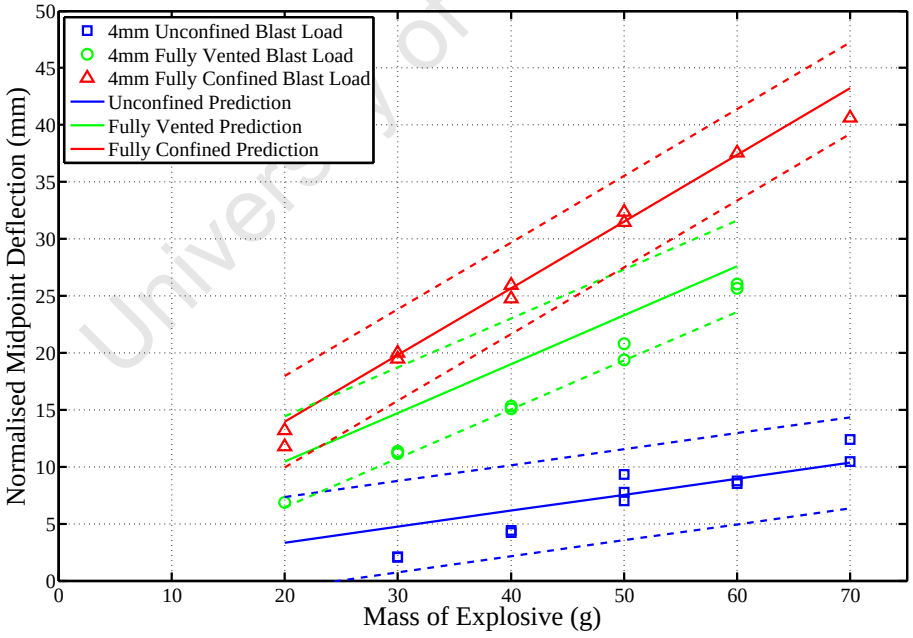

Figure 5.20: Comparison of Predicted and Experimental Normalised Midpoint Deflections for $4mm$ Thick Target Plates. Note: $\pm 4mm$ confidence envelopes have been plotted as dashed lines.

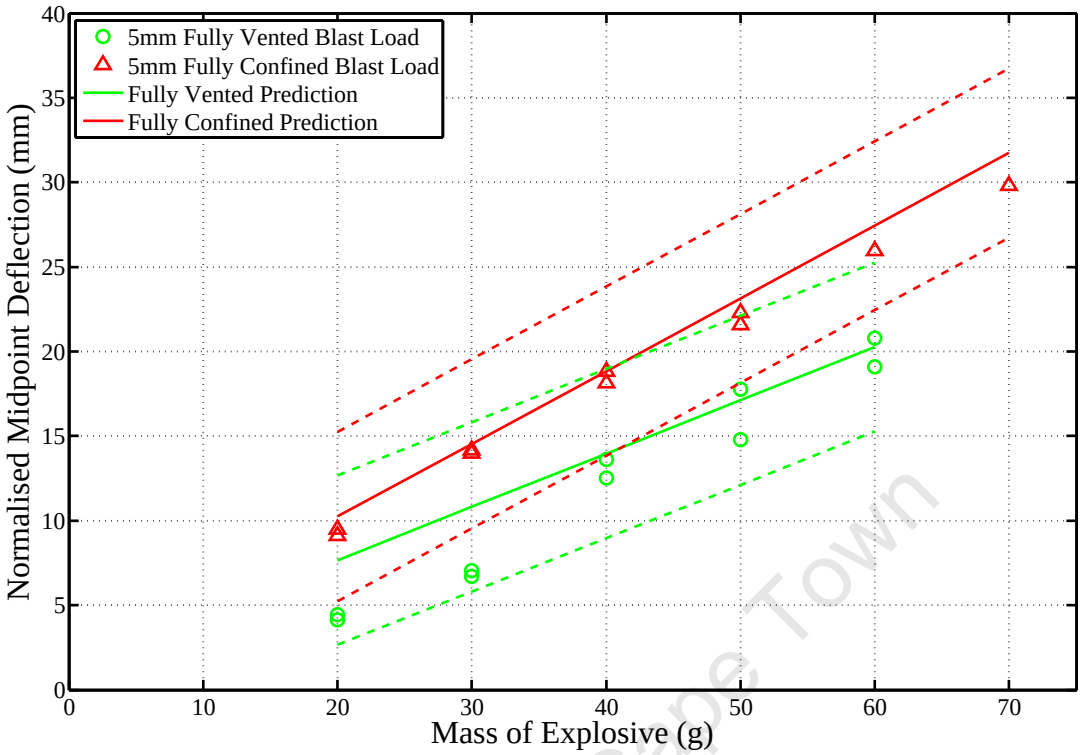

Figure 5.21: Comparison of Predicted and Experimental Normalised Midpoint Deflections for $5mm$ Thick Target Plates. Note: $\pm 5mm$ confidence envelopes have been plotted as dashed lines.

5.4 The Effects of Different Boundary Conditions

The effects of different boundary conditions present in the fully confined blast experiments were assessed by comparing final midpoint deflections of all the target plates. The blast load from a spherical charge located and detonated centrally within in a cubic container was expected to load the target plates equally. The method employed to manufacture the containers resulted in three different boundary conditions being present, as illustrated in Figure 5.22.

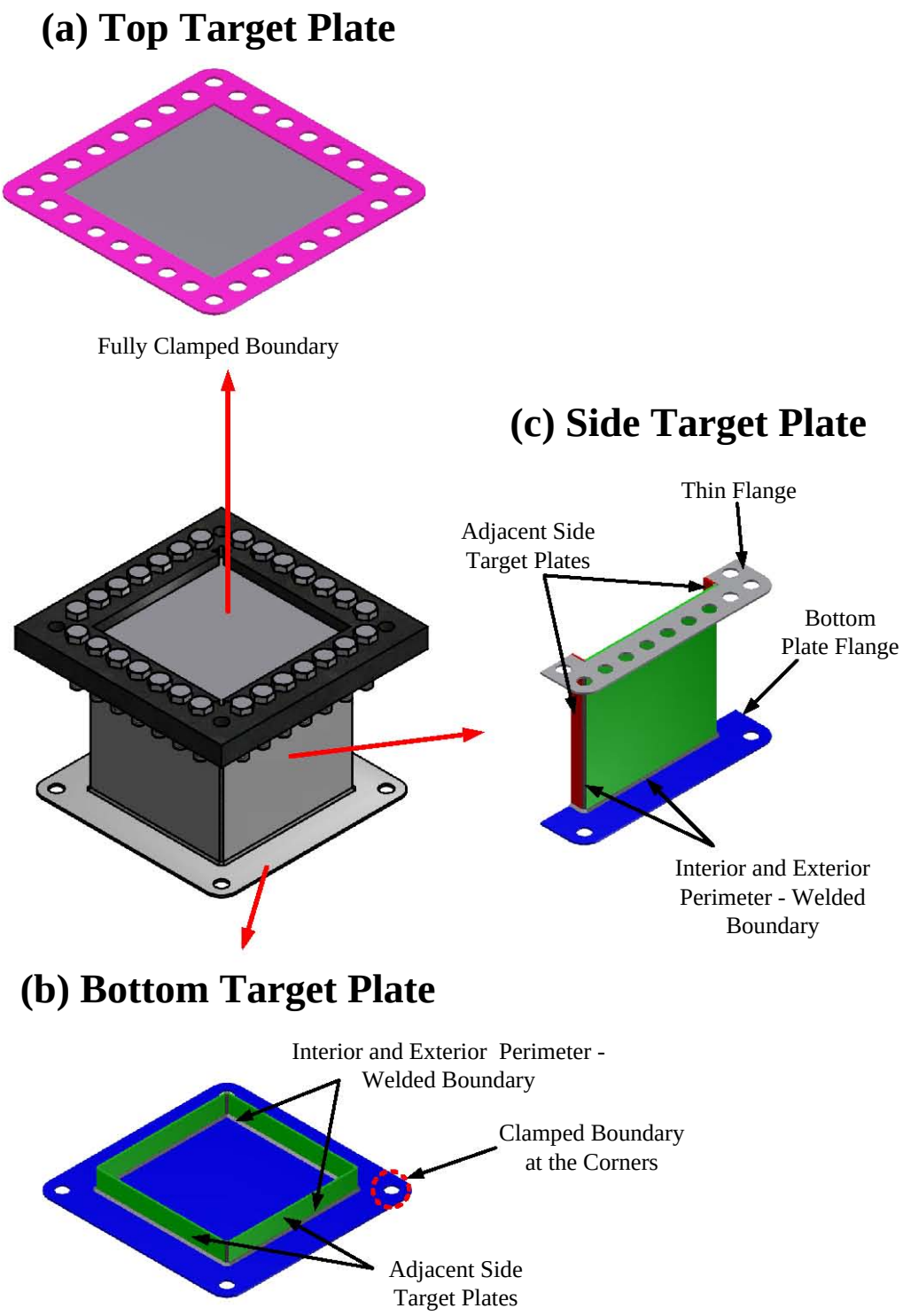

Figure 5.22: Boundary Fixation Conditions Present on Target Plates of Fully Confined Container

The perimeter of the top target plate was bolted to the container producing a fully clamped boundary, see Figure 5.22a. The boundary conditions of the bottom target plate comprised a clamped boundary at the corners of the target plate and a welded boundary ('built-in' boundary) around the perimeter of the exposed area where the side target plates were welded to the bottom target plate as shown in Figure 5.22b. The side target plates provided extra stiffness, normal to the bottom target plate surface, at the boundary of the exposed area of the bottom plate. The deformation of the side target plate also imposed additional forces on the perimeter of the exposed area of the bottom target plate. The boundary conditions of the side target plates comprised a fully welded boundary as illustrated in Figure 5.22c. Extra stiffness at the boundary was present due to the thin top flange, bottom flange and the joining side target plates.

The final midpoint deflections of all the target plates, listed in Table 4.3, versus the mass of explosive for the 3, 4 and 5mm thick fully confined experiments are plotted in Figures 5.23, 5.24 and 5.25 respectively. The midpoint deflections of opposing side target plates was assumed to be equal due to the the similarity of the boundary conditions and the symmetry of the loading as discussed in Section 4.3, hence only two the side target plate midpoint deflections (side AA and side BB) are reported. As expected, the midpoint deflection of the target plates, irrespective of the wall of the container, increased linearly with the increase in mass of explosive.

The midpoint deflections of the side target plates were similar, thus confirming the assumption that the side target plate deform symmetrically. The midpoint deflections of the bottom target plate were well within ± 1 target plate thickness of the midpoint deflections of the side target plates. Consequently, one trend line which incorporates the results for the bottom and side target plates was plotted in Figures 5.23, 5.24 and 5.25. The midpoint deflection results for the bottom and side target plates, which make up the container, demonstrate the spherical nature of the deformation of initially cubic container and symmetry of the deformation observed on the container.

The results show that the top target plates deformed more than the side and bottom target plates. The difference between the midpoint deflection of the top target plate and the side and bottom target plates increases with an increasing charge mass. The increased deflection of the fully clamped top target plate can be attributed to 'pull-in' of the material in the clamped region. It must be noted that at smaller charge masses the midpoint deflection of all the walls of the container, including the top target plate, were similar.

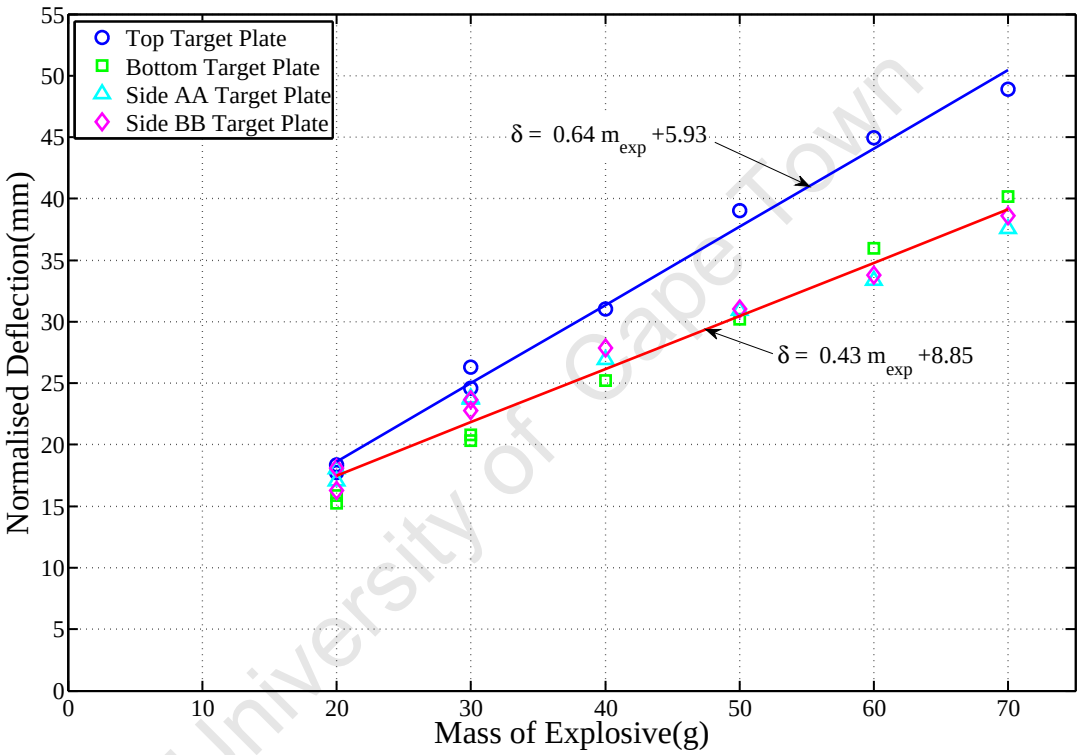

Figure 5.23: Normalised Midpoint Deflection Versus Mass of Explosive for 3*mm* Thick Fully Confined Containers

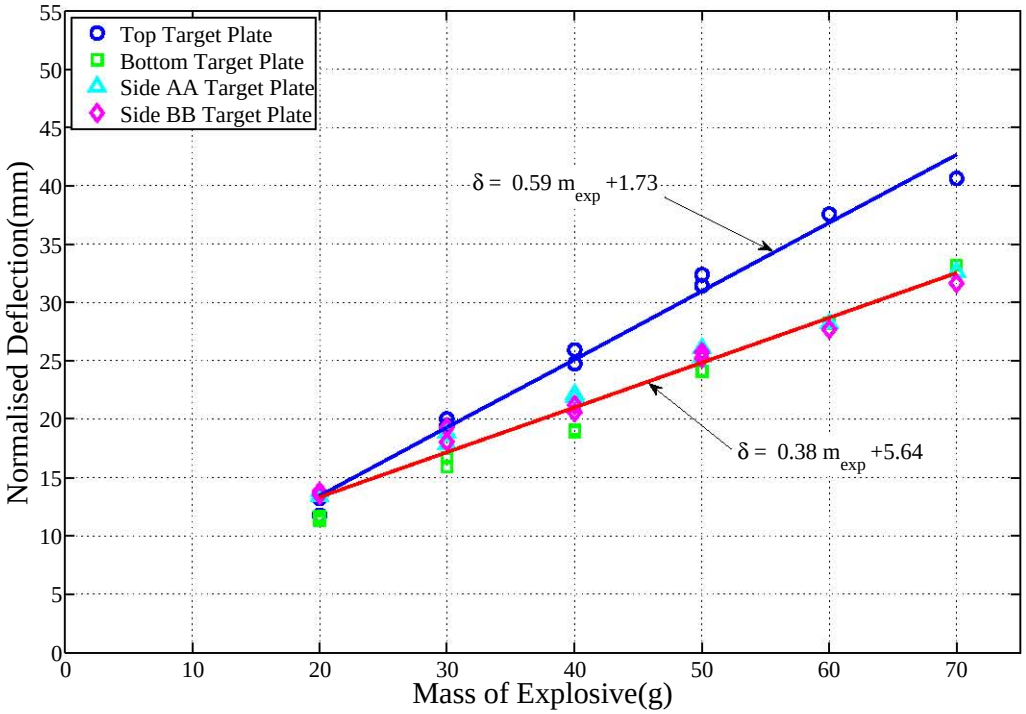

Figure 5.24: Normalised Midpoint Deflection Versus Mass of Explosive for $4mm$ Thick Fully Confined Containers

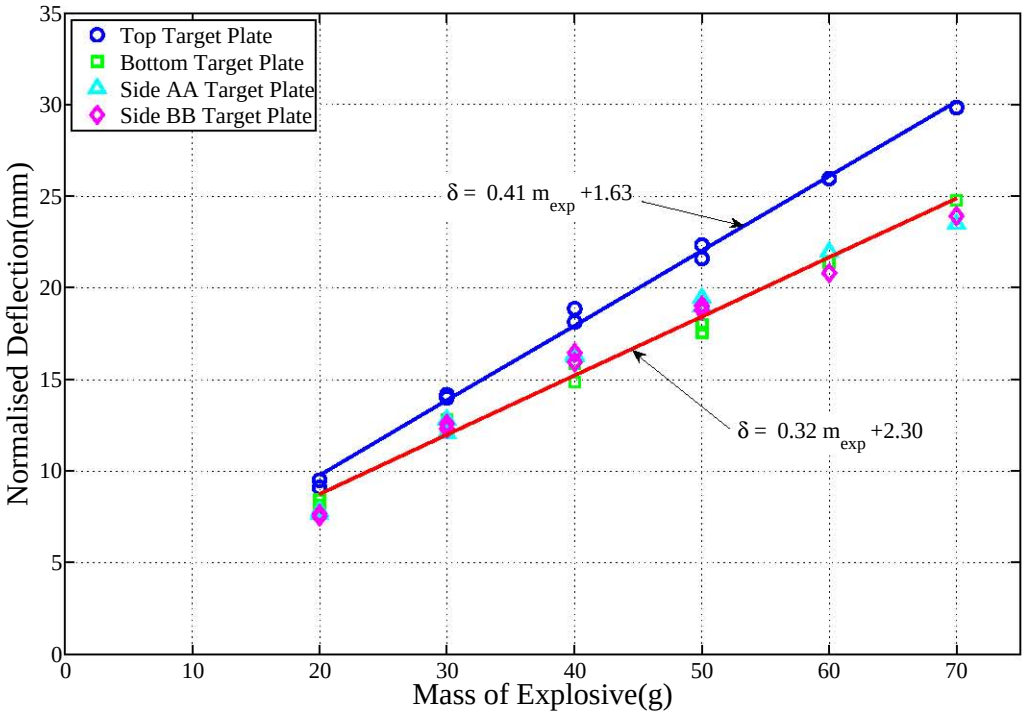

Figure 5.25: Normalised Midpoint Deflection Versus Mass of Explosive for $5mm$ Thick Fully Confined Containers

5.5 Transient Deflections

As discussed in Section 4.4, **the final midpoint deflection obtain from the deflection histories was taken as the average deflection from 2 to 10ms and termed the transient midpoint deflection**. This section of the thesis discusses the midpoint deflection results obtained from the deflection histories.

5.5.1 Comparison of Measured and Transient Final Midpoint Deflection

The transient midpoint deflections were compared to the final midpoint deflection, measured with a height gauge, to determine the accuracy of the photosensors. A graph plotting the transient midpoint deflection versus the final midpoint deflection in presented in Figure 5.26. The results where the sensor/s broke or where the smoke and flash effect was significant were set to a zero deflection.

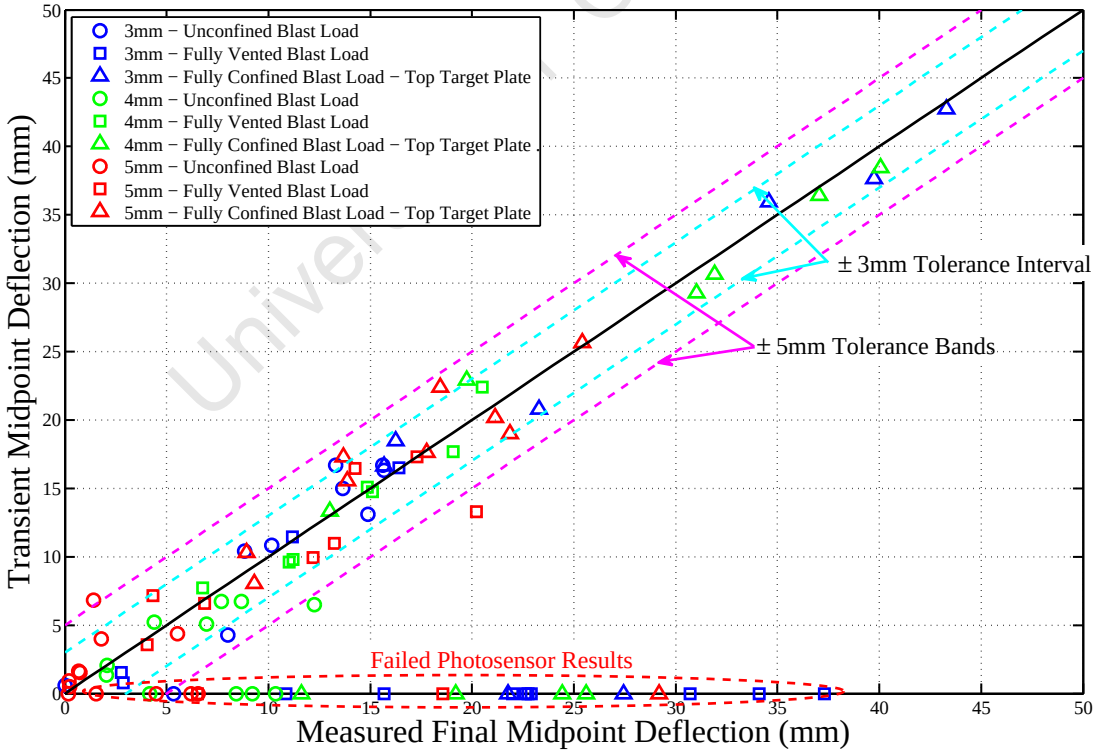

Figure 5.26: Measured Final Midpoint Deflection versus calculated Midpoint Deflection from Transient Response

In total 89 transient deflection histories were recorded. In 25 experiments the sensor either failed or was covered in soot resulting in erroneous results. The results from Figure 5.26 show that there is good agreement between the transient midpoint deflection and the final measured midpoint deflection. Neglecting the data from failed sensors, 88% of the calculated midpoint results fall within the $\pm 3mm$ confidence interval and 95% fall within $\pm 5mm$.

5.5.2 Springback of Target Plate

Springback is usually associated with sheet metal forming where the plastic deformation is followed by an elastic recovery after unloading due to the finite modulus of elasticity inherent in the material [131–133]. In the case of the blast loaded target plates in this investigation the springback was defined as the difference between the peak midpoint deflection and the final transient midpoint deflection. The springback deflections determined from the midpoint deflection histories for the 3, 4 and $5mm$ thick target plates are presented in Tables 4.4, 4.5 and 4.6 respectively. The springback-transient midpoint deflection ratio is plotted versus the impulse in Figure 5.27 to investigate the effects on springback as the blast load is increased.

The impulse for the unconfined and fully vented blast loaded target plate was obtained from the swing of the ballistic pendulum and the results listed in Tables 4.1 and 4.2 respectively. The impulse in the fully confined blast loaded target plates was obtained using Equation 5.27 presented in Section 5.3 and the results are listed in Table 5.2.

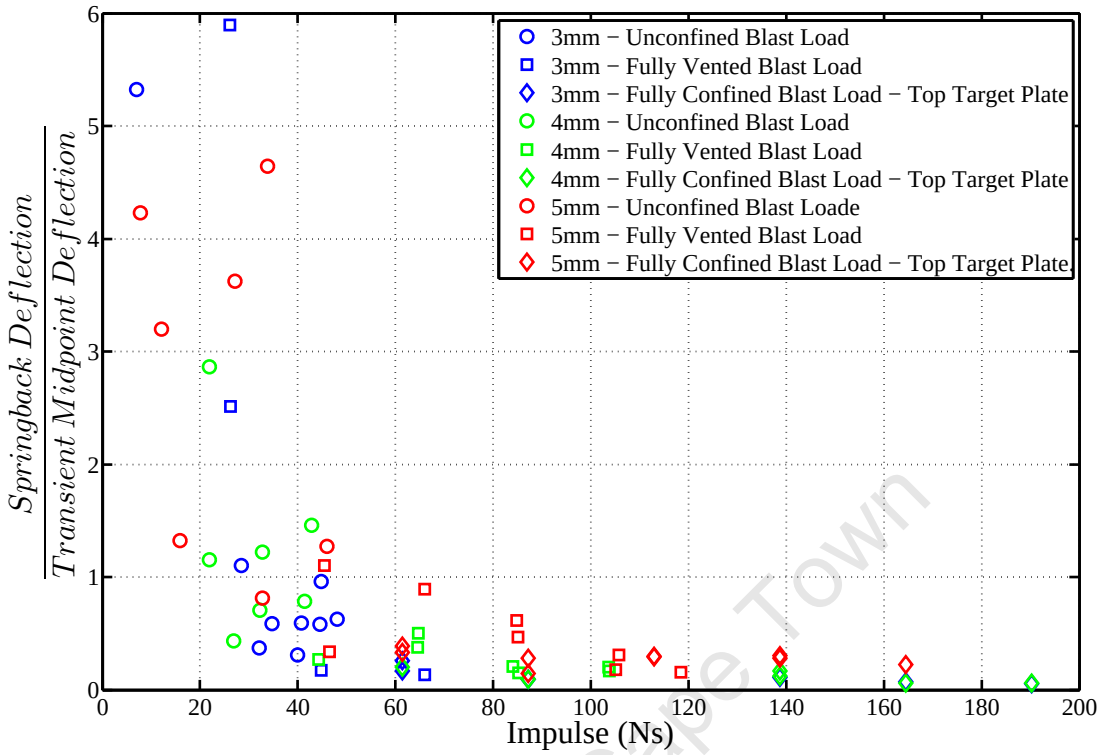

Figure 5.27: Springback-Transient Midpoint Deflection Ratio Versus Impulse for all Thicknesses and Degrees of Confinement

The results show that as the impulse increases the springback-transient midpoint deflection ratio decreases, tending towards zero at larger values of impulse. As shown in Section 5.3.1 the final midpoint deflection is directly proportional to the impulse hence as the midpoint deflection increases the springback deflection decreases. This result indicates that as the plastic deformation of the target plate increases the inherent elastic response of the target plate diminishes and the plastic response of the target plate dominates. Similar response was observed, through experiments and numerical simulations, by Neuberger *et al.* [133] for unconfined blast load circular plates.

Similar to Neuberger *et al.* [133], the springback response illustrated in Figure 5.27 can be divided into two domains namely the plastic and elastic dominated response. The elastic dominated response is characterised by a large springback deflection with a small midpoint deflection being recorded.

The elastic dominated response can be characterised by,

$$\frac{\delta_{springback}}{\delta_{transient}} > 0.5 \tag{5.31}$$

The plastic dominated response is characterised a large final midpoint deflection and a small springback deflection. The plastic dominated response can be characterised by,

$$0.5 > \frac{\delta_{springback}}{\delta_{transient}} \rightarrow 0 \tag{5.32}$$

A sharp inflection point between the elastic and plastic dominated response was observed by Neuberger *et al.* [133] which was not clearly visible in the current data. Further testing in the elastic dominated response is required to distinguish a clear inflexion point.

5.6 Summary

A series of experiments were carried out to investigate the effects of target plate thicknesses and the degree of confinement on the response of square steel plates subjected to blast loading. The experimental results were presented in Chapter 4 and a discussion of the results was presented in Chapter 5. The results were presented in terms of transient and final midpoint deflections. The degrees of confinement examined included unconfined, fully vented and fully confined blasts and target plate thickness of 3, 4 and $5mm$.

The results were presented in terms of the effects of target plate thickness and degree of confinement on the final midpoint deflection. The effect of the different boundary conditions on the target plates in the fully confined experimental setup on the final midpoint deflection was discussed. The transient midpoint deflections and springback of the target plates were analysed and presented. A summary of the experimental results and discussions are given:

- the final midpoint deflection, irrespective of degree of confinement or target plate thickness, increases with an increasing mass of explosive.

- the ratio of midpoint deflection between two different thickness target plates subjected to an identical blast load was found to be inversely proportional to the ratio of target plate thicknesses. The relationship is given by,

$$\frac{\delta_1}{\delta_2} = \frac{h_2}{h_1}$$

- the midpoint deflection ratio between two target plates of the same thickness was found to correlate well with the ratio of the applied impulse. From the correlation the fully confined impulse was found to be,

$$I_{FC} = 2.55 \times m_{exp} + 9.71$$

- the midpoint deflection - thickness ratio versus the dimensionless number correlated well with published trends.

- for this set of experiments a set of predication formulae for the midpoint deflection of a target plate subjected to the different blast loads was made. Using the deflection-thickness relationship and dimensionless damage analysis proposed by [37, 38] a set of formulae was proposed to calculate the midpoint deflection of a target plate in the different degrees of confinement. The formulae given as,

$$\delta_{UC} = 0.48 \times \frac{(0.62 \times m_{exp} + 2.35)}{2 \times h \times \sqrt{BL\rho\sigma_y]}}$$

$$\delta_{FV} = 0.48 \times \frac{(1.89 \times m_{exp} + 8.15)}{2 \times h \times \sqrt{BL\rho\sigma_y]}}$$

$$\delta_{FC} = 0.48 \times \frac{(2.58 \times m_{exp} + 9.82)}{2 \times h \times \sqrt{BL\rho\sigma_y]}}$$

- a comparison of the boundary conditions showed that the fully clamped boundary of the top target plate allowed larger midpoint deflections. The midpoint deflections of the side and bottom target plates were similar.

- the midpoint deflection determined from transient deflection histories correlated well final midpoint deflections.

- springback was observed to decreases with an increase in the midpoint deflection and correlated with published trends.

6 Material Characterisation

6.1 Introduction

Finite element analysis (FEA) of the three degrees of confinement were carried out to investigate the response of the target plates subjected to the different blast loads. FEA requires a constitutive material model which mathematically describes the behaviour of a material subjected to various external forces. Quasi-static and dynamic tests were carried out to obtain material parameters for the constitutive material model.

Mild steel is a common and well understood material however there are still wide variations in its characteristics due to the differences in the manufacturing process and variations in the composition of the steel. Thus the 3 and $4mm$ thick mild steel plates were considered as different materials. The $5mm$ thick $Gr.300\,WA$ steel plate was considered as the third material, Table 6.1 lists the typical chemical compositions of $Gr.300\,WA$ and mild steel.

Table 6.1: Typical Chemical Compositions of Mild Steel [134] and $Gr.300\,WA$ [135]

Material	Thickness	C %	Mn %	P %	S %	Si %
Mild Steel	$3mm$ & $4mm$	0.15	1.00	0.035	0.035	0.30
$Gr.300\,WA$	$5mm$	0.18	1.35	0.020	0.030	0.35

6.2 Quasi-Static Behaviour

6.2.1 Uniaxial Tensile Testing

The quasi-static behaviour of the materials were obtained by performing uniaxial tensile tests on a Zwick 1484 universal testing machine. A load cell and an extensometer measure the force and displacement history of the specimen respectively. The force and displacement histories are captured using a data acquisition system and the results are recorded and stored on a personal computer.

Flat rectangular dog bone specimens were cut from the same sheets of steel as the target plates to ensure the material behaviour of the specimens is representative of the target plates. A detailed dimensional drawing of the dog bone specimen is illustrated in Figure 6.1.

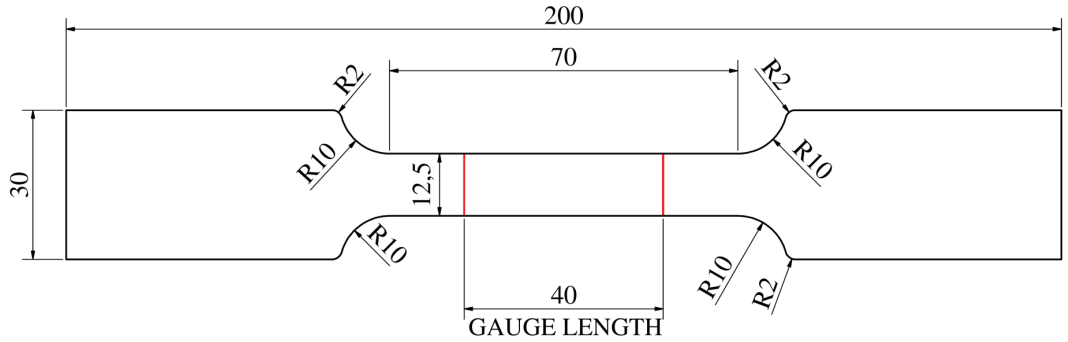

Figure 6.1: Schematic of Rectangular Dog Bone Specimens.

Due to limitations of the extensometer the initial gauge length of the specimen was reduced to $40mm$, centrally within the standard gauge length of $70mm$ (illustrated in Figure 6.1). In some cases the reduced gauge length leads to the onset of necking occurring near or outside the extensometer limits which would result in erroneous post-necking deflection results. However in these scenarios the deflection recorded prior to the onset of necking is valid. Figure 6.2 illustrates the experimental set-up of the uniaxial tensile tests. The experimental procedure for the uniaxial tensile tests was taken from ASTM A370-05 [136] and thus is not described.

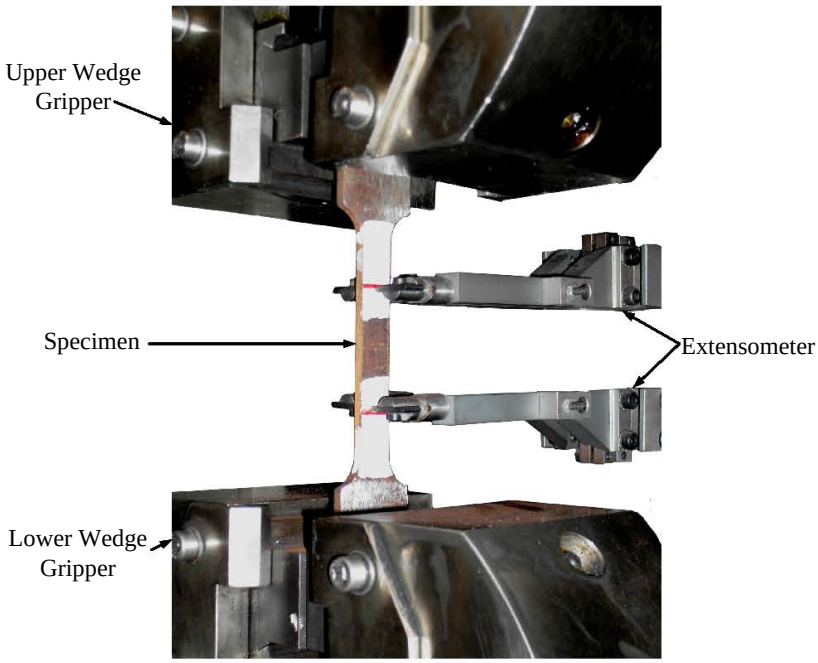

Figure 6.2: Photograph of Uniaxial Tensile Test Setup

Two series of tensile tests, characterised by the respective cross-head speeds, were performed. The first series of tests were performed at a cross-head speed of $1mm/min$, which relates to a nominal strain rate of $4.167 \times 10^{-4}s^{-1}$ over the initial gauge length of $40mm$. This series of tests was performed to determine the strain hardening parameters required for the constitutive material models. The second series of test were performed at a cross-head speed of $100mm/min$ which corresponds to a nominal strain rate of $4.167 \times 10^{-2}s^{-1}$ over the initial gauge length, which is two orders of magnitude greater than the first series. The second series of tests were performed to determine the effect of strain rate on the material response.

6.2.2 Analysing Uniaxial Tensile Data

A typical force-deflection curve obtained from a uniaxial test is illustrated in Figure 6.3. The initial portion of the force deflection curve does not represent the actual behaviour of the specimen as it includes displacement due to machine compliance and the 'bedding in' of the specimen.

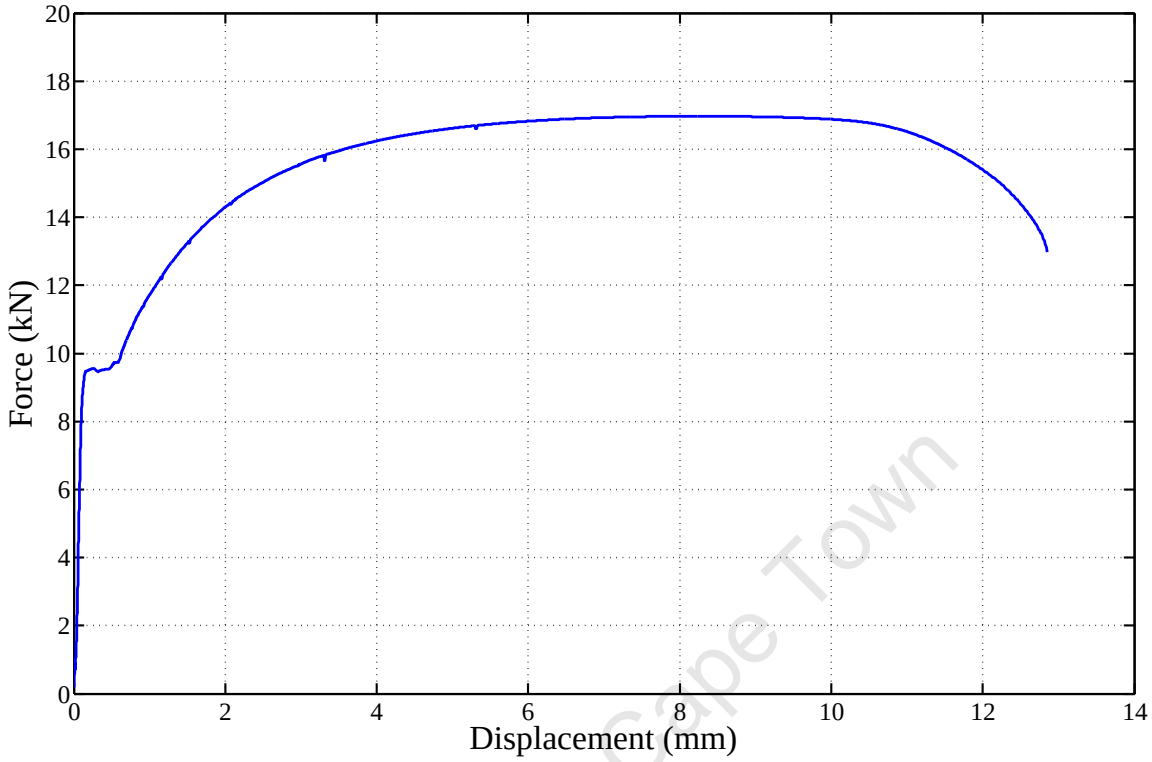

Figure 6.3: Typical Force-Deflection Curve - 3mm Thick Specimen

The effects of machine compliance and 'bedding in' were removed from the curve in order to analyse the actual specimen behaviour. To remove these effects the maximum slope, which represents the effective stiffness of the specimen and is related to the Young's modulus of the specimen, in the linear portion of the force deflection curve was determined. The displacement due to machine compliance and 'bedding in' were removed by shifting the curve so that the linear curve fitted through the maximum slope passes through zero. The displacement (u_m) due to machine compliance and 'bedding in' was determined with Equation 6.1 and is represented graphically in Figure 6.4.

$$u_m = u_{@maxslope} - \frac{F_{@maxslope}}{m} \tag{6.1}$$

where $u_{@maxslope}$ is the displacement at the maximum slope, $F_{@maxslope}$ is the force at the maximum slope and m is the maximum slope.

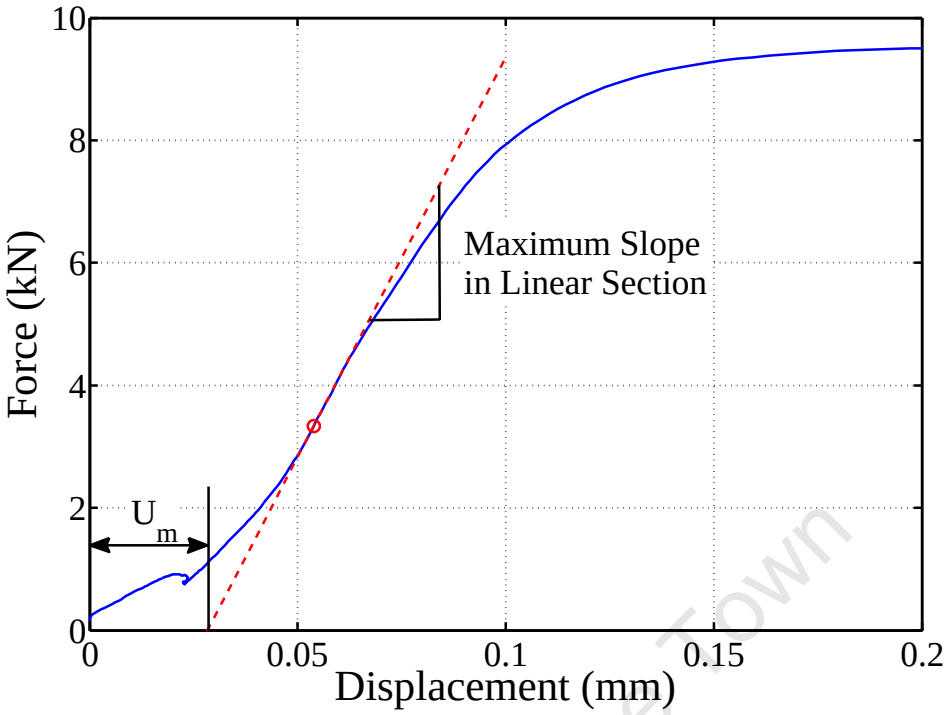

Figure 6.4: Displacement Due to Machine Compliance and 'Bedding in'

The elastic displacement (u_e) of the specimen was also removed from the force displacement curve. The elastic displacement is calculated by,

$$u_e = \frac{F}{m} \tag{6.2}$$

where F is the recorded force data.

Thus the corrected plastic displacement (u_c) was calculated by,

$$u_c = u_{rawdata} - u_e - u_m \tag{6.3}$$

The engineering stress (σ_{eng}) and engineering plastic strain (ε^{pl}_{eng}) are expressed as,

$$\sigma_{eng} = \frac{F}{A_o} \quad \text{and} \quad \varepsilon^{pl}_{eng} = \frac{\Delta u_c}{L_o} \tag{6.4}$$

where F is the force data, A_o is the initial cross-sectional area of the specimen, Δu_c is the actual plastic displacement and L_o is the initial gauge length.

The true stress (σ_T) and the true plastic strain (ε_T^{pl}) are given by,

$$\sigma_T = \sigma_{eng}(1 + \frac{\Delta u}{L_o}) = \sigma_{eng}(1 + \varepsilon_{eng}^{pl}) \qquad \text{and} \qquad \varepsilon_T^{pl} = ln(1 + \varepsilon_{eng}^{pl}) \tag{6.5}$$

6.2.3 Quasi-Static Test Results

The engineering stress-strain results obtained from the quasi-static tensile tests for the 3, 4 and 5mm thick tensile specimens are shown in Figures 6.5, 6.6 and 6.7 respectively. The results show good repeatability between the tests up to the point of necking. There was some experimental variation within the Ludërs band region due local compositions variance between the specimens; however, the remainder of the response was similar.

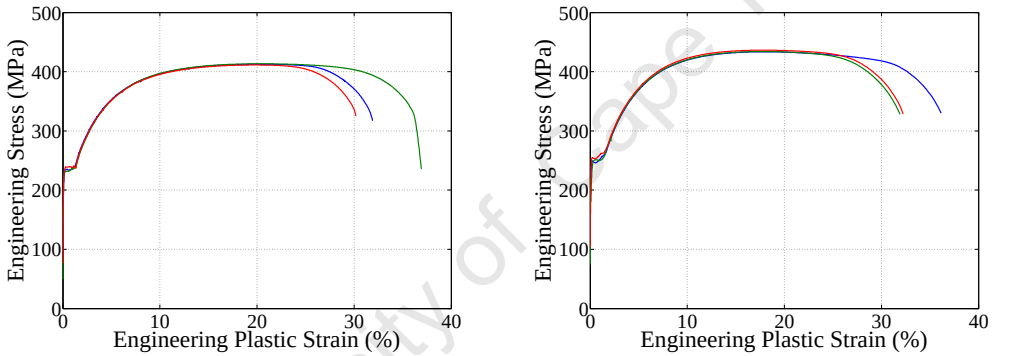

(a) 3mm Thick Plate, $\dot{\varepsilon} = 4.167 \times 10^{-4} s^{-1}$ (b) 3mm Thick Plate, $\dot{\varepsilon} = 4.167 \times 10^{-2} s^{-1}$

Figure 6.5: Engineering Stress-Strain Curves from 3mm Thick Uniaxial Tensile Specimens

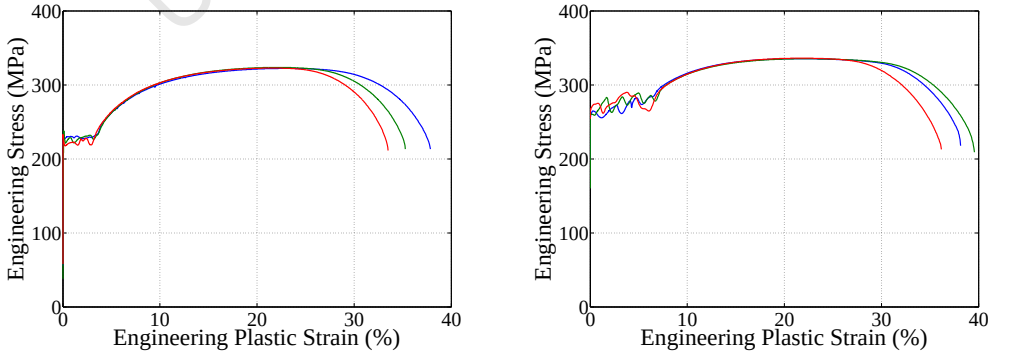

(a) 4mm Thick Plate, $\dot{\varepsilon} = 4.167 \times 10^{-4} s^{-1}$ (b) 4mm Thick Plate, $\dot{\varepsilon} = 4.167 \times 10^{-2} s^{-1}$

Figure 6.6: Engineering Stress-Strain Curves from 4mm Thick Uniaxial Tensile Specimens

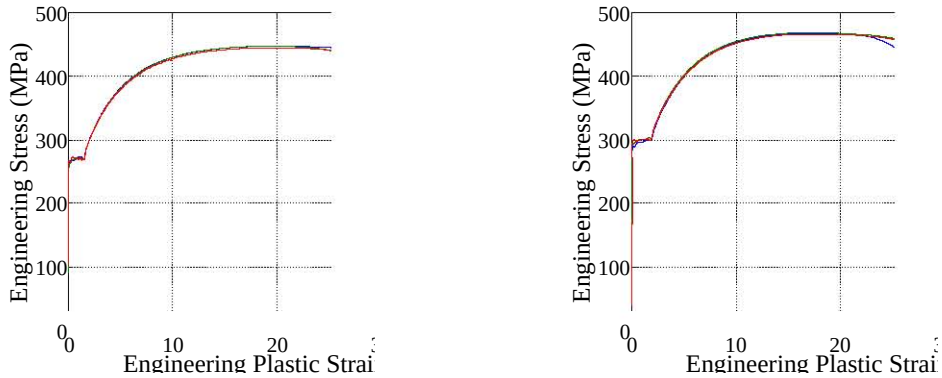

(a) $5mm$ Thick Plate, $\dot{\varepsilon} = 4.167 \times 10^{-4} s^{-1}$ (b) $5mm$ Thick Plate, $\dot{\varepsilon} = 4.167 \times 10^{-2} s^{-1}$

Figure 6.7: Engineering Stress-Strain Curves from $5mm$ Thick Uniaxial Tensile Specimens

The point of necking is also known as the ultimate tensile strength (UTS). The UTS was determined applying Consideré criteria [137] (see Equation 6.6), which states that the location of the UTS occurs where the slope of the true stress strain curve at a certain point was equal to the true stress at that point. The UTS also corresponds to the maximum stress on the engineering stress-strain curve.

$$\frac{d\sigma_T}{d\varepsilon_T} = \sigma_T \tag{6.6}$$

The presence of Ludërs bands in all three materials was anticipated as annealed low carbon steels under uniaxial tension often exhibit Ludërs bands [138, 139]. A Ludërs band is the region after the initial yield point where the stress plateaus whilst the Ludërs band propagates through the length of the specimen [138, 140]. A Ludërs band propagates at a constant stress and hence the stress plateau until the Ludërs band has spread across the length of the specimen and strain hardening becomes apparent [140]. Figure 6.8 highlights the Ludërs band present in a $5mm$ thick tensile specimen.

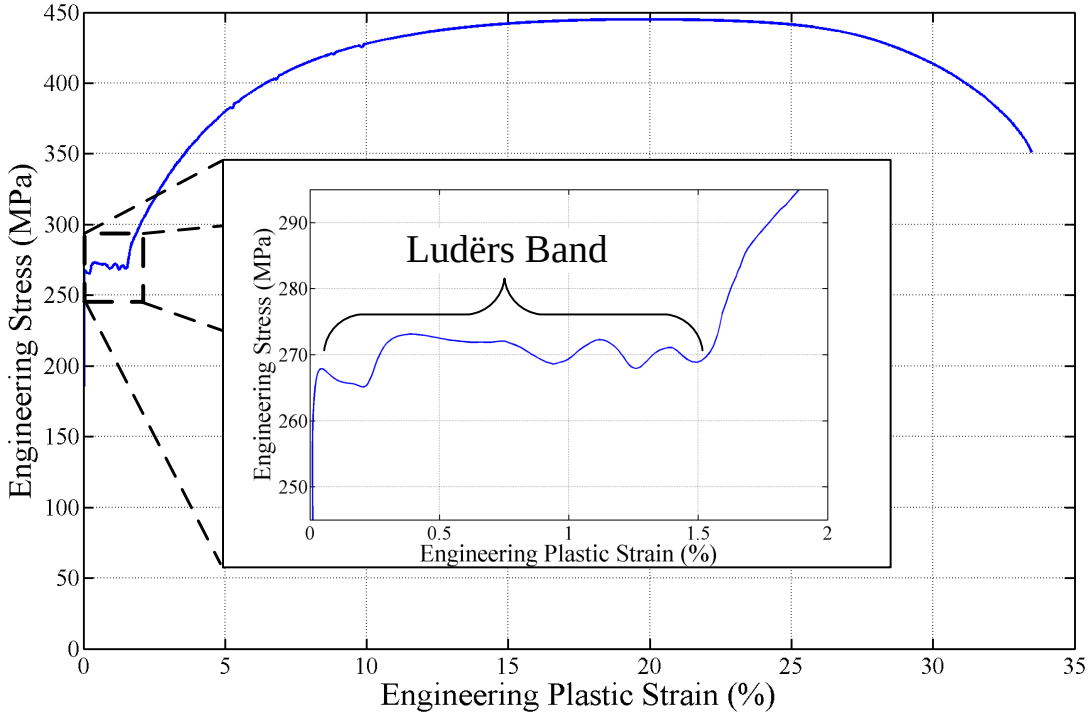

Figure 6.8: Example of Ludërs Band Present 5mm Thick Material

The presence of Ludërs bands complicates the selection of the yield point of the material as the common 0.2% offset yield point can lead to doubtful values of the yield strength. The yield strength of the materials was thus determined in a conservative manner where yield strength was taken as the lowest stress value within the Ludërs band. The yield strain was determined by projecting a horizontal line from the yield strength back to zero strain. The intersection of the projected line and the experimental data was taken as the yield strain. A graphical representation of this procedure is illustrated in Figure 6.9.

The actual true stress-strain of the material was only known up to the UTS as the portion of the true stress-strain curve after the UTS does not represent the actual material behaviour of the material. The measured stresses are typically greater than the true material stress due to the presence of hydrostatic forces and the cross-sectional area of the specimen in the necking region is not uniform. Thus Equation 6.5 is only valid up to the UTS of the specimen.

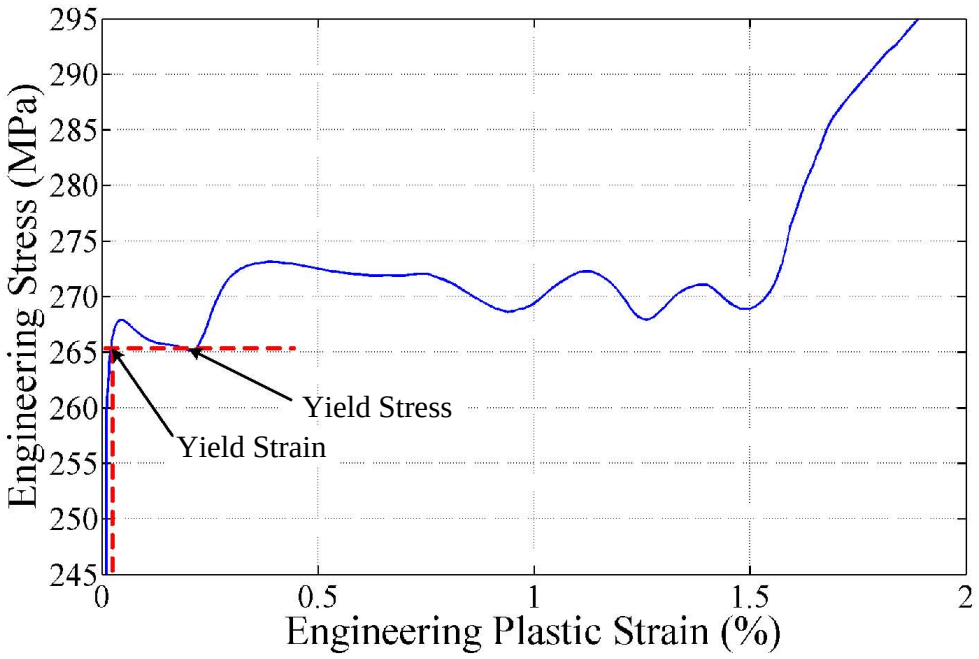

Figure 6.9: Determination of Yield Stress and Yield Strain

Zhang *et al.* [141] proposed a method to determine the actual true stress-strain relation after necking by combining the correction equation proposed by Bridgman [142] (Equation 6.7) and a neck geometry parameter ($\frac{a}{R}$) proposed by Le Roy *et al.* [143] (Equation 6.8).

$$\frac{\sigma_{corrected}}{\sigma_{uncorrected}} = \frac{1}{\left(1 + \frac{2R}{a}\right) ln\left(1 + \frac{\sigma}{2R}\right)} \tag{6.7}$$

$$\frac{a}{R} = 1.1(\varepsilon - \varepsilon_{P_{max}}) \tag{6.8}$$

where a is the current radius of the neck, R is the curvature of the neck surface in the longitudinal plane, ε is the current strain and $\varepsilon_{P_{max}}$ is the strain at maximum load.

Comparing finite element simulations and experimental results Choung and Cho [144] proposed Equation 6.9 to determine the equivalent true flow stress (σ_{eq}) to account for the behaviour after necking has occurred.

$$\sigma_{eq} = \sigma_{a,av}\zeta(\varepsilon_p) \tag{6.9}$$

where $\sigma_{a,av}$ is the average uniaxial flow stress and $\zeta(\varepsilon_p)$ is a correction parameter and is defined as,

$$\zeta(\varepsilon_p) = \begin{cases} 1 & \text{for } \varepsilon_p \leq 1.4\text{n} \\ \alpha\varepsilon_p^2 + \beta\varepsilon_p + \gamma & \text{for } \varepsilon_p > 1.4\text{n} \end{cases} \tag{6.10}$$

where n is the hardening exponent of the material. α, β and γ obtained by fitting a second order polynomial to the correction factor versus plastic strain curves determined using finite element calculations.

The methods proposed by Zhang *et al.* [141] and Choung [144] both require accurate measurements of the cross-sectional area of the necking region throughout the experiments. As the testing facilities do not provide a means for measuring the reduction in cross-sectional area during an uniaxial tensile test, hence neither of these methods could be utilized to determine the post-UTS behaviour of the material. It was decided that a finite element analysis would be performed to determine the post-UTS behaviour of the materials. The post-UTS behaviour was determined by iteratively adjusting a trial stress-strain curve until the force-deflection response of the simulation agrees with the experimental response.

6.3 Uniaxial Tensile Test Simulations

The uniaxial tensile tests were simulated with LS-DYNA® V971 R5.1. The implicit time integration algorithm, which is unconditionally stable, was implemented as it is better suited for solving long duration events such as a tensile test [145].

Only the tensile tests performed at a strain rate of $4.167 \times 10^{-4} s^{-1}$ were simulated as the strain hardening parameters required for the constitutive materials models are based on the full material response of these tests.

Applying the appropriate boundary conditions, an $1/8^{th}$ symmetry model was constructed to simulate the tensile specimen. The length of the wide area of the dog-bone specimen was reduced in order to increase the computational efficiency. A prescribed velocity boundary condition was placed on the remainder of the wide area of the specimen. The modified dog-bone specimen and the applied velocity boundary condition is illustrated in Figure 6.10. The prescribed velocity was set to half the nominal cross-head (i.e. $0.5mm/s$) speed due to the symmetry boundaries. The models were meshed with 8 node constant stress solid elements with Belytschko-Binderman assumed strain co-rotational stiffness form hourglass control [145].

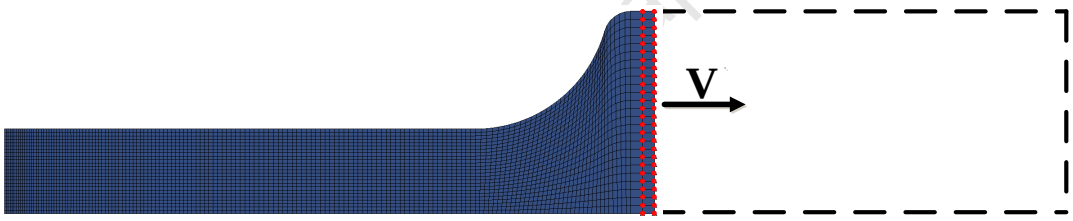

Figure 6.10: FEA Model and Application of Prescribed Velocity Boundary Condition

The behaviour of the material post-UTS was determined by inputting a trial stress-strain curve in to LS-DYNA using a predefined material model, *MAT_024 (piecewise linear plasticity), which allows the user to input a trial stress-strain curve in a tabular format. LS-DYNA interpolates stress and strain values between the points in the table. The simulation was then run and the resulting force-deflection was compared to the experimental force-deflection, the trial stress-strain curve was altered until the simulated and experimental curves agree.

The trial curves were divided into two sections, the first section was comprised of the experimentally determined true stress-strain data up to the UTS and the second section, extending from the UTS to a significantly large strain ($\varepsilon_t = 3$), following the power law

form $A + B\varepsilon^n$. The stress (σ_{con}) at a strain value of 3 was defined as a control value for the curve. A, B and n were then determined so that the slope between the two sections agree at the UTS, the trial curve passes through the control value and the experimental UTS. The stress at the control point was iteratively adjusted, and hence the values of A, B and n changed, so that the simulated force-deflection curve matched the experimentally obtain force-deflection curve. Figure 6.11 gives an example of the trial curve entered into LS-DYNA to determine the post-UTS behaviour of the $4mm$ thick material.

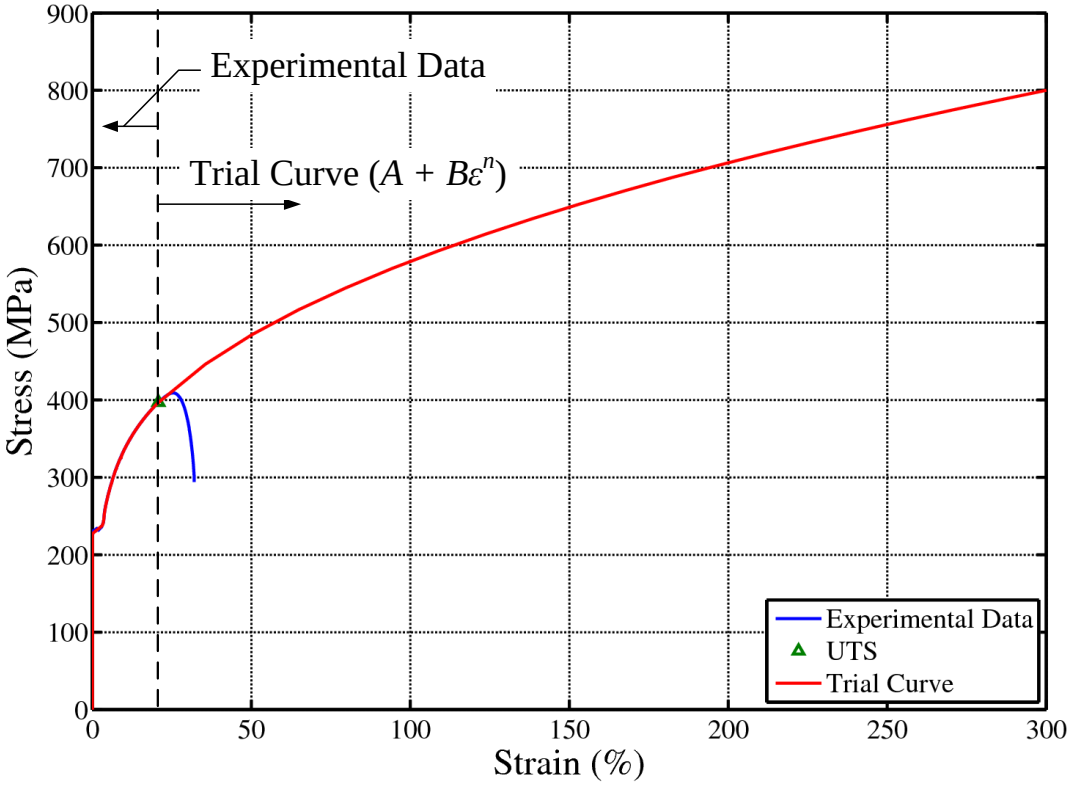

Figure 6.11: Example of Trial Curve for Determining the Post-UTS Behaviour of $4mm$ Thick Plate

The trial curve was further simplified by reducing the Ludërs band region to a linear line that extended from the yield point to the end on the Ludërs band region. The intersection of the line with the experimental curve was smoothed to remove any discontinuities in the curve. Figure 6.12 illustrates an example of the simplification of the Ludërs band region in the $4mm$ thick specimen.

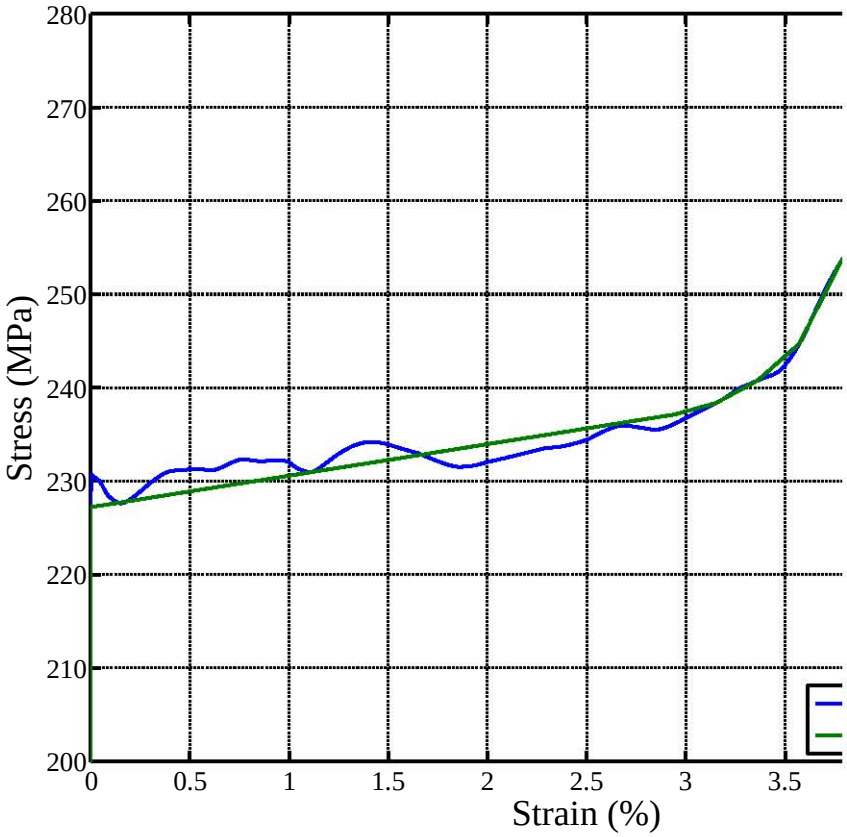

Figure 6.12: Example of Simplification of Ludërs band in $4mm$ Thick Plate

Convergence of the tensile test simulations to the respective experimental results was checked through two convergence studies. The first study examined the effect of the maximum allowable time step (DTMAX) between equilibrium calculations and the second study examined the effects of mesh size of the simulated results. The $3mm$ thick models were meshed such that the elements were biased towards the necking region in the model. The aspect ratio of the elements was kept as close to one as possible and the elements were biased towards the centre of the specimen. The simulations had identical boundary and loading conditions and the same material model so that a meaningful comparison could be made. The default values in the *CONTROL_IMPLICIT cards were used with the exception of DTMAX in the *CONTROL_IMPLICIT_AUTO card.

The DTMAX convergence study was performed on a medium size meshed model where three time step values of DTMAX (100,10 and $5s$) were examined. The results for the DTMAX study are illustrated in Figure 6.13. The results obtained for a DTMAX of 5

and 10s gave very similar results indicating convergence of the results. As a DTMAX of 5s was computationally more expensive than a DTMAX of 10s, the value of DTMAX was set to 10s in subsequent simulations as a time saving mechanism.

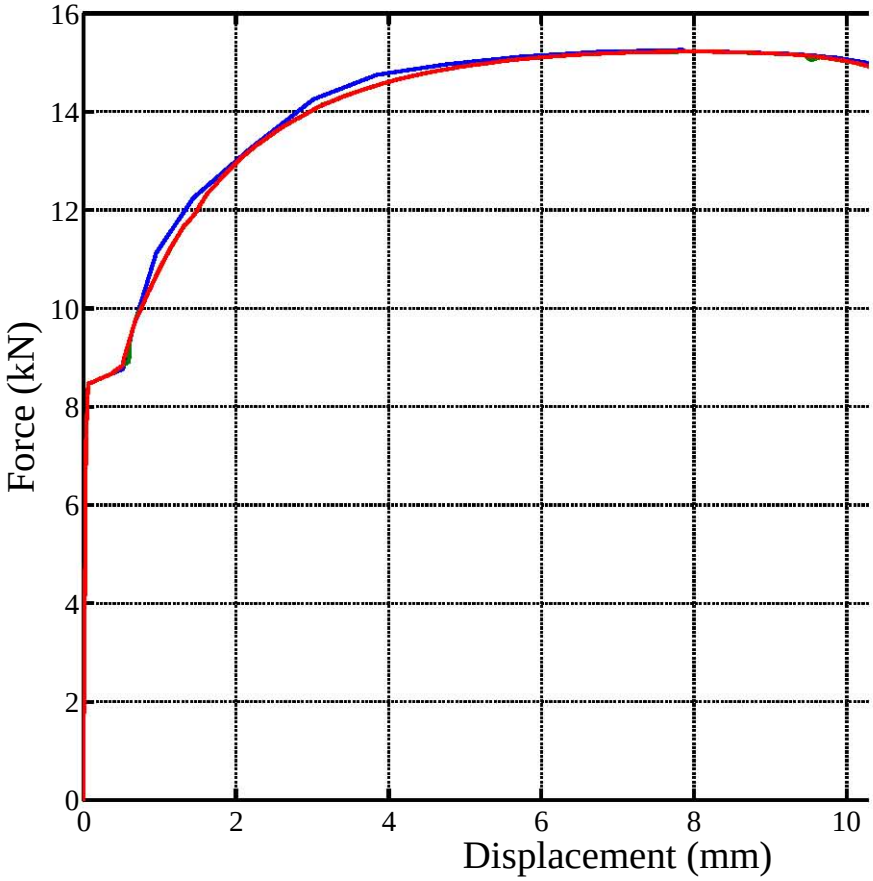

Figure 6.13: Study of Maximum Allowable Time Step

The effects of mesh size on the results was determined by performing three identical simulations where the mesh size varied. The mesh sizes were based on the number of elements through the thickness of the specimen, the coarse, medium and fine mesh had three, six and twelve elements through the thickness of the specimen respectively. The three mesh sizes considered are illustrated in Figure 6.14.

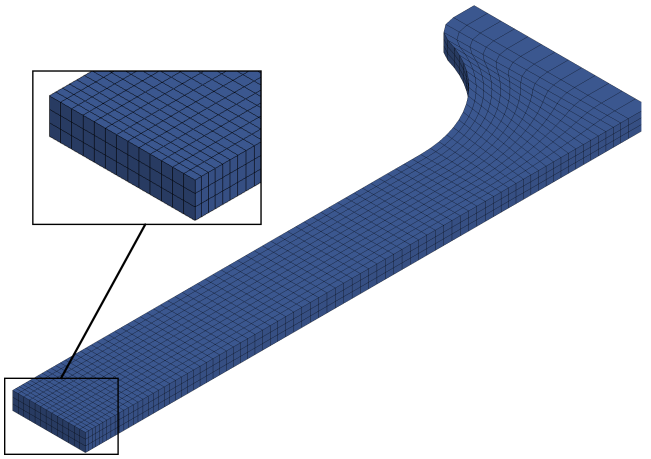

(a) Coarse Mesh - Three Elements Through Thickness

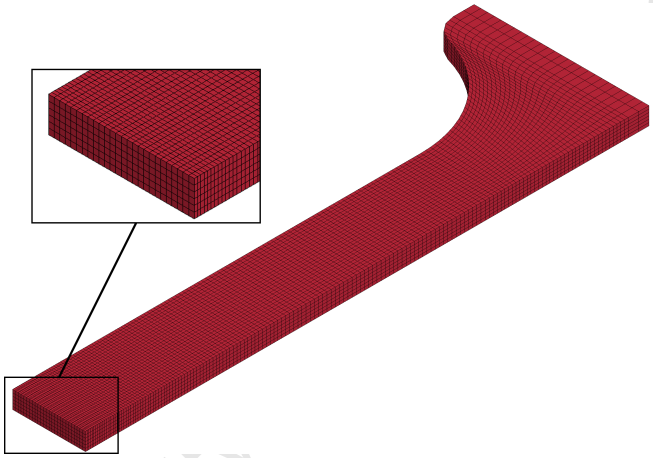

(b) Medium Mesh - Six Elements Through Thickness

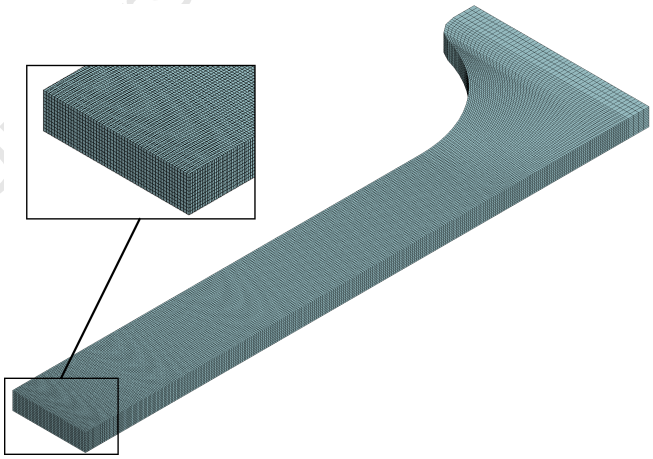

(c) Fine Mesh - Twelve Elements Through Thickness

Figure 6.14: Mesh sizes of Tensile Specimen in Convergence Study

The results for the effect of mesh size are presented in Figure 6.15. The results of all three mesh sizes show good agreement until a displacement of approximately $12.7mm$ where the result from the coarse mesh diverges. The results for the medium and fine mesh show good agreement, from this observation a medium size mesh was implemented in the tensile test simulations.

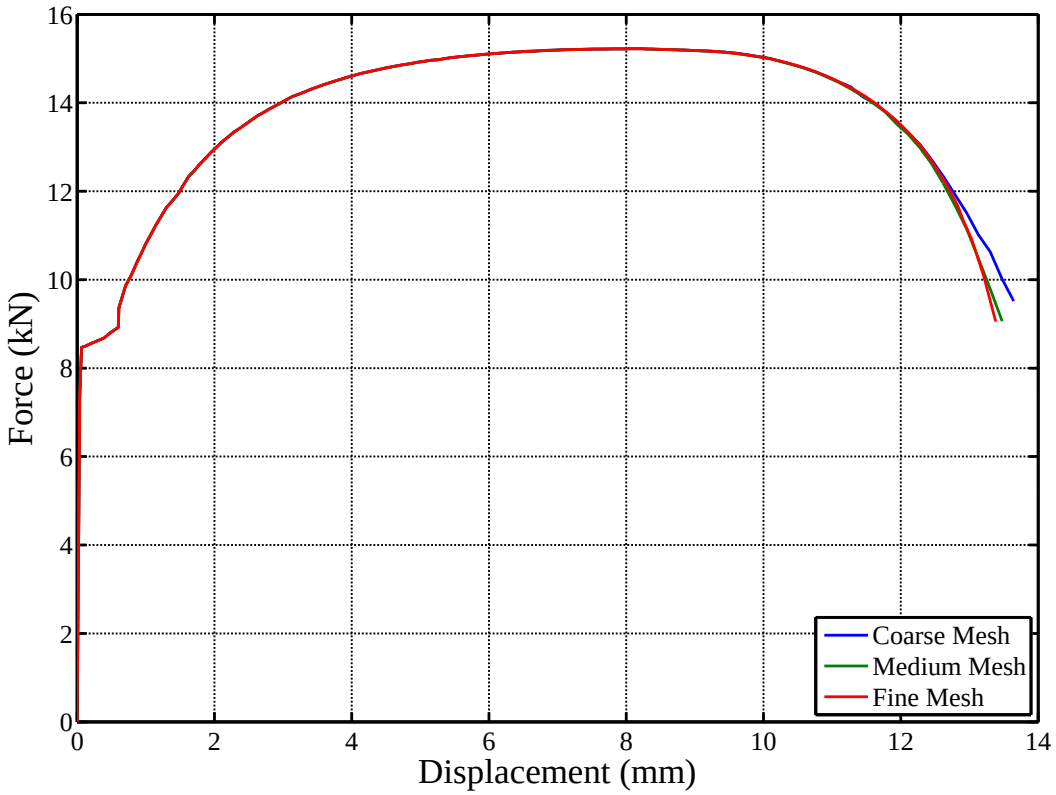

Figure 6.15: Results of Mesh Convergence Study

6.3.1 Simulation Results

Determining the actual true stress-strain curve was an iterative process where the simulated force-displacement curve was compared to the experimental curve. An example of the iterative process is illustrated in Figure 6.16. The simulated force-deflection curves will never match the experimental curve after the UTS because the material model does not incorporate damage.

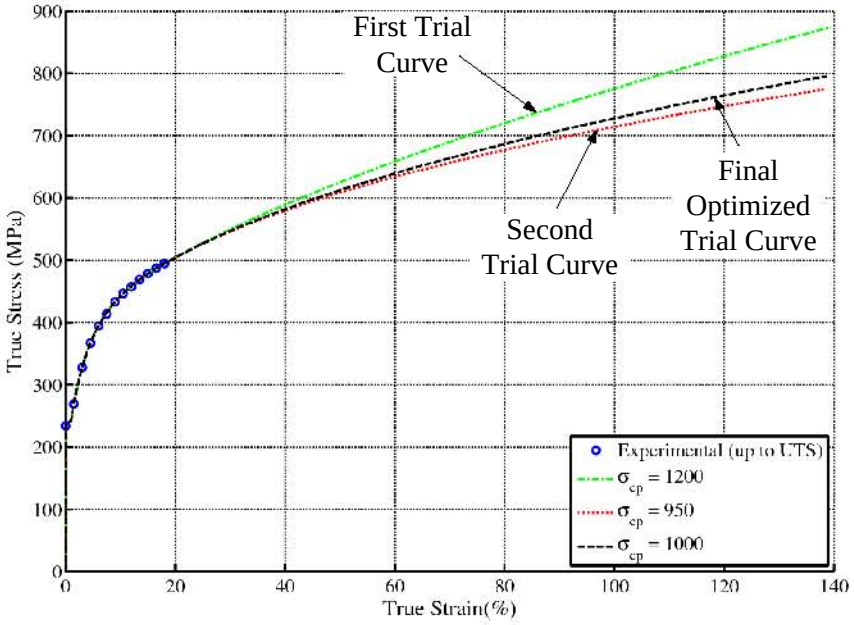

(a) Trial Stress Strain Curves

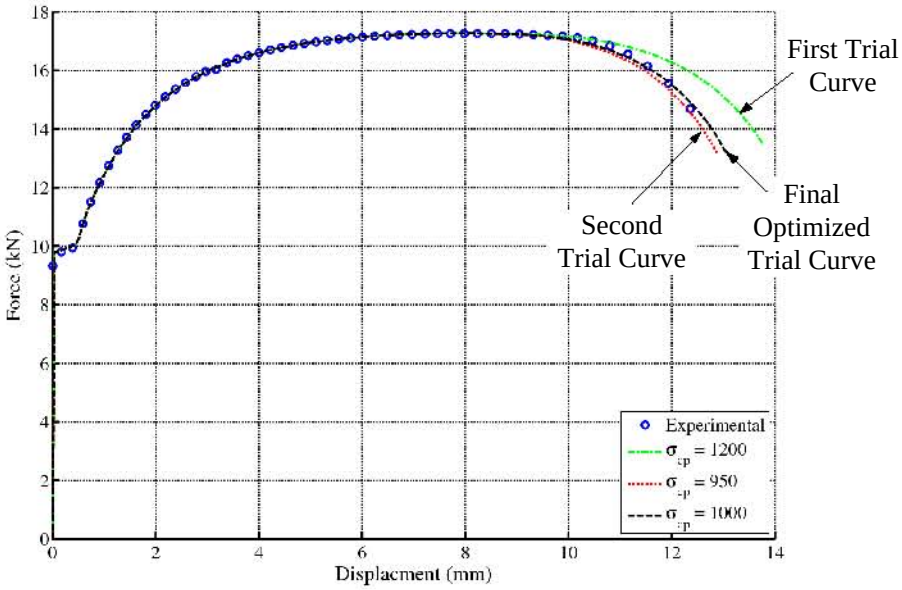

(b) Resulting Force Deflection Curves

Figure 6.16: Iterative Process to Determine Actual Stress-Strain Curve

Figure 6.17 depicts the final quasi-static true stress-strain curves obtained from the experimental and numerical simulations for the three materials tested. It was evident from the results that the material response of the three materials was different and that a material characterisation of the three different thicknesses plates was required.

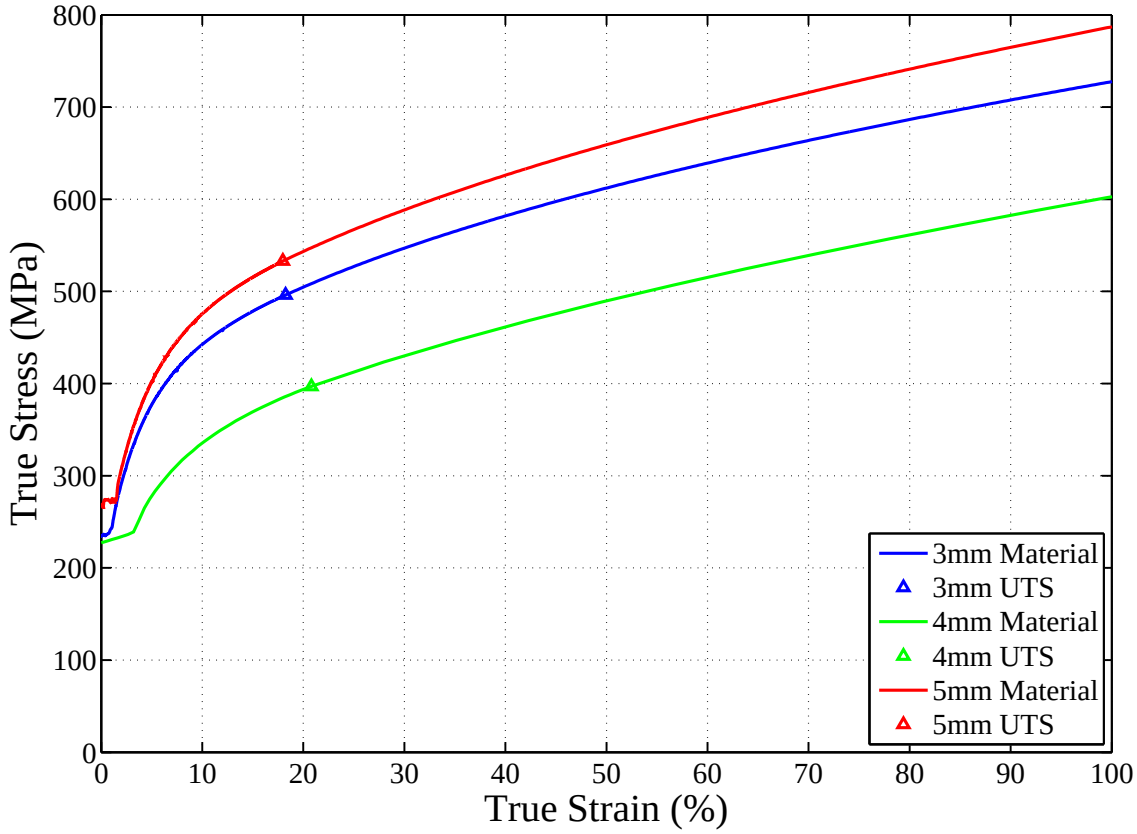

Figure 6.17: Optimized True Stress-True Plastic Strain for the Three Different Materials

6.4 Dynamic Behaviour

6.4.1 High Strain Rate Testing

Hopkinson [146] introduced a novel method of measuring the pressures and loading durations of high velocity impacts by studying the propagation of the stress pulses travelling down a long metallic bar which was impacted on one end. The Split Hopkinson Pressure Bar (SHPB), where a thin cylindrical specimen placed between two Hopkinson bars in series was later introduced by Kolsky [147]. Applying a known pressure pulse to the end of the input bar and recording the stress pulses in both the input and output bars the high strain rate properties of a material are determined.

The SHPB has now become a standard apparatus for measuring the response of materials at high strain rates. The SHPB is capable of testing materials at strain rates of between 100 and $10000s^{-1}$ [148]. There is however no standard design defined for the SHPB but typical designs features include:

- A gas gun to accelerate the striker
- Two long symmetrical bars
- A rigid support frame
- Alignment fixtures that allow for accurate alignment of the bars whilst allowing free axial movement.
- Velocity sensor to measure the velocity of the striker before impact.
- Strain gauges placed on both the incident and transmitted bars to measure the stress wave propagation in the bars. The strain gauges are arranged in a Wheatstone bridge formation, two gauges are mounted diametrically opposite on the bars whilst the other two gauges are mounted to dummy material to cancel temperature effects.
- Amplifiers with a frequency range of at least $1MHz$.
- Data acquisition equipment with a sample rate of at least $10MHz$.

Figure 6.18 illustrates the schematic of a compression SHPB with all the design elements required to perform high strain rate testing.

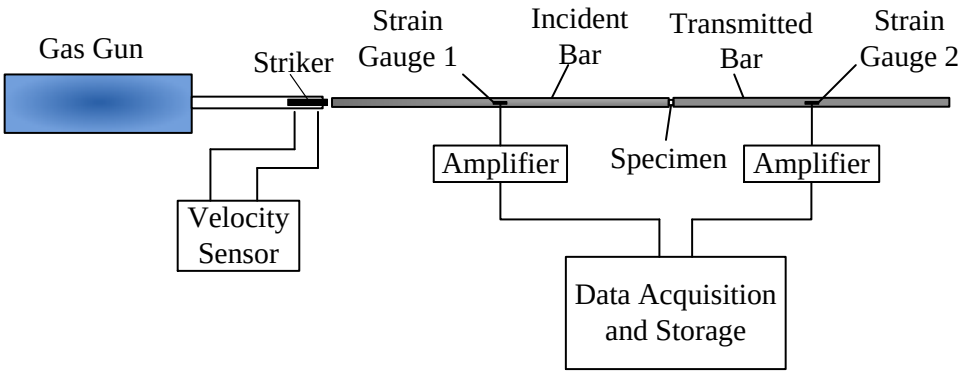

Figure 6.18: Layout of Compression SHPB

6.4.2 Dynamic Test Results

The high strain rate response of the materials were investigated on the SHPB. The specimens were cylindrical in shape with an aspect ratio as close to one as possible, where the length of the specimen was the same as the plate thickness. Specimens were cut through the thickness of the material and in both in-plane directions (rolling direction and transverse to rolling direction) to investigate the isotropic behaviour of the materials. Figure 6.19 illustrates typical geometries of a $3mm$ specimen before and after testing.

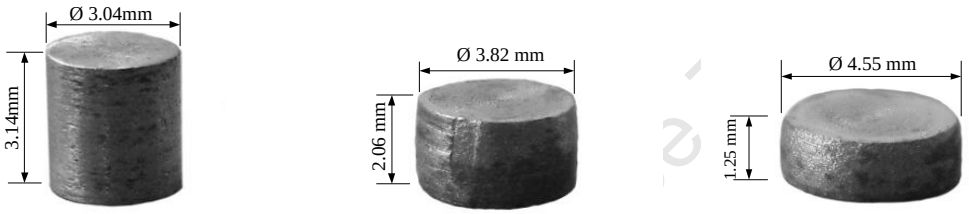

(a) Example of $3mm$ SHPB Specimen Pre-testing (b) Result obtained at a Strain Rate of $2037s^{-1}$ (c) Result obtained at a Strain Rate of $3645s^{-1}$

Figure 6.19: Photographs of $3mm$ SHPB Specimen Before and After Testing

The true stress-strain relationships of the materials at high strain rates were determined from the SHPB theory laid out in Appendix B. Figure 6.20 depicts the results for the $3mm$ thick plate at two different strain rates. Further detailed results for the 3, 4 and $5mm$ thick materials are found in Appendix C. It is evident from the results of all the material thicknesses that the response is isotropic and that there is an increase in the flow stress as the strain rate is increased.

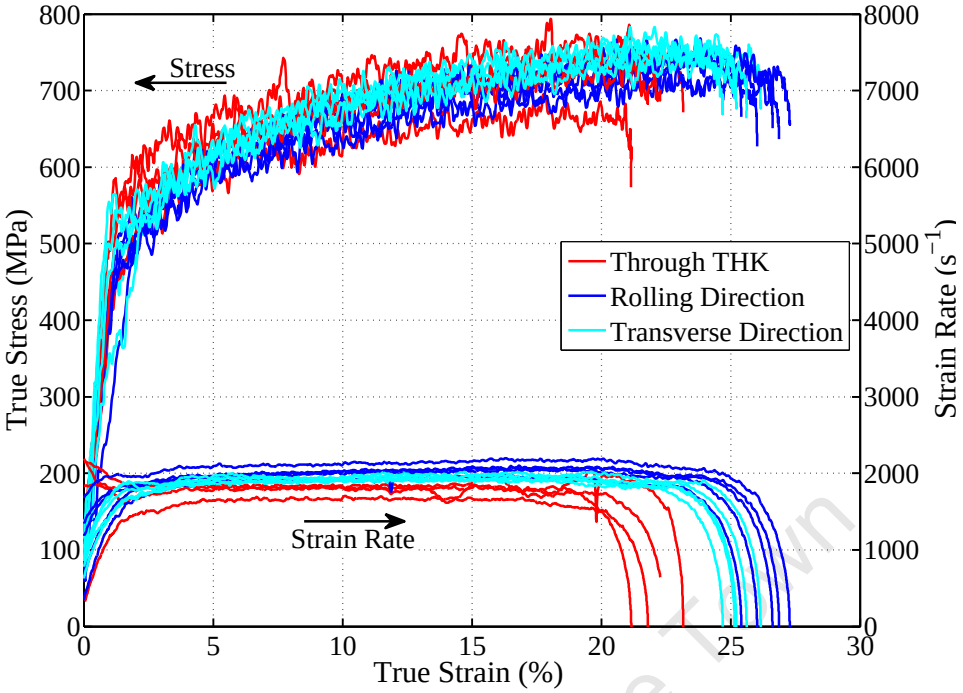

(a) Results for $3mm$ Thick Plate at a Strain Rate of Approximately $1800s^{-1}$

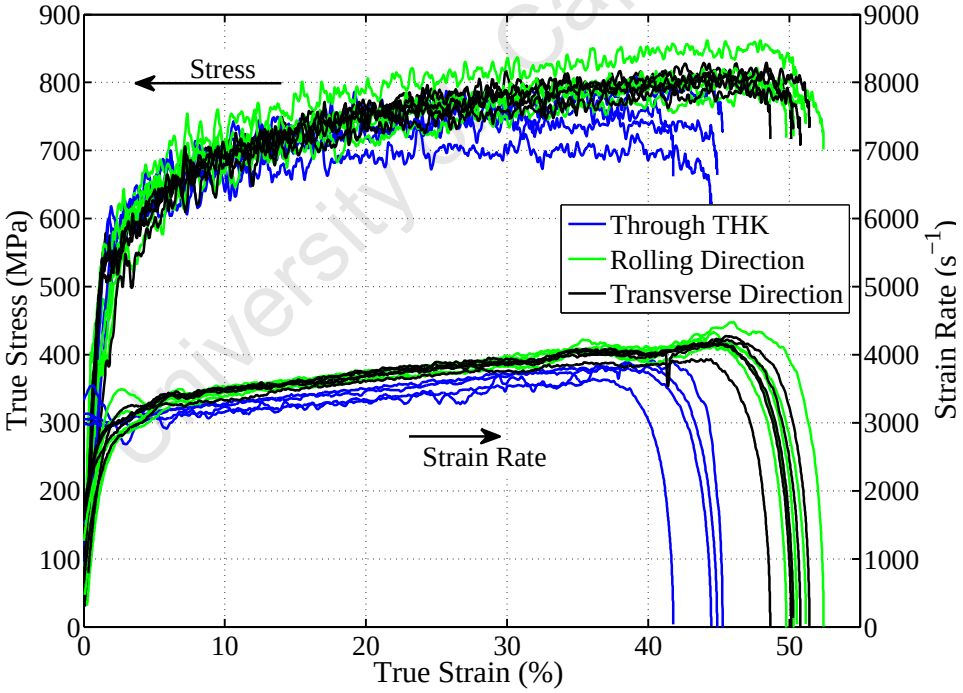

(b) Results for $3mm$ Thick Plate at a Strain Rate of Approximately $3300s^{-1}$

Figure 6.20: High Strain Rate Response of $3mm$ Thick Plate

6.5 Constitutive Material Models

Material characterisation was carried out to obtain material parameters for a constitutive material model which is required to finite elements analysis of the test setups. A constitutive model describes the response of a material as a function of the strain (ε), strain rate effects ($\dot{\varepsilon}$), thermal softening (T) and damage (D) as indicated in Equation 6.11. Many constitutive models have been published [58, 149–151] and vary in complexity and ease of attaining the various material parameters that characterise the material.

$$\sigma = f(\varepsilon, \dot{\varepsilon}, T, D) \tag{6.11}$$

6.5.1 Cowper-Symonds Material Model

Cowper-Symonds [58] proposed a constitutive material model for the numerical simulation of cantilever beams subjected to impact loading. The material model incorporates the effects of strain rate hardening on the flow stress, however the effects of strain hardening and thermal effects would have to be included separately. The Cowper-Symonds material model takes the form of Equation 6.12.

$$\sigma_f = \sigma_o \left(1 + \left(\frac{\dot{\varepsilon}_{eff}}{D}\right)^{\frac{1}{q}}\right) \tag{6.12}$$

where σ_o is the static yield strength, $\dot{\varepsilon}_{eff}$ is the effective plastic strain rate, D and q are strain rate constants.

Common values of D and q reported in literature for annealed mild steel are $40.4s^{-1}$ and 5 respectively. These values of D and q were obtained by fitting Equation 6.12 to experimental data, up to a strain rate of $100s^{-1}$, performed by Manjoine [152]. Marais [153] reported values of D and q for locally produced mild steel produced to be $844s^{-1}$ and 2.207 respectively.

6.5.2 Johnson and Cook Material Model

Johnson and Cook [151] proposed a constitutive model for metals subjected to large strains, high strain rates and high temperatures which is applicable to the response of structures observed in high-velocity impact and explosive detonation. The material model was intended for numerical computations and was easy to implement in finite element packages.

Johnson and Cook [151] acknowledged that more complicated material models, such as the material mode proposed by Zerilli and Armstrong [149], may lead to more accurate material response and that material models tailored to a particular material may describe the response of material more accurately. However these material models are difficult to incorporate in the finite element packages and determining the parameters in these complicated material models can be a complex task. Due to the simplicity and the relative ease of determining the Johnson-Cook material parameters, the Johnson-Cook material has become a very popular and is readily available as a default material model in numerous finite elements codes .

The Johnson-Cook material model for the von Mises equivalent flow stress is expressed in Equation 6.13. The three key material responses namely strain, strain rate effects and thermal softening are combined in a multiplicative manner. The term in the first set brackets represents the effects of strain hardening, the term in the second set of brackets represents the effects of strain rate hardening, the term in the third set of brackets represents the effects of temperature on the flow stress (σ_f) of a material.

$$\sigma_f = \underbrace{[A + B(\varepsilon_{eff})^n]}_{\text{Strain Hardening Effects}} \times \underbrace{[1 + Cln\,(\dot{\varepsilon}^*)]}_{\text{Strain Rate Sensitivity}} \times \underbrace{[1 - (T^*)^m]}_{\text{Thermal Effects}} \tag{6.13}$$

where

$$\dot{\varepsilon}^* = \frac{\dot{\varepsilon}}{\dot{\varepsilon}_o} \quad \text{and} \quad T^* = \frac{T - T_{ref}}{T_{melt} - T_{ref}}$$

where T^* is the homologous temperature, ε_{eff} is the effective plastic strain, $\dot{\varepsilon}$ is the effective plastic strain rate, $\dot{\varepsilon}_o$ is the reference strain rate, T_{melt} is the melting temperature of the material and T_{ref} is the reference temperature. A, B, n, m and C are the five Johnson-Cook material parameters.

The role of reference strain rate ($\dot{\varepsilon}_o$) in the Johnson-Cook model is often misunderstood as a parameter that makes the strain rate term in the Johnson-Cook model non-dimensional [154] and often chosen to be $1s^{-1}$. The reference strain rate is the strain rate at which the material parameters A, B and n are calculated. However it is possible to choose a different value for the reference strain rate as long as the values of A and B are scaled by the ratio of stress between the quasi-static strain rate and the desired reference strain rate [151].

In many ductile materials such as mild steel there is a sudden increase in strength at higher strain rates. The strain rate effects term in the standard Johnson-Cook is a linear function in the logarithm of the strain rate which does describe the sudden increase of strength. To describe the sudden increase in strength revised versions of the strain rate effect term have been presented. Huh and Kang [155] proposed Equation 6.14, which describes the strain rate effects as a quadratic function in the logarithm of the strain rate.

$$f(\dot{\varepsilon}) = 1 + C_1 ln\left(\dot{\varepsilon}^*\right) + C_2 \left[ln\left(\dot{\varepsilon}^*\right)\right]^2 \tag{6.14}$$

Allen *et al.* [156] proposed incorporating the strain rate effects as an exponential of the effective plastic strain rate as set out in Equation 6.15.

$$f(\dot{\varepsilon}) = \left(\dot{\varepsilon}^*\right)^C \tag{6.15}$$

Comparing experimental results of $A36$ hot rolled steel to numerical results for the different strain rate forms, Schwer [154] reported that the best overall results were obtained with the standard Johnson-Cook strain rate term.

Johnson and Cook [157] later expanded their model to incorporate fracture based on cumulative-damage. The form of the damage model is similar to the material model with three terms combining in a multiplicative manner to include the effects of stress triaxiality, strain rate and local heating. The cumulative-damage fracture model, proposed by Johnson and Cook [157], is expressed in Equation 6.16.

$$\varepsilon^f = \left(D_1 + D_2 exp \left[D_3 \frac{\sigma_m}{\sigma_{eff}} \right] \right) (1 + D_4 ln\dot{\varepsilon}^*) (1 + D_5 T^*) \tag{6.16}$$

where ε^f is the equivalent strain to fracture, σ_m is the average of the three normal stresses and σ_{eff} is the von Mises equivalent stress. $\dot{\varepsilon}^*$ and T^* are identical to those in Equation 6.13. $D_1 \cdots D_5$ are the five damage constants that need to be determined to accurately model the fracture of a material.

6.6 Johnson-Cook Material Parameters

The standard Johnson-Cook material model was chosen to represent the materials in this investigation as the material parameters are easily obtainable and the material model is available in LS-Dyna. The material parameters required for the material model were obtained from the quasi-static (Section 6.2.3) and dynamic (Section 6.4.2) results.

6.6.1 Determining Parameters A, B and n

In order to determine the Johnson-Cook material parameters the reference strain rate ($\dot{\varepsilon}_o$) and temperature (T_{ref}) were taken as $416,7 \times 10^{-6} s^{-1}$ and $298K$ respectively. Parameter A, which is the yield stress at the reference strain rate and temperature was taken as the average of the yield stress of the uniaxial tensile tests performed at a strain rate of $416,7 \times 10^{-6} s^{-1}$, Table 6.2 lists the values of the average yield stresses for the three different materials.

Under the reference conditions and assuming that the temperature effects due to deformation are negligible the Johnson-Cook material model reduces to Equation 6.17.

$$\sigma_f = A + B(\varepsilon_{eff})^n \tag{6.17}$$

The parameters B and n which describe the strain hardening response of the material are obtained by curve fitting Equation 6.17 (with A set to the average yield stress of the material) to the experimental true stress-strain curve between 10% to 100% in order to remove the effects of the Ludërs band. Figure 6.21 illustrates the curve fit to the experimental result for the $3mm$ thick plate. The values of the material parameters B and n for the different materials are listed in Table 6.2.

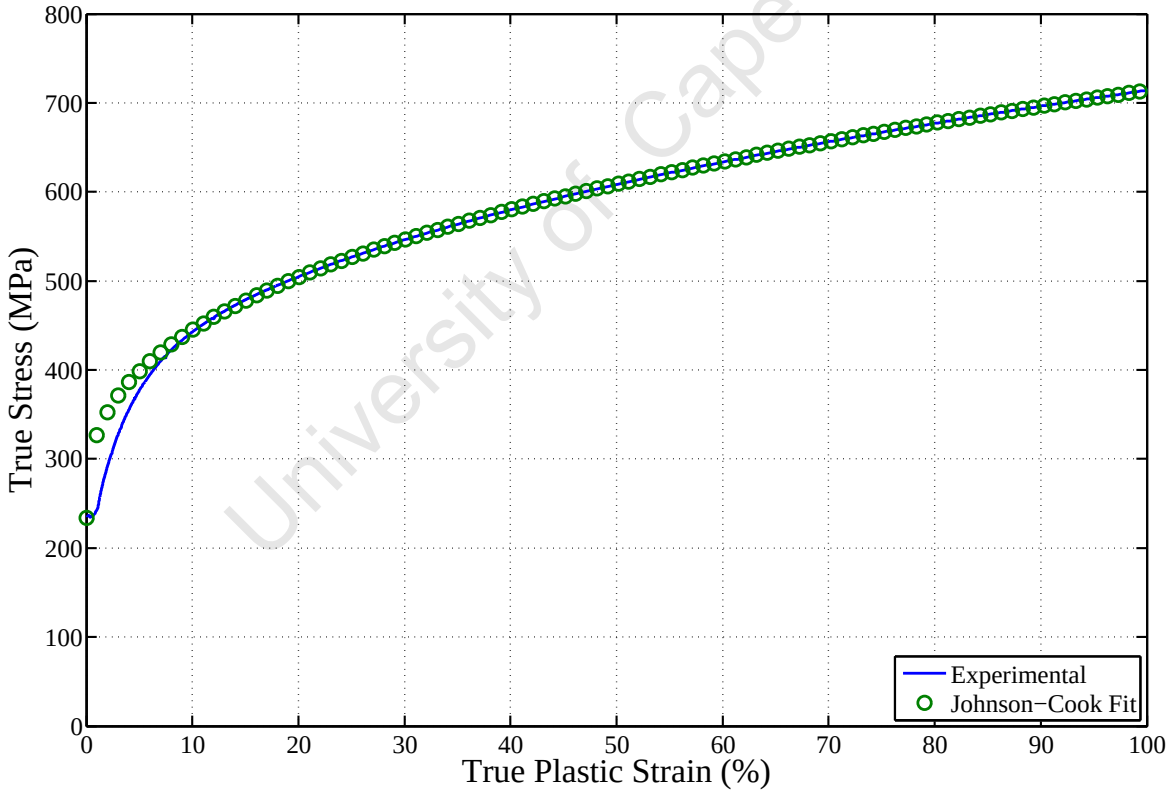

Figure 6.21: Graph Showing Fitted Strain Hardening Function for $3mm$ Thick Plate

Table 6.2: Strain Hardening Parameters

Thickness	$3mm$	$4mm$	$5mm$
Material	Mild Steel	Mild Steel	Gr. 300WA
A(MPa)	233.47	221.67	263.58
B(MPa)	480.37	361.35	519.64
n	0.3565	0.4746	0.3843

6.6.2 Determining Parameter C

The parameter C in the Johnson-Cook material is used to define the strain rate effects on the material behaviour. The standard Johnson-Cook model used in this investigation scales the flow stress as a linear function of the strain rate. The Johnson-Cook material model may be rewritten (Equation 6.18) in order to determine the strain rate effects.

$$\left(\frac{\sigma_f}{A + B\varepsilon_{eff}^n} - 1\right) = Cln(\dot{\varepsilon}^*) \tag{6.18}$$

where A, B and n are the material parameters determined in Section 6.6.1 and listed in Table 6.2, ε_{eff} is the effective plastic strain and σ_f is the experimental true stress corresponding to a effective plastic strain.

An effective plastic strain of 10% was chosen to determine the value of C as the corresponding stress occurs after the Ludërs band in the quasi-static experiments and avoids the initial ring up in the high strain rate experiments. A least squares technique is applied to fit the strain rate function to the experimental data. The value of parameter C is taken as the slope of the linear fit. Figure 6.22 illustrates the fit of the Johnson-Cook strain rate parameter to the experimental data of the $3mm$ thick plate. The values of the strain rate effects parameters for the three materials are listed in Table 6.3.

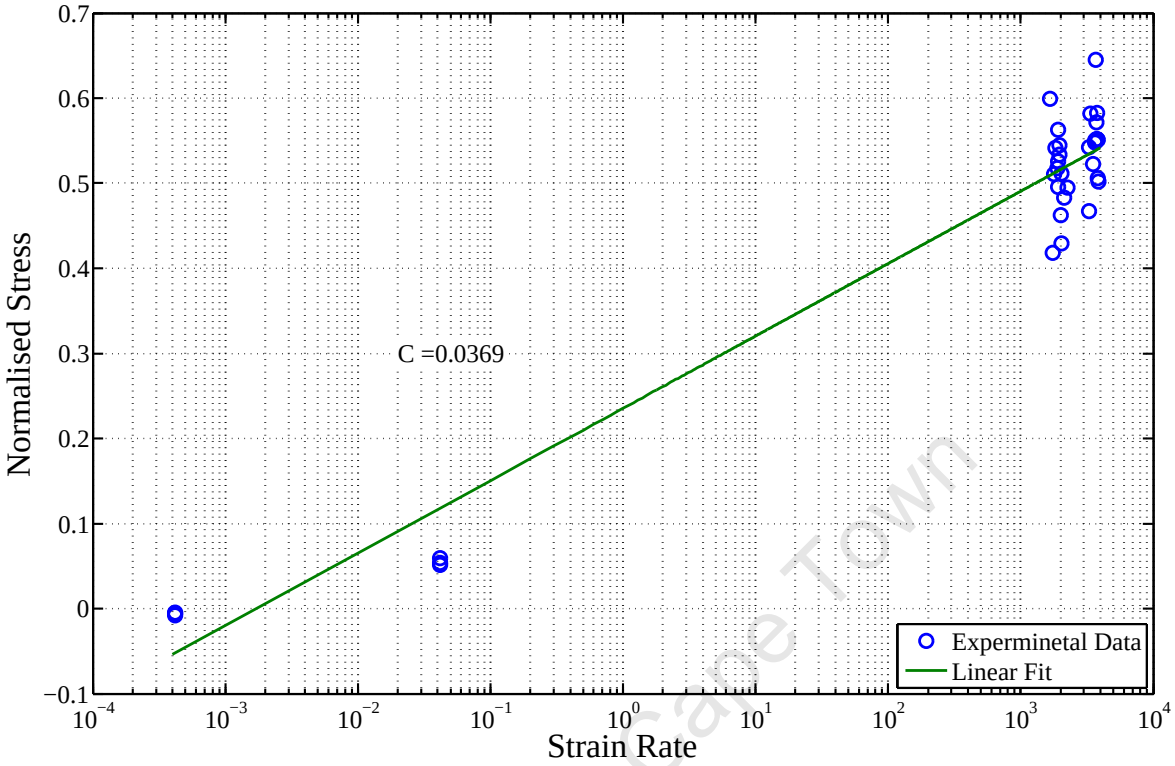

Figure 6.22: Graph Showing Fitted Strain Rate Function for $3mm$ Thick Plate

Table 6.3: Strain Rate Effect Parameters

Thickness	$3mm$	$4mm$	$5mm$
Material	Mild Steel	Mild Steel	Gr. 300WA
C	0.0369	0.0481	0.0259

6.6.3 Determining Parameter m

Generally the flow stress of metals decreases with the increase in temperature and decrease in strain rate [158–161]. This generalisation holds true except for a band of temperature at lower strain rates where the flow stress increases. The increase in the flow stress may be attributed to dynamic strain ageing. The effects of dynamic strain ageing are illustrated in Figures 6.23a and 6.24a and to a lesser effect in Figure 6.24b between temperatures of approximately $300 - 650°K$.

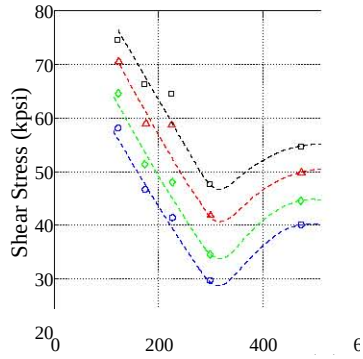

(a) Stress versus Temperature for a Strain Rate of $0.006s^{-1}$

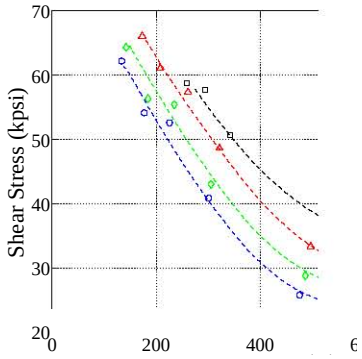

(b) Stress versus Temperature for a Strain Rate of $10^3s{-}1$

Figure 6.23: Shear Stress versus Temperature Results Reported by Eleiche for Mild Steel [158]

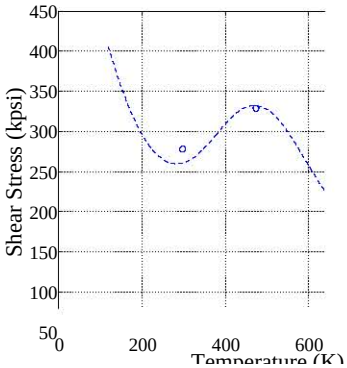

(a) Stress versus Temperature for a Strain Rate of $5 \times 10^{-4}s^{-1}$

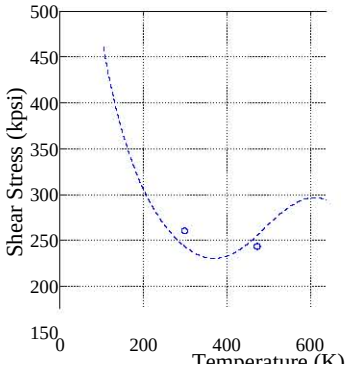

(b) Stress versus Temperature for a Strain Rate of $2s^{-1}$

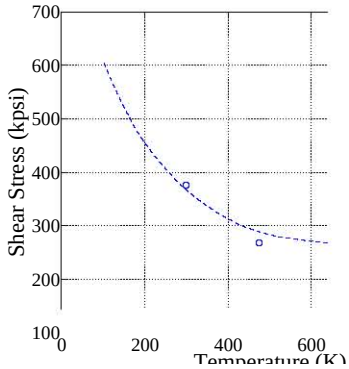

(c) Stress versus Temperature for a Strain Rate of $1000s^{-1}$

Figure 6.24: Shear Stress versus Temperature Results Reported by Gilat and Wu for hot-rolled HRS1020 steel [161]

It is also evident from Figures 6.23 and 6.24 that effects of dynamic strain ageing decrease as the strain rate increases due to the short duration of the experiment which limits the evolution of strain ageing [158]. Further details on dynamic strain ageing may be found in references [158, 161–163].

The effects of temperature on the flow stress are incorporated in the last term of the Johnson-Cook material model. In order to determine the value of m in the last term a series of high temperature-high strain rates experiments are required. As the current testing facilities do not permit high temperature-high strain rate tests the parameter m was determined by extracted data reported by Gilat and Wu [161] on $HRS1020$ steel (which has similar physical properties to mild steel) and mild steel results presented by Eleiche [158].

In order to compare the extracted results the flow stress was normalised by the stress occurring at the lowest temperature. The value of m is determined by curve fitting Equation 6.19 to the extracted data.

$$\sigma_{norm} = 1 - (T^*)^m \tag{6.19}$$

where T_{ref} was taken as $300K$ and T_{melt} was taken as $1811K$ [151].

The best fits to the extracted data are illustrated in Figure 6.25. Reviewing the results of the fitted curves it was decided that the value of m would be determined as the best fit of Equation 6.19 to all the extracted experimental data which resulted in a m value of 0.6655.

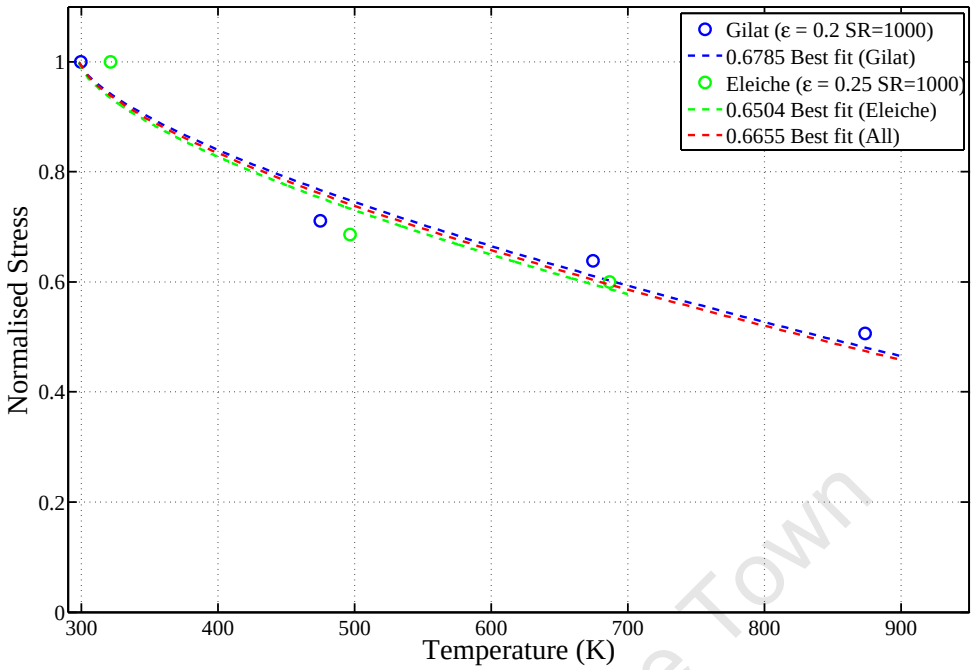

Figure 6.25: Graph Showing Fitted Temperature Function

6.6.4 Summary

The Johnson-Cook material parameters for the three different plate thicknesses were determined from the methods described in Section 6.6. Table 6.4 list the various parameters for the three plate thicknesses. It is evident from Table 6.4 that even though the material specified for the 3 and $4mm$ thick plates is mild steel the material behaviours and hence the Johnson-Cook material parameters are significantly different.

Table 6.4: Johnson-Cook Parameters for Different Plate Thicknesses

Thickness	$3mm$	$4mm$	$5mm$
Material	Mild Steel	Mild Steel	Gr. 300WA
A (MPa)	233.47	221.67	263.58
B (MPa)	480.37	361.35	519.64
n	0.3565	0.4746	0.3843
C	0.0369	0.0481	0.0259
m	0.6655		

This page has been intentionally left blank.

7 Development of Numerical Blast Models

7.1 Introduction

The finite element models used to simulate the three different degrees of confinement are presented in this chapter. The aim of the simulations was to determine the simplest numerical model that would provide adequate correlation with the experiments.

The simulations were carried out in an explicit time integration finite element package LS-DYNA® V971 R6.6220. LS-DYNA is a general purpose finite element code that can be used to analyse a structure subjected to static and/or dynamic loads [164]. LS-DYNA has the ability to simulate highly non-linear transient dynamic events, such as explosions, high velocity impact and penetration. LS-DYNA is capable of solving complex problems with both Lagrangian and Eulerian formulations working in unison. The mesh in the Lagrangian formulation deforms with the movement of the material and is typically implemented to obtain solutions for solid continuum structures [165, 166]. The mesh in the Eulerian formulation is fixed in space and material flow through the mesh. Typically Eulerian formulations are implemented to model gases and liquids where the deformations of the materials are expected to be large [165, 167].

Quarter symmetry models were implemented to increase the computational efficiencies of the simulations. The clamp frames and bolts were included in the simulations as the interaction between the target plate, clamp frames and bolts provided a more realistic response of the target plate under blast loading. Simulating the clamp frames and bolts

allowed for pull-in of the target plates to occur for large midpoint deflections [39].

This section of the report starts with a description of the equations of states and material models implemented in the simulations, this is followed by a description of two mesh convergence studies to optimize element sizes for the numerical models. The blast models are described in detail and finally the loading phases implemented in the simulations are presented.

7.2 Equations of State and Material Models

The behaviour of the structural elements (test rig models) and the fluid materials (air and explosive models) were represented by different equations of states (EOS) and material models. This section of the report presents the EOS, material models and the required parameters implemented in the simulations.

7.2.1 Target Plate

The Johnson-Cook material was implemented to described the behaviour of the target plates. The material parameters required for the Johnson-Cook material model were determined in Section 6.5.2 by means of a material characterisation process. The material parameters for the Johnson-Cook models are re-listed in Table 7.1 for convenience.

Table 7.1: Johnson-Cook Material Parameters

Thickness	Material	A (MPa)	B (MPa)	n	C	m
$3mm$	Mild Steel	233.47	480.37	0.3565	0.0369	
$4mm$	Mild Steel	221.67	361.35	0.4746	0.0481	0.6655
$5mm$	Gr. 300WA	263.58	519.64	0.3843	0.0259	

7.2.2 Air

The air was modelled with LS-DYNA's null material (*MAT_NULL) and an ideal gas (gamma law) [145] form of EOS, defined as,

$$P = (\gamma - 1)\left[\frac{\rho}{\rho_o}E\right] \tag{7.1}$$

where P is the pressure, ρ is the current density, ρ_o is the initial density, E is the internal energy per unit reference volume and γ is the ratio of specific heats ($\frac{C_p}{C_v} = 1.4\,(\text{for air})$).

The air was modelled as an ideal gas with LS-DYNA's linear polynomial EOS (Equation 7.2) [145] by setting $C_0 = C_1 = C_2 = C_3 = C_6 = 0$ and $C_4 = C_5 = \gamma - 1$.

$$P = C_o + C_1\mu + C_2\mu^2 + C_3\mu^3 + (C_4 + C_5\mu + C_6\mu^2)E \tag{7.2}$$

where $C_1 - C_6$ are user defined constants, E is the internal energy per unit reference volume and μ is a volumetric parameter defined as,

$$\mu = \frac{\rho}{\rho_o} - 1$$

where ρ is the current density and ρ_o is the initial density.

The material properties of the air are given in Table 7.2 and were obtained from Kinney and Graham [1].

Table 7.2: Material and Equation of State Parameters for Air

$\rho_o(kg/m^3)$	γ	$E_o(kJ/m^3)$
1.184	1.4	2.533

7.2.3 Explosive

The Jones-Wilkins-Lee (JWL) EOS was implemented in conjunction with the high explosive burn material model to describe the explosive materials. The JWL EOS has been widely implemented due to its simplicity and accuracy over a wide range of explosive materials [168]. The JWL EOS defines the pressure as a function of the internal energy per unit reference volume (E) and the relative volume (ν) and is expressed as,

$$P = A\left(1 - \frac{\omega}{R_1\nu}\right)e^{-R_1\nu} + B\left(1 - \frac{\omega}{R_2\nu}\right)e^{-R_2\nu} + \frac{\omega E}{\nu} \tag{7.3}$$

where A, B, R_1, R_2 and ω are material constants.

The JWL EOS and material parameters for the explosive material (PE4) are listed in Table 7.3.

Table 7.3: Material and JWL equation of State Constants for Explosive (PE4) [118]

ρ_o (kg/m^3)	D (m/s)	P_{CJ} (GPa)	A (GPa)	B (GPa)	R_1	R_2	ω	E_o (GPa)
1601	8193	28	609.77	12.95	4.5	1.4	0.25	9.0

The detonation process was modelled with the high explosive burn material model. The material model controls the release of energy during the detonation process with the implementation of a burn fraction. The pressure during the detonation process was a function of the JWL EOS pressure (P_{JWL}) and the burn fraction (F) and is expressed as [164],

$$P = P_{JWL} \times \underbrace{min(1, max(F_1, F_2))}_{\text{Burn Fraction}(F)} \tag{7.4}$$

where F_1 and F_2 are burn mass functions computed by,

$$F_1 = \begin{cases} \frac{2(t-t_1)DA_{e_{max}}}{3\mathrm{v}_e} & \text{if } t > t_1 \\ 0 & \text{if } t \leq t_1 \end{cases} \tag{7.5}$$

$$F_2 = \beta = \frac{1-V}{1-V_{CJ}} \tag{7.6}$$

where t is the current time, t_1 is the lighting time, D is the detonation velocity, $A_{e_{max}}$ is the maximum surface area of the element, v_e is the volume of the element, V is the actual specific volume and V_{CJ} is the specific volume at the Chapman-Jouguet pressure (P_{CJ}). The relation between V_{CJ} and P_{CJ} is given by [168],

$$V_{CJ} = 1 - \frac{P_{CJ}}{\rho_o D^2} \tag{7.7}$$

The lighting time (t_1) of an element was calculated by dividing the distance between the centre of the element and the defined detonation point by the detonation velocity (D) [164].

Equation 7.5 represents the programmed burn model in LS-DYNA which controls the detonation process with the lighting times of the explosive elements. The programmed burn model smears the detonation process over several time steps [145]. Equation 7.6 represents the beta burn model in which volumetric compression of an explosive element resulted in the detonation of the explosive element [169].

The finite element investigation carried out in the report implemented both the programmed and beta burn models to describe the detonation of the explosive.

7.3 Mesh Convergence Studies

Two mesh convergence studies were carried out to determine the effects of element size of the target plate and air domain on the final midpoint deflection. The studies were undertaken to determine the optimal element sizes for efficient models which produced converged finite element solutions.

7.3.1 Target Plate

The optimal element size for the target plate was determined by loading the target plates of different element sizes with an identical idealised blast load and comparing the final midpoint deflections and computational efficiencies. The element sizes, characterised by the element length (h), corresponding to 0.25, 0.5, 1, 2 and $4mm$ were investigated.

The geometry of the target plate was simplified to a square plate with dimensions $150 \times 150mm$ by removing the bolts holes and the corner radius (see Figure 7.1). The target plates were meshed with unity aspect ratio 4-node uniform quadrilateral Belytschko-Tsay shell elements with Flanagan-Belytschko viscous hourglass control. Through thickness integration was performed with Gauss quadrature with five integration points.

The fully clamp region (highlighted in Figure 7.1) of the target plate was modelled as a rigid boundary where the translation movement of the nodes were constrained ($\delta_x = \delta_y = \delta_z = 0$). The target plate was assigned the Johnson-Cook material parameters for the $3mm$ thick plate (see Table 7.1).

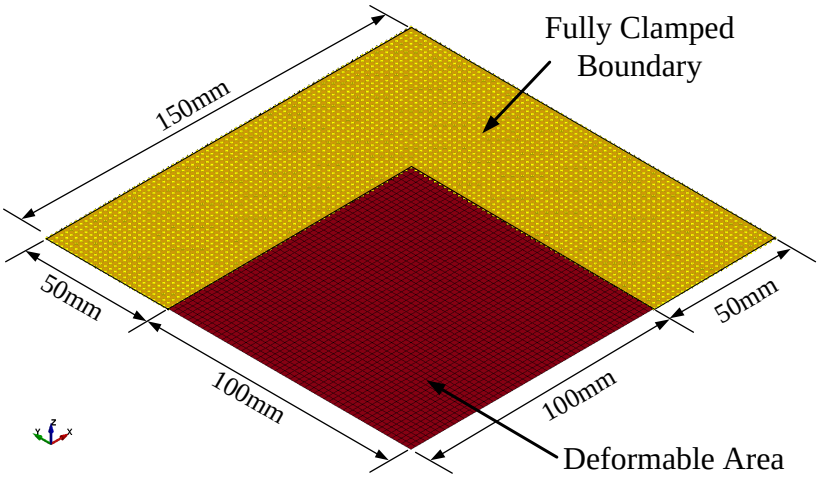

Figure 7.1: Target Plate with Imposed Boundary Conditions

The target plate was loaded with an empirically based blast load generated by the CONWEP blast model. CONWEP was implemented in LS-DYNA by Randers-Pehrson and Bannister [170] and pressure profiles were based on work presented by Kingery and Bulmash [171] for spherical TNT charges detonated in free air and hemispherical charges detonated on a reflective surface. CONWEP generates an idealised pressure profile which acts on a surface/s. The application of the CONWEP blast load decreases the computational time of the simulation as the load was applied directly to a Lagrangian structure (target plate) without having to simulate the computationally expensive Eulerian elements (air and explosive models) [170]. In the study, the CONWEP blast load applied to the target plates corresponded to a $50g$ spherical charge of PE4 detonated at a stand off distance of $100mm$.

The final deformations and total CPU times for the five different elements sizes were taken into consideration when determining the optimal element size and the respective results are depicted in Figure 7.2. The final midpoint deflection was taken as the average deflection of the target plate after the peak deflection where the plate response is characterised by elastic vibrations ($> 0.5ms$). The final midpoint displacement results for $h = 0.25$, 0.5 and $1mm$ were within 4% which was viewed as an acceptable tolerance to indicate convergence of the solution.

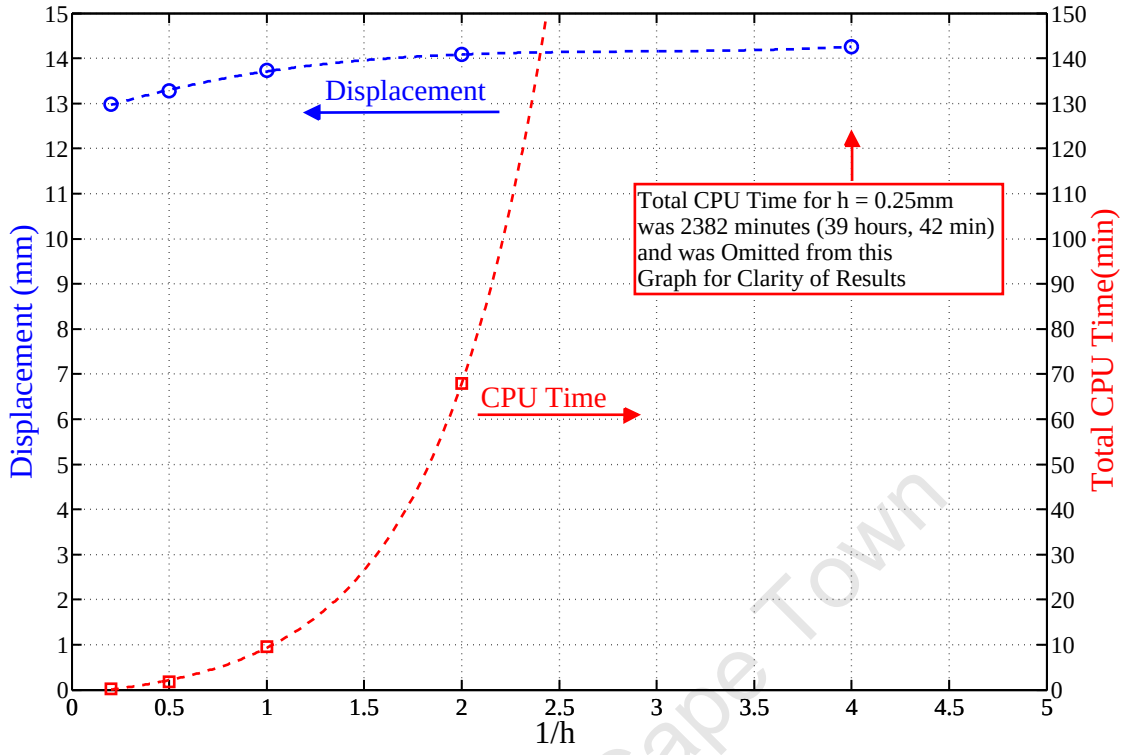

Figure 7.2: Results From Mesh Convergence Study Performed to Determine Optimal Mesh Size For the Simulation of the Target Plates Subjected to Blast Loads

Another consideration was the total CPU time taken to solve the problem, it was evident that the smaller the value of h the longer the CPU time. Considering both the final midpoint displacement and CPU time an element size of $1mm$ was selected as there was no significant difference on the final midpoint deflection when reducing the element size any further.

7.3.2 Air and Explosive

The air model was meshed with 3 dimensional, 8 node 1 point integration ALE multi-material brick elements with Flanagan-Belytschko viscous form hourglass control with exact volume integration. The air model had dimensions of $100 \times 100 \times 200mm$ and was meshed with elements that had an unity aspect ratio (*i.e.* 1:1:1). Element sizes, characterised by the element length (h), of 4, 2 and $1mm$ were investigated.

Figure 7.3 illustrates the numerical setup of the model implemented for the mesh convergence study of the air domain. The stand off distance between the target plate and the explosive charge was set to $100mm$ as in the experiments. The geometry, boundary conditions and material models of the target plate were identical to the target plate with an element size of $1 \times 1mm$ implemented in Section 7.3.1. A spherical explosive charge of $50g$ was initialised within the air model and detonated. The air and explosive domains were coupled to the target plate with a penalty based coupling algorithm which allowed the energy of the blast wave to transfer to the target plate.

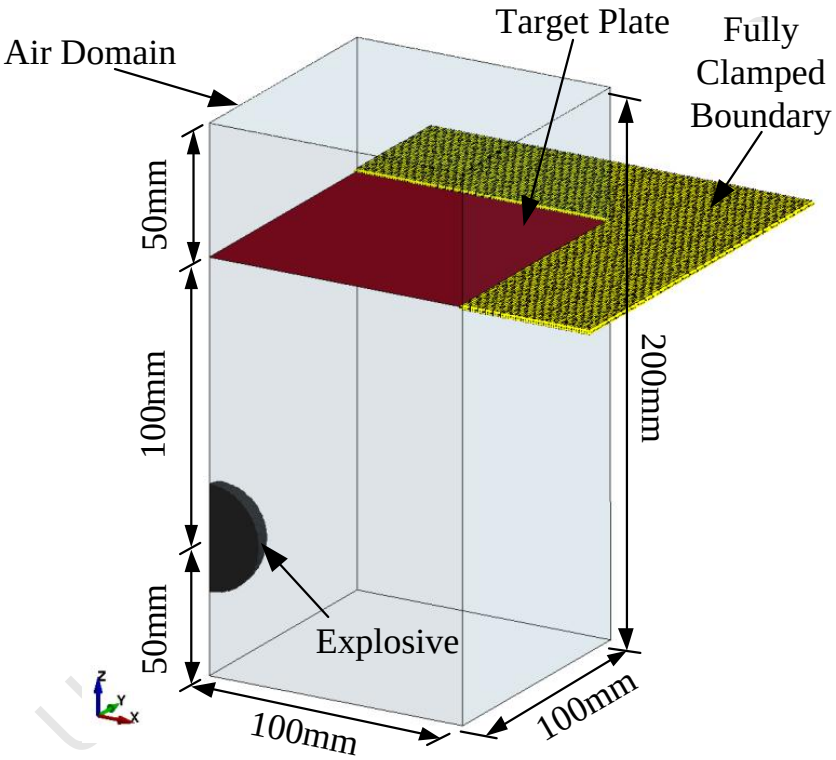

Figure 7.3: Model Setup for Mesh Convergence Study of Air Mesh Size

The reflection of the blast wave off the clamp frames was incorporated in the simulation by creating a reflective boundary condition where the clamp frames were located. The reflective boundary prevents the outflow of gaseous products and creates a reflective surface. Figure 7.4 illustrates the reflective boundary condition imposed on the air mesh representing the $12mm$ thick clamp frame.

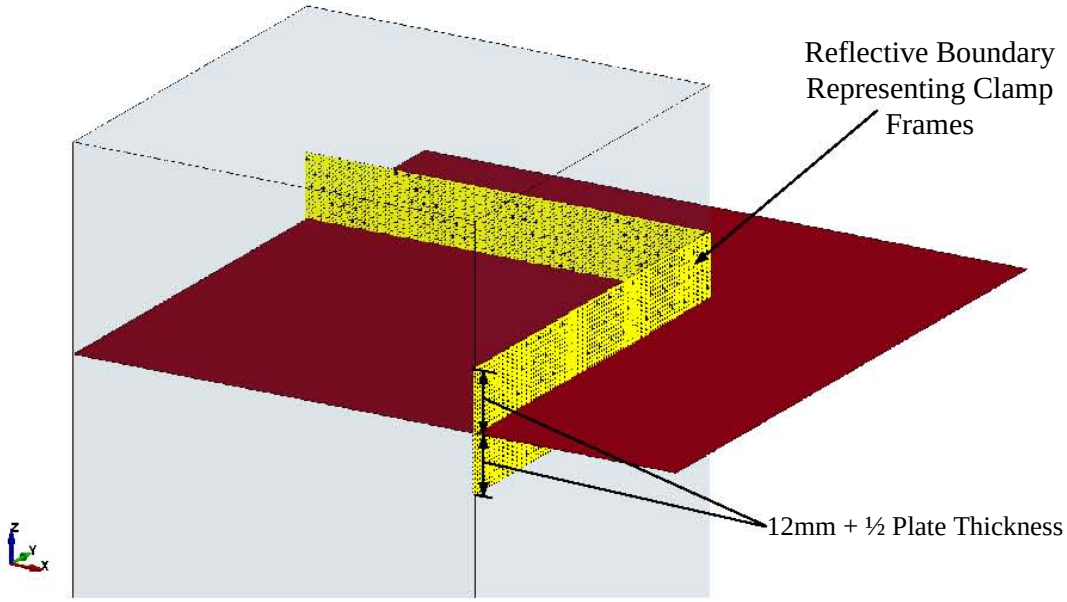

Figure 7.4: Reflective Boundary Imposed on Air Mesh to Represent Clamp Frames in Mesh Convergence Study

The final midpoint displacement and the total CPU time for the different mesh sizes were considered when selecting the optimal mesh size for the air domain. The final midpoint deflection and total CPU times for the different mesh sizes investigated are illustrated in Figure 7.5. The final midpoint deformations for the different mesh sizes are very similar clearly showing the results have converged. However the explosive charge should have a minimum of eight elements through the radius of the explosive charge to effectively describe the detonation process [172] hence $h = 4mm$ could not be implemented as the explosive charge would represented by too few elements across its radius. The total CPU time for $h = 1mm$ was approximately three times longer than for $h = 2mm$ and provided similar results. Consequently an element size of $h = 2mm$ was selected for the mesh of the air domain.

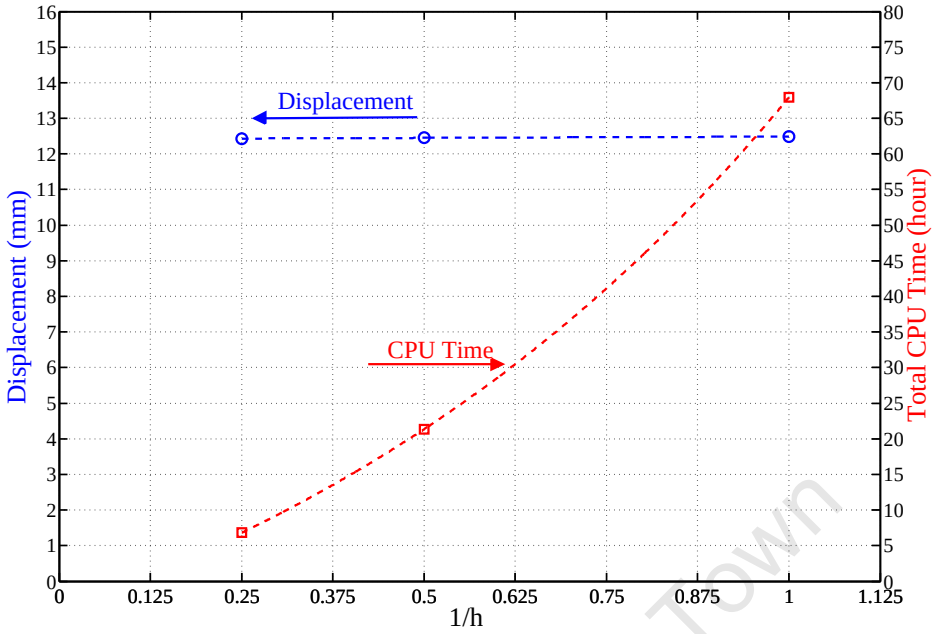

Figure 7.5: Results for Mesh Convergence Study on Air Domain

7.4 Blast Models

The blast models were comprised of main components, namely the test rig model and the combination of the air and explosive models. The test rig comprised of the different structural elements such as the target plate, clamp frames and bolts.

7.4.1 Test Rig Models

7.4.1.1 Target Plate

The target plate illustrated in Figure 7.6 was common to the three different degrees of confinement simulations. The target plate was meshed with 4-node uniform quadrilateral Belytschko-Tsay shell elements with Flanagan-Belytschko viscous hourglass control. The target plate was divided into two regions characterised by the mesh geometry. The first region of the target plate was comprised of the exposed area of the plate ($100 \times 100mm$), highlighted in red in Figure 7.6, and a segment which extended $10mm$

under the clamp frame, highlighted in green in Figure 7.6. The elements in this region were uniform elements with dimensions $1 \times 1mm$. The remainder of the target plate which was located entirely between the two clamp frames, highlighted in blue in Figure 7.6, was meshed with quadrilateral elements where the maximum element length was $2.5mm$.

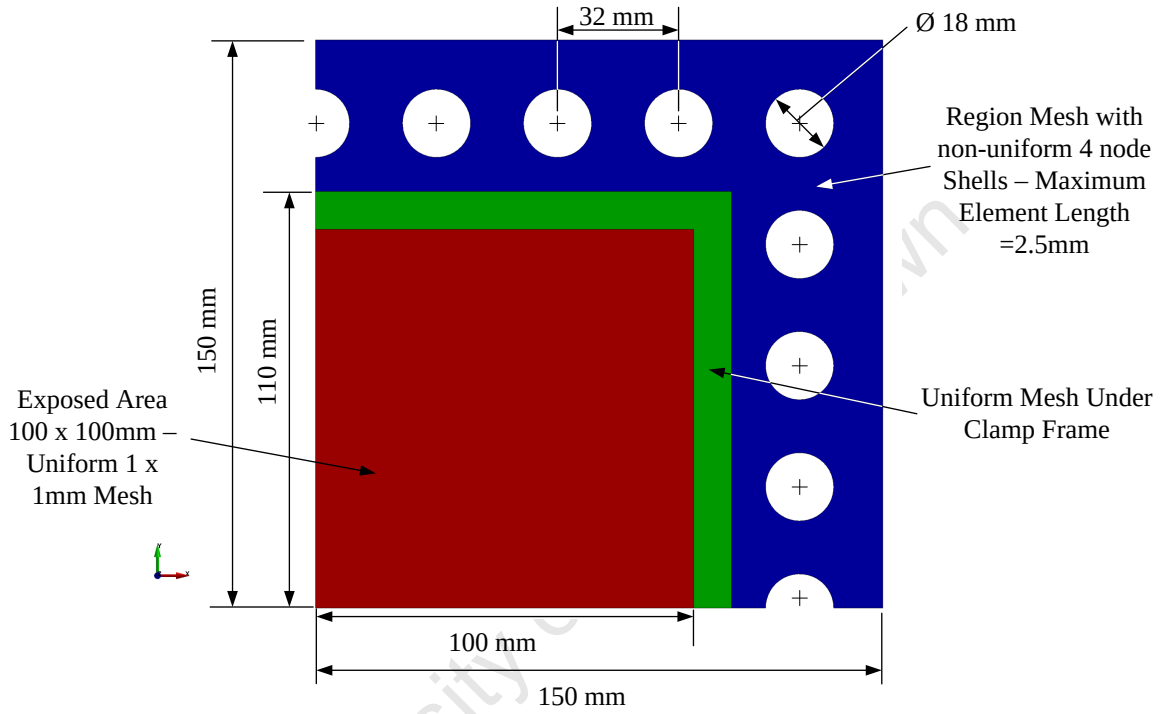

Figure 7.6: Numerical Model of Target Plate

7.4.1.2 Unconfined Blast Load Test Rig

Figure 7.7a illustrates the unconfined blast load test rig model. The clamp frames and bolts were meshed with 3 dimensional 8 node constant stress elements with Flanagan-Belytschko viscous hourglass control with exact volume integration for solid elements. The clamp frames and bolts were modelled as elastic materials with an Elastic modulus (E) of $206GPa$, density (ρ) of $7850kg/m^3$ and Poisson's ratio of 0.3.

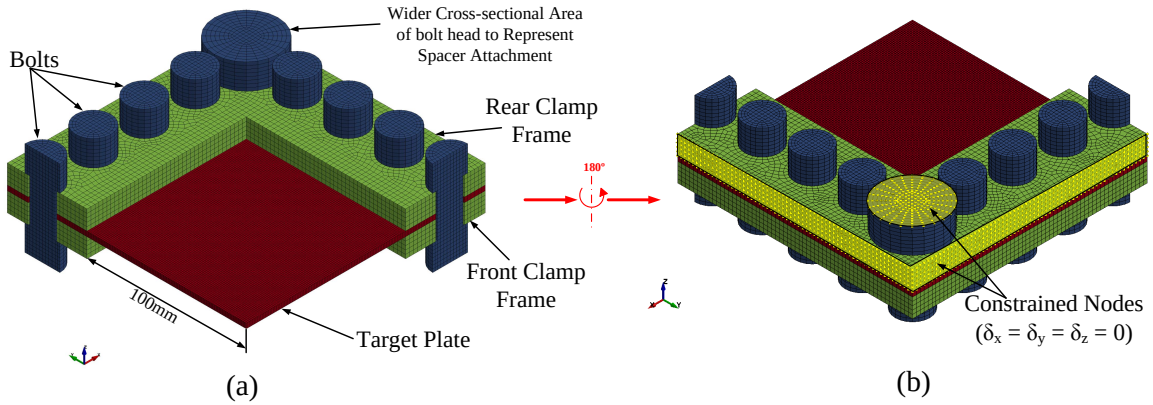

Figure 7.7: Quarter Symmetric Model of a Test Rig for Unconfined Blast Load Simulations with Applied Boundary Conditions

The spacer attachment which held the test rig to the ballistic pendulum was represented by increasing the diameter of the head of the corner bolt of the rear side of the test rig to match the actual dimension of the spacer.

In order to simulate the attachment of the test rig to the ballistic pendulum the nodes highlighted in Figure 7.7b were constrained from translation in all directions ($\delta_x = \delta_y = \delta_z = 0$). The constrained nodes on the rear clamp frame represented the welded connection between the rear clamp frame and the steel shroud.

7.4.1.3 Fully Vented Blast Load Test Rig

The fully vented test rig was identical to the unconfined blast test rig model with the exception of the front clamp frame. The confinement tube in the fully vented simulations was directly substituted for the front clamp frame in the unconfined test rig. The material properties of the confinement tube were identical to the front clamp frame of the unconfined test rig model. The boundary conditions imposed on the fully vented test rig were identical to the boundary conditions in the unconfined test rig model. The fully vented test rig model and the relevant dimensions are depicted in Figure 7.8.

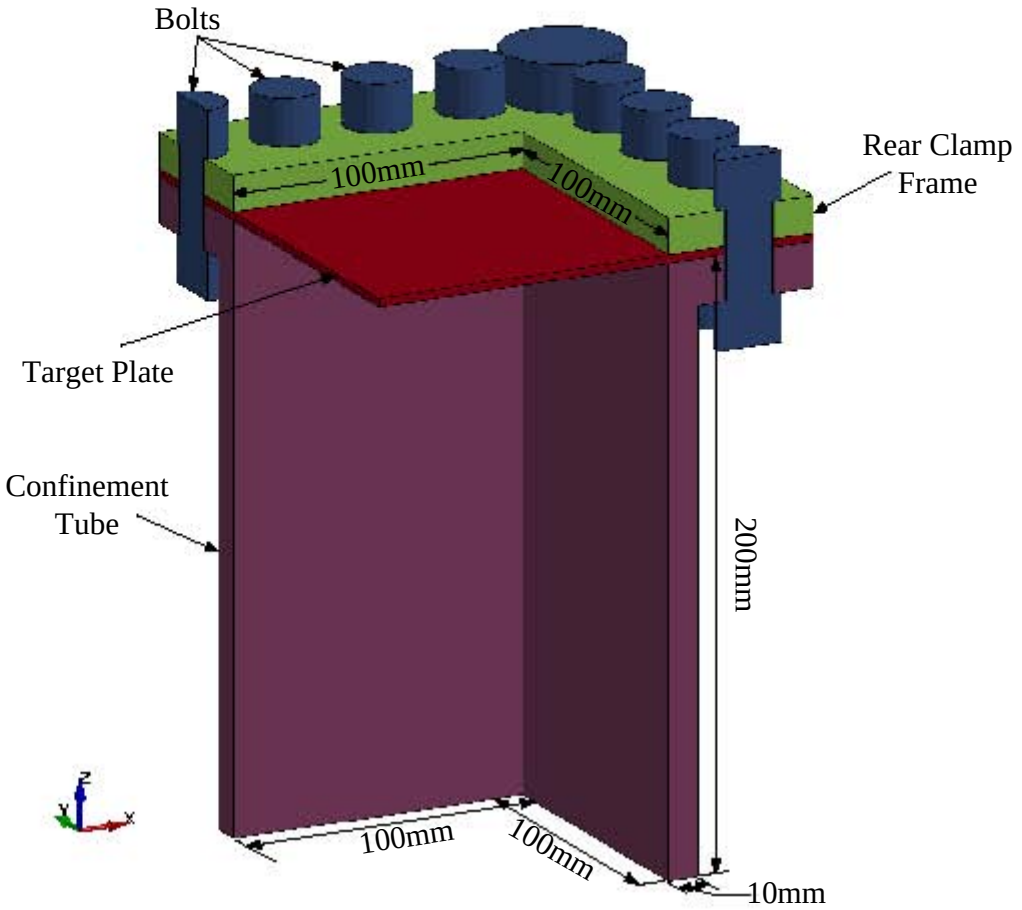

Figure 7.8: Quarter Symmetric Model of a Test Rig for Fully Vented Blast Load Simulations

7.4.1.4 Fully Confined Blast Test Rig Model

Figures 7.9a and 7.9b are illustrations of the fully confined test rig model. The test rig in the fully confined blast was, as in the experimental setup, comprised of a target plate, container, top and bottom clamp frame and bolts.

The clamp frames and bolts were constructed with 8 node brick elements and were constructed to represent the actual dimensions of the experimental clamp frames. The flanged connection between the clamp frames, container and target plate is illustrated in Figure 7.9c .

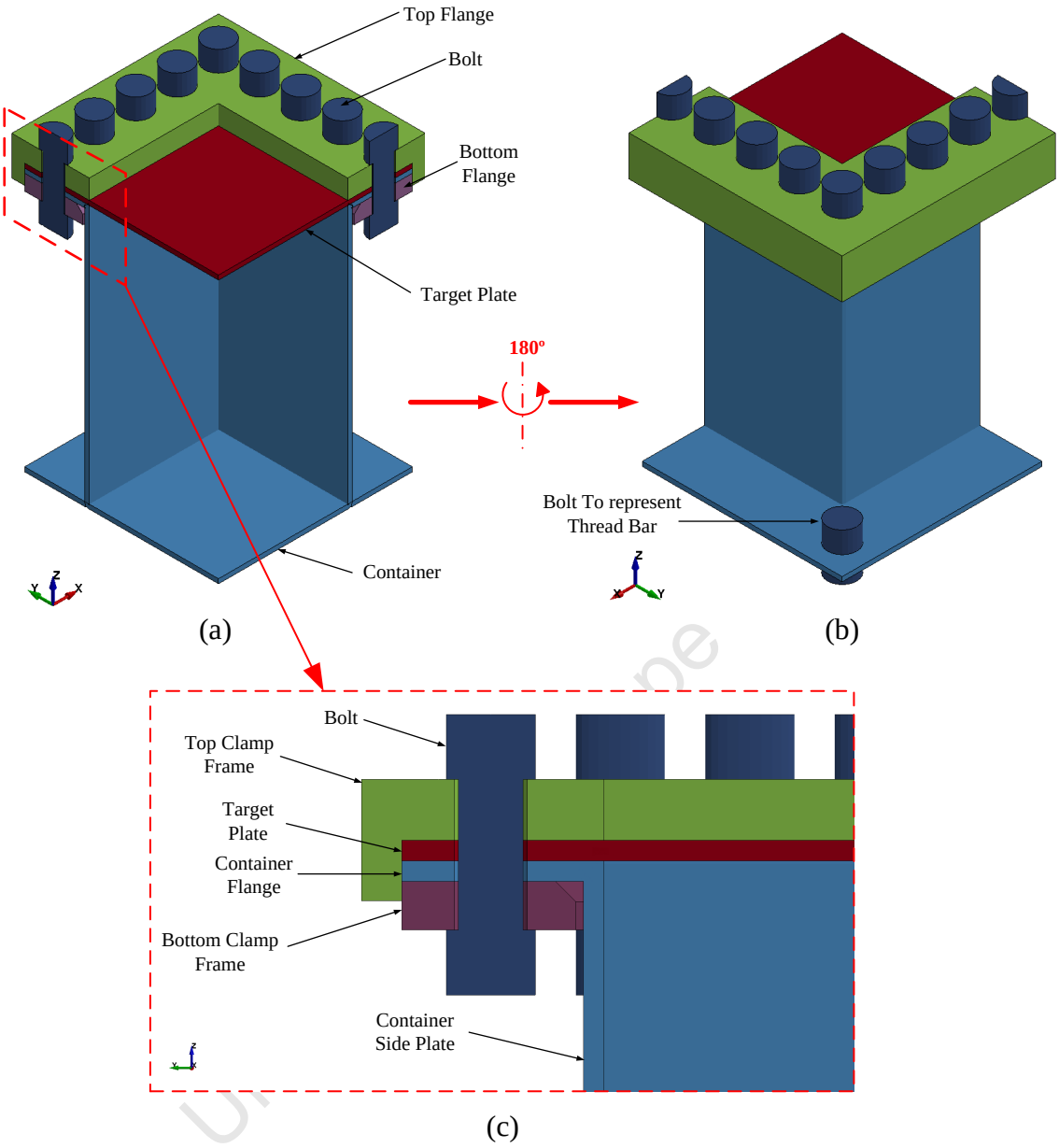

Figure 7.9: Quarter Symmetric Model of a Test Rig for Fully Confined Blast Load Simulations

To improve the computational efficiency of the simulations the container was divided into three regions characterised by the element size namely an uniform $1 \times 1mm$ mesh, an uniform $2 \times 1mm$ and a non-uniform meshed region. The regions of the three different meshes are illustrated in Figure 7.10. The region highlighted in red in Figure 7.10 represent the surfaces exposed to the blast load (side and bottom target plates) and the welded joints and were meshed with uniform $1 \times 1mm$ elements. The region

highlighted in green in Figure 7.10 was meshed with uniform $2 \times 1mm$ elements. The blue regions in Figure 7.10 were meshed with a non-uniform mesh where the maximum element edge length was prescribed to $2.5mm$.

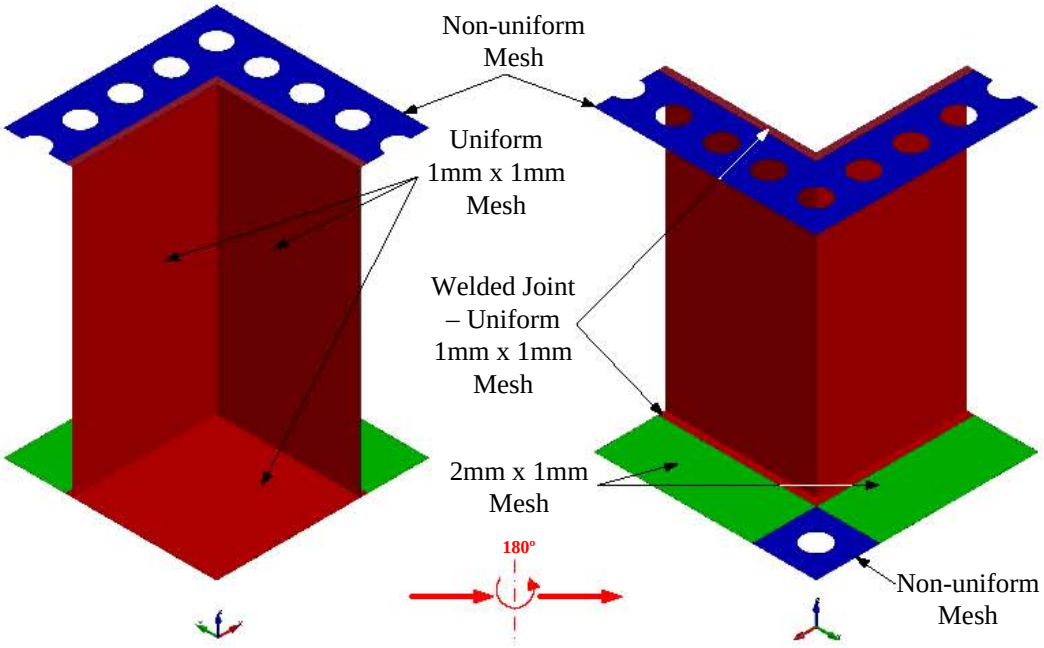

Figure 7.10: Three Different Meshed Regions of the Fully Confined Containers

In order to simulate the boundary conditions imposed by the threaded bar, which connected the test rig to the heavy base (see Section 3.4.2 - Figure 3.16), the heads of the corner bolt in the clamped region (highlighted in yellow in Figure 7.11a) and the heads of the bolt located in the bolt hole of the bottom target plate flange (highlighted in orange in Figure 7.11a) were constrained from translation movements ($\delta_x = \delta_y = \delta_z = 0$). .

The welds which joined the target plates and flange of the container were represented by prescribing rotation constraints ($R_x = R_y = R_z = 0$) on the nodes in the welded areas of the containers. The welds were taken to be 45° fillet welds where the length of the weld (l_{weld}), which accounted for shell thickness, was given by,

$$l_{weld} = 1\frac{1}{2} \times t_{plate}$$

where t_{plate} is the thickness of the target plate.

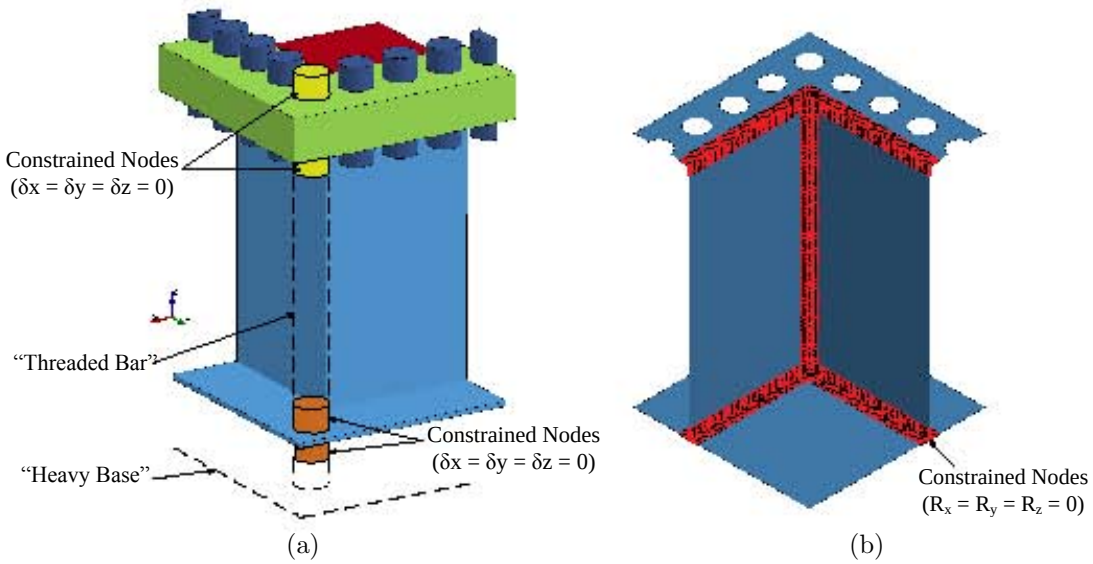

Figure 7.11: (a) Boundary Conditions Prescribed to Corner Bolts to Represent Threaded Bar and (b) Constrained Nodes Representing the Welded Joints

Figure 7.11b highlights the constrained nodes representing the weld. Representing the welds as a rotation constraint did not provided structural strength to the connection, it did however provide the stiffness of the welded joint.

7.4.1.5 Contact

The contact between two surfaces (e.g. the target plate and clamp frames and the clamp frames and bolt heads) was controlled with LS-DYNA's surface to surface penalty based contact algorithm and the contact between nodes and a surface (e.g. the bolts and the edge of the bolt holes in the target plate) were controlled with the node to surface contact penalty based algorithm.

The friction between the surface was defined by Coulomb friction with a constant coefficient of friction. A parametric study of the frictional coefficient (μ) between the surfaces was carried out in all three blast models at different charge masses (30g and 60g). Frictional coefficients of 0.8 [173], 0.34 [174] and 0.17 were investigated. The frictional coefficient of 0.17 resulted in a solution that correlated with the experimental results and was defined as the coefficient of friction for all the blast models.

7.4.2 Air and Explosive Models

The air models of the three models were meshed with uniform cubic elements with element lengths of $2mm$ (i.e. element dimensions $2\times2\times2mm$). The elements were single point integration ALE multi-material elements with Flanagan-Belytschko viscous form hourglass control with exact volume integration. The dimensions of the air domains for the unconfined, fully vented and fully confined blast simulations are illustrated in Figures 7.12a, 7.12b and 7.12c respectively.

The outer surfaces of the air domains (i.e. not the symmetry planes) were set as transmission boundaries allowing air and explosive products to flow out of the simulation when reaching the boundary and play no further role in the simulation. The air domains were created to extended $50mm$ past the target plates which allowed the plate to deform into this region whilst maintaining the interaction between the gas pressures and the target plate after the target plate had began deforming. The location of the explosive charges is also depicted in Figure 7.12. The explosive charge was located away from the transmission boundary to eliminate any effects the boundary conditions will have on the simulation.

Figures 7.13a and 7.13b illustrate the relative locations of the test rigs models in the air domains for the fully vented and fully confined blast models. In both cases the air domains were constructed such that the air domains did not extend the entire length of the clamp frames. Substantial computational savings were achieved with the 'reduced' air domain with little effect on the final midpoint deflection of the target plate ($< 1\%$ difference in finite element simulations). Creating the boundaries of the air domain within the clamp frames region allowed fluid materials (air and explosive) that was forced between the clamp frame and target plate to flow out of the simulation and play no further role in the simulation.

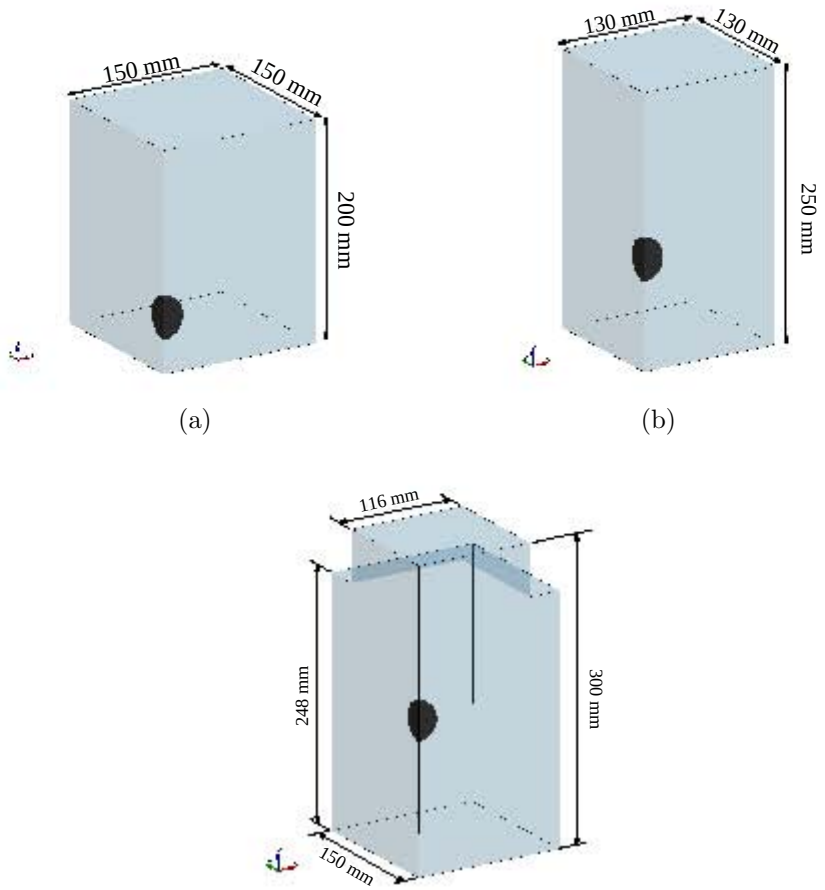

(a) (b)

(c)

Figure 7.12: Air and Explosive Domains for: (a) 50g Unconfined Blast Simulation, (b) 50g Fully Vented Blast Simulation, and (c) 50g Fully Confined Blast Simulation.

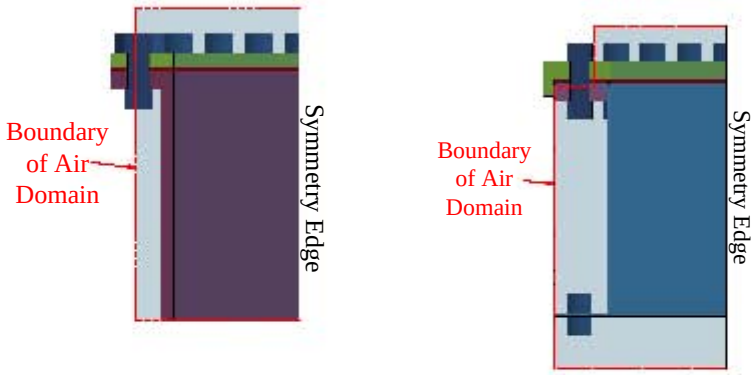

(a) (b)

Figure 7.13: Cut Out in Air Domain of: (a) Fully Vented Air Domain, and (b) Fully Confined Air Domain.

7.4.3 Final Blast Models

Figures 7.14a, 7.14b and 7.14c illustrated the complete blast models for the unconfined, fully vented and fully confined blast models respectively. The full blast models for the respective blast loads were generated by combining the test rig models and the air and explosive models. A fluid-structure interface (FSI) [145] was defined between the test rig model and the air explosive models which coupled the test rig and air and explosive model. The coupling between the models was controlled by a penalty based coupling algorithm.

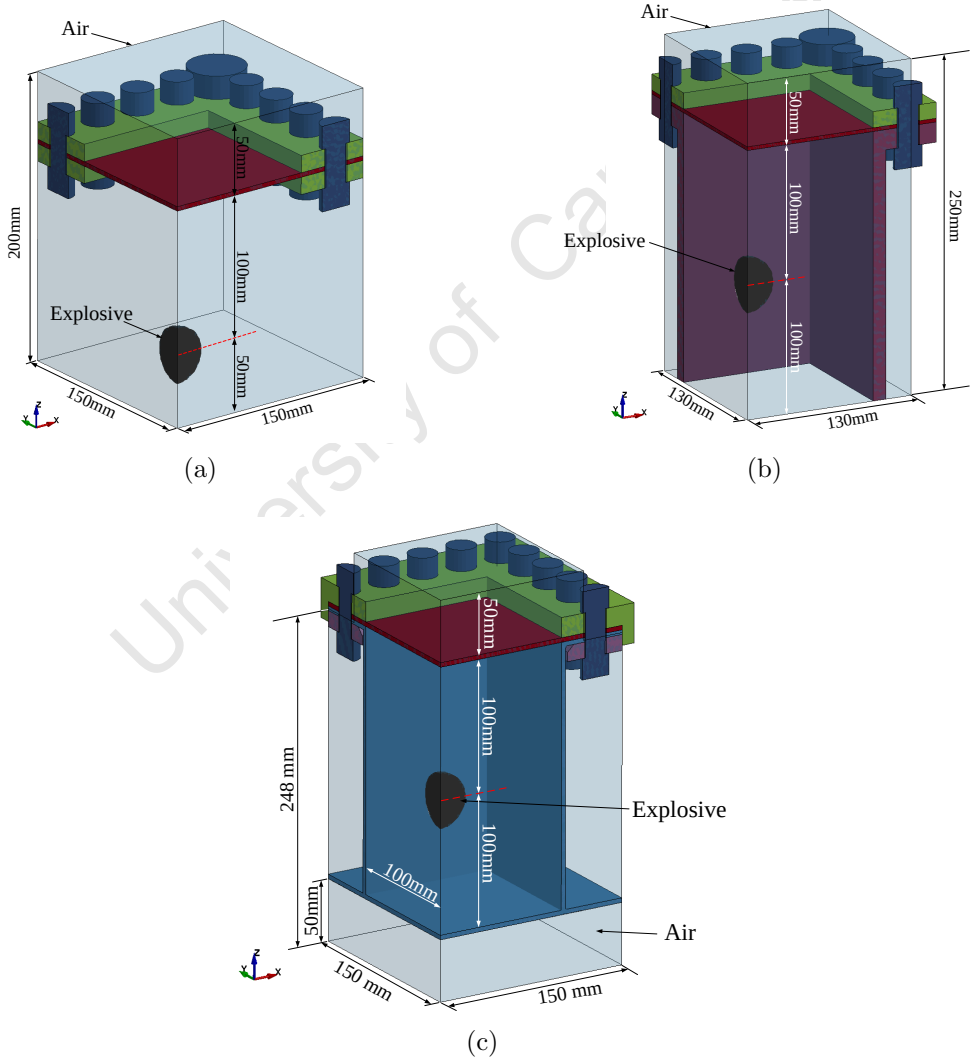

Figure 7.14: Fully Assembled Blast Models : (a) Unconfined Blast Model, (b) Fully Vented Blast Load Model, and (c) Fully Confined Blast Model.

7.5 Loading Phases

The simulations were broken up into three loading phases namely,

1. Bolt Pre-Load
2. Blast Loading
3. Unloading

Figure 7.15 illustrates of the temporal discretisation of the loading phases. The blast loading termination time (a) was set to $1ms$ for the unconfined and fully vented simulations and $1.5ms$ for the fully confined simulations.

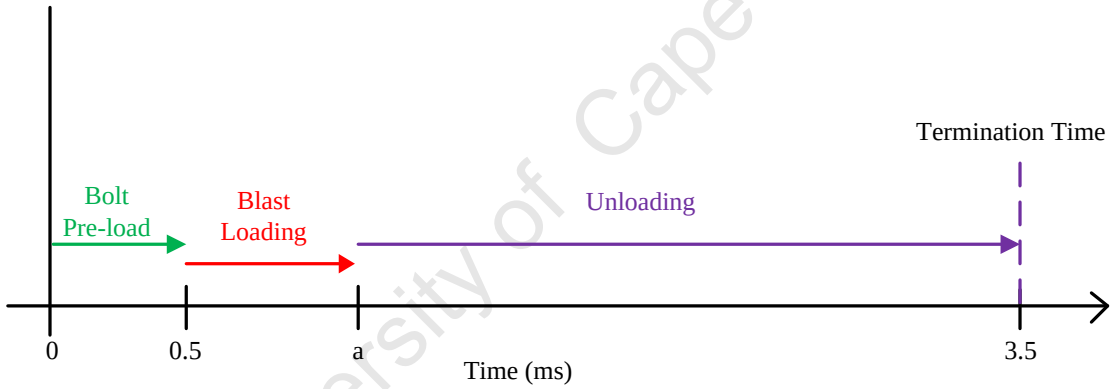

Figure 7.15: Time Line of Loading Phases

In the first loading phase a pre-load was applied to the bolts in the test rig models. A tensile stress was prescribed to the bolts to represent the pre-load force. The magnitude of the tensile stress was determined through several experiments where an instrumented bolt was tightened and the stress levels in the bolts recorded. The average tensile stress recorded in the bolts over thirteen experiments was $240MPa$. The tensile stress in the bolts was prescribed as a triangular loading pulse where the maximum stress was reached at $0.5ms$ and was maintained for the remainder of the simulation. Figure 7.16 illustrates the stress contours of an unconfined test rig model after the application of the pre-load.

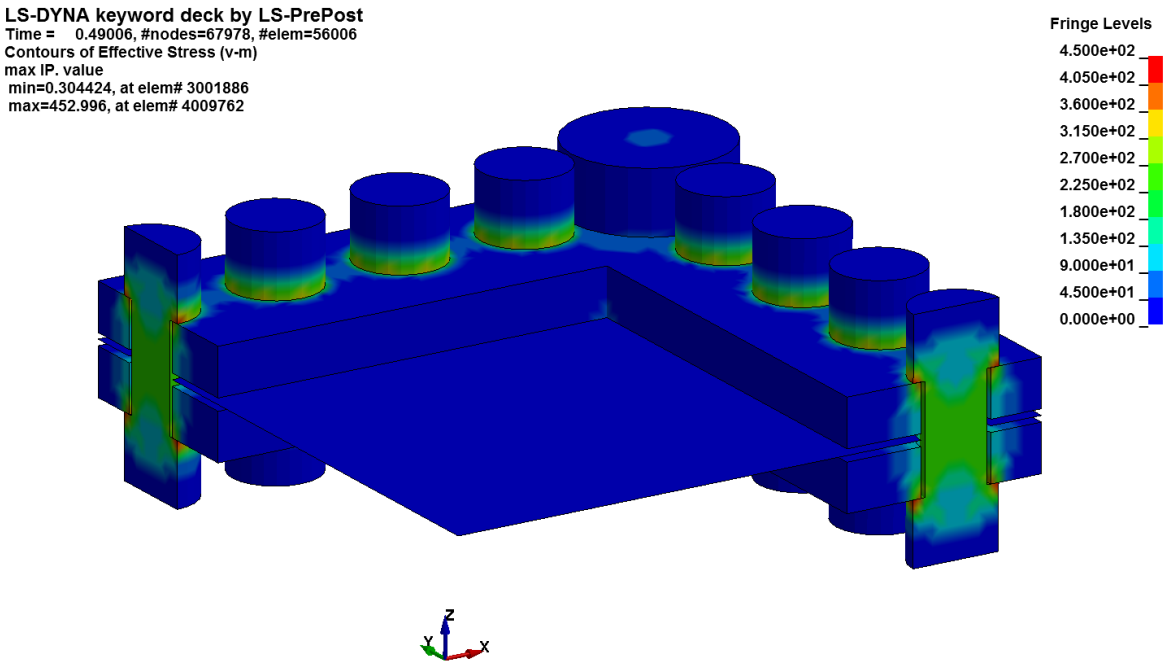

Figure 7.16: Stress Contours of a Unconfined Test Rig Model after Application of Bolt Pre-load (Fringe Levels in MPa)

In the second loading phase, blast loading, the complete blast model (test rig, air and explosive models) was initialised. The bolt pre-load results were mapped on to the test rig model thereafter the explosive was detonated. The resulting blast wave was interacted with the test rig model and caused deformation. In the case of the unconfined and fully vented simulations the termination time of the second loading phase was set to $1ms$. At this point the pressure acting on the target plate has cleared and no additional loading was present meaning the plate was deforming under the applied impulse. In the fully confined blast load simulations the effects of the shock loads ($< 1ms$) and the gas pressure loads, causing deformation, were captured by extending the termination time to $1.5ms$.

In the third loading phase, unloading, the test rig model with the nodal and elemental histories from the blast loading phase was initialised and allowed to run to the final termination time of $3.5ms$. As no further loading from the explosion was present the air and explosive models were not included. The target plate was allowed to deform under the previously applied loads until the final midpoint deflection was reached.

8 Numerical Blast Model Results

The results obtained from the numerical simulations of the three degrees of confinement are presented in this chapter. The results include the final midpoint deflection, target plate deformation profiles, transient midpoint deflection and pressure histories.

8.1 Comparison of Experimental and Numerical Deflections

8.1.1 Comparison of Midpoint Deflections

The numerical models were validated using final midpoint deflections and deformed target plate profiles. Three masses of explosive (30, 50 and 60g) were modelled in each degree of confinement and plate thickness series to obtain numerical results that span the masses of explosive tested experimentally. Table 8.1 lists the midpoint deflections obtained from the numerical models and the corresponding experimental results. The simulations were run for 3ms and the vertical displacement of the midpoint node recorded. The final midpoint deflection from the numerical simulations was taken as the average vertical displacement of the midpoint node from 1 to 3ms. The 5mm thick target plates subjected to unconfined blast loads were not simulated as the experimental results were discarded, as discussed in Section 4.1. The final midpoint deflections obtained from the simulation are plotted against the experimental midpoint deflections in Figure 8.1. The two dashed lines in Figure 8.1 are offset by 3mm from the ideal

45° line in both the positive and negative direction. The dashed lines represent the confidence interval (±1 target plate thickness) of the thinnest target plate tested. In general the results show a good correlation between the numerical and experimental results for all the degrees of confinement.

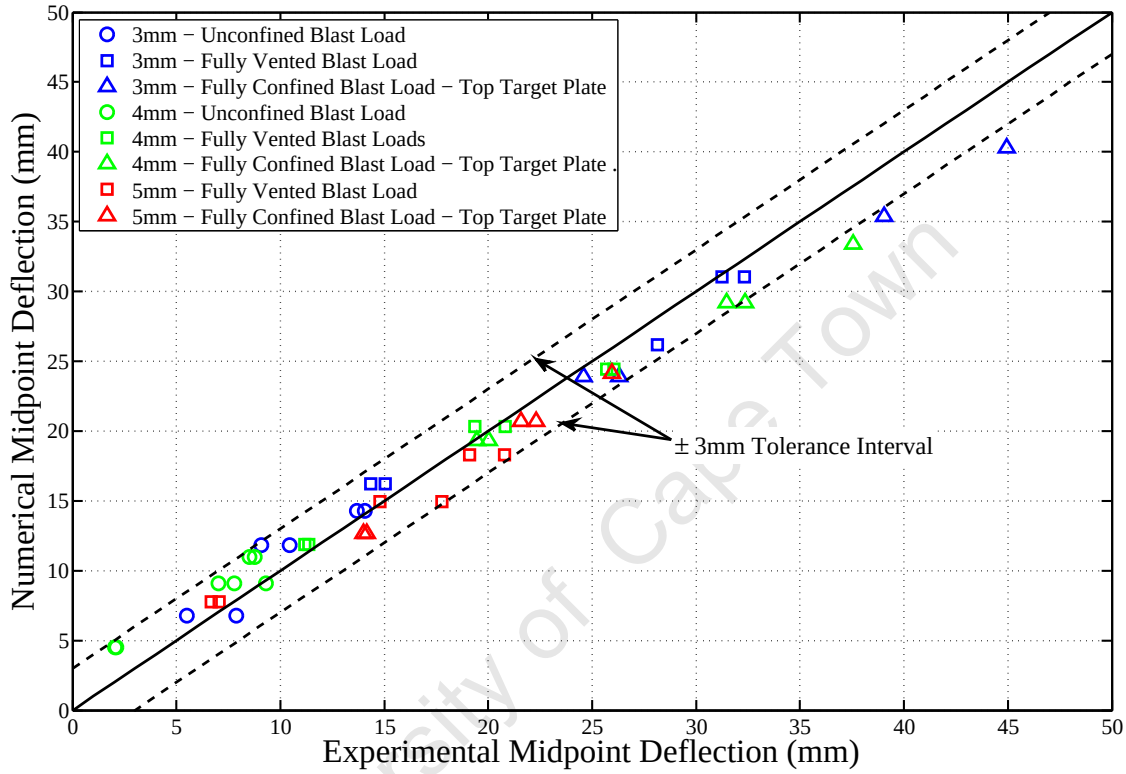

Figure 8.1: Numerical Versus Experiential Midpoint Deflections

The comparison between the numerical and experimental midpoint deflection versus the mass of explosive for the 3, 4 and 5mm thick target plates are illustrated in Figures 8.2, 8.3 and 8.4. The results show the numerical results are contained within the respective ±1 target plate thickness confidence envelope.

Table 8.1: Comparison between Experimental and Numerical Midpoint Deflections. Note: Unconfined Blast Loaded 5mm Thick Target Plate Not Simulated

Mass of Explosive (g)	$\delta_{exp\,trend}$ (mm)	δ_{num} (mm)	Difference $\delta_{exp\,trend} - \delta_{num}$ (mm)
3mm Thick Target Plate			
Unconfined			
30	6.14	6.76	-0.62
50	10.93	11.83	-0.91
60	13.32	14.29	-0.97
Fully Vented			
30	15.28	16.21	-0.94
50	26.47	26.20	0.27
60	32.07	31.03	1.04
Fully Confined			
30	25.00	23.89	1.11
50	37.72	35.41	2.31
60	44.07	40.28	3.79
4mm Thick Target Plate			
Unconfined			
30	2.85	4.50	-1.65
50	7.15	9.07	-1.92
60	9.30	10.99	-1.70
Fully Vented			
30	11.08	11.85	-0.77
50	20.54	20.35	0.19
60	25.27	24.42	0.85
Fully Confined			
30	19.28	19.32	-0.04
50	30.99	29.18	1.80
60	36.84	33.42	3.42
5mm Thick Target Plate			
Fully Vented			
30	7.68	7.76	-0.08
50	16.16	14.94	1.22
60	20.40	18.29	2.12
Fully Confined			
30	13.86	12.66	1.20
50	22.01	20.72	1.29
60	26.09	24.16	1.93

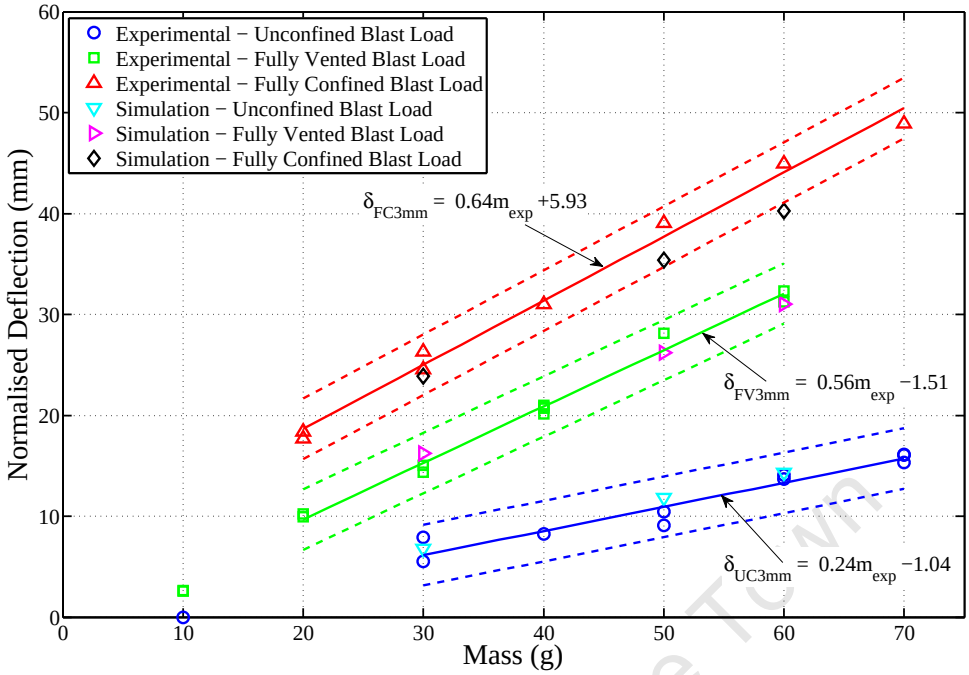

Figure 8.2: Normalised Midpoint Deflection Comparison for Experimental and Numerical Results 3*mm* Target Plate

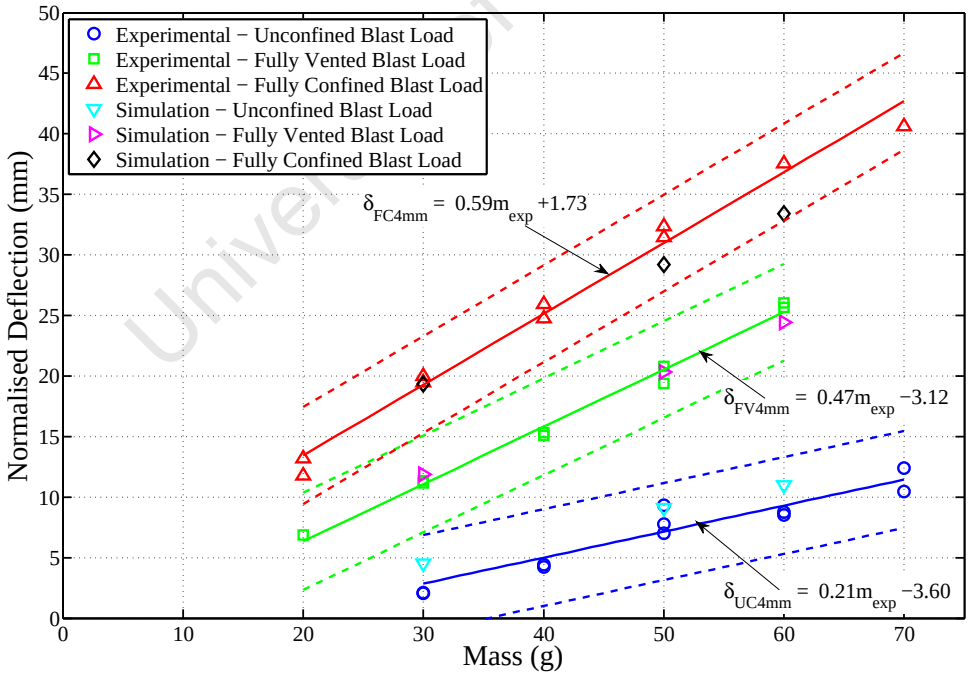

Figure 8.3: Normalised Midpoint Deflection Comparison for Experimental and Numerical Results 4*mm* Target Plate

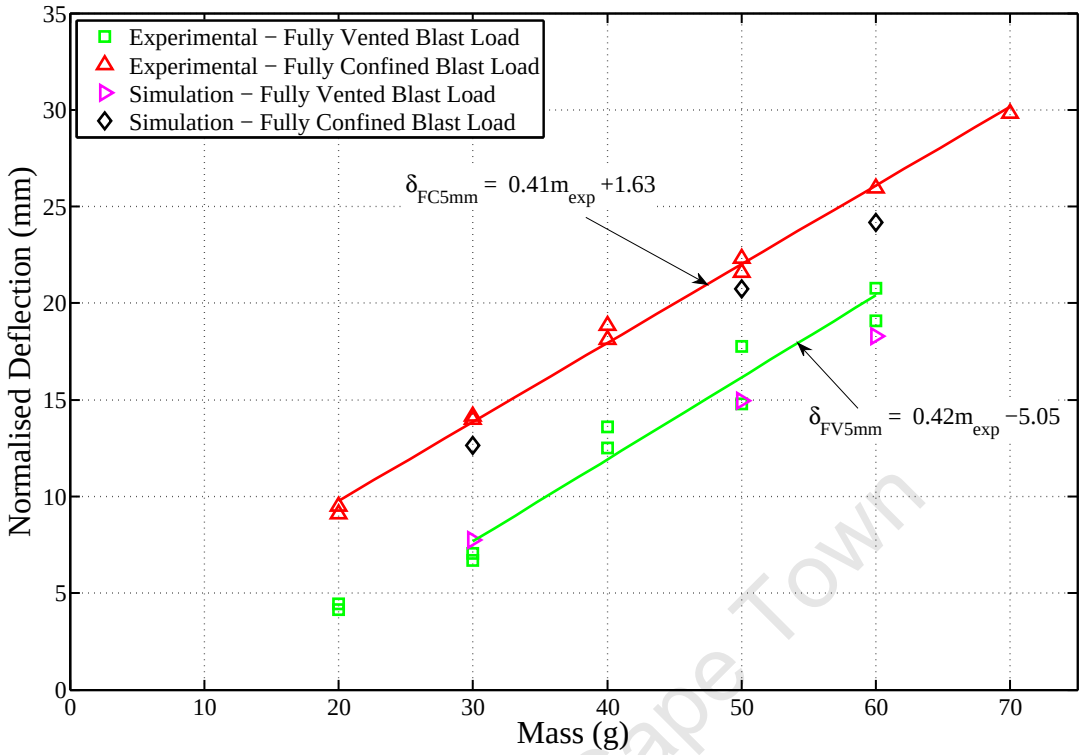

Figure 8.4: Normalised Midpoint Deflection Comparison for Experimental and Numerical Results 5*mm* Target Plate

8.1.2 Comparison of Cross Sectional Deformation Profiles

For a better evaluation of the numerical model the cross section deformation profiles obtained from the numerical models were compared to the experimental deformation profiles. The numerical deformation profiles of the 3, 4 and 5*mm* thick target plates have been superimposed onto the corresponding experimental deformation profiles in Figures 8.5, 8.6 and 8.7 respectively. The results show that there is good correlation between the numerically and experimentally obtained deformation profiles. A comparison of the deformation profiles show:

1. The deformation profiles obtained from the numerical models are always symmetrical which is not always the case with the experimental deformation profiles.

2. The numerical deformation profiles exhibit the same trend as the experimental deformation profiles

3. Generally the numerical deformation profile is within one plate thickness of the experimental deformation profile.

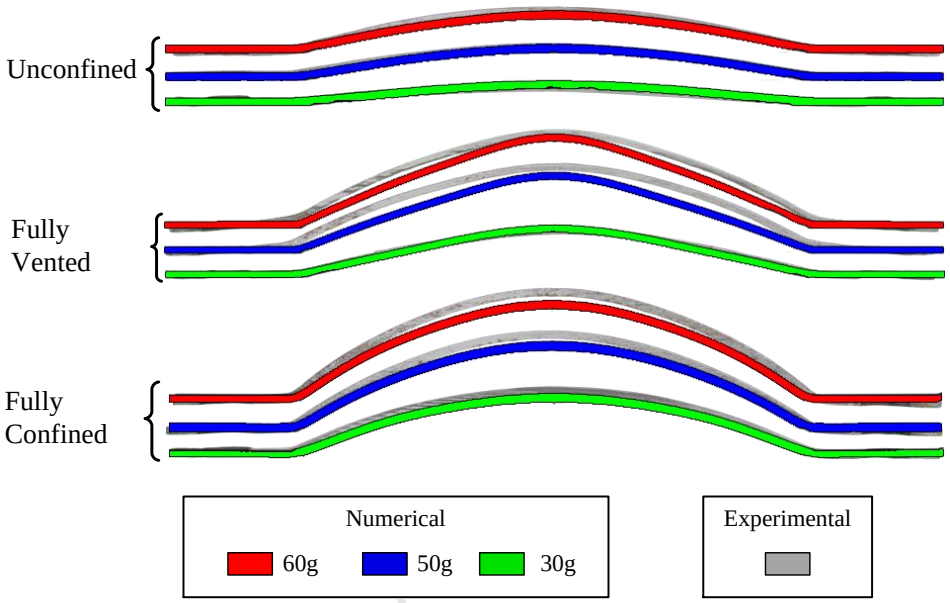

Figure 8.5: Numerical and Experimental Cross Section Deformation Profiles of 3*mm* Thick Target Plates

Note: In some cases in Figures 8.5, 8.6 and 8.7 the experimental and numerical deformed plate profiles overlap therefore the experimental profile cannot be seen.

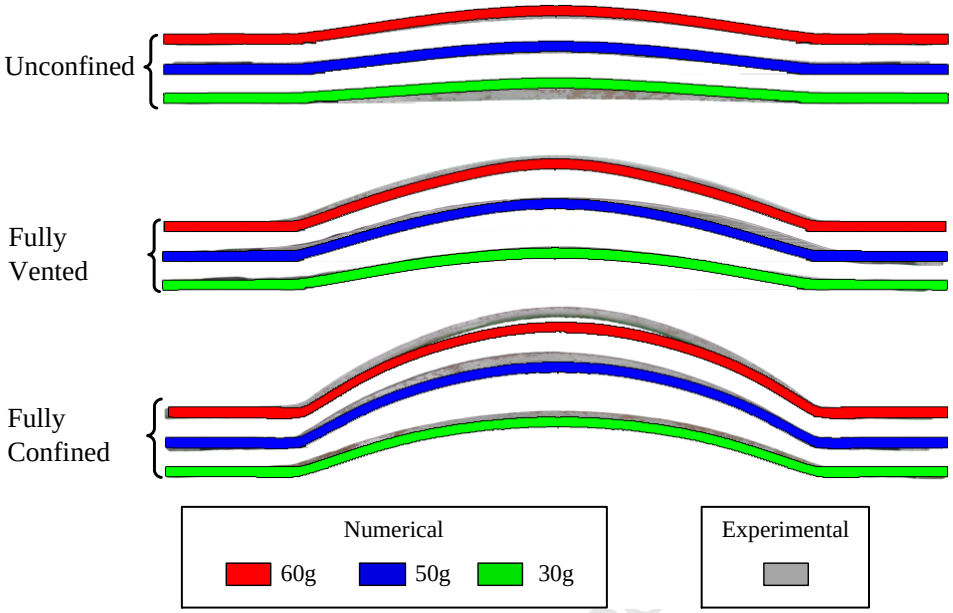

Figure 8.6: Numerical and Experimental Cross Section Deformation Profiles of $4mm$ Thick Target Plates

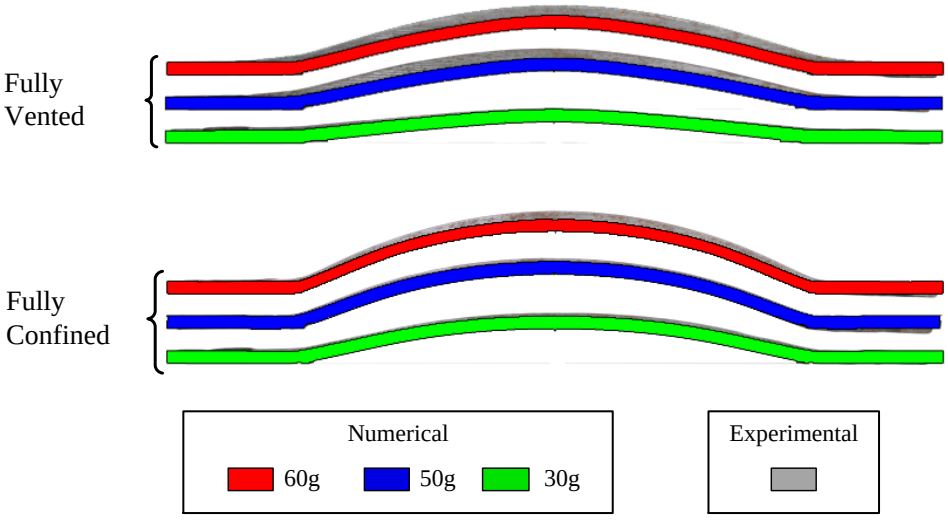

Figure 8.7: Numerical and Experimental Cross Section Deformation Profiles of $5mm$ Thick Target Plates

8.1.3 Parametric Study

A series of numerical models with target plate thicknesses of 2 and 6mm were carried out for the three degrees of confinement to test the validity of the equations presented in Section 5.3.3 (Equations 5.28, 5.29 and 5.30). The numerical models implemented in this study were identical to the numerical models used to simulate the experiments in the different degrees of confinement. The material models prescribed for the 2 and 6mm thick material were the material models for 3 and 5mm thick target plate material respectively.

The predicted and numerical final midpoint deflections are listed in Table 8.2. The numerical midpoint deflections are plotted against the predicted midpoint deflections in Figure 8.8. The confidence envelope around the ideal 45° line is $\pm 3mm$ representing the confidence envelope of the thinnest target plate tested experimentally. The results shows that the predicted midpoint deflections correlate well with the numerical midpoint deflections.

The region enclosed by a midpoint deflection-thickness ratio of 12.5 represents mode I failure (large inelastic deformation) as observed by Olson *et al.* [53] and Nurick and Martin [38]. Data outside the region, illustrated in Figure 8.8, would suggest Mode II failure (tearing at the boundary) of the target plate would occur. Both the numerical simulations and the equations used to calculate the midpoint deflection do not incorporate failure and hence the accuracy of the results beyond a midpoint deflection-thickness ratio of 12.5 may not be representative of actuality.

Table 8.2: Predicted and Numerical Midpoint Deflections for 2 and 6mm Thick Target Plates

Mass of Explosive (g)	$\delta_{predicted}$ (mm)	δ_{num} (mm)	Difference (mm) ($\delta_{predicted} - \delta_{num}$)	$\frac{\delta_{predicted}}{h}$	$\frac{\delta_{num}}{h}$	
2mm Thick Target Plate						
Unconfined						
10	3.79	3.12	0.67	1.89	1.56	
30	9.29	11.98	-2.69	4.64	5.99	
60	17.53	21.86	-4.33	8.76	10.93	
Fully Vented						
10	11.99	9.82	2.17	5.99	4.91	
30	28.74	25.27	3.47	14.37	12.64	*
Fully Confined						
10	14.32	13.59	0.73	7.16	6.80	
30	34.27	31.60	2.67	17.13	15.80	*
6mm Thick Target Plate						
Unconfined						
100	8.95	9.71	-0.77	1.49	1.62	
200	17.57	20.91	-3.34	2.93	3.48	
300	26.19	29.90	-3.71	4.36	4.98	
Fully Vented						
30	9.02	5.43	3.59	1.50	0.90	
60	16.90	13.77	3.13	2.82	2.30	
100	27.41	23.58	3.83	4.57	3.93	
200	53.69	43.11	10.58	8.95	7.18	
300	79.97	56.52	23.45	13.33	9.42	
Fully Confined						
30	10.75	9.98	0.77	1.79	1.66	
60	20.14	20.00	0.14	3.36	3.33	
100	32.65	30.28	2.37	5.44	5.05	

* Mode II failure

Note: Explosive data missing due to simulations not incorporating failure in the target plates for the 2mm thick target plate simulations and similarly the clamp frames in the 6mm thick target plate simulations.

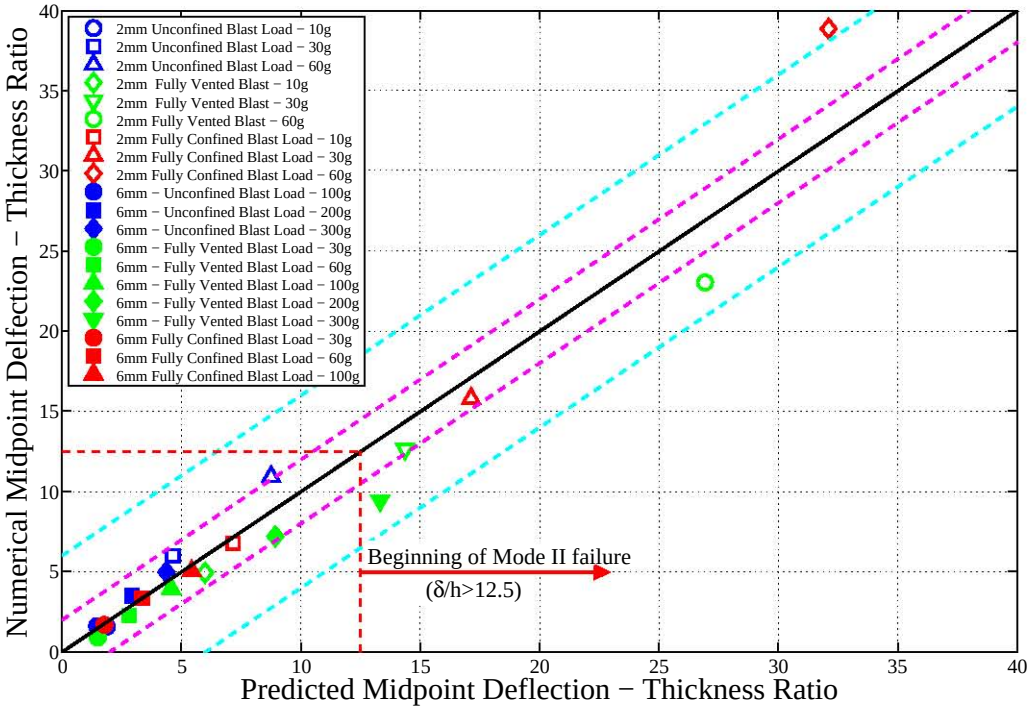

Figure 8.8: Predicted Versus Numerical Midpoint Deflection - Thickness Ratio Graph for 2 and 6mm Thick Target Plates

8.2 Comparison of Experimental and Numerical Transient Deflections

8.2.1 Comparison of Transient Midpoint Deflections

In Figures 8.9, 8.10 and 8.11 a selection of the transient midpoint deflection histories obtained from the numerical simulations and the experiments are compared. Generally the numerical simulations show similar trends as observed in the experiments. However the initial peak midpoint deflection in the numerical simulations underpredicts and the elastic response of the midpoint node in the simulations settles in a shorter period of time, i.e. the amplitude and period of the oscillations in the numerical simulations are smaller than experimental values.

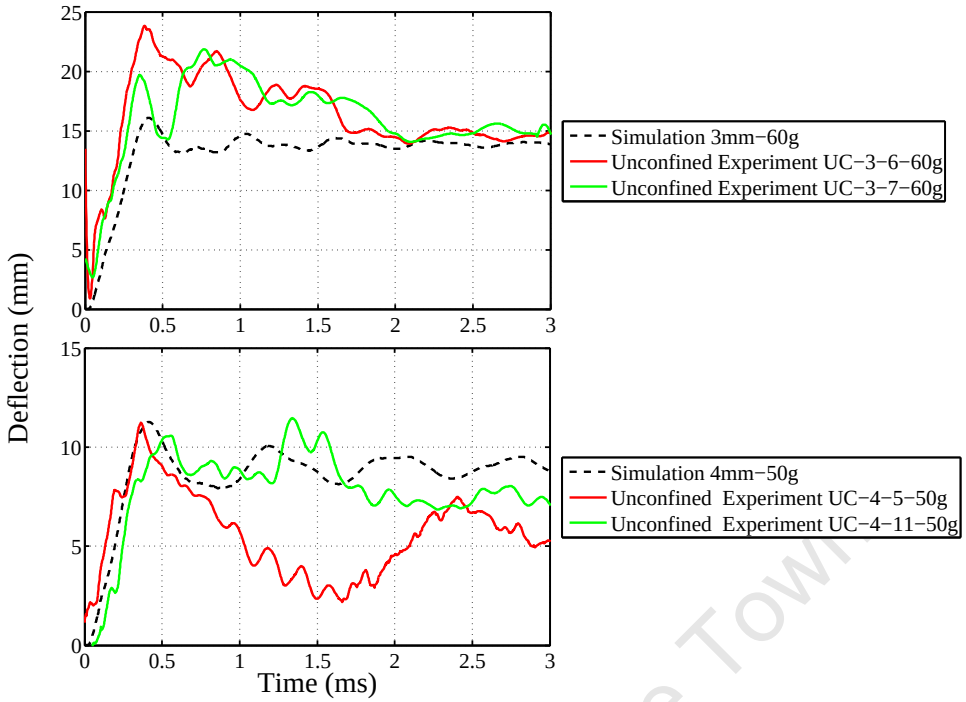

Figure 8.9: Comparison of Unconfined Numerical and Experimental Transient Midpoint Deflections

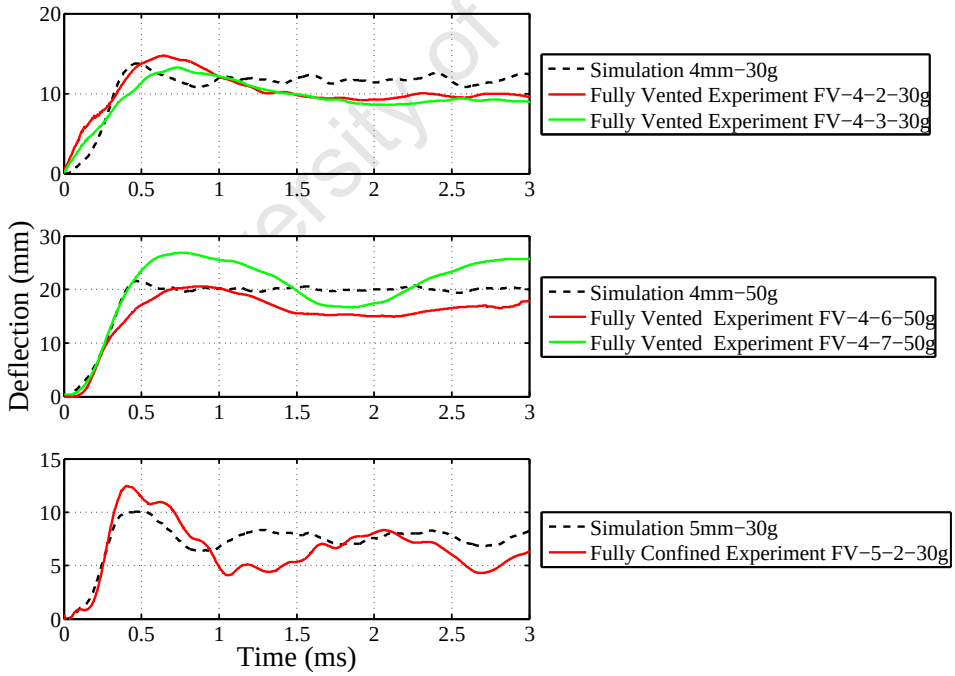

Figure 8.10: Comparison of Fully Vented Numerical and Experimental Transient Midpoint Deflections

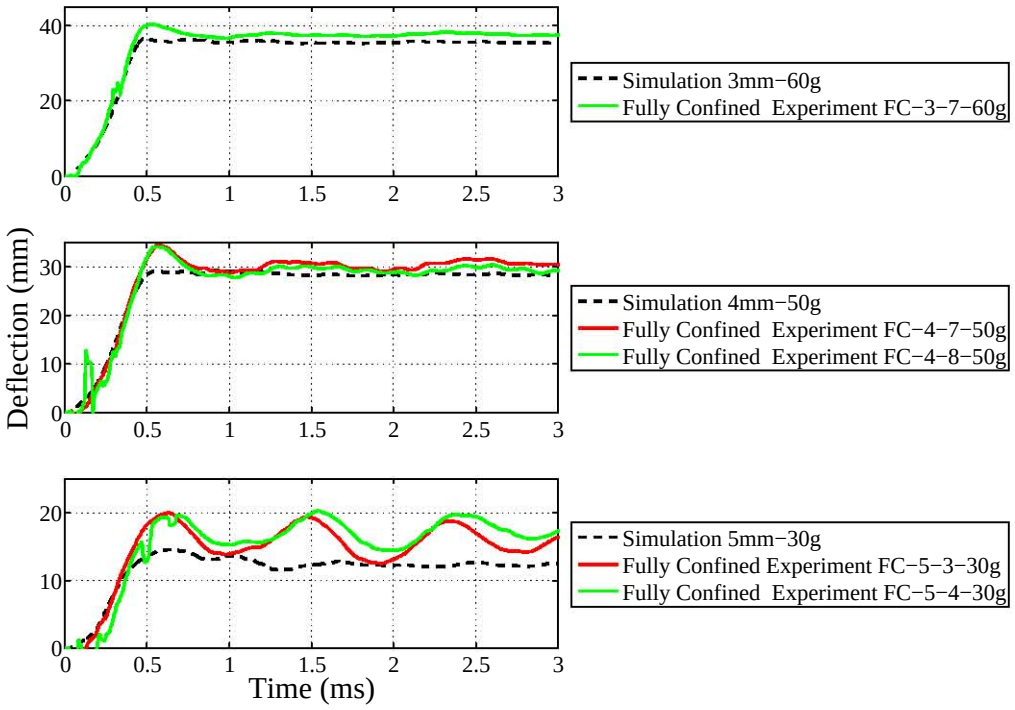

Figure 8.11: Comparison of Fully Confined Numerical and Experimental Transient Midpoint Deflections

8.2.2 Transient Target Plate Deformations

The transient target plate deformations of a $3mm$ thick target plate subjected to a $60g$ explosive mass, detonated in an unconfined, a fully vented and a fully confined blast simulation are illustrated in Figures 8.12, 8.13 and 8.14 respectively. The target plates in the unconfined, fully vented and fully confined blast models accelerate to the peak deflections in the first 410, 460 and $500\mu s$ respectively. Thereafter the target plate oscillates around the final midpoint deflection.

The progression of the deformation profile was similar to the profile observed by Zhu [59] and Olson *et al.* [53] for square plates subjected to an unconfined blast. The central region of the plate was observed to remain 'flat' during the initial deformation process, as the deformation increased the central flat region decreased in size and eventually deforms to the characteristic global domed shape with the maximum deflection occurring at the centre of the target plate.

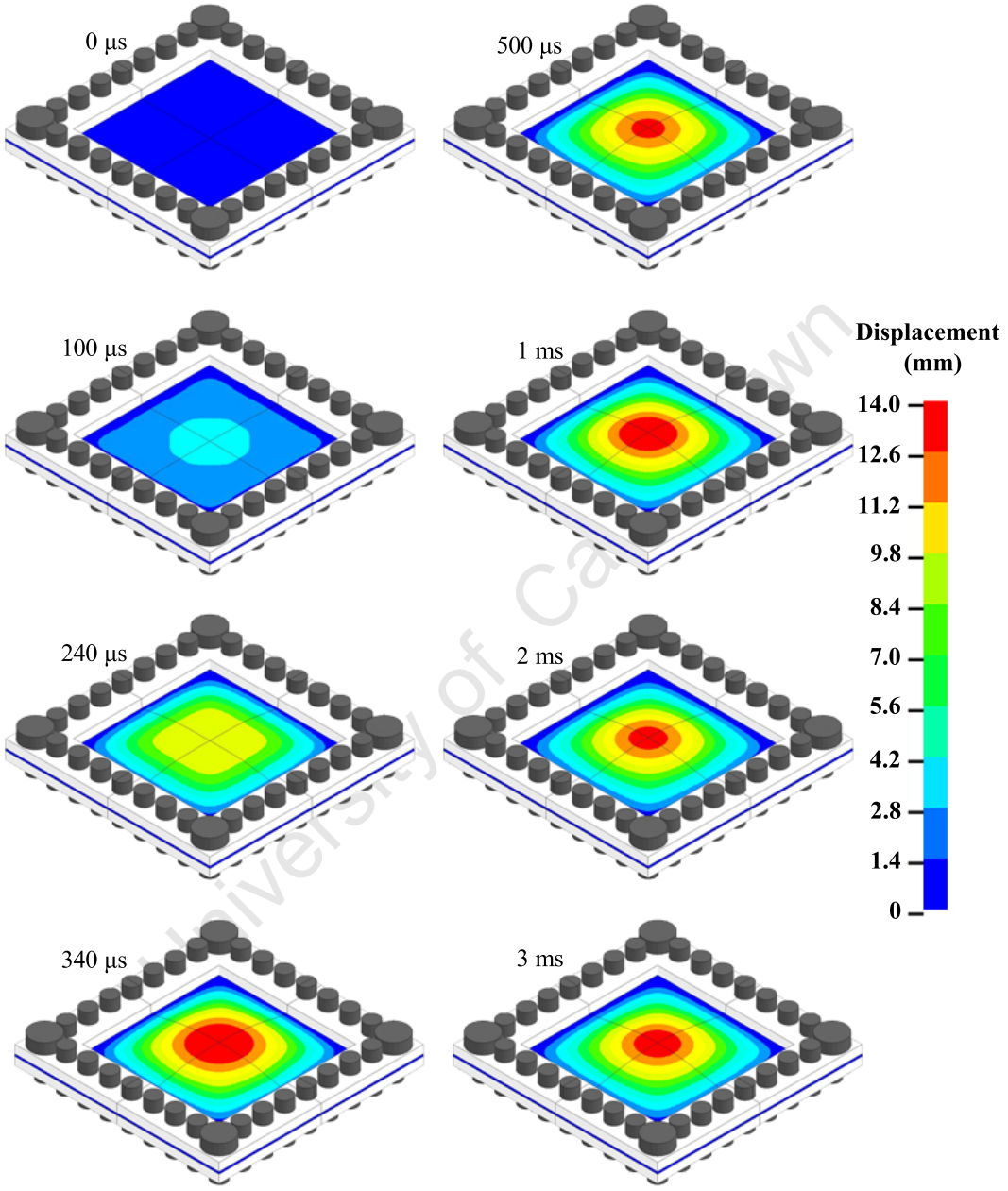

Figure 8.12: Predicted Transient Response of a $3mm$ Thick Target Plate Subjected to a $60g$ Unconfined Blast

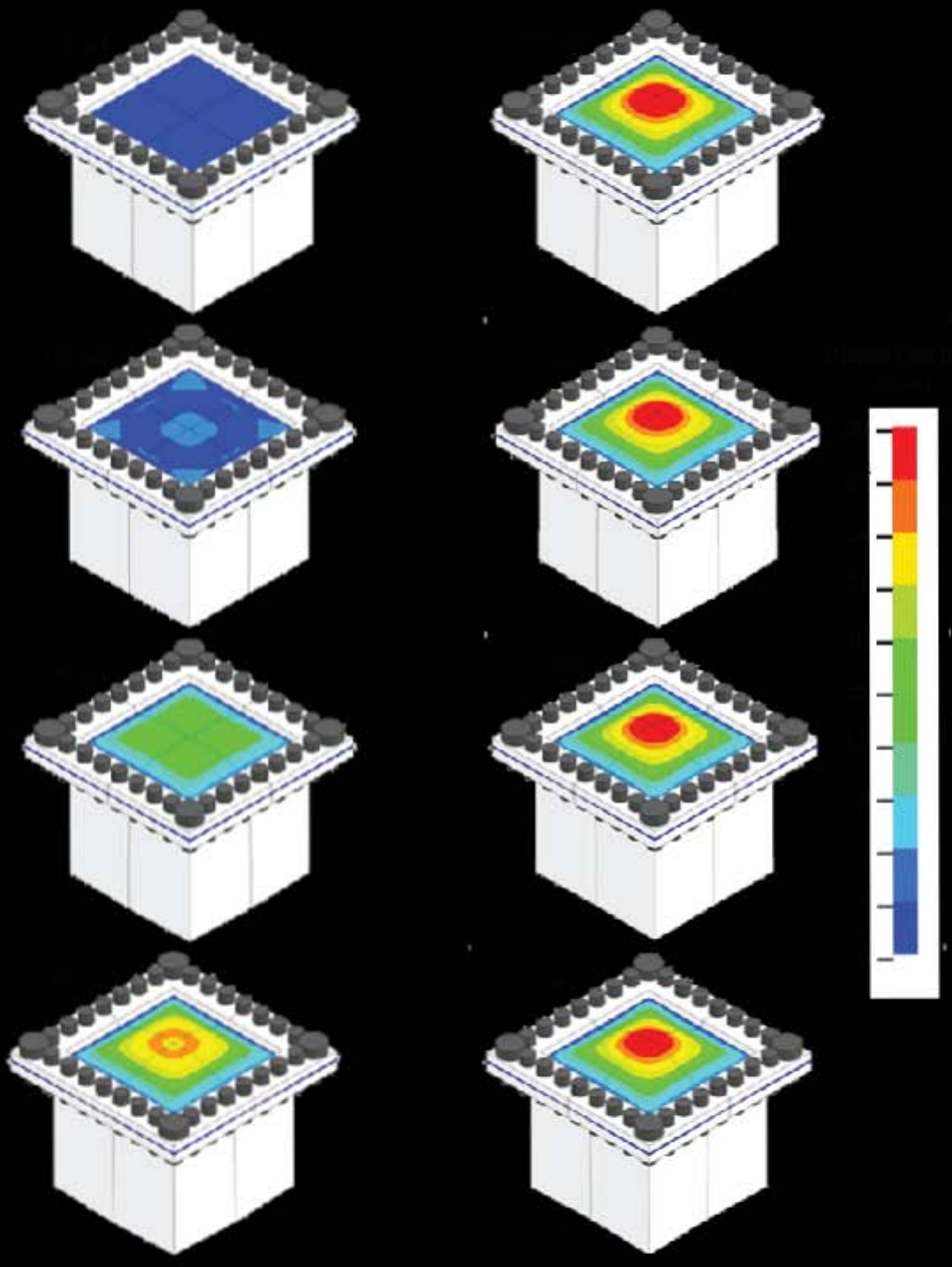

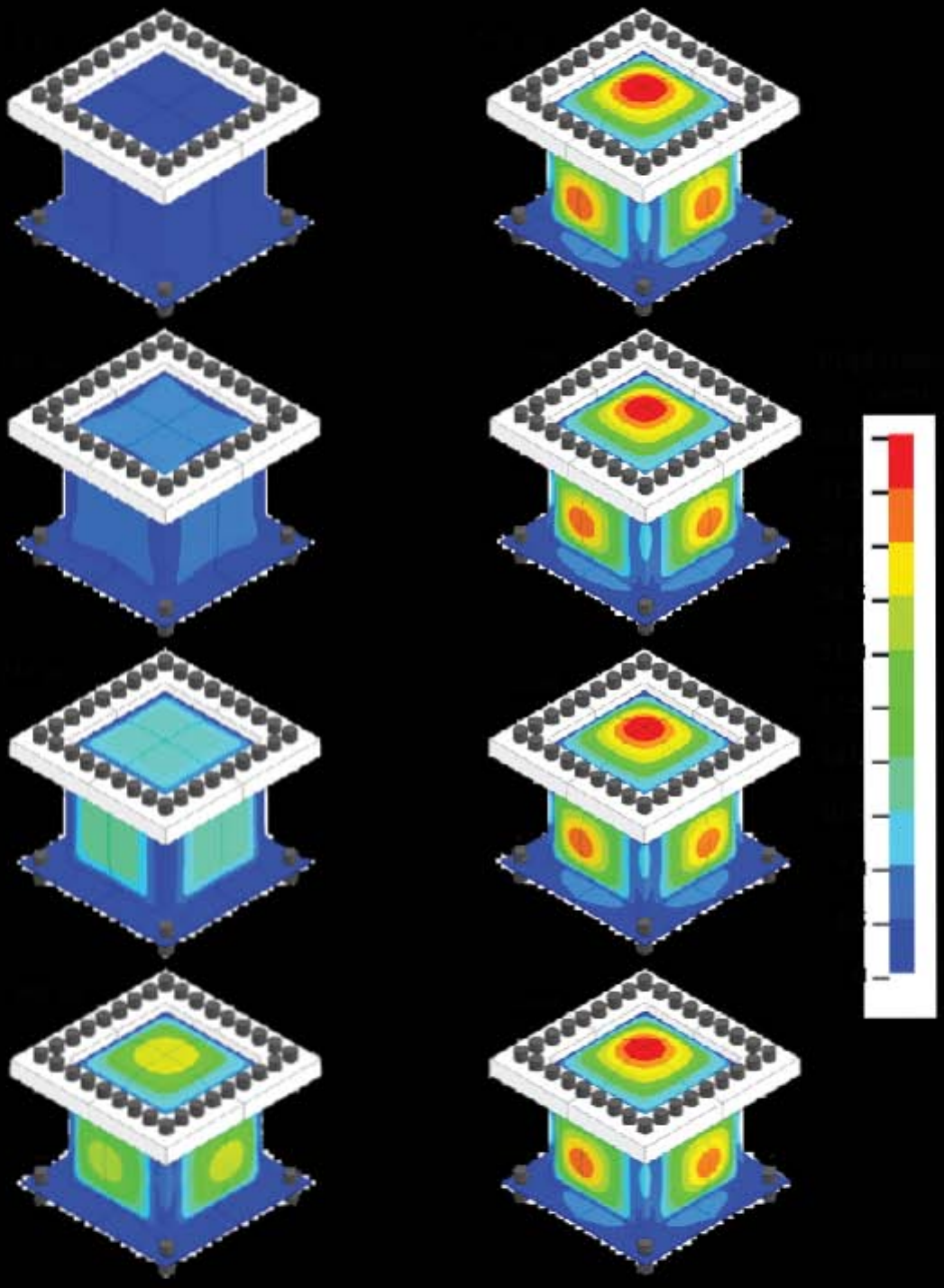

8.3 Comparison of Numerical Pressure Histories

It should be noted that no pressure histories were recorded in the experiments. A qualitative analysis of the numerical results is carried out to compare the pressure histories and distributions for the three different degrees of confinement.

The pressure histories at the midpoint of the target plate (midpoint pressure), the midpoint of the boundary (edge pressure) and the corner of the boundary (vertex pressure) were investigated. Figure 8.15 illustrates the locations of interest when comparing the pressure histories between the degrees of confinement. The three locations were chosen because:

1. **Midpoint Pressure**

   The pressure at the midpoint of the target plate was of interest as it was the first location where the blast wave interacted with the target plate. It was also the location where no blast wave focusing occurs.

2. **Edge Pressure**

   The edge pressure was of interest as it was the location where the reflected blast wave from two adjacent surfaces merged and were reflected back to the point of detonation.

3. **Vertex Pressure**

   The pressures at the vertex were assessed to analyse the effects of the reflected blast wave from three adjacent surfaces merging.

The pressure histories at the three locations afforded a comparison in which an indication to the level of blast wave focusing at the boundaries of the target plate can be determined and the effects on the target plate deformation.

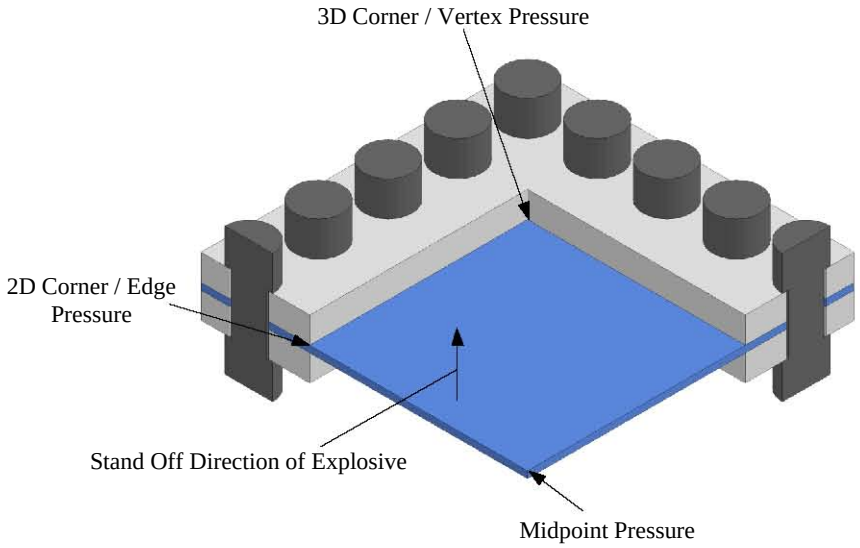

Figure 8.15: Location of Pressure Gauges in Numerical Model

The progression of the blast wave generated from the detonation of a $60g$ explosive in an unconfined, fully vented and fully confined blast simulation are illustrated in Figures 8.16, 8.17 and 8.18 respectively. As expected, the blast wave expands radially outwards from the point of detonation until impacting the central area of the target plate at $\pm 20\mu s$, irrespective of the degree of confinement. After the initial impact the pressure contour plots deviate from one another, however similarities between the pressure contours were observed. The arrival times of the blast wave at the edge ($\pm 35\mu s$) and the vertex ($\pm 40\mu s$)were similar through the degrees of confinement.

In the unconfined blast simulation there was a local pressure build-up between the clamp frame and the target plate at both the edge and vertex locations at $\pm 35\mu s$ and $\pm 40\mu s$ respectively (See Figure 8.16). The pressure build up was reflected back towards the midpoint of the target plate, however the magnitude of the reflected wave diminished rapidly as the blast wave dissipated into the atmosphere. The blast wave continues to expand and flowed out of the simulation when reaching the boundary of the air domain.

In Figure 8.16 the pressures from $\pm 150\mu s$ have returned to ambient conditions, hence pressure contours are absent. The beginning stages of the deformation process was observed from $\pm 150\mu s$ in Figure 8.16.

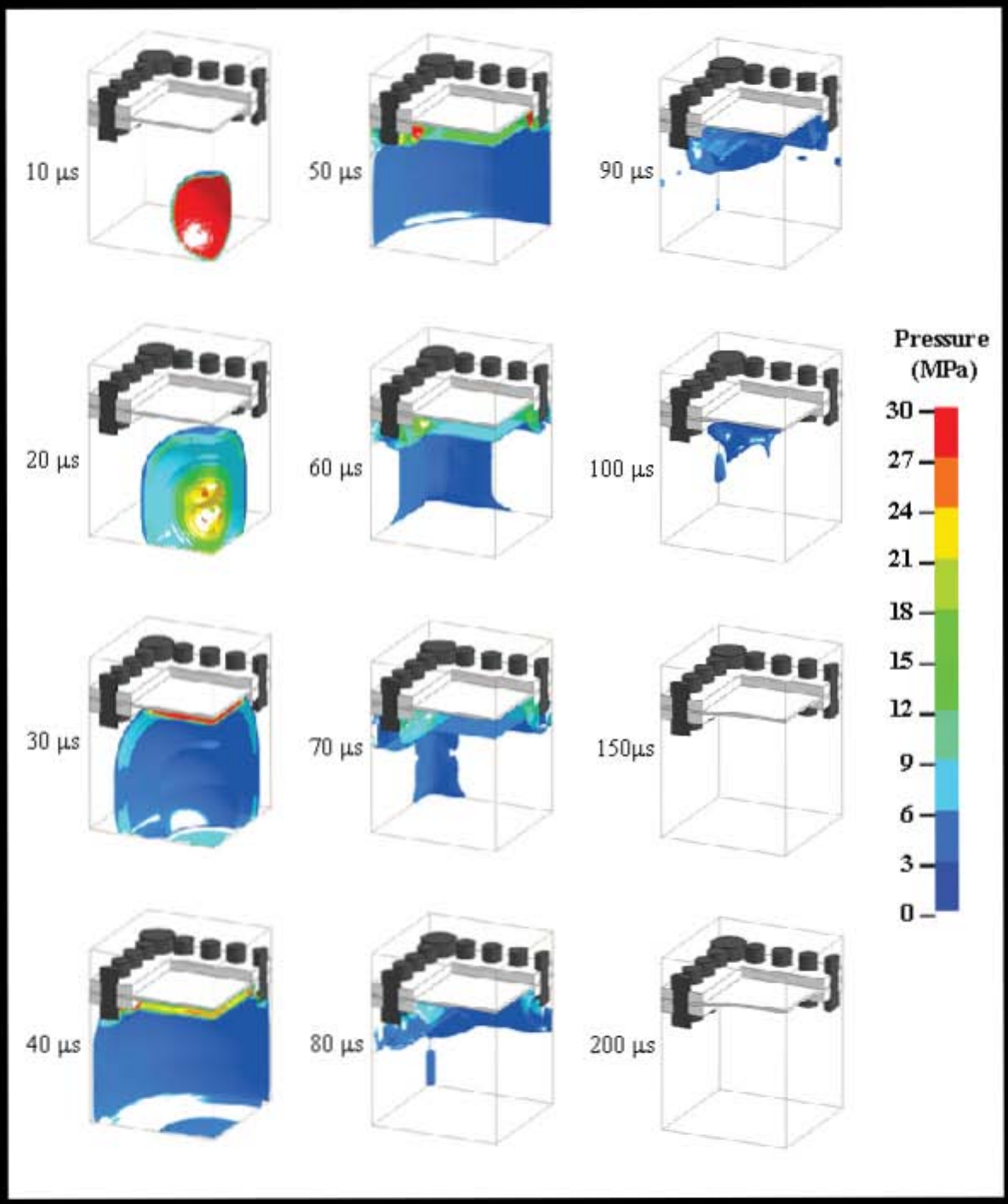
10 μs
50 μs
90 μs
20 μs
60 μs
100 μs
30 μs
70 μs
150μs
40 μs
80 μs
200 μs
Pressure (MPa)
30
27
24
21
18
15
12
9
6
3
0

The fully vented pressure contours plotted in Figure 8.17 show that the initial impact of the blast wave on the target plate as $\pm 25\mu s$ coincides with the impact of the blast wave on the walls of the confinement tube. The radial expansion of the blast wave continues and reaches the edge location at approximately $35\mu s$. There is a significant pressure build up at the edge, unlike an unconfined blast, as the pressures can not vent to the atmosphere. The reflection of the local pressure build-up back towards the detonation point can be seen from 50 to $100\mu s$. The magnitude of the reflected edge pressure is initially high but decays as time and a distance travelled increases. The blast wave reaches the vertex at approximately $40\mu s$, though not illustrated. There is a large pressure build-up similar to the edge pressure but larger in magnitude. The reflected pressure from the edge and vertex return to the point of detonation where a complex interaction between the reflected wave occurs, as shown in Figure 8.17 from 100 to $150\mu s$. Thereafter the blast wave and the reflections are vented to the atmosphere.

From Figure 8.17 the initial stage of the target plate deformation was observed from $\pm 100\mu s$. The first movement of the target plate occurs whilst the target plate was still being loaded from the blast wave.

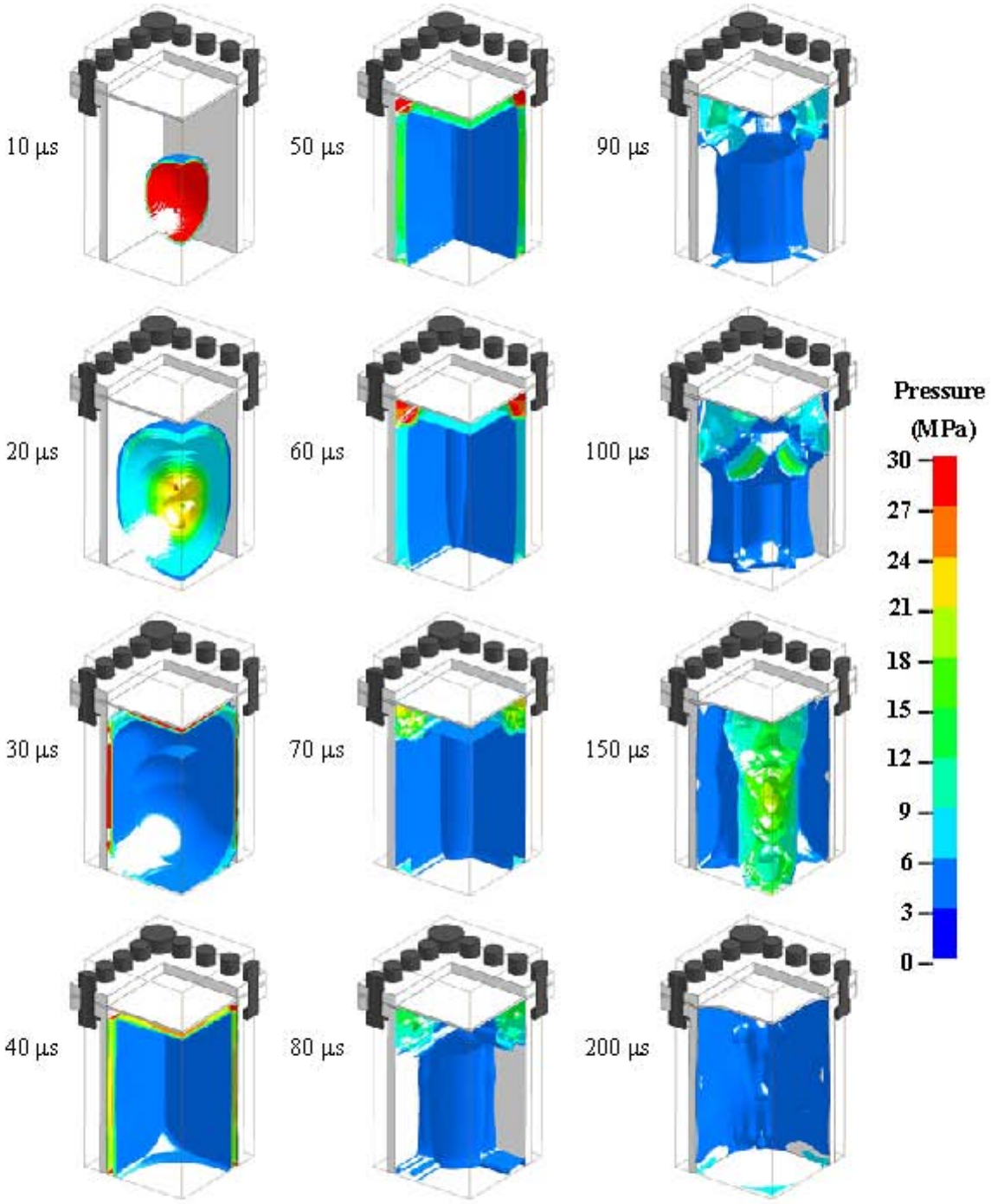

Figure 8.17: Transient Pressure Contours for 60g Fully Vented Blast

The pressure contours observed in the fully confined blast simulations are illustrated in Figure 8.18. Subsequent to the initial expansion the blast wave impacts all the walls of the container at $\pm 25\mu s$. The pressure contour plot at $30\mu s$ shows regions of high pressure at the central area of the target plates due to the interaction of the blast wave on the target plate. Further expansion of the blast wave results in pressure build-up at the edges at $\pm 35\mu s$ and at the vertices at $\pm 40\mu s$. The merging of the two reflected waves at the edge location created a region of high pressure which was reflected back to the centre of the container, i.e. the detonation point. At approximately $100\mu s$ the reflected blast wave from the edges and vertices were observed returning to the centre of the container.

At $150\mu s$ the reflected blast waves begin interacting and create a high pressure region at the centre of the container. The interactions of the multiple reflected waves at the centre of the container results in a complex series of 're-reflected' blast waves which return to the walls of the container, as shown from 200 to $500\mu s$ in Figure 8.18. The 're-reflected' blast waves propagate back to the container walls and induce a series of extra, lesser magnitude, loads on the walls of the container. The complex blast wave interactions were observed to continue after a significant portion of the target plate deformation had occurred, see Figure 8.18 at $500\mu s$.

The deformation of the target plates in the fully confined blast simulations are visible from $100\mu s$ in Figure 8.18.

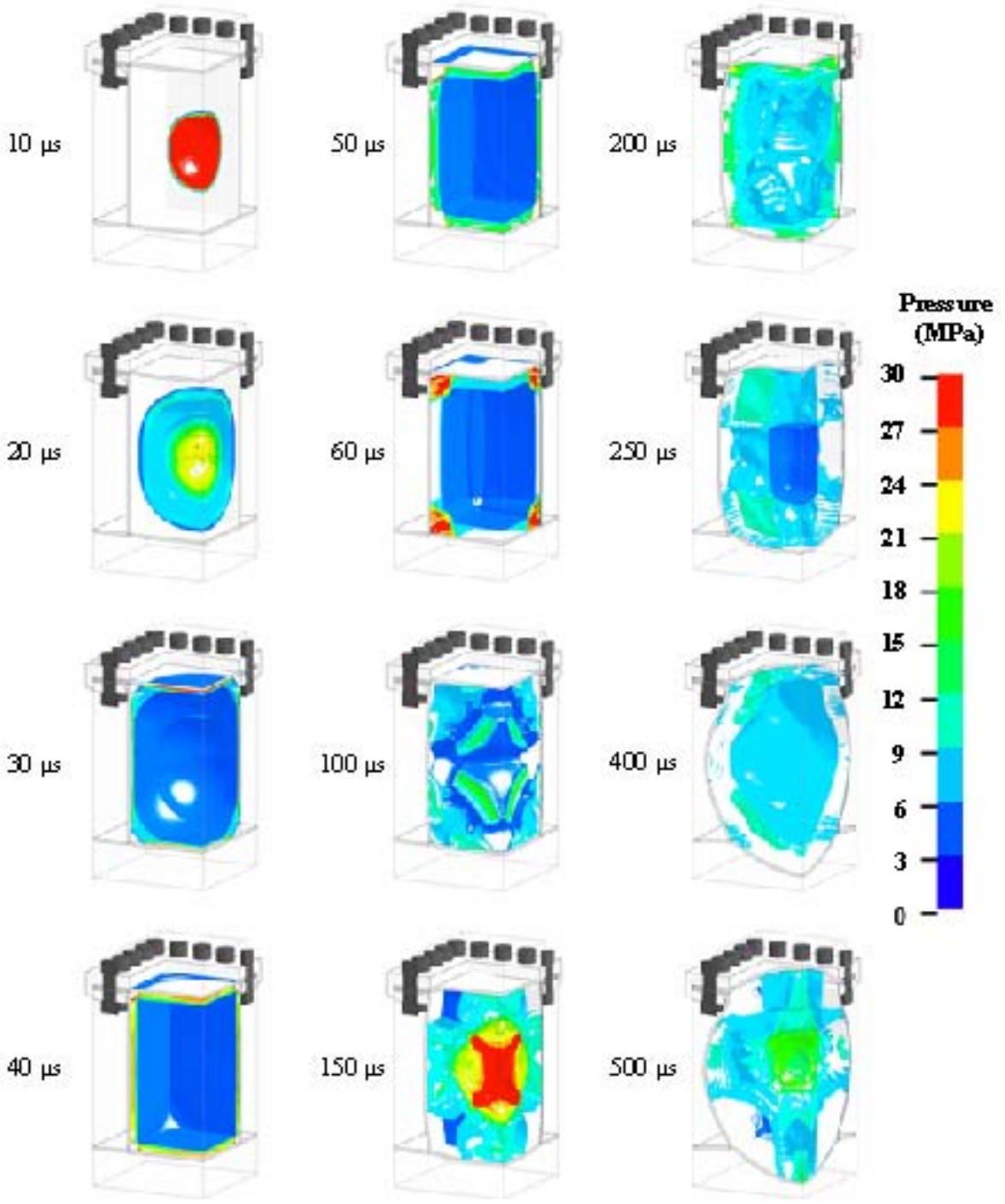

Figure 8.18: Transient Pressure Contours for 60g Fully Confined Blast

The pressure histories at the midpoint of the target plate, edge and vertex locations obtained from the numerical simulations, illustrated in Figures 8.16, 8.17 and 8.18, are depicted in Figures 8.19, 8.20 and 8.21 respectively.

As expected, the primary pressure pulse at the midpoint of the target plate (Figure 8.19) were similar in arrival time, magnitude and duration. The pressure history obtained in an unconfined blast followed the general profile of a typical unconfined pressure profile, discussed in Section 2.1 and 2.2, which was characterised by a rapid increase in pressure followed by a decay of the pressure back to ambient conditions.

A second pressure pulse due to the reflection of the primary pressure pulse off the confinement tube and side target plate was observed in the fully vented and confined blast simulations respectively. The magnitude of the second pressure pulse was approximately 60% of the primary pressure pulse, however the duration of the second pressure pulse ($\pm 166\mu s$) was approximately double the duration of the primary pressure pulse ($\pm 79\mu s$). A comparison of the specific impulse ($I_o = \int P(t)dt$) of the primary ($\pm 900Pas$) and second ($\pm 1500Pas$) pressure pulses suggest that the second pressure pulse loads the midpoint of the target plates with almost double the specific impulse of the primary pressure pulse.

The presence of a third pressure pulse was observed in the fully vented blast simulation, however the magnitude was small in comparison to the primary and second pressure pulse. Thereafter the pressure at the midpoint decay to ambient conditions as the blast wave vented out of the confinement tube.

In the fully confined blast simulations the presence of a third pressure pulse was observed, the specific impulse of the third pressure was calculated to be $280Pas$ which in comparison to the primary and second pressure pulse was small. The pressure history at the midpoint of the target plate in the fully confined blast simulations after the third pressure pulse reverberated around the static overpressure which would remain in the container after the blast has occurred. The reverberation in the pressure history was due to the multiple 're-reflection' of the blast wave within the container.

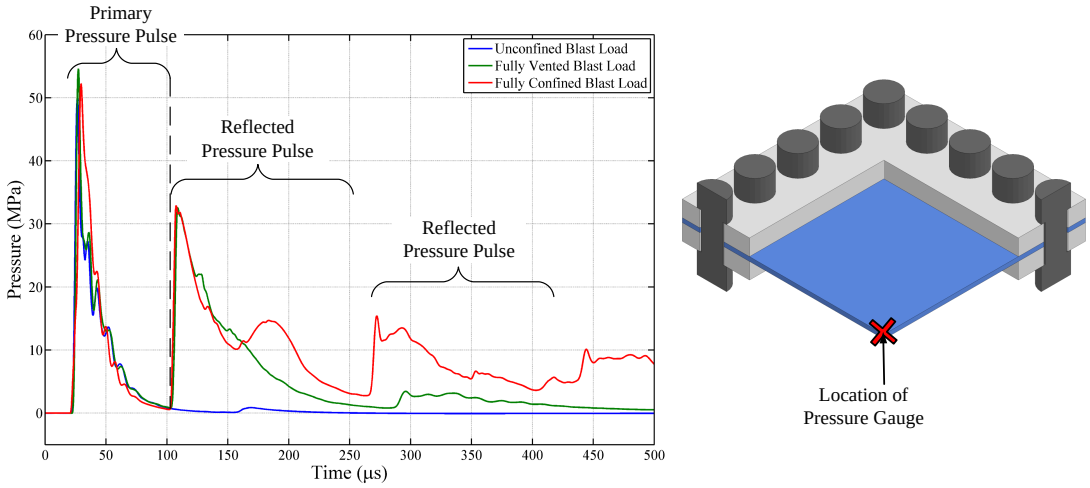

Figure 8.19: Pressures Histories Obtained in the Different Degrees of Confinement for a Mass of Explosive of $60g$ at the Midpoint

The edge pressures obtained from the different numerical simulations are depicted in Figure 8.20. As expected, the blast waves arrive at the edge of the target plate at similar times ($\pm 32\mu s$) irrespective of the degree of confinement. Upon arrival at the edge of the target plate there is a sharp increase in the pressure to the peak pressure thereafter the pressure decays. The peak pressures observed at the edge of the target plate were greater than the peak pressure observed at the midpoint of the target plate.

The peak pressure was expected to be significantly greater than the midpoint point peak as it was the location where merging of the primary blast wave from two adjacent surfaces merge. The peak pressures at the edge in the fully vented and confined blast simulations were approximately equal to the summation of two midpoint peak overpressures, however the peak pressure at the edge in the unconfined blast simulation was only 40% greater than the midpoint peak pressure. The difference in the peak pressure for the unconfined simulations, in comparison to the fully vented and confined blast simulations, were due to the pressure build-up at the edge in the unconfined blast simulation venting rapidly to the atmosphere, not allowing time for the development and interactions of the pressures to reach the same peak pressures observed in the fully vented and fully confined blast simulations.

The fully vented and fully confined pressure histories exhibit multiple, lesser magnitude, pressure pulses after the primary pressure pulse. The fully vented pressure history was observed to decay back to ambient conditions as time progressed. The fully confined pressure history exhibits multiple pressure pulses which decay in strength as time progressed. The period between the consecutive pressure pulses was observed to remain relatively constant and was measured to be approximately $84\mu s$. After a period of time the pressure would decay to the static overpressure value that would exists in the container after the explosive had been detonated.

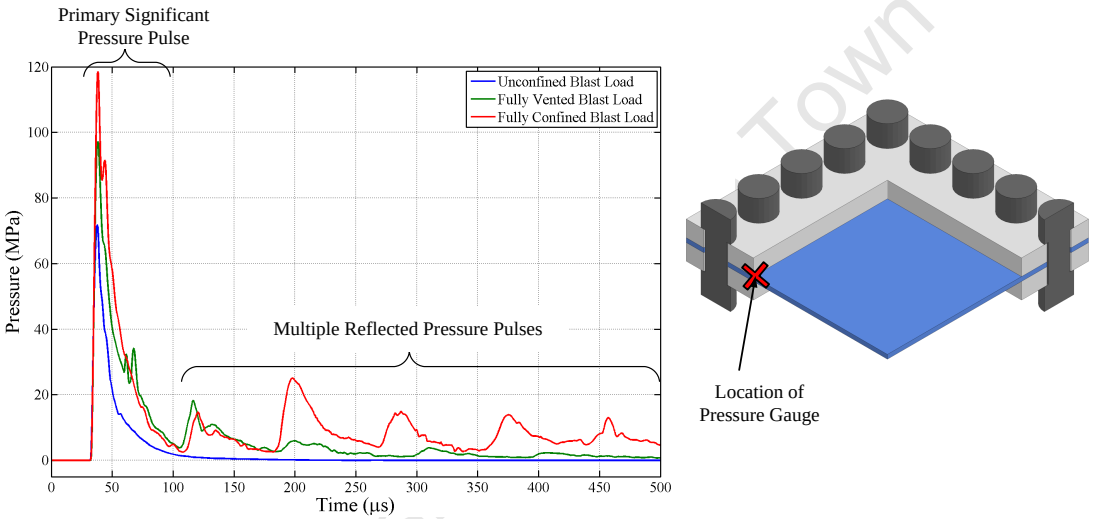

Figure 8.20: Pressures Histories Obtained in the Different Degrees of Confinement for a Mass of Explosive of $60g$ at the Edge

The pressure histories at the vertex location for the three degrees of confinement are depicted in Figure 8.21. As expected, the arrival time of the blast wave at the vertex ($\pm 40\mu s$) was the same irrespective of the degree of confinement. The peak pressures of the first pressure pulse are significantly greater than the peak pressure recorded at the midpoint of the target plate. The increased peak pressures were due to the merger of the reflected primary pressure pulse from three adjacent surfaces. The vertex pressure of the unconfined blast simulation was characterised by an initial peak which decayed back to ambient conditions as the blast wave vented to the atmosphere.

The vertex pressure histories obtained from fully vented and fully confined blast simulations were characterised by two pressure pulses 166μs apart. The peak pressure of the second pressure pulse in both cases was approximately half the peak pressure of the first pressure pulse. The magnitude of the peak pressure in the second pressure pulse was observed to be greater than the midpoint peak pressure.

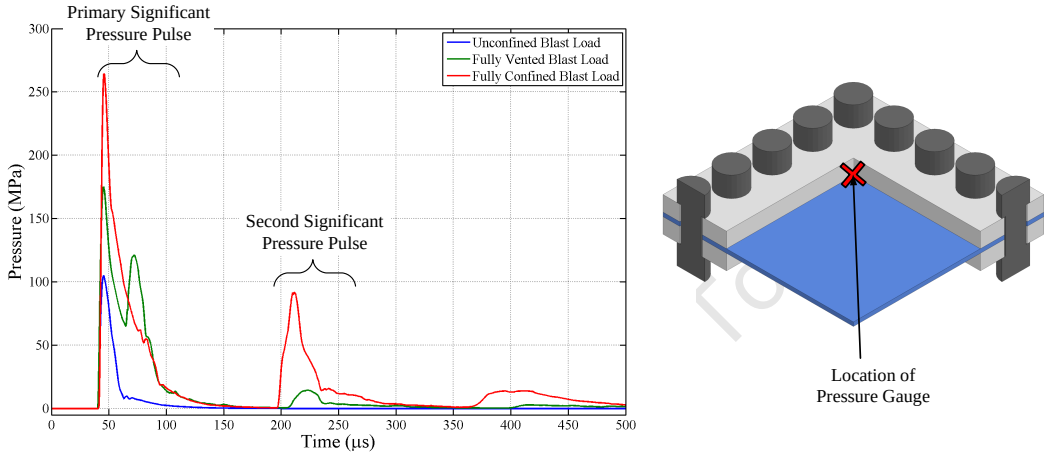

Figure 8.21: Pressures Histories Obtained in the Different Degrees of Confinement for a Mass of Explosive of 60g at the Vertex

The pressure histories obtained from the numerical simulations for the three degrees of confinement show the effects of blast wave focusing. The magnitude of the peak pressures increases with the number of adjoining reflective surfaces.

8.4 Comparison of Numerical and Empirical Blast Pressures

The pressure histories for the midpoint, edge and vertex of the target plate obtained from the numerical simulations were compared to the corresponding pressure histories generated from an empirical blast model (CONWEP). The numerical model implemented an ALE mesh to describe the air and explosive and an explosive model to determine the pressure within the elements. The empirical blast model, *LOAD_BLAST_ENHANCED card within LS-DYNA, generates an ideal pressure

history based on the stand off distance, angle of incidence and the mass of explosive detonated. The empirical blast model was implemented in LS-DYNA by Randers-Pehrson and Bannister [170] and pressure profiles were based on work presented by Kingery and Bulmash [171]. The empirical blast model does not take into account reflections, interactions nor shadowing[1] [175]; hence can only be compared to the unconfined blast simulations.

Figures 8.22a, 8.22b and 8.22c depict the pressure histories obtained from the numerical (ALE) and empirical models for the detonation of a $60g$ mass of explosive at the midpoint, edge and vertex location respectively. The results show the midpoint pressure history of ALE model significantly underpredict the peak reflected pressure in comparison to the empirical model. The ALE model predicts a higher peak pressure at the edge and vertex locations. The higher peak pressures at the edge and vertex locations in the ALE models are attributed to the capability of the ALE model to capture complex blast interactions and blast wave focusing at the edges and vertices.

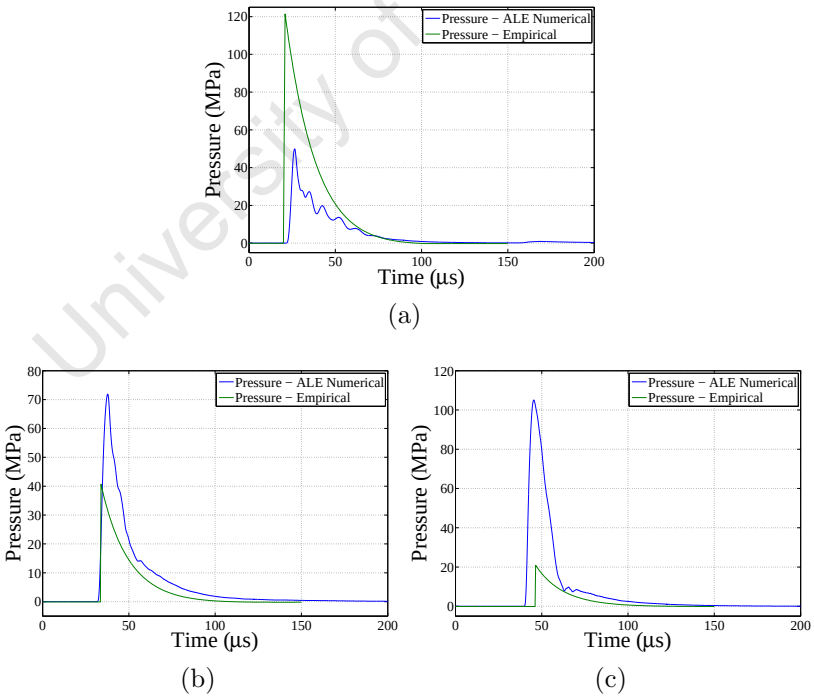

Figure 8.22: Comparison of Empirical and Numerical Pressure Histories, (a) Midpoint Pressure History, (b) Edge Pressure History and (c) Vertex Pressure History

[1]Interaction of the blast wave on an obstacle before the surface of interest

A series of simulations were carried out where the unconfined test rig model was loaded with the empirical blast loads. The final midpoint deflections for the empirical blast loading simulations are plotted in Figures 8.23 and 8.24, together with experimental and ALE numerical final midpoint deflections. The results show the final midpoint deflections obtained from the empirical blast load simulations overpredict the experimental and the ALE model values. However the results obtained for the 3 and 4mm thick target plates are within one target plate thickness.

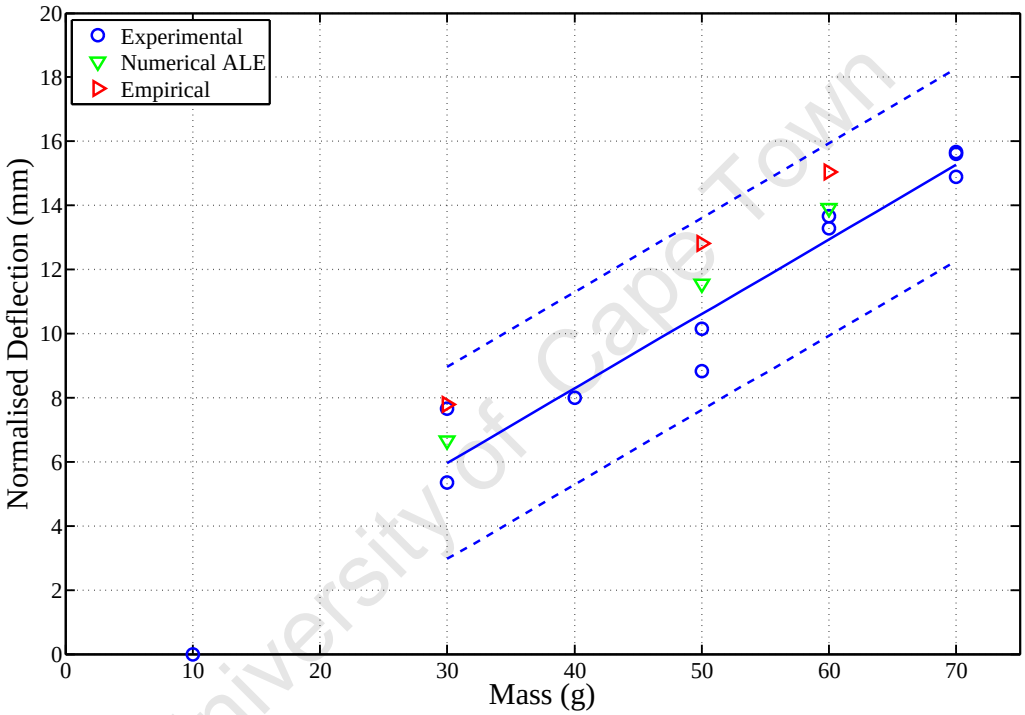

Figure 8.23: Comparison of Midpoint Deflections from 3mm Target Plates for Numerical, Empirical and Experimental Results

The underprediction of the peak pressure in the ALE blast simulations was dependent of the mesh density of the air domain, due to hardware limitations a finer mesh could not be implemented to increase the accuracy of the peak pressure. Similar findings, underprediction of blast pressure but accurately predicting structural response such as midpoint deflection, have been observed by Yiannakopoulos [14].

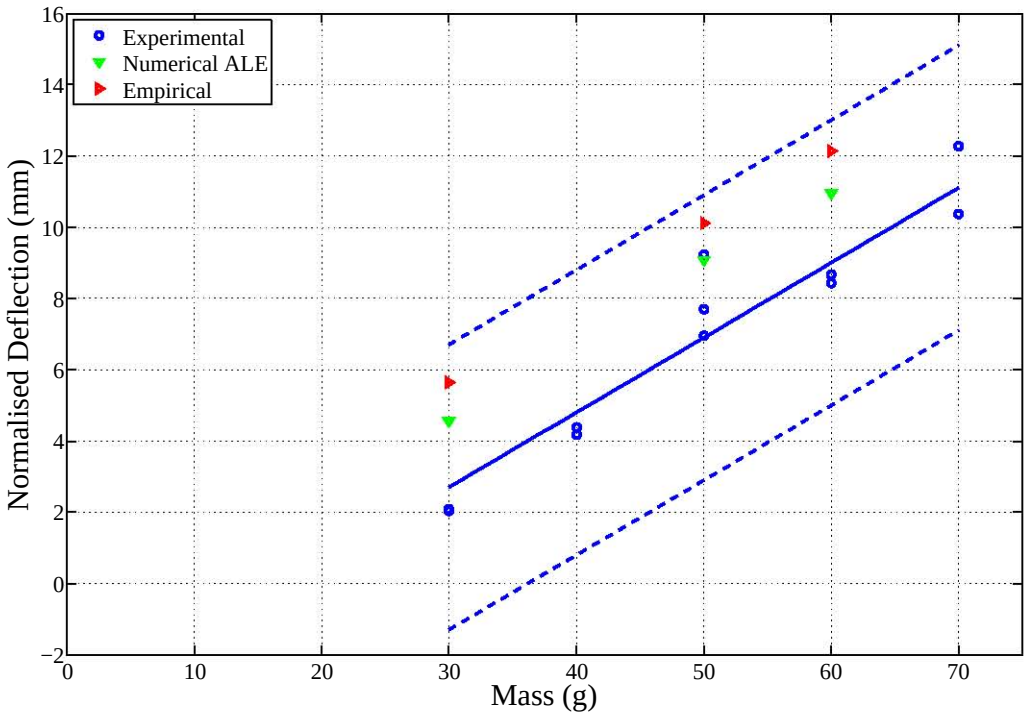

Figure 8.24: Comparison of Midpoint Deflections from $4mm$ Target Plates for Numerical, Empirical and Experimental Results

8.5 Summary

A series of numerical simulations were developed to simulate the response of three different thickness target plates subjected to different loads generated by three different degrees of confinement. The models were developed to simulate mode I failure as was the case in the experiments. The final midpoint deflection and deformation profile results obtained from the numerical model correlated well with the experiments.

Equations 5.28, 5.29 and 5.30 determined in Section 5.3.3 to predict the final midpoint deflection of a target plate were validated with the numerical blast models. A 2 and $6mm$ thick target plate were simulated and the midpoint deflection results correlated well with the predicted value from Equations 5.28, 5.29 and 5.30.

In terms of the transient midpoint deflection the numerical simulation predicted the final midpoint deflection well. However, the initial peak deflection was underpredicted

and the amplitude of the elastic response was reduced. The experimental transient midpoint deflections exhibited more springback than the numerical simulations.

The peak pressure histories in the numerical models underpredicted the peak pressures at the midpoint of the target plate as observed in the qualitative analysis. However, the resulting midpoint deflection and plate profiles correlated well with the experiments. The qualitative analysis demonstrated that the peak pressure increased with the number of adjoining reflective surfaces.

This page has been intentionally left blank.

9 Conclusions

The effects of three different degrees of confinement of blast load on the transient and final response of square target plates of different thicknesses were investigated experimentally and numerically. As set out in Chapter 1, the principle objectives of this thesis were:

(a) carry out experiments to assess the performance of the degrees of confinement on the final and transient midpoint deflections.

- the final midpoint deflection, irrespective of degree of confinement or target plate thickness, increases with an increasing mass of explosive.
- The blast load generated between the degrees of confinement was found to be, within acceptable limits, directly proportional to the midpoint deflection ratio. The correlation lead to a calculated impulse for the fully confined blast, given as,

$$I_{FC} = 2.55 \times m_{exp} + 9.71$$

- the midpoint deflection - thickness ratio versus the dimensionless number correlated well with published trends.

- using the deflection-thickness relationship and dimensionless damage analysis proposed by Nurick and Martin [37, 38] a set of formulae was derived for this set of experiments (for target plated with exposed areas of $200 \times 200mm$ subjected to different types of blast loads)

$$\delta_{UC} = 0.48 \times \frac{(0.62 \times m_{exp} + 2.35)}{2 \times h \times \sqrt{BL\rho\sigma_y]}}$$

$$\delta_{FV} = 0.48 \times \frac{(1.89 \times m_{exp} + 8.15)}{2 \times h \times \sqrt{BL\rho\sigma_y]}}$$

$$\delta_{FC} = 0.48 \times \frac{(2.58 \times m_{exp} + 9.82)}{2 \times h \times \sqrt{BL\rho\sigma_y]}}$$

- a comparison of the boundary conditions showed that the fully clamped boundary of the top target plate allowed larger midpoint deflections than the side and bottom target plate which had welded boundaries (built-in). The midpoint deflections of the side and bottom target plate were similar.

- final midpoint deflection data from devised transient midpoint deflection system correlated well with experiments.

- springback was observed to decreases with an increase in the midpoint deflection increased and the trends followed published trends.

(b) carry out a material characterisation of the locally obtain mild steel target plate for use in the numerical simulations.

Johnson-Cook material parameters for the three different plate thicknesses were determined. The parameters were obtained from a series of uniaxial tensile (quasi-static) and split Hopkinson bar (high strain rate) tests. Table 6.4 list the various parameters for the three plate thicknesses.

Table 9.1: Johnson-Cook Parameters for Different Plate Thicknesses

Thickness	$3mm$	$4mm$	$5mm$
Material	Mild Steel	Mild Steel	Gr. 300WA
A(MPa)	233.47	221.67	263.58
B(MPa)	480.37	361.35	519.64
n	0.3565	0.4746	0.3843
C	0.0369	0.0481	0.0259
m	0.6655		

(c) *carry out numerical analyses to model the dynamic response of the target plates.* and

(d) *compare the experimental results to the numerical predictions.*

A series of numerical models were developed to simulate the experiments. Mesh convergence studies were carried out to determine the optimal mesh sizes for the target plate and air domains. The final midpoint deflection and deformation profile results obtained from the numerical models show good correlation with the experimental results.

Parametric studies were also performed using the numerical simulation to model the response of 2 and $6mm$ thick target plates. The results compare well with midpoint deflections predicted using experimental trends.

The numerical simulations showed similar transient response for th midpoint deflections. However, the initial peak deflection was underpredicted and the amplitude of the elastic response was reduce. The experimental transient midpoint deflections exhibited more spring back than the numerical simulations.

The peak pressure histories in the numerical models underpredicted the peak pressures at the midpoint of the target plate as observed in the qualitative analysis. However, the resulting midpoint deflection and plate profiles correlated well with the experiments. The qualitative analysis demonstrated that the

primary pressure pulse at the midpoint of the target plate was similar in all the degrees of confinement as well as the peak pressure increased with the number of adjoining reflective surfaces.

10 Recommendations

Based on the findings and the conclusions of this thesis, the following recommendations are made:

- **Experimental Tests**
  - The effects of the degree of confinement should be extended to include target plates with different exposed areas, plate thicknesses and different materials.
  - Pressure measurements at several locations on the target plate should be measured.
  - The experiments should be expanded to include different target plate thicknesses and masses of explosive.
  - The remaining degrees of confinement (air and surface burst and partially vented explosions) should be investigated.
  - The effects of the degree of confinement should be extended to include elastic response of the target plate.
  - The effects of the degree of confinement should be extended to include tearing of the target plates.
  - The design of the transient deflection measuring system could be improved to increase vibration isolation and the eliminate the effects of the smoke/soot

on the output signal.

- **Material Characterisation**
  - Material behaviour at intermediate ($1 < \dot{\varepsilon} < 100$) and high strain rates ($\dot{\varepsilon} > 3000$) should be carried out to obtain a more representative behaviour over a larger strain rate range.
  - Tests at elevated strain rates and temperatures should be performed to investigate the thermal softening effects of the materials.
- **Numerical Simulations**
  - If pressures measurement is available, numerical simulations can be correlated with not only midpoint deflection and deformation profiles but also with pressure data.
  - The numerical models should include failure in the material model.
  - The interactions of the blast wave within the confinement structure, particularly at the corners, should be investigated by carrying out a velocity vector analysis in the air domain.

References

[1] G.F. Kinney and K.J. Graham. *Explosive Shocks in Air*. The Macmillan Company, New York, 2nd edition, 1985. (Cited on pages 1, 7, 8, 9, 11, 12, 14, 15, 81, 82, 83, 84, 85, 87 & 207).

[2] W.E. Baker. *Explosions in Air*. University of Texas Press, Austion and London, 1973. (Cited on pages 1, 12, 14, 15, 81, 82, 83, 84 & 85).

[3] M.Y.H. Bangash and T. Bangash. *Explosion-resistant buildings: design, analysis, and case studies*. Springer Verlag, 2006. (Cited on page 1).

[4] G.C Mays and P.D. Smith, editors. *Blast effects on buildings: design of buildings to optimize resistance to blast loading*. Thomas Telford, 1995. (Cited on pages 1 & 9).

[5] N.M. Elsayed and J.L. Atkins. *Explosion and Blast-Related Injuries: Effects of Explosion and Blast from Military Operations and Acts of Terrorism*. Academic Press, 2008. (Cited on page 1).

[6] G. Ben-Dor, O. Igra, and T. Elperin, editors. *Handbook of Shock Waves*, volume 1 – Theoretical, Experimental, and Numerical Techniques. Academic Press, 525 B Street, Suite 1900, San Diego, CA 92101-4495, USA, 2001. (Cited on pages 1, 8, 9, 12, 14, 65 & 80).

[7] US Army Corps of Engineers, Naval Facilities Engineering Command, Air Force Civil Engineer Support Agency. Structure to Resist the Effects of Accidental Explosions. Report UFC 3-340-02 formally TM 5-1300, US Dept of the Army and Defense Special Weapons Agency, Washington, DC, December 2008. (Cited on pages 1, 7, 8, 9, 10, 11, 12, 14, 15, 35, 36, 37, 38, 39, 41, 42, 43, 44, 45, 83, 99 & 101).

[8] W.E. Baker. The Elastic-Plastic Response of Thin Spherical Shells to Internal Blast Loading. *Journal of Applied Mechanics*, 27:139–144, 1960. (Cited on pages 2, 46, 47 & 48).

[9] T.A. Duffey and D. Mitchell. Containment of Explosions in Cylindrical Shells. *International Journal of Mechanical Science*, 15(3):237–249, 1973. (Cited on pages 2, 7, 55, 56, 57 & 58).

[10] J.A. Gatto. Hardened Luggage Container Design Survey. Final Report DOT/FAA/CT-93/18, Federal Aviation Administration Technical Center

Aviation Security Research and Development Service, September 1993. (Cited on pages 2, 65, 79 & 80).

[11] Staff of the Structures & Materials Department, Design and Production Standards Division of the Civil Aviation Authority Safety Regulation Group. Aircraft hardening research programme. Final Overview Report, CAA Paper 2001/9, Civil Aviation Authority, London, December 2001. (Cited on pages 2, 7, 65, 78 & 79).

[12] W.A. Hoffman and D.T. Wilson. Development of a low-cost package-bomb containment vessel. In *Proceedings of the 28th DOD Explosives Safety Seminar, Orlando,FL*, August 1998. (Cited on pages 2 & 77).

[13] H.H. Klein, M.J. Vander Vorst, and Jaycor Inc. Containment devices for small terrorist bombs for law enforcement. Final Report, Document Number – 189582, National Institute of Justice, August 2001. (Cited on pages 2, 7, 46, 77 & 78).

[14] G. Yiannakopoulos. FE modelling of an internal airblast inside a steel cubicle. Technical report, Platform Science Laboratory, Defence Science and Technology Organisation, Australia, 2005. (Cited on pages 2, 68, 69, 70, 71, 72, 73, 74, 136 & 255).

[15] D. Ambrosini, B. Luccioni, A. Jacinto, and R. Danesi. Location and mass of explosive from structural damage. *Engineering structures*, 27(2):167–176, 2005. (Cited on page 2).

[16] T.A. Duffey, E.A. Rodriguez, and C. Romero. Design of Pressure Vessels for High Strain Rate Loading: Dynamic Pressure and Failure Criteria Part 1: Detonation-Induced Dynamic Pressure Loading in Containment Vessels. *Pressure Vessel Research Council of the Welding Research Council, WRC Bulletin*, 477, December 2002. (Cited on pages 2, 35 & 54).

[17] A.L. Brundage, K.E Metzinger, D.J. Vangoethem, S.W. Attaway, and Sandia National Laboratories. Model validation of a structure subjected to internal blast loading, imac-xxv. In *Society for Experimental Mechanics Proceedings*, 2007. (Cited on pages 2, 75, 76 & 129).

[18] K.A. Marchand, P.A. Cox, and M.A. Polcyn. A Design Guide and Specification for Small Explosive Containment Structures. Technical Report SAND94-2255, Sandia National Labs., Albuquerque, NM (United States), December 1994. (Cited on page 7).

[19] K.M. Gaulke. *Mitigation Systems for Confined Blast Loading-Crew Protection in Armoured Vehicles*. PhD Thesis, University of Maryland, 2009. (Cited on page 7).

[20] N. Dobbs, E. Cohen, and S. Weissman. Blast Pressures and Impulse Loads for use in the Design and Analysis of Explosive Storage and Manufacturing Facilities.

Annals of the New York Academy of Sciences, 152(1):317–338, 1968. (Cited on pages 7, 8, 10, 11, 14, 15, 35 & 43).

[21] M.J. Hargather, G.S. Settles, and J.A. Gatto. Full-Scale Optical Experiments on the Explosive Failure of a ULD–3 Air Cargo Container. In *The 4th International Aviation Security Technology Symposium*, 2006. (Cited on page 7).

[22] K.G. Webster. *Investigation of Close Proximity Underwater Explosion Effects on a Ship-Like Structure Using the Multi-Material Arbitrary Lagrangian Eulerian Finite Element Method*. PhD Thesis, Virginia Polytechnic Institute and State University, 2007. (Cited on page 7).

[23] T. Ngo, P. Mendis, A. Gupta, and J. Ramsay. Blast loading and blast effects on structures–an overview. *Electronic Journal of Structural Engineering*, 7:76–91, 2007. (Cited on pages 7, 9 & 13).

[24] L.J. Van der Meer. Dynamic response of high-rise building structures to blast loading. Master's Thesis, Eindhoven University of Technology, 2008. (Cited on page 7).

[25] R.C. Wilkinson and J.G. Anderson. An Introduction to Detonation and Blast for the Non-Specialist. Technical report, Australian Government Department of Defence - Defence Science and Technology Organisation, 2003. (Cited on pages 8 & 11).

[26] P.D. Smith and J.G. Hetherington. *Blast and Ballistic Loading of Structures*. Butterworth-Heinemann, 1994. (Cited on pages 8, 9, 11, 12, 14, 44, 80, 81, 82, 83, 84, 86, 87 & 97).

[27] A.M. Remennikov. The State of the Art Explosive Loads Characterisation. In *The Australian Earthquake Engineering Society Proceedings*, 2007. (Cited on pages 8 & 11).

[28] A.C. Jacinto, R.D. Ambrosini, and R.F. Danesi. Experimental and Computational Analysis of Plates Under Air Blast Loading. *International Journal of Impact Engineering*, 25:927–947, 2001. (Cited on pages 8 & 14).

[29] W.E. Baker, P.A. Cox, P.S. Westine, J.J. Kulez, and R.A Strehlow. *Explosion Hazards and Evaluation*. Elsevier Scientific Publishing Company, 1983. (Cited on pages 9, 44 & 85).

[30] Great Britain. Health, Safety Executive, Health, Safety Executive Staff, Steel Construction Institute (Great Britain), British Gas Research, and Technology (ERS). *Effects of Simplification of the Explosion Pressure-Time History*. Offshore Technology Report Series. HSE Books, 1992. (Cited on pages 9 & 13).

[31] G.K. Schleyer. Predicting the effects of blast loading arising from a pressure vessel failure: a review. *Proceedings of the Institution of Mechanical Engineers,*

Part E: Journal of Process Mechanical Engineering, 218(4):181–190, 2004. (Cited on pages 9 & 13).

[32] NORSOK Standard, N–004. Design of steel structures. Rev. 2. October 2004. (Cited on page 9).

[33] C.J. Gantes and N.G. Pnevmatikos. Elastic-plastic response spectra for exponential blast loading. *International Journal of Impact Engineering*, 30(3): 323–343, 2004. (Cited on page 13).

[34] G.H. Farrow, G.N. Nurick, and G.P. Mitchell. Modelling of impulsively loaded circular plates using the abaqus finite element code. In *13th Symposium of Finite Elements in South Africa*, pages 186–198, January 1995. (Cited on page 13).

[35] C. Kingery, R. Schumacher, W. Ewing Jr, and the Army Ballistic Research Laboratory Aberdeen Proving Ground MD. Internal Pressure from Explosions in Suppressive Structures. Final Report ARBRL–MR–02848, US Army Armament Research and Development Command, Ballistic Research Laboratory, Aberdeen Proving Ground, Maryland, 1978. (Cited on pages 14, 35, 39 & 43).

[36] N. Jones. *Structural impact*. Cambridge University Press, 1989. (Cited on pages 16, 26, 30, 31, 32, 33 & 85).

[37] G.N. Nurick and J.B. Martin. Deformation of thin plates subjected to impulsive loading–a review:: Part I: Theoretical considerations. *International Journal of Impact Engineering*, 8(2):159–170, 1989. (Cited on pages 16, 29, 33, 34, 146, 152, 155, 159, 160, 172 & 260).

[38] G.N. Nurick and J.B. Martin. Deformation of thin plates subjected to impulsive loading–a review:: Part II: Experimental studies. *International Journal of Impact Engineering*, 8(2):171–186, 1989. (Cited on pages 16, 29, 33, 34, 146, 152, 155, 159, 160, 172, 234 & 260).

[39] D. Bonorchis and G.N. Nurick. The effect of welded boundaries on the response of rectangular hot-rolled mild steel plates subjected to localised blast loading. *International Journal of Impact Engineering*, 34(11):1729–1738, 2007. (Cited on pages 16, 143 & 206).

[40] D. Bonorchis. *Analysis and Simulation of Welded Plates Subjected to Blast Loading*. PhD Thesis, Blast Impact and Survivability Research Centre, University of Cape Town, December 2007. (Cited on pages 16, 90 & B-7).

[41] G.N. Nurick, M.E. Gelman, and N.S. Marshall. Tearing of blast loaded plates with clamped boundary conditions. *International Journal of Impact Engineering*, 18(7-8):803–827, 1996. (Cited on pages 16, 17, 20, 21 & 29).

[42] N. Jacob. The Effect of Stand-off Distance on the Failure of Thin Plates Subjected to Blast Loads. Master's Thesis, University of Cape Town, 2005. (Cited on page 16).

[43] N. Jacob, G.N. Nurick, and G.S. Langdon. The Effect of Stand-Off Distance on the Failure of Fully Clamped Circular Mild Steel Plates Subjected To Blast Loads. *Engineering Structures*, 29:2723–2736, 2007. (Cited on pages 16 & 90).

[44] G.N. Nurick, M.D. Olson, J.R. Fagnan, and A. Levin. Deformation and tearing of blast-loaded stiffened square plates. *International Journal of Impact Engineering*, 16(2):273–291, 1995. (Cited on pages 16 & 90).

[45] G.S. Langdon, S. Chung Kim Yuen, and G.N. Nurick. Experimental and numerical studies on the response of quadrangular stiffened plates. Part II: localised blast loading. *International Journal of Impact Engineering*, 31(1):85–111, 2005. (Cited on pages 16, 90 & 143).

[46] S. Chung Kim Yuen and G.N. Nurick. Experimental and numerical studies on the response of quadrangular stiffened plates. Part I: subjected to uniform blast load. *International Journal of Impact Engineering*, 31(1):55–83, 2005. (Cited on pages 16, 90 & 143).

[47] Y.W. Lee and T. Wierzbicki. Fracture prediction of thin plates under localized impulsive loading. part ii: discing and petalling. *International Journal of Impact Engineering*, 31(10):1277–1308, 2005. (Cited on page 16).

[48] N. Jacob, S. Chung Kim Yuen, G.N. Nurick, D. Bonorchis, S.A. Desai, and D. Tait. Scaling aspects of quadrangular plates subjected to localised blast loads–experiments and predictions. *International Journal of Impact Engineering*, 30 (8-9):1179–1208, 2004. (Cited on pages 16 & 143).

[49] D. Bonorchis and G.N. Nurick. The influence of boundary conditions on the loading of rectangular plates subjected to localised blast loading–Importance in numerical simulations. *International Journal of Impact Engineering*, 36(1):40–52, 2009. (Cited on page 16).

[50] R.A. Benham and T.A. Duffey. Experimental-theoretical correlation on the containment of explosions in closed cylindrical vessels. *International Journal of Mechanical Sciences*, 16(8):549–554, 1974. (Cited on page 16).

[51] S. Menkes and H. Opat. Broken beams. *Experimental Mechanics*, 13:480–486, 1973. (Cited on pages 16 & 17).

[52] R.G. Teeling-Smith and G.N. Nurick. The deformation and tearing of thin circular plates subjected to impulsive loads. *International Journal of Impact Engineering*, 11(1):77–91, 1991. (Cited on pages 17, 18 & 27).

[53] M.D. Olson, G.N. Nurick, and J.R. Fagnan. Deformation and Rupture of Blast Loaded Square Plates–Predictions and experiments. *International Journal of Impact Engineering*, 13(2):279–291, 1993. (Cited on pages 17, 18, 21, 22, 23, 24, 25, 234 & 238).

[54] G.N. Nurick and G.C. Shave. The deformation and tearing of thin square plates subjected to impulsive loads–an experimental study. *International Journal of Impact Engineering*, 18(1):99–116, 1996. (Cited on pages 17, 18, 19, 76, 90 & 116).

[55] B.M. Thomas and G.N. Nurick. The effect of boundary conditions on thin plates subjected to impulsive loads. In *PLASTICITY 95-The 5th International Symposium on Plasticity and its Current Applications*, pages 85–88, July 1995. (Cited on pages 19, 20, 29 & 125).

[56] T. S. Koko and M. D. Olson. Non-linear analysis of stiffened plates using super elements. *International Journal for Numerical Methods in Engineering*, 31(2): 319–343, 1991. (Cited on page 21).

[57] T.S. Koko and M.D. Olson. Nonlinear transient response of stiffened plates to air blast loading by a superelement approach. *Computer Methods in Applied Mechanics and Engineering*, 90(13):737–760, 1991. (Cited on page 21).

[58] G.R. Cowper and P.S. Symonds. Strain-hardening and strain-rate effects in the impact loading of cantilever beams. Technical Report 28, Division of Applied Mathematics, Brown University, September 1957. (Cited on pages 21 & 194).

[59] L. Zhu. Transient deformation modes of square plates subjected to explosive loadings. *International Journal of Solids and Structures*, 33(3):301–314, 1996. (Cited on pages 26, 27, 28, 116, 131, 143 & 238).

[60] V.H. Balden and G.N. Nurick. Numerical simulation of the post-failure motion of steel plates subjected to blast loading. *International Journal of Impact Engineering*, 32(14):14 – 34, 2005. (Cited on pages 27 & 28).

[61] N.K. Gupta and Nagesh. Deformation and tearing of circular plates with varying support conditions under uniform impulsive loads. *International Journal of Impact Engineering*, 34(1):42 – 59, 2007. (Cited on page 29).

[62] W. Johnson. *Impact Strength of Materials*. Edward Arnold, 1975. (Cited on pages 29 & 32).

[63] Y.P. Zhao. Suggestion of a new dimensionless number for dynamic plastic response of beams and plates. *Archive of Applied Mechanics*, 68:524–538, 1998. (Cited on pages 32 & 33).

[64] Q. M. Li and N. Jones. On dimensionless numbers for dynamic plastic response of structural members. *Archive of Applied Mechanics*, 70:245–254, 2000. (Cited on page 32).

[65] I. Edri, Z. Savir, V.R. Feldgun, Y.S. Karinski, and D.Z. Yankelevsky. On blast pressure analysis due to a partially confined explosion: I. experimental studies. *International Journal of Protective Structures*, 2(1):1–20, 2011. (Cited on pages 35, 39, 40, 42 & 43).

[66] W.A. Keenan and J.E. Tancreto. Design criteria for frangible covers in ordnance facilities. In *Twentieth Department of Defence Explosives Safety Seminar, Norfolk, Virginia*, August 1982. (Cited on page 35).

[67] *Blast resistant structures.* Naval Facilities Engineering Command, December 1986. (Cited on pages 35, 37, 99 & 101).

[68] W.A. Keenan and J.E. Tancreto. Blast Environment from Fully and Partially Vented Explosions in Cubicles. Technical Report TR–828, Civil Engineering Laboratory, Naval Construction Battalion Center, Port Hueneme, California, November 1975. (Cited on pages 36, 37, 38, 39, 41, 98 & 99).

[69] H.R.W. Weibull. Pressures Recorded in Partially Closed Chambers at Explosion of TNT Charges. *Annals of the New York Academy of Sciences*, 152(1):357–361, 1968. (Cited on pages 39 & 40).

[70] W.E. Baker, C.E. Anderson Jr, B.L. Morris, and D.K. Wauters. Quasi-Static Pressure, Duration, and Impulse for Explosions in Structures. Technical report, Southwest Research Institute, San Antonio, TX, August 1982. (Cited on page 39).

[71] J.E. Tancreto and E.S. Helseth. Effect of frangible panels on internal gas pressures. In *Department of Defence Explosives Safety Board Minutes of the 21st Explosives Safety Seminar*, volume 1, pages 365–394, 1984. (Cited on page 41).

[72] M. Beyer. Effect of frangible covers on internal loads. Test Data Report NCEL TM 51-86-16, Naval Civil Engineering Laboratory, Port Hueneme,CA, July 1983. (Cited on page 41).

[73] J.E. Tancreto and W.H. Zehrt Jr. Design for internal quasi-static pressures from partially confined explosions. In *28th Department of Defence Exploisve Safety Seminar, Orlando FL*, August 1998. (Cited on pages 41 & 42).

[74] F.H. Gregory. Analysis of the loading and response of a suppressive shield when subjected to an internal explosion. In *Minutes of 17th Explosive Safety Seminar. Denver, Colorado*, 1976. (Cited on page 45).

[75] T.A. Duffey and C. Romero. Strain Growth in Spherical Explosive Chambers Subjected to Internal Blast loading. *International Journal of Impact Engineering*, 28(9):967–983, 2003. (Cited on pages 46 & 54).

[76] W.E. Baker, P.S. Westine, and F.T. Dodge. *Similarity Methods in Engineering Dynamics: Theory and Practice of scale modeling.* Spartan Books; [distributed by] Hayden Book Co. Rochelle Park, N.J., 1973. (Cited on pages 49 & 53).

[77] T.A. Duffey, R.R. Karpp, and T.R. Neal. Response of containment vessels to explosive blast loading. Technical Report LA-8082, Los Alamos Scientific Laboratory, June 1980. (Cited on pages 49 & 50).

[78] F. Auslender and A. Combescure. Spherical elastic–plastic structures under internal explosion: Approximate analytical solutions and applications. *Engineering Structures*, 22(8):984–992, 2000. (Cited on pages 51, 52 & 53).

[79] J.J. White III, B.D. Trott, and J.E. Backofen Jr. The Physics of Explosion Containment. *Physics in Technology*, 8(3):94–100, 1977. (Cited on pages 53 & 54).

[80] A.A. Buzukov. Characteristics of the Behaviour of the Walls of Explosion Chambers Under the Action of Pulsed Loading. *Combustion, Explosion, and Shock Waves*, 12(4):549–554, 1976. (Cited on page 54).

[81] A.A. Buzukov. Forces Produced by an Explosion in an Air-filled Explosion Chamber. *Combustion, Explosion, and Shock Waves*, 16(5):555–559, 1980. (Cited on page 54).

[82] Z. Whenhui, X. Honglu, Z. Guangquan, and G.K. Schleyer. Dynamic response of cylindrical explosive chambers to internal blast loading produced by a concentrated charge. *International Journal of Impact Engineering*, 19(9-10):831–845, 1997. (Cited on page 54).

[83] Q.M. Li, Q. Dong, and J.Y. Zheng. Strain growth of the in-plane response in an elastic cylindrical shell. *International Journal of Impact Engineering*, 35(10): 1130–1153, 2008. (Cited on page 54).

[84] W. Zhu, H. Xue, H. Zhou, and G.K. Schleyer. Dynamic Response of Cylindrical Explosive Chambers to Internal Blast Loading. *International Journal of Impact Engineering*, 19:831–845, 1977. (Cited on page 54).

[85] J. Zheng, Q. Dong, and Q. Li. Recent progress of explosion containment vessels (Part II): Strain growth in explosion containment vessels. *Journal of Pressure Equipment and Systems*, 6:199–207, 2008. (Cited on page 54).

[86] Q. Dong, Q.M. Li, and J.Y. Zheng. Interactive mechanisms between the internal blast loading and the dynamic elastic response of spherical containment vessels. *International Journal of Impact Engineering*, 37(4):349 – 358, 2010. (Cited on page 54).

[87] Q. Dong, Q.M. Li, and J.Y. Zheng. Further study on strain growth in spherical containment vessels subjected to internal blast loading. *International Journal of Impact Engineering*, 37(2):196–206, 2010. (Cited on page 54).

[88] A. I. Abakumov, V. V. Egunov, A. G. Ivanov, A. A. Uchaev, V. I. Tsypkin, and A. T. Shitov. Calculation and experiments on the deformation of explosion-chamber shells. *Journal of Applied Mechanics and Technical Physics*, 25:455–458, 1984. (Cited on page 54).

[89] T.A. Duffey, J.M. Greene, W.E. Baker, and B.B. Lewis. Containment of Explosions in Spherical Vessels. In *Pressure Vessel and Piping Conference, Denver, CO*, volume 1, pages 25–29, 1992. (Cited on page 54).

[90] M. Giglio. Spherical Vessel Subjected to Explosive Detonation Loading. *International Journal of Pressure Vessels & Piping*, 74:83–88, 1997. (Cited on page 54).

[91] T.A. Duffey and E.A. Rodriguez. Overview of pressure vessel design criteria for internal detonation (blast) loading. Technical Report LA-UR-01-2621, Los Alamos Scientific Laboratory, May 2001. (Cited on page 54).

[92] T.A. Duffey and E.A. Rodriguez. Plastic instabilities in statically and dynamically loaded spherical vessels. In *ASME Pressure Vessels and Piping Division Conference, Bellevue, Washington, USA*, July 2010. (Cited on page 54).

[93] E.A. Rodriguez and R. Romero. Hydrodynamic modeling of detonations for structural design of containment vessels. In *ASME Pressure Vessels and Piping Division Conference, Vancouver, British Columbia, Canada*, July 2006. (Cited on page 54).

[94] T.A. Duffey and E.A. Rodriguez. Remaining life of containment vessels for repeated explosive testing. Technical Report LA-UR-00-5424, Los Alamos Scientific Laboratory, May 2001. (Cited on page 54).

[95] R.E. Nickell and E.A. Rodriguez. Design rules for vessels subject to extreme design – basis internal detonation loads. In *12th international Chemical Weapons Demilitarization Conference, Stratfor–upon–Von, Warwickshire,UK*, 2009. (Cited on page 54).

[96] E.A. Rodriguez, R.E. Nickell, and J.E. Pepin. Design considerations for blast loads in pressure vessels. In *Transaction of the 19th International Association for Structural Mechanics in Reactor Technology, Tronto, Canada*, August 2007. (Cited on page 54).

[97] R.E. Nickell, T.A. Duffey, and E.A. Rodriguez. ASME code ductile failure criteria for impulsively loaded pressure vessels. In *ASME Pressure Vessels and Piping Division Conference, Cleveland, OH*, July 2003. (Cited on page 54).

[98] J.F. Proctor. Containment of Explosions in Water-filled Right-circular Cylinders. *Experimental Mechanics*, 10:458–466, 1970. (Cited on pages 55 & 56).

[99] R.A. Benham and T.A. Duffey. Experimental–Theoretical Correlation on the Containment of Explosions in Closed Cylindrical Vessels. *International Journal of Mechanical Science*, 16(8):549–658, 1974. (Cited on pages 56, 58, 59, 60, 61 & 62).

[100] Q.M. Li and N. Jones. Blast loading of a short cylindrical shell with transverse shear effects. *International Journal of Impact Engineering*, 16(2):331 – 353, 1995. (Cited on page 62).

[101] R.L. Martineau, C.A. Anderson, and F.W. Smith. Expansion of cylindrical shells subjected to internal explosive detonations. *Experimental Mechanics*, 40(2):219–225, 2000. (Cited on pages 62, 63 & 64).

[102] M. Held. Blast effects of high explosive charges detonating in cylindrical steel tubes. *Propellants, Explosives, Pyrotechnics*, 25(6):307–311, 2000. (Cited on page 64).

[103] J. Zheng, Y. Chen, G. Deng, X. Wu, L. Zhao, Q. Li, Y. Hu, Y. Ma, and G. Sun. Recent progress of explosion containment vessels (Part I): Methods for design of explosion containment vessels. *Journal of Pressure Equipment and Systems*, 6: 185–198, 2008. (Cited on page 64).

[104] A.G. Fedorenko, M.A. Syrunin, and A.G. Ivanov. Dynamic strength in explosive loading for shells made of oriented fibrous composites (review). *Journal of Applied Mechanics and Technical Physics*, 34:123–128, 1993. (Cited on page 64).

[105] M.A. Syrunin, A.G. Fedorenko, and A.G. Ivanov. Dynamic strength of cylindrical fiberglass shells under multiple explosive loading. *Combustion, Explosion, and Shock Waves*, 33(6):713–717, 1997. (Cited on page 64).

[106] V. Ryzhanskii, V. Rusak, and A. Ivanov. Estimating the explosion resistance of cylindrical composite shell. *Combustion, Explosion, and Shock Waves*, 35: 103–108, 1999. (Cited on page 64).

[107] G. Yiannakopoulos. A comparison of accelerometer mounting techniques in internal blast cubicle experiments undergoing elasto-plastic deformation. In *76th Shock and Vibration Symposium, Destin, Florida, USA*, 2005. (Cited on pages 65, 66, 67 & 68).

[108] G. Yiannakopoulos. Accelerometer adaptor for measurement of metal plate response from near field explosive detonation. *Review of Scientific Instruments*, 68(8):3254–3255, 1997. (Cited on page 65).

[109] G. Yiannakopoulos and P. Kiernan. Pressure transducer mounts for internal blast measurements on thin metal walls. *Review of Scientific Instruments*, 70(4):2122–2126, 1999. (Cited on pages 65, 67, 68, 69 & 136).

[110] H.J. Fleisher. Design and explosive testing of a blast resistant luggage container. In *4th International Conference on Structures Under Shock and Impact - SUSI96*, 1996. (Cited on page 79).

[111] G. Ben-Dor. A State-of-the-Knowledge Review on the Pseudo-steady Shock-wave Reflections and their Transition Criteria. *Shock Waves*, 15(3-4):277–294, 2006. (Cited on page 84).

[112] A. Neuberger, S. Peles, and D. Rittel. Scaling the Response of Circular Plates Subjected to Large and Close-range Spherical Explosions. Part I: Air-blast Loading. *International Journal of Impact Engineering*, 34:859–873, 2007. (Cited on page 85).

[113] E.J. Conrath, T. Krauthammer, K.A. Marchand, and P.F. Mlakar. *Structural Design for Physical Security: State of the Practice*. American Society of Civil Engineers, 1999. (Cited on pages 85 & 86).

[114] B. Hopkinson. *British Ordnance Board Minutes, 13565*, 1915. (Cited on page 85).

[115] C. Cranz. Lehrbuch der ballistik. *Springer-Verlag*, 1926. (Cited on page 85).

[116] T. Krauthammer. Blast Effects and Related Threats. Technical report, Penn State University, University Park, USA, 1999. (Cited on page 86).

[117] R.K. Wharton, S.A. Formby, and R. Merrifield. Airblast TNT Equivalence for a Range of Commercial Blasting Explosives. *Journal of Hazardous Materials*, 79 (1-2):31 – 39, 2000. (Cited on page 89).

[118] B.M. Dobratz and P.C. Crawford. LLNL handbook of explosives: Properties of chemical explosives and explosive simulants. Technical Report UCRL-52997, Lawrence Livermore National Laboratory, University Of California, CA (USA), January 1985. (Cited on pages 89 & 208).

[119] I.M. Snyman. Impulsive loading events and similarity scaling. *Engineering Structures*, 32(3):886–896, 2010. (Cited on page 90).

[120] T. Wierzbicki and G.N. Nurick. Large Deformation of Thin Plates Under Localised Impulsive Loading. *International Journal of Impact Engineering*, 18 (7–8):899–918, 1996. (Cited on page 90).

[121] G.N. Nurick. *Large Deformations of Thin Plates Subjected to Impulsive Loading*. PhD Thesis, University of Cape Town, 1987. (Cited on pages 90, 108, A-10, A-11 & A-12).

[122] S.R. Bodner and P.S. Symonds. Experiments on dynamic plastic loading of frames. *International Journal of Solids and Structures*, 15(1):1–13, 1979. (Cited on pages 90, 106, 116 & A-5).

[123] L.K. Enstock and P.D. Smith. Measurement of impulse from the close-in explosion of doped charges using a pendulum. *International Journal of Impact Engineering*, 34(3):487–494, 2007. (Cited on page 90).

[124] G. Yiannakopoulos. Internal pressure measurements from explosively loaded cubicles. In *14th International Symposium on Military Aspects of Blast and Shock(MABS14), Las Cruces, New Mexico, U.S.A*, 1995. (Cited on pages 131 & 136).

[125] T.A. Duffey and S.W. Key. Experimental-theoretical correlations of impulsively loaded clamped circular plates. *Experimental Mechanics*, 9(6):241–249, 1969. (Cited on pages 131, A-5 & A-6).

[126] V. Tiwari, M.A. Sutton, SR McNeill, S. Xu, X. Deng, W.L. Fourney, and D. Bretall. Application of 3D image correlation for full-field transient plate deformation measurements during blast loading. *International Journal of Impact Engineering*, 36(6):862–874, 2009. (Cited on pages 131, A-7 & A-8).

[127] *Hot Strip Mill Product Tolerances - Hot Rolled Strip in Coil*. Arcelor Mittal South Africa, October 2005. File Reference : A1.2. (Cited on page 143).

[128] Personal Communication with Mr. R.G. Child of Conrbako (Pty.) Ltd. , June 2011. (Cited on page 143).

[129] G.N. Nurick. An empirical solution for predicting maximum central deflections of impulsively loading plates. In *4th Oxford Conference on Mechanical Properties of Materials at High Rates of Strain, Oxford, England*, March 1989. (Cited on page 147).

[130] S. Chung Kim Yuen, G.N. Nurick, W. Verster, N. Jacob, A.R. Vara, V.H. Balden, D. Bwalya, R.A. Govender, and M. Pittermann. Deformation of mild steel plates subjected to large-scale explosions. *International Journal of Impact Engineering*, 35(8):684–703, 2008. (Cited on page 147).

[131] R.M. Cleveland and A.K. Ghosh. Inelastic effects on springback in metals. *International Journal of Plasticity*, 18(56):769 – 785, 2002. (Cited on page 168).

[132] W.D. Carden, L.M. Geng, D.K. Matlock, and R.H. Wagoner. Measurement of springback. *International Journal of Mechanical Sciences*, 44(1):79 – 101, 2002. (Cited on page 168).

[133] A. Neuberger, S. Peles, and D. Rittel. Springback of circular clamped armor steel plates subjected to spherical air-blast loading. *International Journal of Impact Engineering*, 36(1):53–60, 2009. (Cited on pages 168, 169 & 170).

[134] *General Purpose and Commercial Steels - Hot Rolled Steel Plate and Coil for General Applications*. Arcelor Mittal South Africa, April 2010. File Reference : A2.1. (Cited on page 173).

[135] Sabs 1431:1987 - weldable structural steel, 2011. (Cited on page 173).

[136] ASTM A370-05 Standard Test Methods and Definitions for Mechanical Testing of Steel Products. Technical report, ASTM International, May 2005. (Cited on page 174).

[137] L. Weber, M. Kouzeli, C. San Marchi, and A. Mortensen. On the use of considere's criterion in tensile testing of materials which accumulate internal damage. *Scripta Materialia*, 41(5):549 – 551, 1999. (Cited on page 179).

[138] H.B. Sun, F. Yoshida, M. Ohmori, and X. Ma. Effect of strain rate on Ludërs band propagating velocity and Ludërs strain for annealed mild steel under uniaxial tension. *Materials Letters*, 57(29):4535 – 4539, 2003. (Cited on page 179).

[139] N. Tsuchida, Y. Tomota, K. Nagai, and K. Fukaura. A simple relationship between ludërs elongation and work-hardening rate at lower yield stress. *Scripta Materialia*, 54(1):57 – 60, 2006. (Cited on page 179).

[140] R. Hutanu, L. Clapham, and R.B. Rogge. Intergranular strain and texture in steel ludërs bands. *Acta materialia*, 53(12):3517–3524, 2005. (Cited on page 179).

[141] Z.L. Zhang, M. Hauge, J. Ødegård, and C. Thaulow. Determining material true stress-strain curve from tensile specimens with rectangular cross-section. *International Journal of Solids and Structures*, 36(23):3497–3516, 1999. ISSN 0020-7683. (Cited on pages 181 & 182).

[142] P.W. Bridgman. *Studies in large plastic flow and fracture*. Mc. Graw-Hill, 1952. (Cited on page 181).

[143] G. Le Roy, J.D. Embury, G. Edwards, and M.F. Ashby. A model of ductile fracture based on the nucleation and growth of voids. *Acta Metallurgica*, 29(8): 1509–1522, 1981. (Cited on page 181).

[144] J.M. Choung and S.R. Cho. Study on true stress correction from tensile tests. *Journal of Mechanical Science and Technology*, 22(6):1039–1051, 2008. ISSN 1738-494X. (Cited on page 182).

[145] *LS-Dyna® - Keyword User's Manual Volume I, Revision 806*. Livermore Software Technology(LSTC), September 2011. (Cited on pages 182, 183, 207, 209 & 224).

[146] B. Hopkinson. A Method of Measuring the Pressure Produced in the Detonation of High Explosives or by the Impact of Bullets. *Philosophical Transactions of the Royal Society of London. Series A, Containing Papers of a Mathematical or Physical Character*, 213:437–456, 1914. (Cited on page 190).

[147] H. Kolsky. An Investigation of the Mechanical Properties of Materials at Very High Rates of Loading. *Proceedings of the Physical Society. Section B*, 62:676–700, 1949. (Cited on page 190).

[148] M.M. Al-Mousawi, S.R. Reid, and W.F. Deans. The Use of the Split Hopkinson Pressure Bar Techniques in High Strain Rate Materials Testing. *Proceedings of the Institution of Mechanical Engineers, Part C: Journal of Mechanical Engineering Science*, 211(4):273–292, 1997. (Cited on pages 191, B-2 & B-3).

[149] F.J. Zerilli and R.W. Armstrong. Dislocation-mechanics-based constitutive relations for material dynamics calculations. *Journal of Applied Physics*, 61(5): 1816–1825, 1987. (Cited on pages 194 & 195).

[150] H. Zhao. A constitutive model for metals over a large range of strain rates identification for mild-steel and aluminium sheets. *Materials Science and Engineering: A*, 230(1):95–99, 1997. (Cited on page 194).

[151] G.R. Johnson and W.H. Cook. A constitutive model and data for metals subjected to large strains, high strain rates and high temperatures. In *Proceedings of the 7th International Symposium on Ballistics*, pages 541–547. Netherlands, 1983. (Cited on pages 194, 195, 196 & 202).

[152] M.J. Manjoine. Influence of rate of strain and temperature on yield stresses of mild steel. *Journal of Applied Mechanics*, 11:A211–218, 1944. (Cited on page 194).

[153] S.T. Marais. Development and proving of a split hopkinson pressure bar used for high strain rate materials testing. Master's Thesis, University of Cape Town, 2001. (Cited on page 194).

[154] L. Schwer. Optional strain-rate forms for the johnson cook constitutive model and the role of the parameter epsilon_0. *LS-DYNA Anwenderforum, Frankenthal*, 2007. (Cited on page 196).

[155] H. Huh and W.J. Kang. Crash-worthiness assessment of thin-walled structures with the high-strength steel sheet. *International Journal of Vehicle Design*, 30 (1):1–21, 2002. (Cited on page 196).

[156] D.J. Allen, W.K. Rule, and S.E. Jones. Optimizing material strength constants numerically extracted from taylor impact data. *Experimental mechanics*, 37(3): 333–338, 1997. (Cited on page 196).

[157] G.R. Johnson and W.H. Cook. Fracture characteristics of three metals subjected to various strains, strain rates, temperatures and pressures. *Engineering Fracture Mechanics*, 21(1):31–48, 1985. (Cited on page 197).

[158] A.S.M. Eleiche. Strain-rate history and temperature effects on the torsional-shear behavior of a mild steel. *Experimental Mechanics*, 21(8):285–294, 1981. (Cited on pages 200, 201 & 202).

[159] A. Rusinek, R. Zaera, and J.R. Klepaczko. Constitutive relations in 3-d for a wide range of strain rates and temperatures-application to mild steels. *International Journal of Solids and Structures*, 44(17):5611–5634, 2007. (Cited on page 200).

[160] W.S. Lee and C.Y. Liu. The effects of temperature and strain rate on the dynamic flow behaviour of different steels. *Materials Science and Engineering: A*, 426(1-2): 101–113, 2006. (Cited on page 200).

[161] A. Gilat and X. Wu. Plastic deformation of 1020 steel over a wide range of strain rates and temperatures. *International Journal of Plasticity*, 13(6-7):611–632, 1997. (Cited on pages 200, 201 & 202).

[162] T. Nakagawa and Y. Ikai. Strain ageing and the fatigue limit in carbon steel. *Fatigue & Fracture of Engineering Materials & Structures*, 2(1):13–21, 1979. (Cited on page 202).

[163] A.H. Cottrell and B.A. Bilby. Dislocation theory of yielding and strain ageing of iron. *Proceedings of the Physical Society. Section A*, 62:49–62, 1949. (Cited on page 202).

[164] *LS-Dyna® - Theory Manual*. Livermore Software Technology(LSTC), March 2006. Compiled by J.O.Hallquist. (Cited on pages 205, 208 & 209).

[165] T. Trevino. Applications of Arbitrary Lagrangian Eulerian (ALE) Analysis Approach to Underwater and Air Explosion Problems. Master's Thesis, Naval Postgraduate School, Monterey, California, September 2000. (Cited on page 205).

[166] B. Zakrisson, B. Wikman, and H.A. Häggblad. Numerical simulations of blast loads and structural deformation from near-field explosions in air. *International Journal of Impact Engineering*, 38(7):597–612, 2011. (Cited on page 205).

[167] B. Zakrisson. Numerical and Experimental Studies of Blast Loading. Master's Thesis, Luleå University of Technology, 2010. (Cited on page 205).

[168] M. Larcher. Simulation of the effects of an air blast wave. Technical Report PUBSY JRC41337, European Commission, JRC, 2007. (Cited on pages 208 & 209).

[169] *LS-Dyna® - Keyword User's Manual Volume II - Material Models, Revision 804*. Livermore Software Technology(LSTC), September 2011. (Cited on page 209).

[170] G. Randers-Pehrson and K.A. Bannister. Airblast Loading Model for DYNA2D and DYNA3D. Technical Report ARL-TR-1310, Army Research Laboratory, March 1997. (Cited on pages 211 & 254).

[171] C.N. Kingery and G. Bulmash. Air blast parameters from TNT spherical air burst and hemispherical surface burst. Technical Report ARBRL-TR-02555, US Army Ballistic Research Laboratory Aberdeen Proving Ground, 1984. (Cited on pages 211 & 254).

[172] Email Correspondence with Dr. L. Schwer of Schwer Engineering & Consulting Services , 2011–2. (Cited on page 214).

[173] E. Oberg, F.D. Jones, H.L. Horton, and H.H. Ryffel. *27^{th} Edition Machinery's Handbook*. Industrial Press Inc., 2004. (Cited on page 221).

[174] G.Y. Grondin, M. Jin, and G. Josi. Slip critical bolted connection – a reliability analysis for design at the ultimate limit state. Structural Engineering Report 270, University of Alberta, Department of Civil & Environmental Engineering, October 2007. (Cited on page 221).

[175] L. Schwer. A Brief Introduction to Coupling Load Blast Enhanced with Multi-Material ALE: The Best of Both Worlds for Air Blast Simulations. *LS-DYNA Forum*, 2010. (Cited on page 254).

[176] P. Horowitz and W. Hill. *The Art of Electronics*. Cambridge University Press, Cambridge, Second edition, 1995. (Cited on pages A-3 & A-7).

[177] *Omega - AC LVDT Displacement Sensor Manual*, 2011. (Cited on page A-3).

[178] E. Hughes, J. Hiley, K. Brown, and I.M.K. Smith. *Hughes Electrical and Electronic Technology*. Pearson Education Limited, Ninth edition, 2005. (Cited on pages A-3 & A-7).

[179] *Capacitive Displacement Sensors - Nanometrology Solutions*. Physik Instrumentation, 2011. (Cited on page A-6).

[180] *Omega - Adjustable Capacitive Proximity Sensor*, 2011. (Cited on page A-7).

[181] *Capacitive Sensors KXS Catalogue*. Rechner Sensors, October 2007. (Cited on page A-7).

[182] M.J. Hargather and G.S. Settles. Laboratory-scale techniques for the measurement of a material response to an explosive blast. *International Journal of Impact Engineering*, 36(7):940–947, 2009. (Cited on pages A-7 & A-8).

[183] B. Pan, K. Qian, H. Xie, and A. Asundi. Two-dimensional digital image correlation for in-plane displacement and strain measurement: a review. *Measurement Science and Technology*, 20(6):062001, 2009. (Cited on page A-8).

[184] *iKnow™Guide to Sensing - An Overview of Banner's Extensive Knowledge Base for Photoelectrics, Lasers, Ultrasonics and Vision Sensing*. Banner Engineering Corporation, First edition, 2004. (Cited on page A-9).

[185] M.F. Spotts. *Mechanical Design Analysis*. Prentice-Hall, 1964. (Cited on page B-2).

[186] G.T. Gray. Classic Split-Hopkinson Pressure Bar Testing. *Materials Park, OH: ASME International, 2000.*, pages 462–476, 2000. (Cited on pages B-2 & B-8).

[187] A.L. Window and G.S. Holister. *Strain Gauge Technology*. Applied Science Publishers Ltd., Barking Essex England, 1982. (Cited on page B-6).

[188] ATI Allegheny Ludlum. Stainless Steel AL 17-4 Precipitation Hardening Alloy - Data Sheet, October 2010. (Cited on page B-9).

Appendices

A Transient Displacement Sensor Design

Contents

Figures

A.1 Introduction

The measurement of the transient midpoint displacement of a target plate subjected to an explosive load is a complex problem due to the rapid deformation/movement of the target plate and the blast environment where the measurement is taken. Traducers utilizing different physical effects such as optic, light, capacitance, resistance and magnetism were investigated. Several factors, such as resolution, range, excitation frequency and cost were considered when selecting the appropriate sensor.

Initial specifications for the displacement sensor were,

1. Measurable displacement range of $0 - 50mm$.
2. Sampling frequency of at least $500kHz$.
3. Robust design to withstand the blast environment.
4. The sensor must provide a voltage output signal in the range of $\pm 5V$

A.2 Sensors Considered

The sensors considered were divided into two categories namely contact and non-contact sensors. As the names suggests contact sensors measure displacement by making physical contact with the surface/point whilst non-contact sensor measures the displacement without any contact with the surface/point.

A.2.1 Contact Sensors

A.2.1.1 Linear Variable Differential Transformers

Linear variable differential transformer (LVDT) (see Figure A.1a) are a popular method of measuring displacement as they are relatively easy to implement, accurate and

(a)

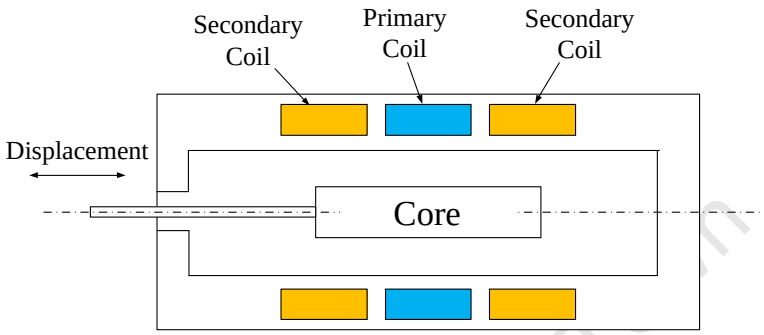

(b)

Figure A.1: Linear Variable Differential Transformer (a) Example of a LVDT [177] and (b) Cross Section of a LVDT [176]

reliable. An LVDT is an electromagnetic device constructed with three coils (one primary coil and two secondary coils) and a movable magnetic core as depicted in Figure A.1b. The primary coil is excited with a constant AC voltage, as the core moves it induces a voltage in the secondary coils. The voltage difference between the secondary coils is linearly proportional to the displacement [176]. Even though LVDT's have a wide measuring range and have a typical accuracy of $0.1 - 1\%$ [176] they are however limited in sampling frequencies(50 to $30kHz$ [176]) which does not meet the required specification and hence LVDT's were not considered any further.

A.2.1.2 Linear Variable Potentiometers

A linear variable potentiometer (LVP) (see Figure A.2a) is constructed of a housing, resistive track and a movable terminal/contact [178]. Figure A.2b is a schematic of a LVP circuit where a known voltage is applied to the track and the displacement

is tracked by measuring the potential difference between the contact and the known voltage. As the contact slides along the track the resistance changes and the potential difference changes which is related to the displacement of the target point. The advantages of implementing LVPs are they have infinite resolution, simple circuitry required to measure the displacement and come in a variety of displacement ranges. However, the amount of electrical noise generated between the track and contact at high velocities will limit the accuracy of the measurement.

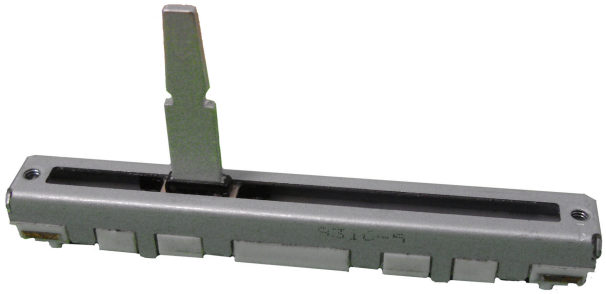

(a)

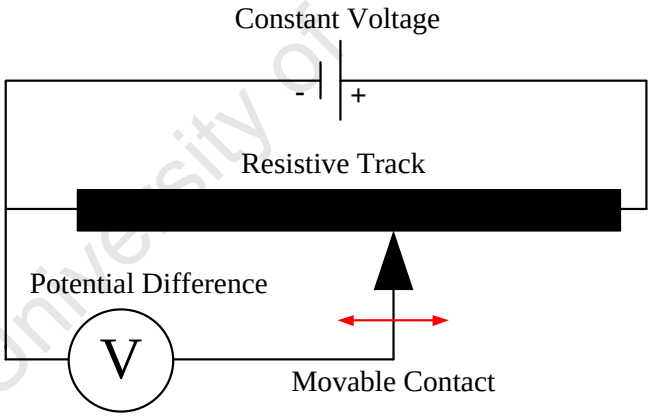

(b)

Figure A.2: Linear Variable Potentiometer (a) an Example and (b) a Schematic

The difficulty of measuring the transient displacement with a contact sensor is attaching the sensor to the plate. Experiments were carried out to determine the optimal attachment of a $M5$ bolt to the target plate, the sensor would be fixed to the $M5$ bolt. Methods such as glueing (Scotch-Weld Epoxy DP490), welding and silver soldering the $M5$ bolt to the midpoint of the plate were investigated. Figures A.3a and A.3b are

photographs of the attachment points after testing had been performed for a glued and silver soldered connection respectively.

In the case of the glued connection (Figure A.3a), the bond between the target plate and the $M5$ bolt failed resulting in the bolt and shaft connected to the sensor detaching from the target plate and destroying the sensor.

(a) (b)

Figure A.3: (a) Failure of Scotch-Weld Epoxy DP490 Bond with Target Plate and (b) Result of M5 Bolt Silver Soldered in Place

Figure A.3b illustrates a target plate after a test where a $M5$ bolt had been silver soldered in place. The profile of the attachment nut, which locates the shaft from the sensor to the $M5$ bolt, can be seen indented into the plate. It must be noted in this experiment the thread of the attachment nut failed resulting in the shaft separating from the bolt and breaking the sensor. No reliable attachment mechanism could be created to fix the sensor to the target plate hence contact sensors were not considered any further.

A.2.1.3 Strain Gauges

Strain gauges have been previously implemented to measure local strains and strain rates of plates subjected to blast loads [122, 125]. Experimental results presented byDuffey and Key [125] showed good correlation to the strains calculated theoretically

and numerically.

Applying the method presented by Duffey and Key [125], five tests were performed on $10mm$ thick target plates with strain gauges bonded at the midpoint of the target plates. The target plates were subjected to varying explosive loads (2, 4 and $25g$ of explosive) in a fully confined blast setup (see Section 3.4.1).

In all five tests the strain gauges remained bonded to the plate however the soldering tab and the connecting cables debonded from the plate and tore off the strain gauge due to the explosively generated transverse stress wave in the plate. Figure A.4 is a photograph of the strain gauge after a test where the soldering tab and cables have been pulled from the gauge. As no results were obtained from the tests this method of measuring the displacement was not pursued any further.

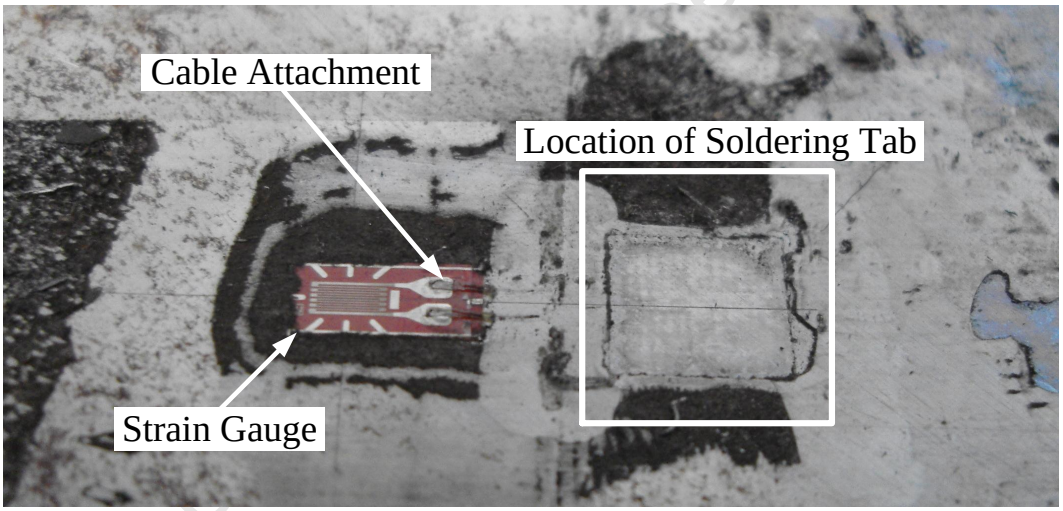

Figure A.4: Results of Cable Whip

A.2.2 Non-Contact Sensors

A.2.2.1 Capacitive-based Sensors

A capacitive-based displacement is a non-contact transducer that uses the electrical property of capacitance to make measurements [179]. Capacitance is an electrical

property of a material ability to store electric charge [178]. The initial capacitance is setup by generating a homogeneous electric field between the sensor and the conductive surface, as the distance between the sensor and the surface changes the capacitance varies, the change in capacitance is proportional to the displacement of the target surface [180]. Figure A.5 illustrates an example of capactive-based displacement sensor.

Figure A.5: Capacitive-based Proximity Transducer [180]

Capacitive transducers have an accurate resolution, into the micrometer range [180] and typically have a small measuring range [176] however large range sensors are available but are costly. The sampling frequencies achievable with capacitive sensors is typically very low ($50Hz$) [176, 181], consequently capacitive traducers were not considered any further.

A.2.2.2 Speckle Interferometry

Three dimensional speckle interferometry has been implemented with success in measuring the full-field transient deformation of explosively loaded plates [126, 182].

Speckle interferometry utilizes a high contrast random speckle pattern on the surface of interest, a coherent light source, two high speed cameras in a stereo configuration and digital image correlation software to determine the full-field displacements and strains of the specimen surface [126, 183]. Figure A.6 presented the experimental setup and speckle pattern utilized by Hargather and Settles [182].

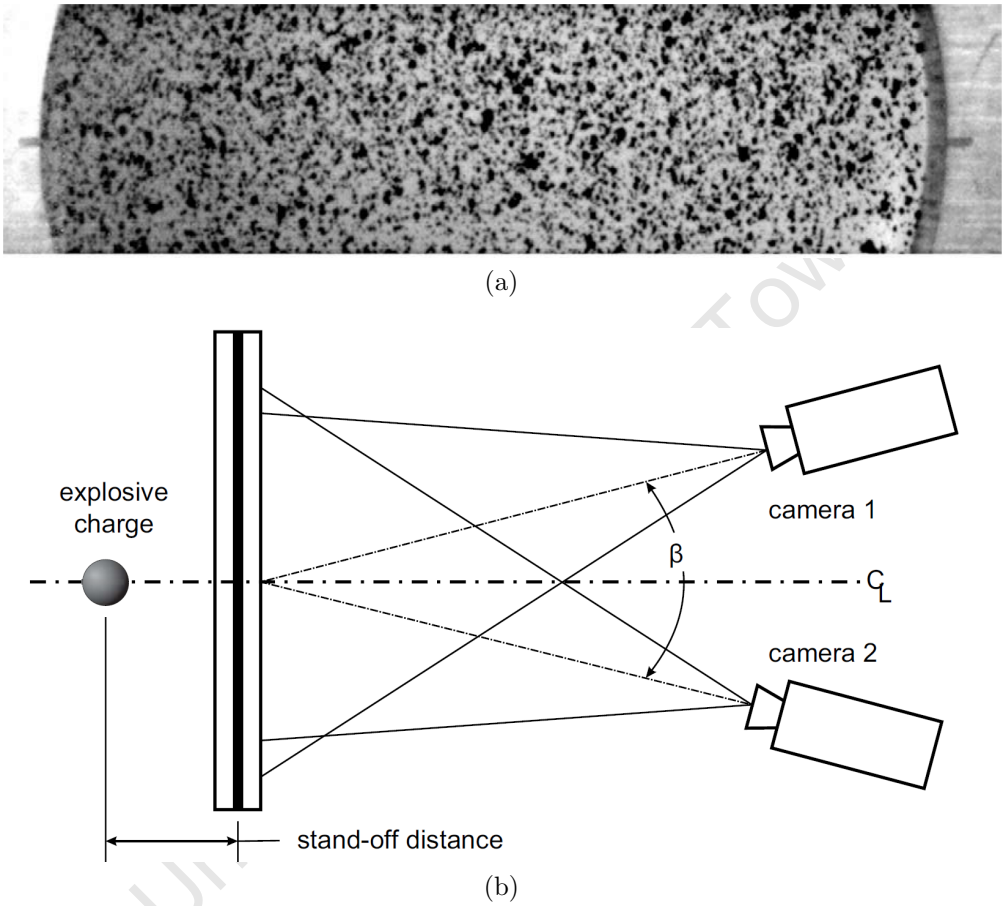

Figure A.6: Three Dimensional Speckle Interferometry Instrumentation [182]: (a) Example of High Contrast Random Speckle Pattern and, (b) Experimental Setup

The main draw backs of implementing speckle interferometry is the cost of the hardware and software and the high risk of damage to the hardware exposed to the blast for these reasons speckle interferometry was not perused any further.

A.2.2.3 Photosensors

Two methods of measuring displacement with photosensors were investigated namely proximity and opposed mode sensors [184]. Figure A.7 illustrates the basic concept of proximity mode sensing where both the receiver and emitter are enclosed in the same housing, the sensor detects the intensity of reflected light from the target surface. As the target surface moves the intensity of the reflected light changes. The sensor converts the change in light intensity, which is related to the displacement of the target surface, into a measurable electrical signal. The draw back of using proximity mode photosensing is that the sensor is heavily reliant on the surface texture of the target surface. As the surface conditions of the target plates are not consistent there will be variations in the sensors output and the light sensor will have to be calibrated to each individual plate for this reason a proximity mode photosensor was not considered any further.

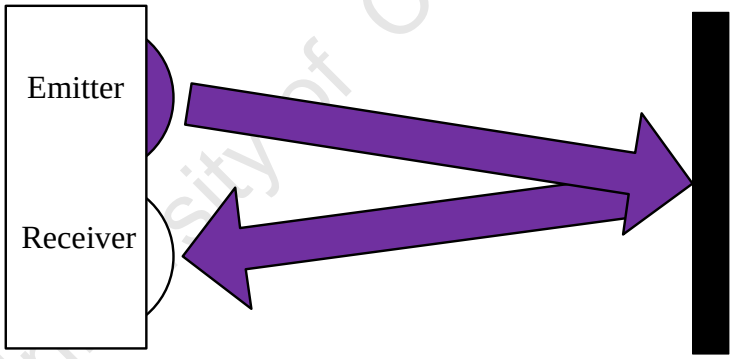

Figure A.7: Schematic of Retro-Reflective Mode Sensor

In an opposed mode sensor the emitter and receiver housed in separate units that are positioned directly opposite each other with the light from the emitter shining directly into the receiver as depicted in Figure A.8. The emitter creates a curtain of light that shines parallel to the plate, as the plate deforms it interrupts the curtain of light and decreases the intensity of light being recorded by the receiver side. The decrease in light is directly related to the displacement of the maximum point of displacement. In this configuration the sensors are independent of the surface texture of the deforming surface.

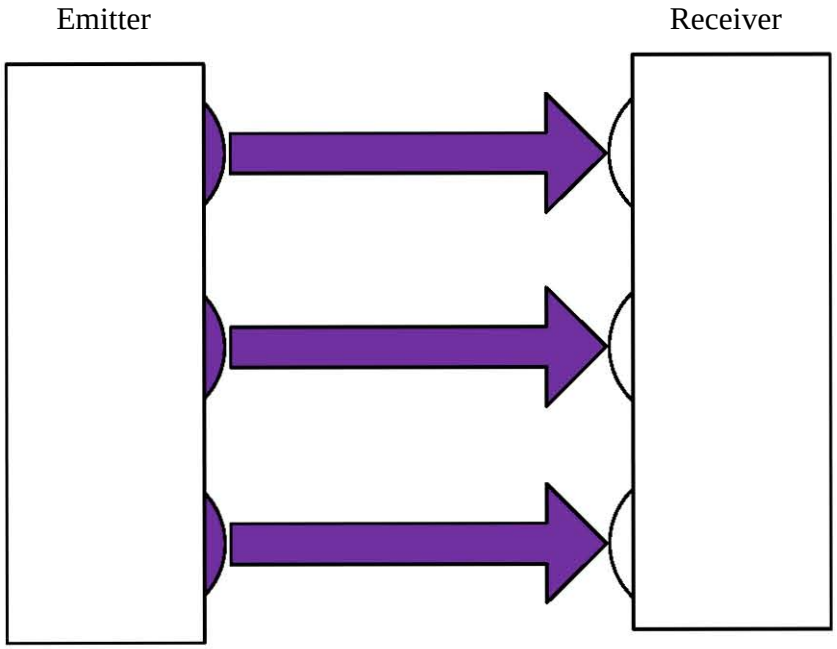

Figure A.8: Schematic of Opposed Mode Sensor

It was decided that transient plate deflection would be measured by opposed mode photosensors. Opposed mode photosensors offer a broad range of measurement, sampling frequency is determined by design, simple circuitry and are inexpensive to manufacture.

A.3 Design of Photosensor

The design of the photosensors was based on the work presented by Nurick [121]. Figure A.9 illustrates the experimental setup of the photosensors implemented by Nurick [121]. A light curtain was generated, with a $250W$ light bulb and two prisms located opposite each other in the clamp frames. The light curtain was parallel to the plate and the reflected into a photovoltaic cell which measures the intensity of light over the cell. When the plate deforms it interrupted the curtain of light, changing the intensity of light on the photovoltaic cell and hence changing the electrical output of the cell which was recorded on an oscilloscope and related to the deflection of the plate.

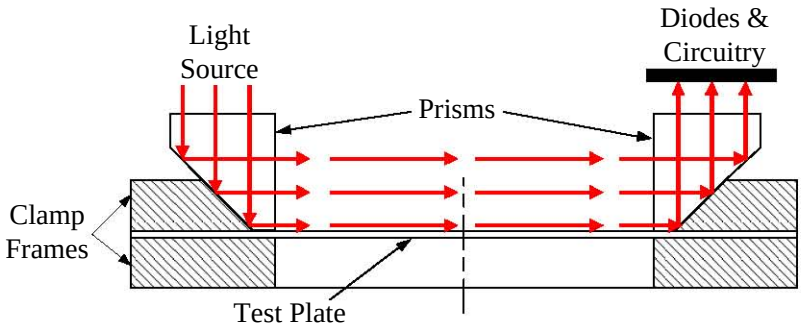

Figure A.9: Photosensors Implemented by Nurick [121]

The conceptual design of Nurick [121] was maintained in the sensor design, however several design changes were made. The photovoltaic cell was replaced with a linear array of silicon infrared photodiodes (OSRAM SFH 229 FA). The photodiodes had a day light filter coating eliminating the effects of ambient light on the measurements. Ten photodiodes, at a spacing of $5mm$ between centres, were soldered in parallel on a printed circuit board (PCB) which gives a measuring range of $50mm$. The PCB and photodiodes were then glued in an aluminium housing which could be secured to the clamp frames as depicted in Figure A.10.

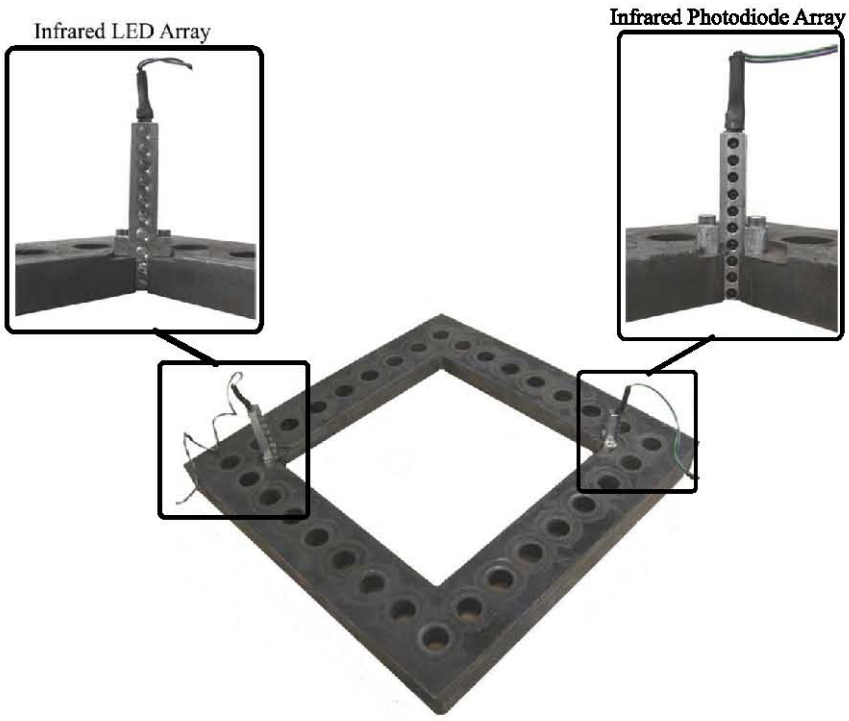

Figure A.10: Location of Infrared Sensor - Fully Confined Top Clamp Frame

The light source implemented by Nurick [121] was replaced with an array of high powered infrared light emitting diodes (LED) (OSRAM SFH 4550). Ten LEDs were connected in series in a linear array at a $7mm$ spacing between centres on a PCB. The PCB and LEDs were glued into a aluminium housing, which was secured to the clamp frame opposite the photodiode array as illustrated in Figure A.10. In this arrangement the infrared beams emitted by the LED overlap and create a solid light curtain that covered the entire length of the photodiode array. Figure A.11 illustrates the light curtain emitted by the LED array and its coverage of the photodiode array.

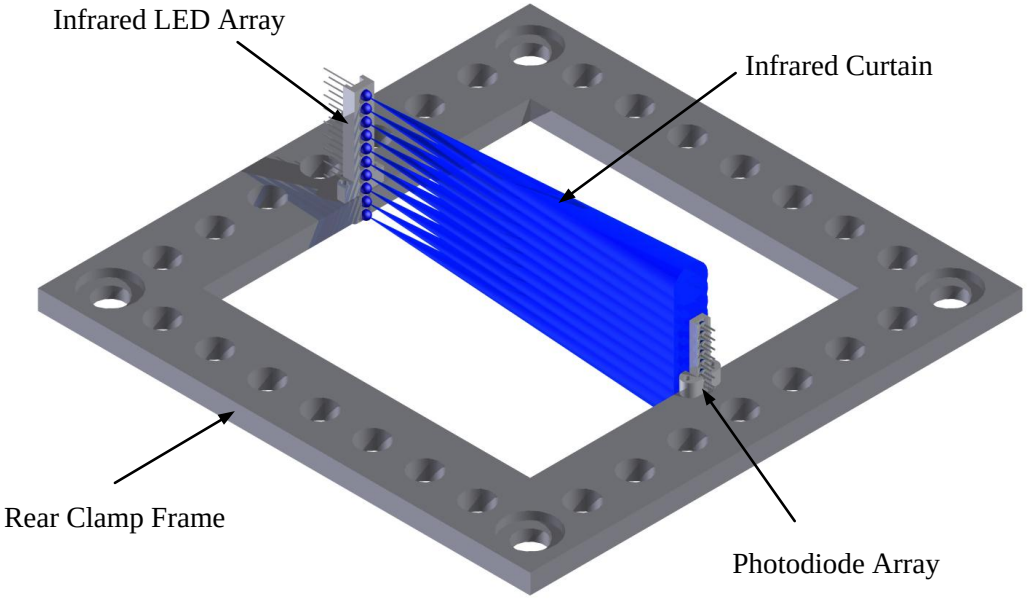

Figure A.11: Light Curtain Emitted from LED Array

The arrays were connected to a circuit which had adjustable voltage power supplies so the initial offsets and intensities of the infrared curtain could be adjusted. The circuit also converted and amplified the light intensity measurements from the photodiode array into a voltage output signal. The circuit was broken in two main sections namely the voltage regulation and amplifier circuits, Figure A.12 is the electrical wiring diagram for the circuit.

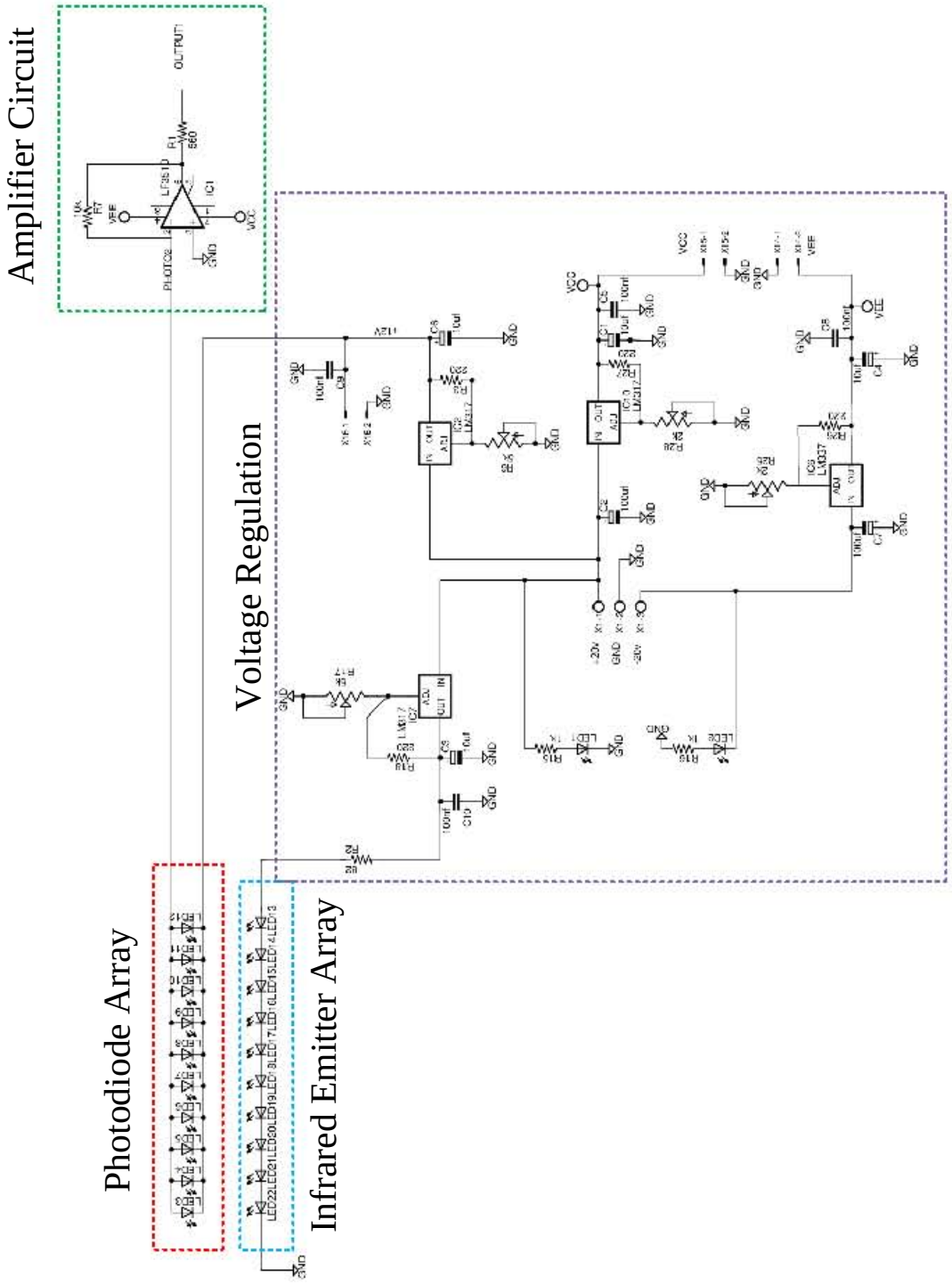

Figure A.12: Circuit Diagram for Opposed Mode Sensor

This page has been intentionally left blank.

B Split Hopkinson Pressure Bar Theory

Contents

Figures

Tables

B.1 Introduction

This appendix lays out the theory implemented to analyse split Hopkinson pressure bar (SHPB) data. The appendix presents the theory of stress waves travelling down bars followed by the theory of one dimensional wave propagation used to analyse the data obtained from the SHPB. Lastly the theory and experimentally obtained Hopkinson bar calibration factors are described.

B.2 Split Hopkinson Bar Theory

This section describes the theory and procedures implemented to analyse SHPB data from which the dynamic stress-strain curves for the materials were obtained. A schematic of the SHPB/specimen interface is illustrated in Figure B.1.

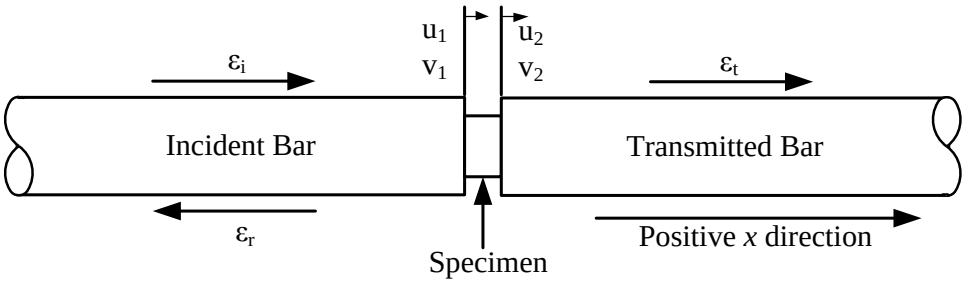

Figure B.1: Schematic of SHPB Specimen Interface

From elementary one dimensional elastic wave theory the wave equation is [148, 185, 186],

$$\frac{\partial^2 u}{\partial x^2} = \frac{1}{C_o^2}\frac{\partial^2 u}{\partial t^2} \tag{B.1}$$

where u is the displacement, t is the time and $C_o = \sqrt{\frac{E}{\rho}}$ is the longitudinal wave speed where E is Young's modulus and ρ id the density of the material.

The general solution to Equation B.1 is,

$$u = f(x - C_o t) + g(x + C_o t) = u_i + u_r \tag{B.2}$$

where f and g are any two functions which represent two waveforms travelling in opposite directions, f in the positive x direction and g in the negative x direction.

The one dimensional strain ($\varepsilon = \frac{\partial u}{\partial x}$, Equation B.3) and velocity ($v = \frac{\partial u}{\partial t}$, Equation B.4) can be determined by differentiating Equation B.2 with respects to x and t respectively.

$$\frac{\partial u}{\partial x} = f' + g' = \varepsilon_i + \varepsilon_r \tag{B.3}$$

$$\frac{\partial u}{\partial t} = -C_o(f' - g') \tag{B.4}$$

where ($'$) denotes the differentiation with respects to the argument $(x + C_o t)$.

Substituting Equation B.3 (strain) into Equation B.4 (velocity) gives,

$$v_1 = \frac{\partial u}{\partial t} = -C_o(\varepsilon_i - \varepsilon_r) \tag{B.5}$$

Noting that in bar wave theory compressive stress is conventionally taken as positive [148] hence the velocity is in the positive x direction.

Substituting $\sigma = E\varepsilon$ and $E = C_o^2\rho$ into Equation B.5, the velocity of the incident bar is written as,

$$v_1 = \frac{1}{C_o\rho}(\sigma_i - \sigma_r) \tag{B.6}$$

The displacement at the end of the incident bar is calculated by integrating Equation B.6 with respects to time.

$$u_1 = \int_o^t v_1 dt = \frac{1}{C_o\rho}\int_o^t (\sigma_i - \sigma_r)dt \tag{B.7}$$

Following the same procedure for the transmitted bar, $u = h(x - C_o t)$, the velocity and displacement at the end of the transmitted bar are,

$$v_2 = \frac{1}{C_o\rho}(\sigma_t) \tag{B.8}$$

$$u_2 = \frac{1}{C_o\rho}\int_o^t (\sigma_t)dt; \tag{B.9}$$

The true strain present in the specimen after testing is given by,

$$\varepsilon_{true} = \int_o^t \frac{dl}{l} = ln\left(\frac{l}{l_o}\right) \tag{B.10}$$

where l_o is the original specimen length and l is the final specimen length.

The instantaneous length of the specimen during the test was calculated as,

$$l_s(t) = l_o - u_1(t) + u_2(t) \tag{B.11}$$

Substituting the instantaneous length of the specimen (Equation B.11) in true strain equation (Equation B.10) the true strain at any time during the test was calculated as,

$$\varepsilon_{true}(t) = ln\left(1 + \frac{u_2(t) - u_1(t)}{l_o}\right) \tag{B.12}$$

The strain rate in the specimen is determined by differentiating the strain with respects to time.

$$\dot{\varepsilon} = \frac{d\varepsilon}{dt} = \frac{v_1 - v_2}{l_s(t)} \tag{B.13}$$

The force at incident bar-specimen interface was given as,

$$F_1 = A_{bar}E(\varepsilon_i - \varepsilon_r) = A_{bar}(\sigma_i - \sigma_r) \tag{B.14}$$

Similarly the force at transmitted bar-specimen interface was given as,

$$F_2 = A_{bar}E\varepsilon_t = A_{bar}\sigma_t \tag{B.15}$$

where A_{bar} is the cross sectional area of the bar and E is the Elastic modulus of the bar.

The true stress in the specimen can only be determined if incompressible plasticity of the specimen is assumed (i.e. volume of specimen remains constant). From the assumption the instantaneous area of the specimen can be calculated with,

$$A_s(t) = \frac{l_o A_o}{l_s(t)} \tag{B.16}$$

where A_s is the instantaneous area of the specimen, A_o is initial area of the specimen, l_o is the initial length of the specimen and $l_s(t)$ is the instantaneous length of the specimen.

The stress at the incident bar-specimen interface is,

$$\sigma_{s1} = \frac{F_1}{A_s(t)} = \frac{A_{bar}}{A_s(t)} (\sigma_i - \sigma_r) \tag{B.17}$$

The stress at the transmitted bar-specimen interface is,

$$\sigma_{s2} = \frac{F_2}{A_s(t)} = \frac{A_{bar}}{A_s(t)} (\sigma_t) \tag{B.18}$$

After the initial 'ringing up' period of the specimen and reaching a stable stress state it can be said that $\sigma_{s1} = \sigma_{s2}$. The use of Equation B.17 to determine the stress is term '2-wave' analysis as the equation incorporates two waves (σ_i, σ_r) whilst the use of Equation B.18 is termed '1-wave' analysis. Large oscillations are present, especially near the yield stress, in the '2-wave' analysis. The dynamic stress-strain curves in this report were constructed with '1-wave' analyse, by combining Equations B.18 and B.12.

B.3 Hopkinson Bar Calibration

A calibration factor (K) was required to convert the strain gauge signals, in volts, to the axial stress in both the incident and transmitted bars. This section describes three methods for calculating the calibration factor and the procedures employed to obtained the required material properties of the bars for the calculation of the calibration factor.

B.3.1 Theoretical Calibration Factor

A theoretical calibration factor based on strain gauge theory and amplifier characteristics was calculated. Based on strain gauge theory the voltage output from the strain gauges in a Wheatstone bridge configuration is [187],

$$V_{out} = \frac{K_{gf} N \varepsilon V_{ex}}{4} \tag{B.19}$$

where V_{out} is the output voltage from the strain gauges, K_{gf} is the gauge factor, N is the number of active strain gauges in the Wheatstone bridge, ε is the strain and V_{ex} is the bridge excitation voltage.

The voltage from the strain gauges (V_{out}) was amplified by a constant gain (G) amplifier circuit. The amplified voltage was recorded by the data acquisition equipment. The voltage read (V_{read}) by the data acquisition equipment was calculated as,

$$V_{read} = V_{out} \times G \tag{B.20}$$

Noting that $\sigma = E\varepsilon$ and performing the appropriate substitutions the stress in the bar can be written as,

$$\sigma = \left(\frac{4E}{G K_{gf} N V_{ex}} \right) V_{read} \tag{B.21}$$

which can be re-written as,

$$\sigma = K V_{read}$$

In the setup of the mini-SHPB the gauge factor (K_{gf}) was 2.12, the number of active strain gauges (N) was 4, and the gain (G) set on the amplifier circuit was 1000 resulting in a theoretical calibration factor of,

$$K_{theory} = \frac{E}{2120 V_{ex}} \tag{B.22}$$

B.3.2 Momentum Balance Calibration Factor

The second method of calculating the calibration factor is based on a momentum balance on the striker before and after impacting the incident bar. The calibration factor based on a momentum balance of the striker can be shown to be [40],

$$K_{mom} = \frac{I}{A_b \int_0^t V_{read} dt} \tag{B.23}$$

where A_b is the area of the incident bar and I is the total impulse transferred during the impact and is calculated using Equation B.24

$$I = m_{striker} \times (v_o - v_{reb}) \tag{B.24}$$

where $m_{striker}$ is the mass of the striker, v_o is the velocity of the striker prior to impact and v_{reb} is the rebound velocity of the striker.

The velocity of the striker before impact was measured with a light trap at the end of the barrel. The rebound velocity was calculated as,

$$v_{reb} = \frac{v_o \left(\frac{A_s}{A_b} - 1 \right)}{\left(\frac{A_s}{A_b} + 1 \right)} \tag{B.25}$$

where A_s is the area of the striker and A_o is the area of the incident bar.

B.3.3 Stress Calculation Calibration Factor

The maximum stress in the bar was calculated with [186],

$$\sigma_{max} = \frac{A_s}{A_s + A_b} C_o \rho v_o \tag{B.26}$$

where A_s is the area of the striker, A_b is the area of the bar, C_o is the wave speed of the bar, ,ρ is the density of the bar and V_o is the impact velocity of the striker.

The maximum voltage (V_{read}^{max}) was taken as the mean voltage of the plateau region of the voltage signal. The stress calibration factor is given as,

$$K_{stress} = \frac{\sigma_{max}}{V_{read}^{max}} \tag{B.27}$$

B.3.4 Experimental Calibration Factor

To obtain the calibration factors presented in Section B.3 material properties of the bars such as the Elastic modulus (E), density of the bars (ρ) and the wave speed of the bars (C_o) are required. This section describes the methods used to obtain the various material properties.

B.3.4.1 Bar Properties

The longitudinal wave speed of the bars was determined by accurately measuring the time for a stress wave to travel a known distance. The incident and transmitted bar were placed in contact with each other (no specimen between the bars) and a stress wave applied to the end of the incident bar. The time taken for the stress wave to travel between the strain gauges on the incident and transmitted bar was recorded. Knowing the distance between the strain gauges the longitudinal wave speed was calculated.

The density of the bars was calculated by accurately weighing the bars and dividing by the volume of the bars. The elastic modulus of the bar was calculated using Equation B.28.

$$E = C_o^2 \rho \tag{B.28}$$

Table B.1 lists the material properties of bars required for calculating the calibration factor. The values listed correlate well with published values of precipitated hardened stainless steel [188].

Table B.1: Physical Properties of Hopkinson Bars

Wave Speed (C_o) (m/s)	Density (ρ) (kg/m^3)	Elastic Modulus (E) (GPa)
5042.9	7719.5	196.3

B.3.4.2 Calibration Factor

Using the material properties listed in Table B.1 the calibration factors presented in Section B.3 were calculated. Table B.2 lists the three calibration factors obtained from ten tests and the averages.

Table B.2: Calibration Factors Determined for Split-Hopkinson Pressure Bars

Test Number	$K_{theory}(MPa/Volt)$	$K_{mom}(MPa/Volt)$	$K_{stress}(MPa/Volt)$
1	58.63	56.27	56.63
2	58.63	55.75	56.40
3	58.63	56.35	56.69
4	58.63	58.00	58.72
5	58.63	59.12	58.87
6	58.63	56.47	57.89
7	58.63	56.45	57.03
8	58.63	57.49	57.44
9	58.63	56.84	57.05
10	58.63	56.43	57.02
Averages	58.63	56.92	57.37

For the analysis of the SHPB data the momentum calibration factor was used to determine the dynamic stress-strain curves. The momentum calibration factor was selected as it closely resembles the actual stress states present in the bars.

C Dynamic Testing Results

Contents

Figures

C.1 Introduction

A series of high strain rate tests were carried out on a split Hopkinson pressure bar (SHPB) to obtain material properties at high strain rates for the different target plate materials. The target plate materials were categorised into three series by the thickness of the target plate (3, 4 and 5mm). Figures C.1, C.2 and C.3 depict the high strain rate results for the tests performed on the 3, 4 and 5mm thick specimens respectively. Each graphs depicts the results for the specimens cut through the thickness of the material and in both in-plane directions (rolling direction and transverse to rolling direction) to illustrate the isotropic behaviour of the materials. Tests were performed at two different strain rates to investigate the effects of strain rate on the response of the materials in question.

There was some variation evident in the results as the exact target strain rate is is not achievable and hence slightly different strain rates were observed and the response varied with the strain rate. The results establish that the increase in the stain rate increases the flow stress.

For clarity, the results in Figures C.1, C.2 and C.3 have been separated into the three directions the specimens were cut in Figures C.4 ,C.5 and C.6 respectively.

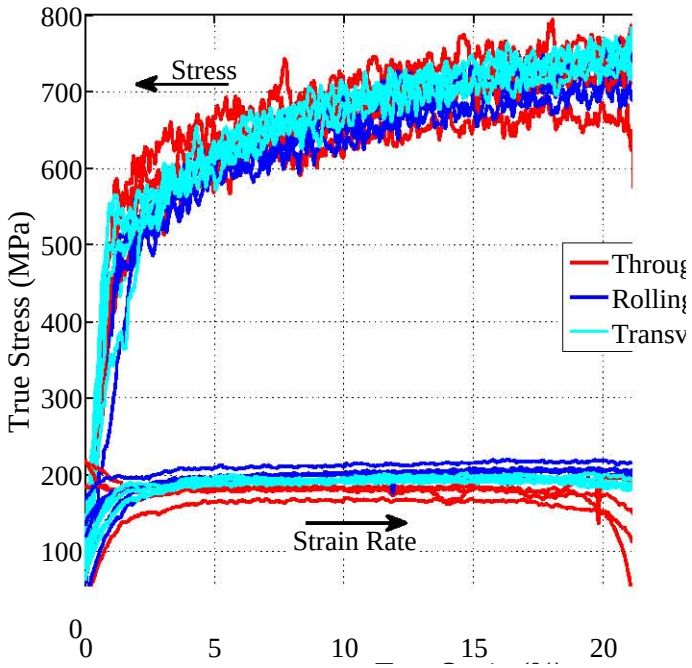

(a) $3mm$ SHPB Results at $\dot{\varepsilon} = \pm 1700 s^{-1}$

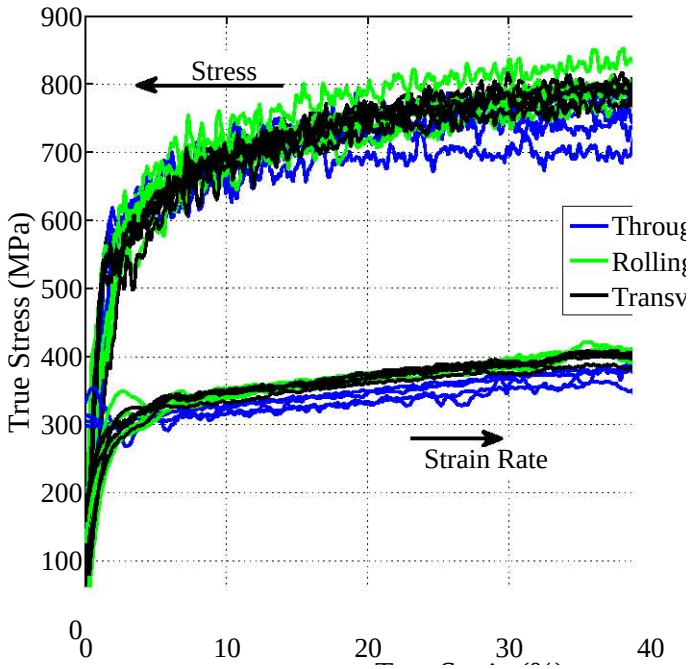

(b) $3mm$ SHPB Results at $\dot{\varepsilon} = \pm 3300 s^{-1}$

Figure C.1: High Strain Rate Response of $3mm$ Thick Plate

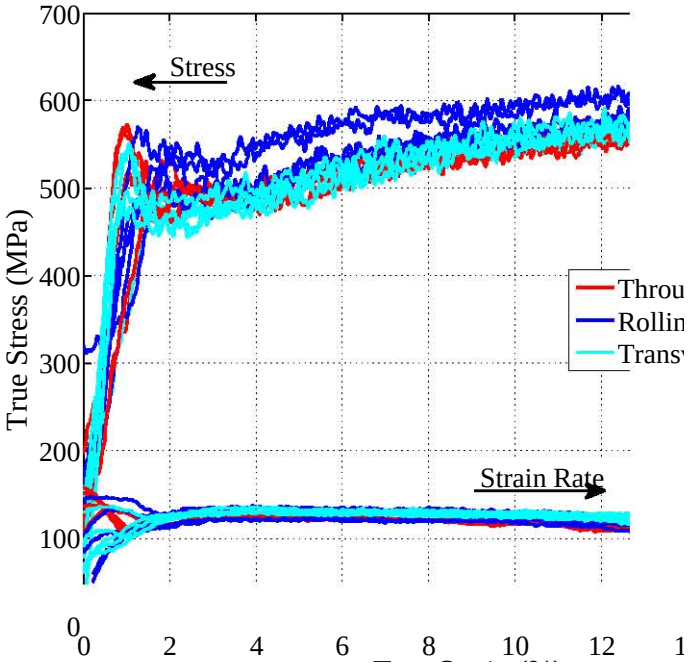

(a) $4mm$ SHPB Results at $\dot{\varepsilon} = \pm 1290 s^{-1}$

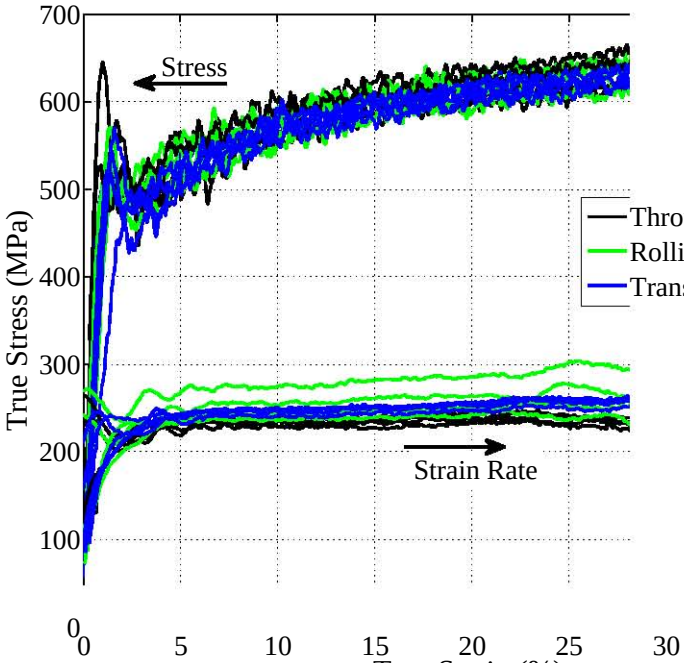

(b) $4mm$ SHPB Results at $\dot{\varepsilon} = \pm 2200 s^{-1}$

Figure C.2: High Strain Rate Response of $4mm$ Thick Plate

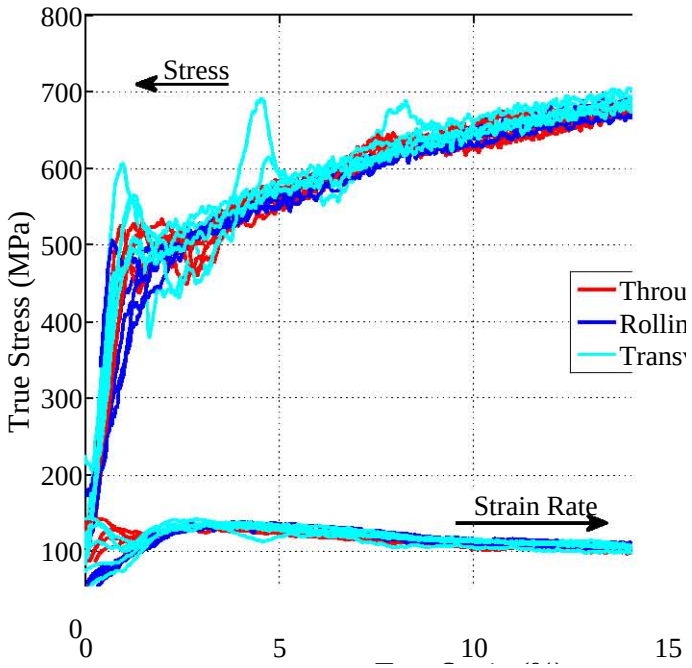

(a) $5mm$ SHPB Results at $\dot{\varepsilon} = \pm 1100 s^{-1}$

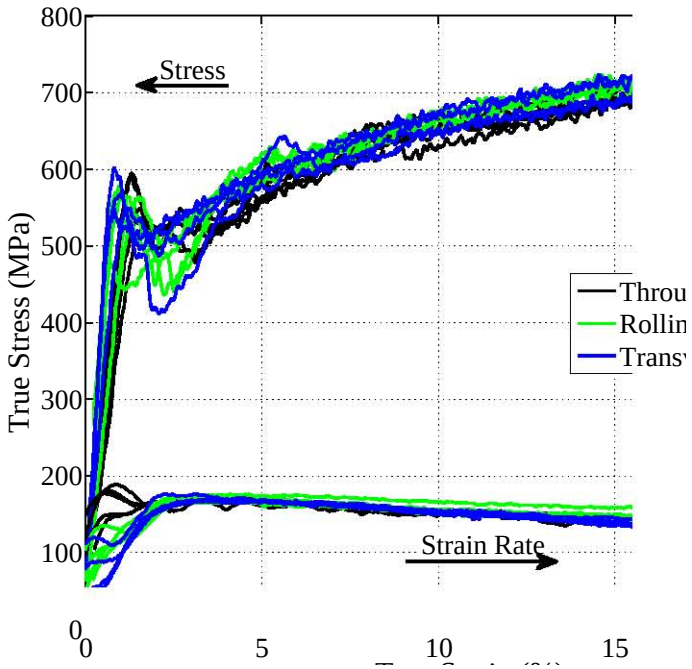

(b) $5mm$ SHPB Results at $\dot{\varepsilon} = \pm 1500 s^{-1}$

Figure C.3: High Strain Rate Response of $5mm$ Thick Plate

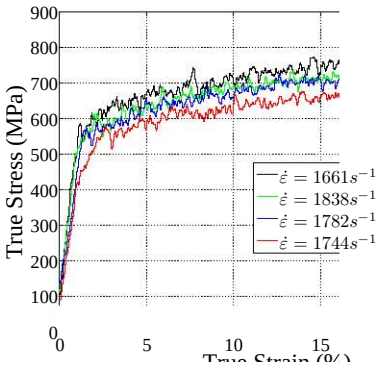

(a) Through Thickness Results at $\dot{\varepsilon} = \pm 1700s^{-1}$

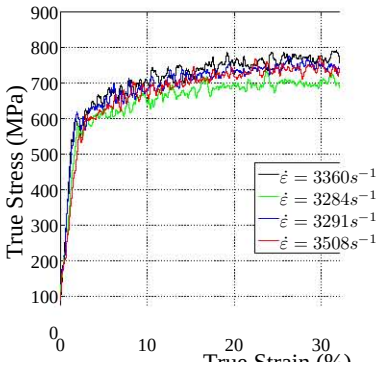

(b) Through Thickness Results at $\dot{\varepsilon} = \pm 3300s^{-1}$

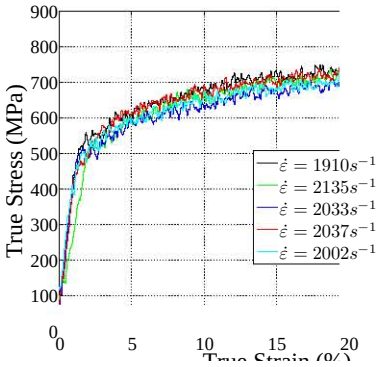

(c) Rolling Direction Results at $\dot{\varepsilon} = \pm 1700s^{-1}$

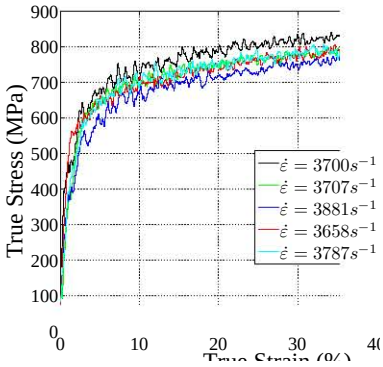

(d) Rolling Direction Results at $\dot{\varepsilon} = \pm 3300s^{-1}$

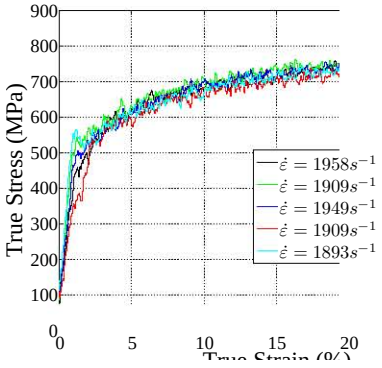

(e) Traverse Direction Results at $\dot{\varepsilon} = \pm 1700s^{-1}$

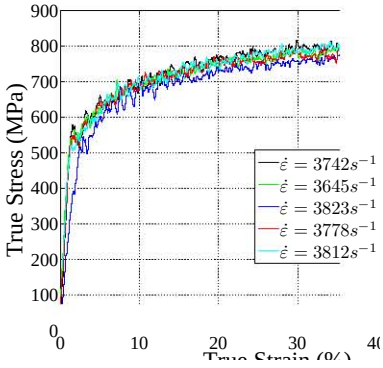

(f) Traverse Direction Results at $\dot{\varepsilon} = \pm 3300s^{-1}$

Figure C.4: High Strain Rate Results for $3mm$ Thick Plate Separated into Different Cut Directions

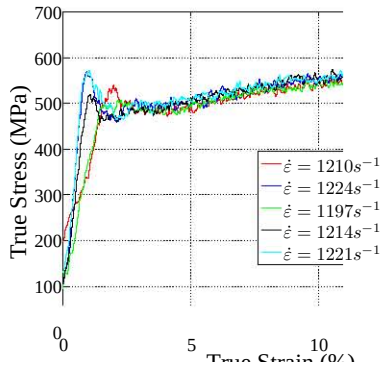

(a) Through Thickness Results at $\dot{\varepsilon} = \pm 1290s^{-1}$

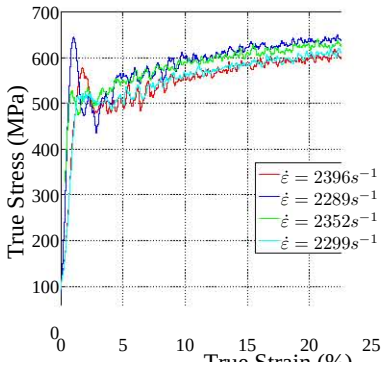

(b) Through Thickness Results at $\dot{\varepsilon} = \pm 2200s^{-1}$

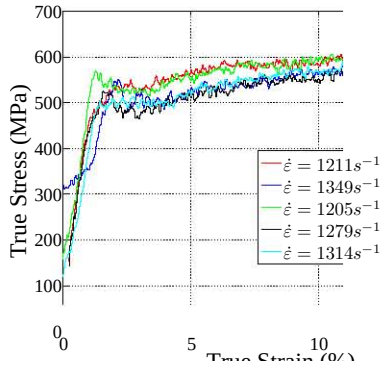

(c) Rolling Direction Results at $\dot{\varepsilon} = \pm 1290s^{-1}$

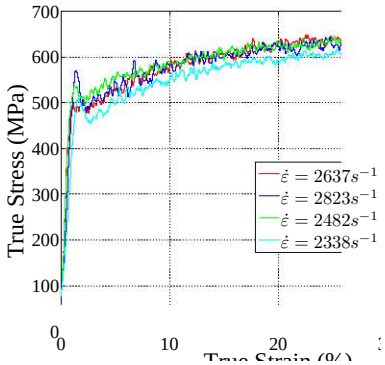

(d) Rolling Direction Results at $\dot{\varepsilon} = \pm 2200s^{-1}$

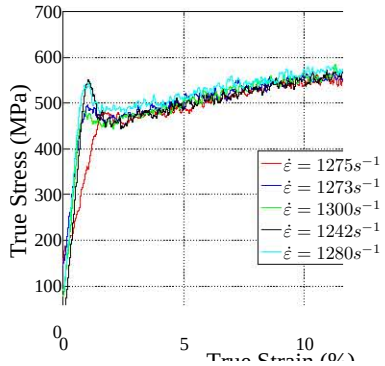

(e) Traverse Direction Results at $\dot{\varepsilon} = \pm 1290s^{-1}$

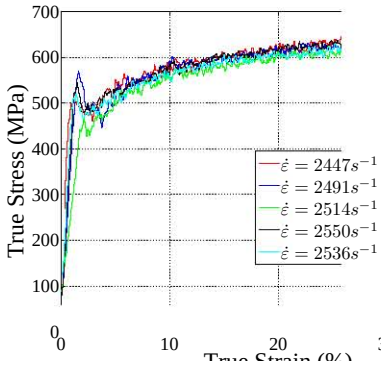

(f) Traverse Direction Results at $\dot{\varepsilon} = \pm 2200s^{-1}$

Figure C.5: High Strain Rate Results for $4mm$ Thick Plate Separated into Different Cut Directions

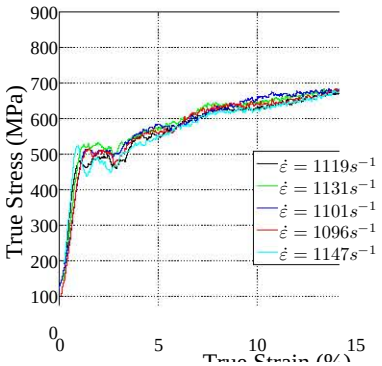

(a) Through Thickness Results at $\dot{\varepsilon} = \pm 1100s^{-1}$

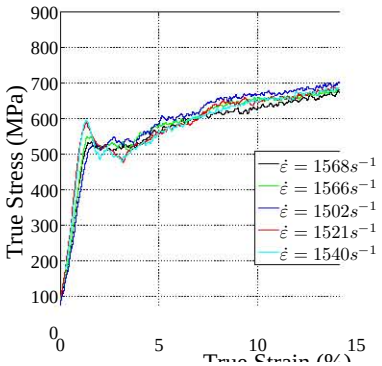

(b) Through Thickness Results at $\dot{\varepsilon} = \pm 1500s^{-1}$

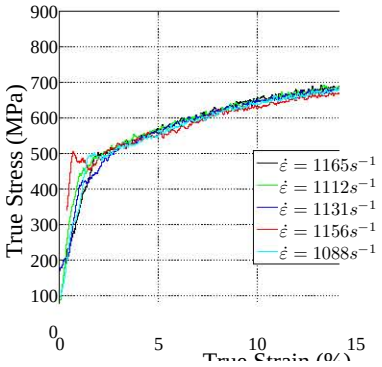

(c) Rolling Direction Results at $\dot{\varepsilon} = \pm 1100s^{-1}$

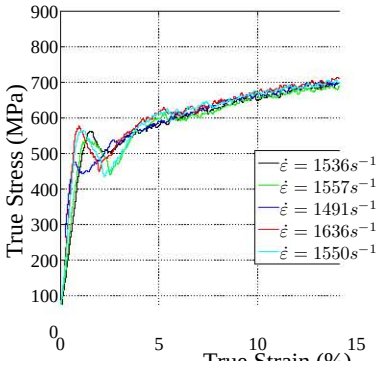

(d) Rolling Direction Results at $\dot{\varepsilon} = \pm 1500s^{-1}$

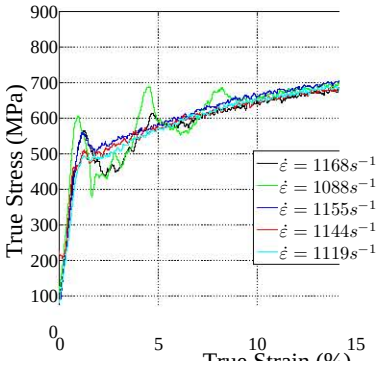

(e) Traverse Direction Results at $\dot{\varepsilon} = \pm 1100s^{-1}$

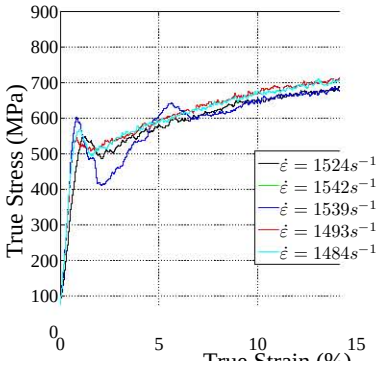

(f) Traverse Direction Results at $\dot{\varepsilon} = \pm 1500s^{-1}$

Figure C.6: High Strain Rate Results for $5mm$ Thick Plate Separated into Different Cut Directions

This page has been intentionally left blank.

D Transient Deflection Results

Contents

Figures

Tables

D.1 Introduction

The transient deflections, measured with the photosensors, for the different degrees of confinement are presented in this Appendix. Tables D.1, D.2 and D.3 list the charge masses and figures associated with the transient deflection of the unconfined, fully vented and fully confined blast load experiments respectively. The tables also lists experiments where the sensors failed and which experiments no data was captured.

Table D.1: Unconfined Transient Midpoint Deflection Results

3mm Thick Plate			**4mm Thick Plate**			**5mm Thick Plate**		
Test Number	Charge Mass(g)	Figure Number	Test Number	Charge Mass(g)	Figure Number	Test Number	Charge Mass(g)	Figure Number
UC-3-1	10	D.1	UC-4-1	30	D.5	UC-5-1	20	D.9
UC-3-2	30	Failure	UC-4-2	30	D.5	UC-5-2	40	D.10
UC-3-3	40	D.1	UC-4-3	40	D.6	UC-5-3	10	D.9
UC-3-4	50	D.2	UC-4-4	40	Failed	UC-5-4	15	D.9
UC-3-5	50	D.2	UC-4-5	50	D.7	UC-5-5	50	Failed
UC-3-6	60	D.3	UC-4-6	50	No Data	UC-5-6	20	Failed
UC-3-7	60	D.3	UC-4-7	60	No Data	UC-5-7	50	D.10
UC-3-8	70	D.4	UC-4-8	60	D.8	UC-5-8	50	D.10
UC-3-9	70	D.4	UC-4-9	70	D.8	UC-5-9	70	Failed
UC-3-10	70	D.4	UC-4-10	70	Failure	UC-5-10	70	D.11
UC-3-11	30	No Data	UC-4-11	50	D.7	UC-5-11	70	No Data
						UC-5-12	60	No Data

Table D.2: Fully Vented Transient Midpoint Deflection Results

3mm Thick Plate			**4mm Thick Plate**			**5mm Thick Plate**		
Test Number	Charge Mass(g)	Figure Number	Test Number	Charge Mass(g)	Figure Number	Test Number	Charge Mass(g)	Figure Number
FV-3-1	10	D.12	FV-4-1	20	D.13	FV-5-1	30	No Data
FV-3-2	10	D.12	FV-4-2	30	D.13	FV-5-2	30	D.15
FV-3-3	30	D.12	FV-4-3	30	D.13	FV-5-3	50	D.17
FV-3-4	30	Failure	FV-4-4	40	D.14	FV-5-4	20	D.15
FV-3-5	40	Failure	FV-4-5	40	D.14	FV-5-5	20	D.15
FV-3-6	40	Failure	FV-4-6	50	D.14	FV-5-6	40	D.16
FV-3-7	20	No Data	FV-4-7	50	D.14	FV-5-7	40	D.16
FV-3-8	40	No Data	FV-4-8	60	No Data	FV-5-8	50	D.17
FV-3-9	40	Failure	FV-4-9	60	No Data	FV-5-9	60	D.17
FV-3-10	20	D.12				FV-5-10	60	Failure
FV-3-11	60	Failure						
FV-3-12	50	Failure						
FV-3-13	60	No Data						

Table D.3: Fully Confined Transient Midpoint Deflection Results

3mm Thick Plate			4mm Thick Plate			5mm Thick Plate		
Test Number	Charge Mass(g)	Figure Number	Test Number	Charge Mass(g)	Figure Number	Test Number	Charge Mass(g)	Figure Number
FC-3-1	20	D.18	FC-4-1	20	No Data	FC-5-1	20	D.20
FC-3-2	20	D.18	FC-4-2	30	No Data	FC-5-2	20	D.20
FC-3-3	30	D.18	FC-4-3	40	No Data	FC-5-3	30	D.21
FC-3-4	30	No Data	FC-4-4	40	Failure	FC-5-4	30	D.21
FC-3-5	40	No Data	FC-4-5	30	D.19	FC-5-5	40	D.22
FC-3-6	50	D.18	FC-4-6	20	D.19	FC-5-6	40	D.22
FC-3-7	60	D.18	FC-4-7	50	D.19	FC-5-7	50	D.23
FC-3-8	70	D.18	FC-4-8	50	D.19	FC-5-8	50	D.23
			FC-4-9	60	D.19	FC-5-9	60	D.24
			FC-4-10	70	D.19	FC-5-10	70	Failed

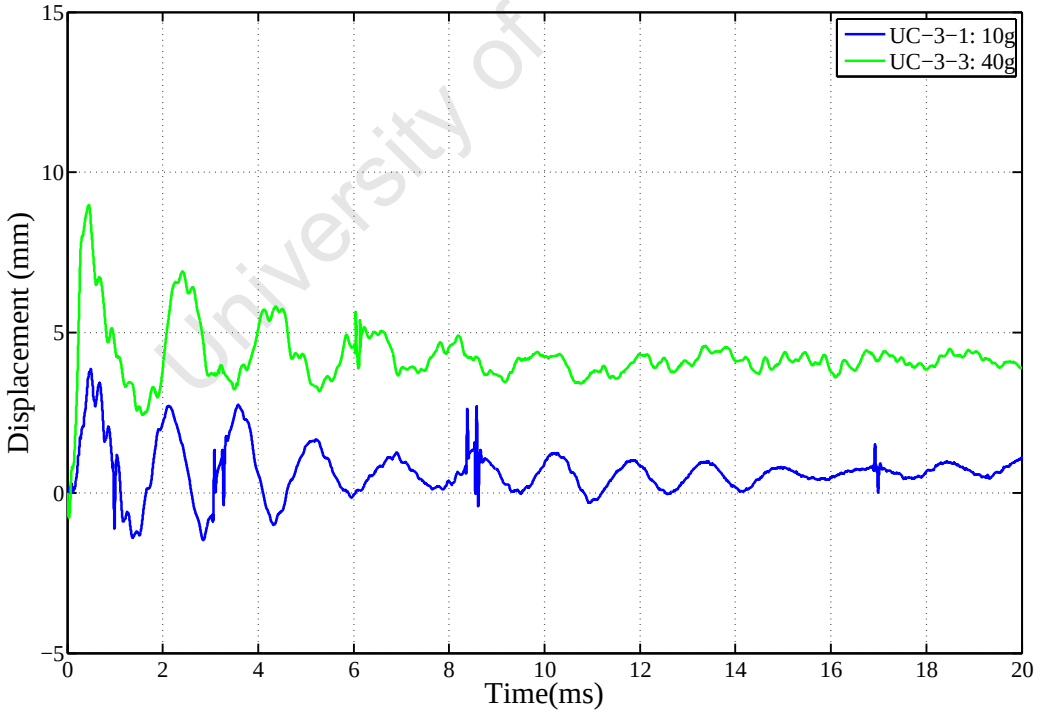

Figure D.1: Transient Deflection Results for UC-3-1 and UC-3-3

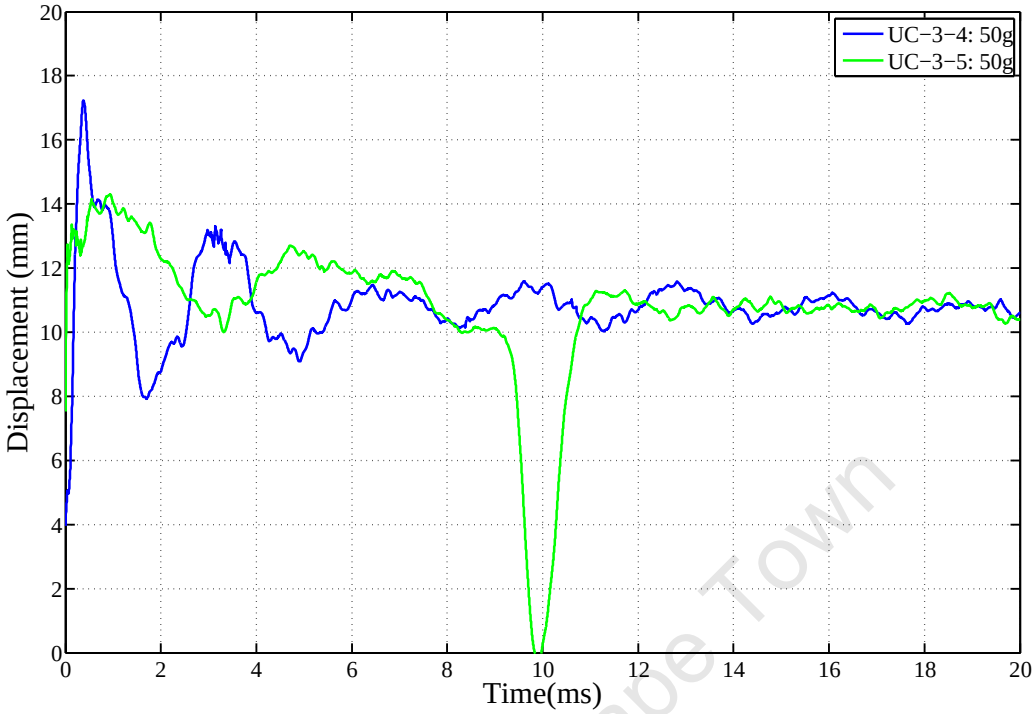

Figure D.2: Transient Deflection Results for UC-3-4 and UC-3-5

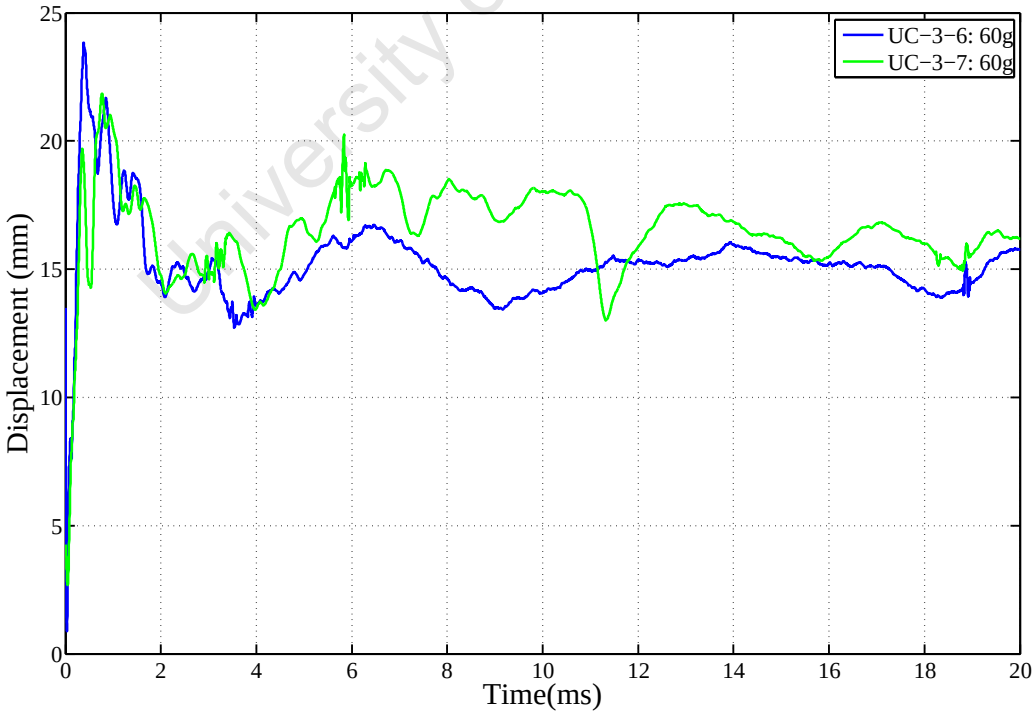

Figure D.3: Transient Deflection Results for UC-3-6 and UC-3-7

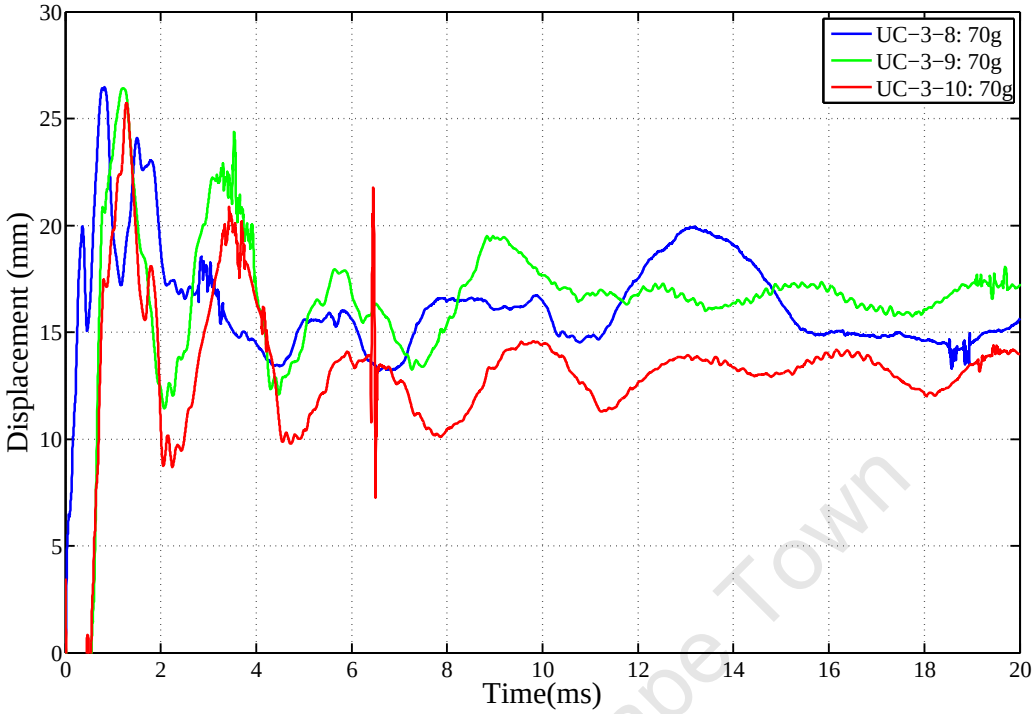

Figure D.4: Transient Deflection Results for UC-3-8, UC-3-9 and UC-3-10

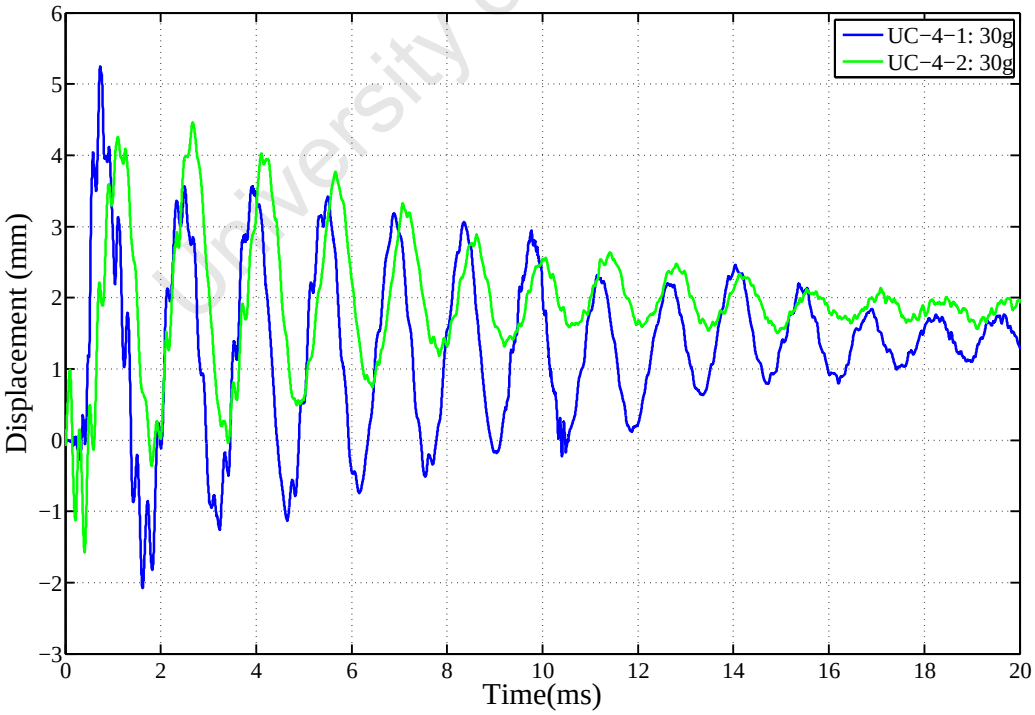

Figure D.5: Transient Deflection Results for UC-4-1 and UC-4-2

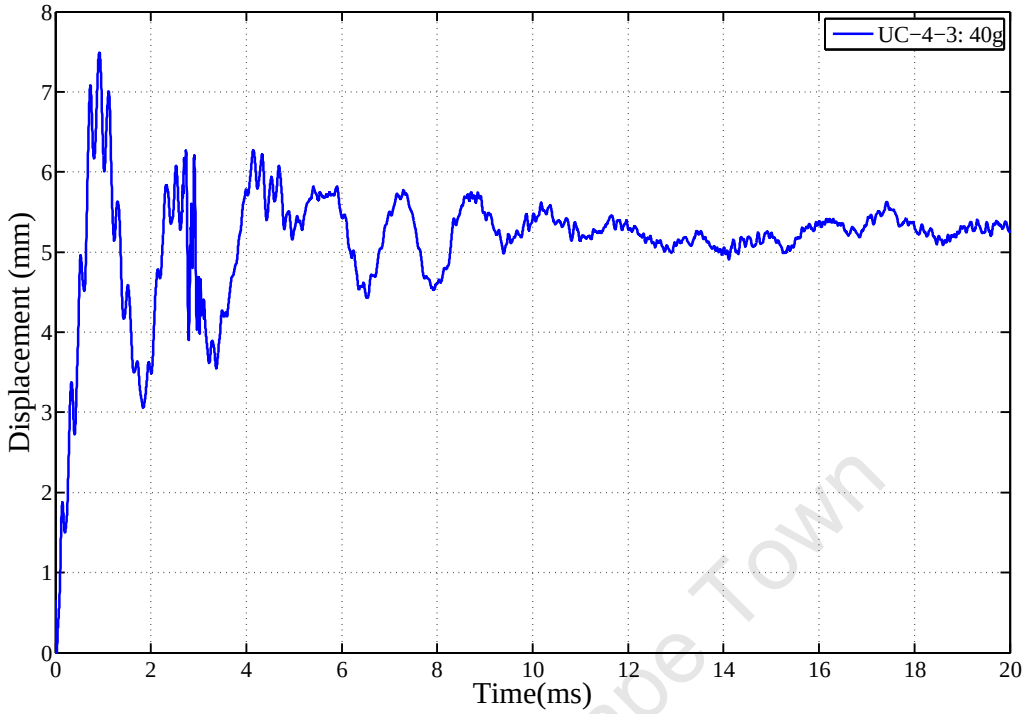

Figure D.6: Transient Deflection Results for UC-4-3

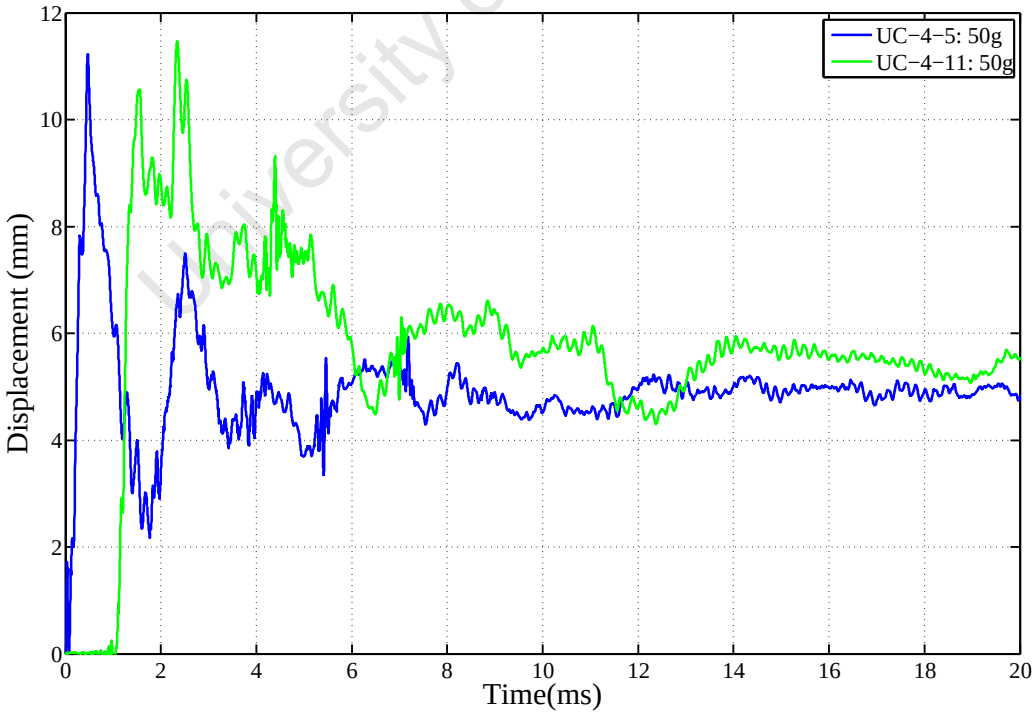

Figure D.7: Transient Deflection Results for UC-4-5 and UC-4-11

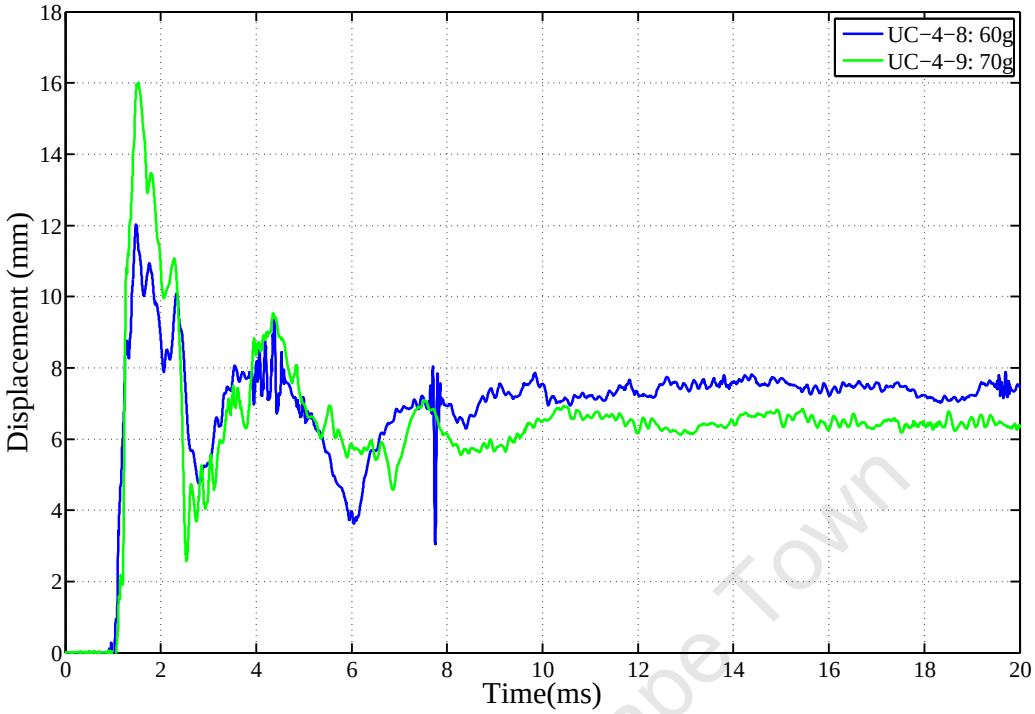

Figure D.8: Transient Deflection Results for UC-4-8 and UC-4-9

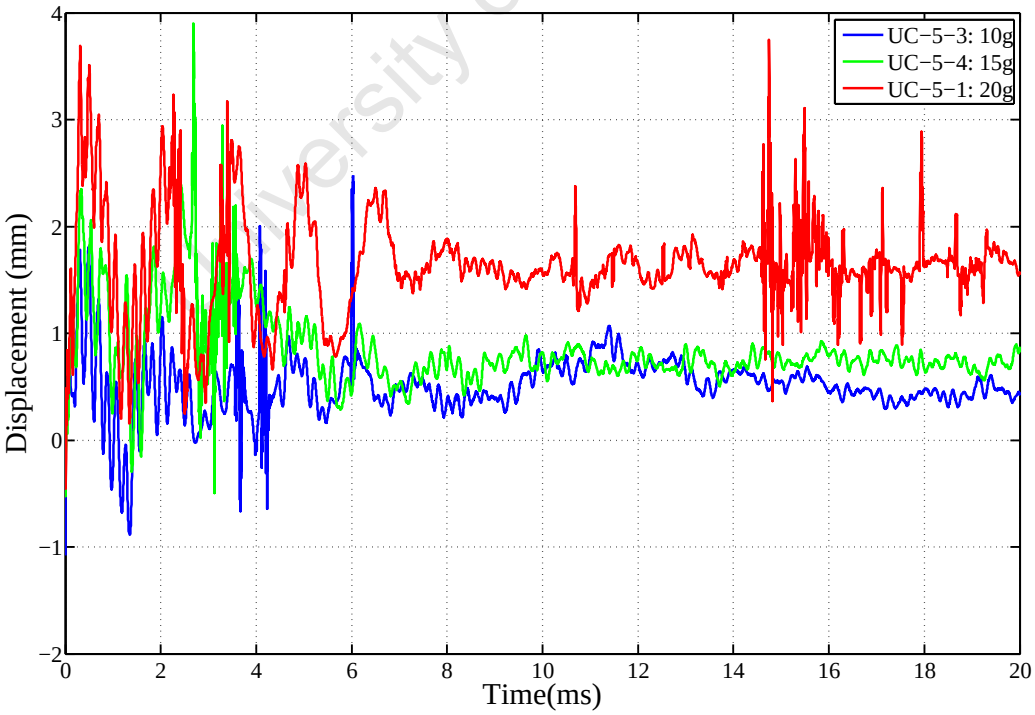

Figure D.9: Transient Deflection Results for UC-5-1, UC-5-3 and UC-5-4

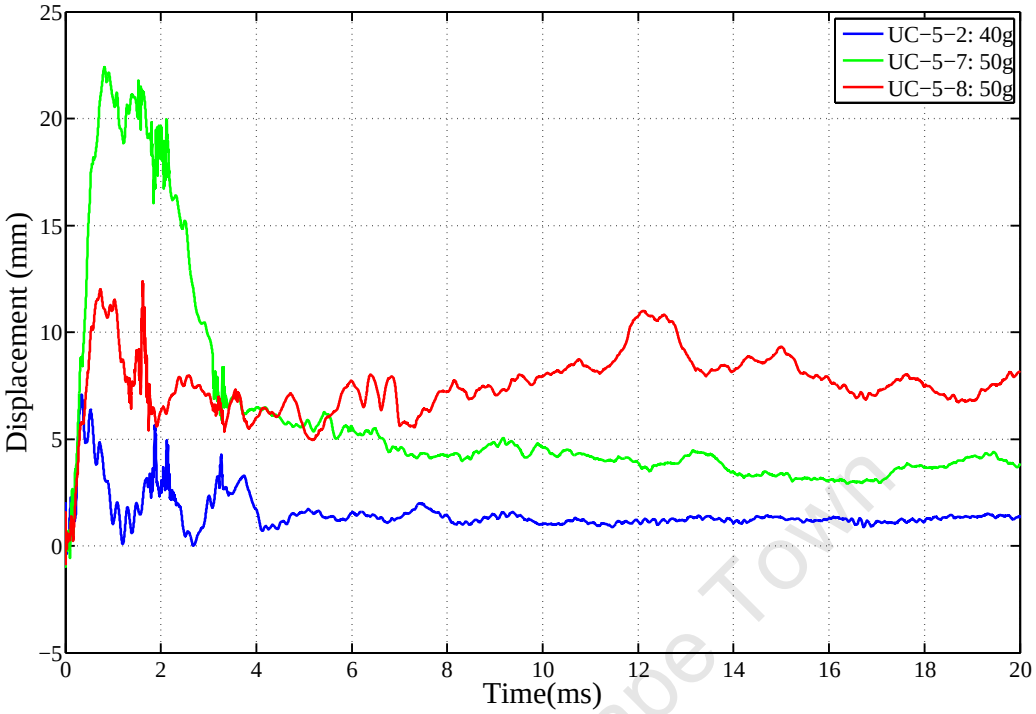

Figure D.10: Transient Deflection Results for UC-5-2, UC-5-7 and UC-5-8

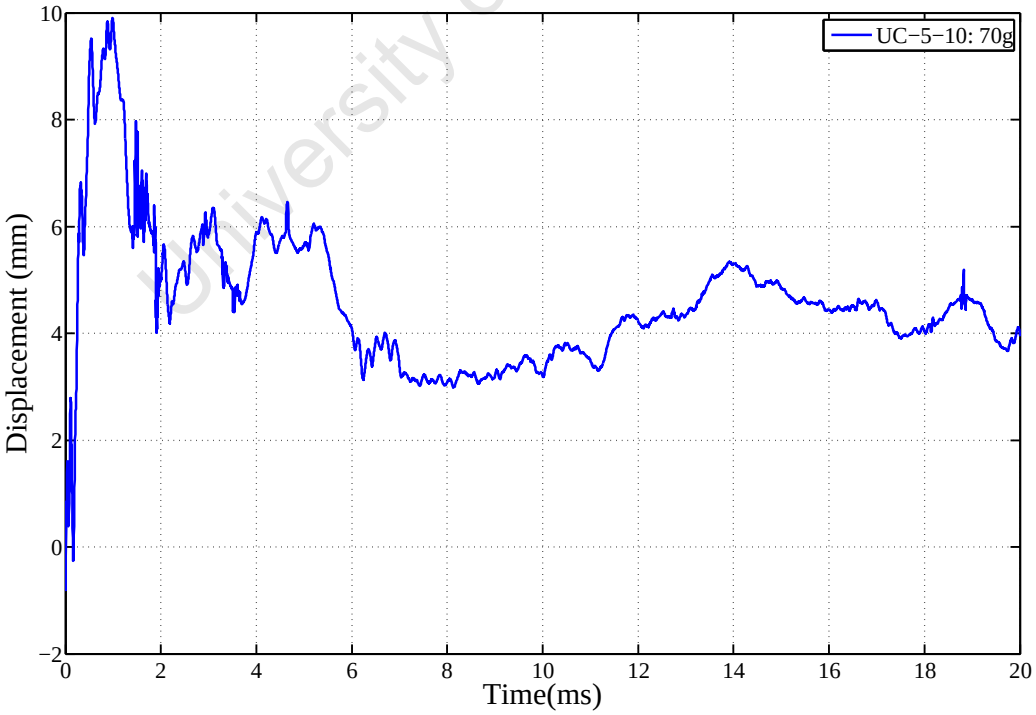

Figure D.11: Transient Deflection Results for UC-5-10

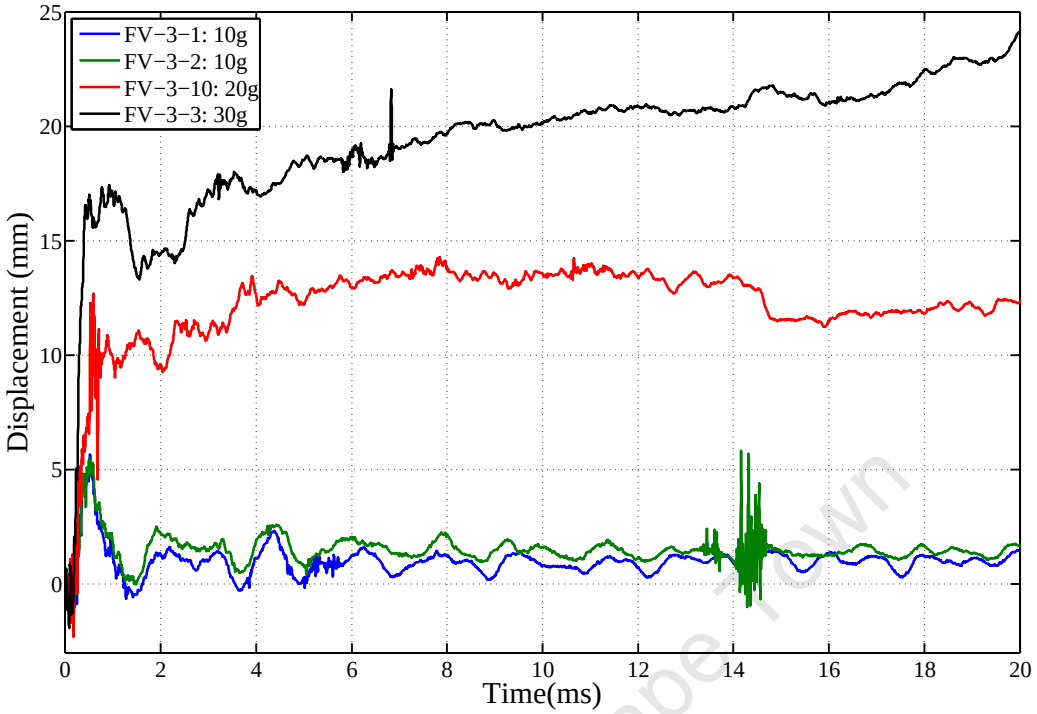

Figure D.12: Transient Deflection Results for FV-3-1, FV-3-3, FV-3-3 and FV-3-10

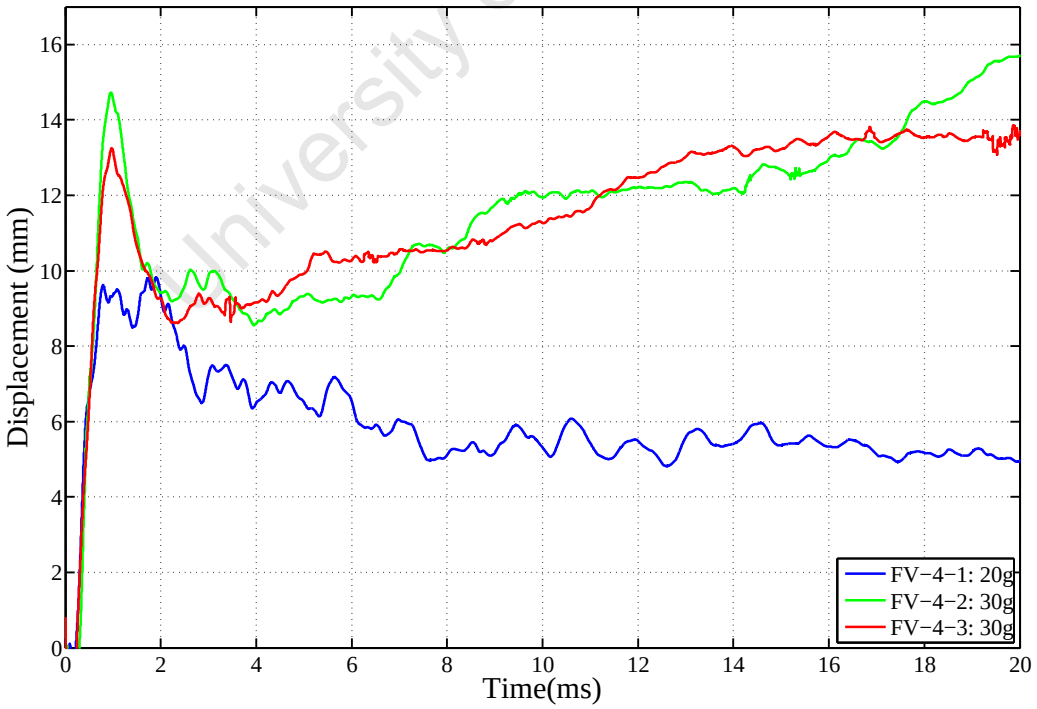

Figure D.13: Transient Deflection Results for FV-4-1, FV-4-2 and FV-4-3

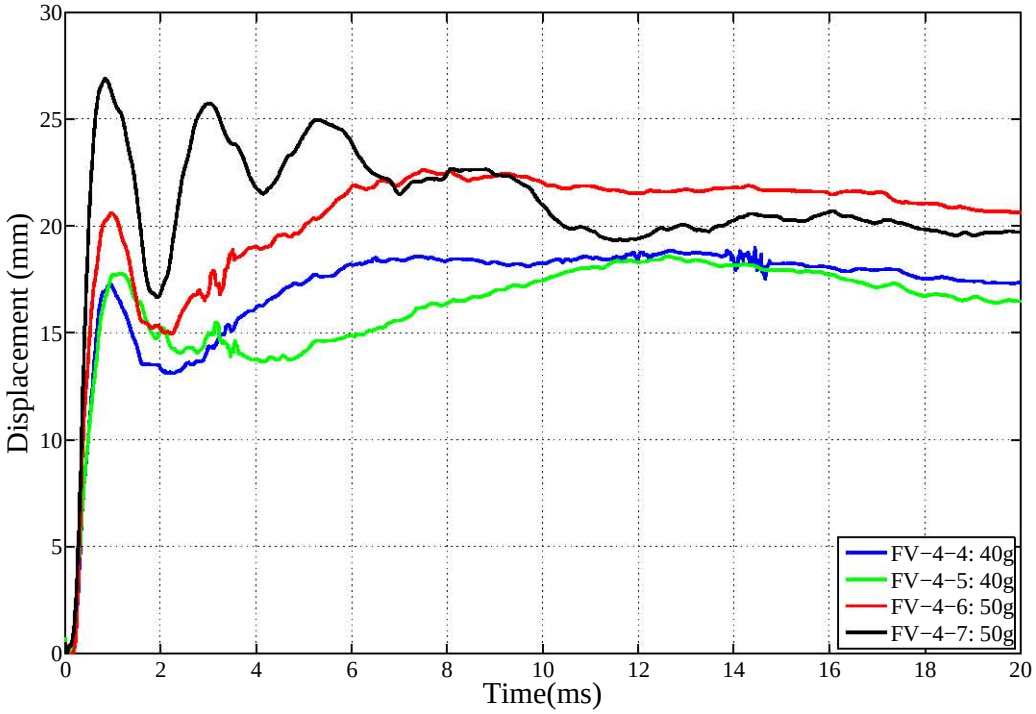

Figure D.14: Transient Deflection Results for FV-4-4, FV-4-5, FV-4-6 and FV-4-7

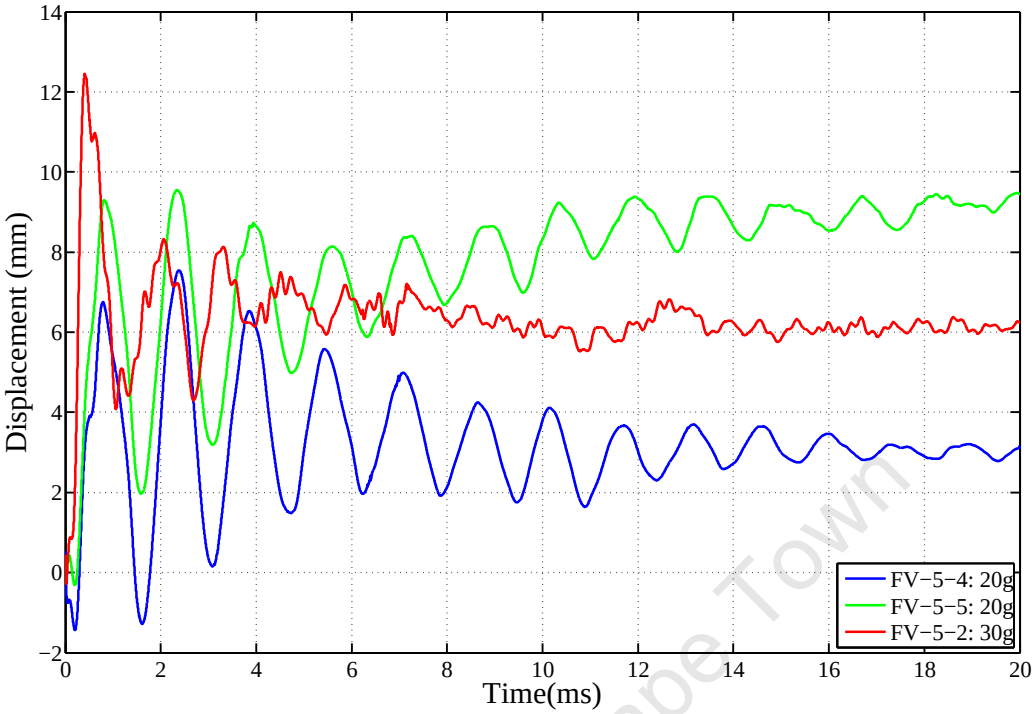

Figure D.15: Transient Deflection Results for FV-5-2, FV-5-3 and FV-5-4

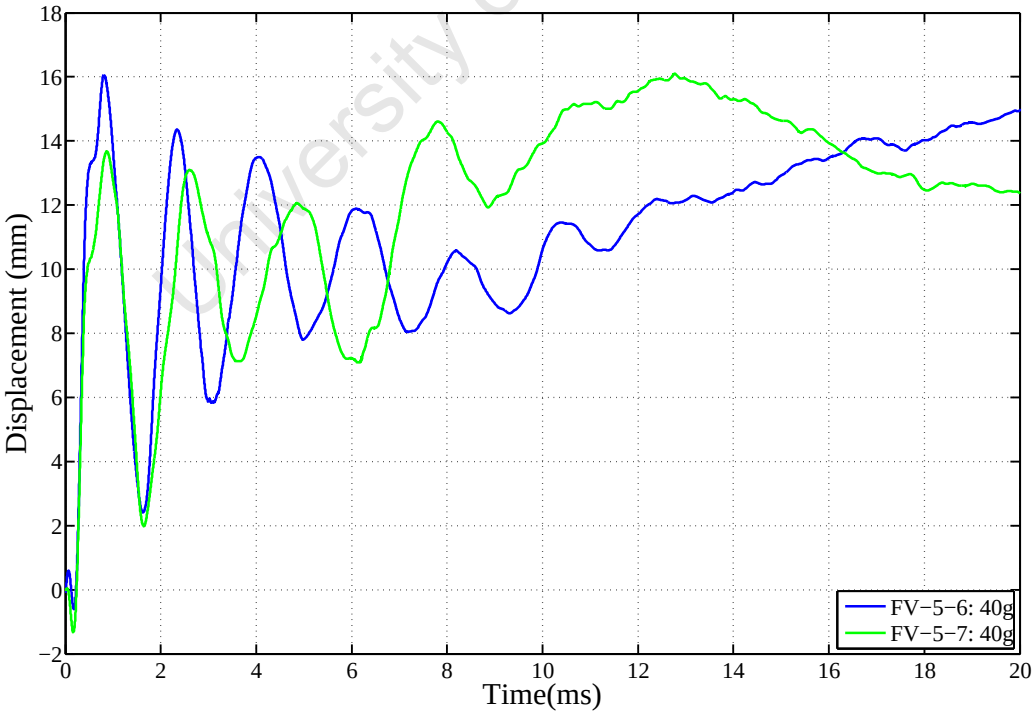

Figure D.16: Transient Deflection Results for FV-5-6 and FV-5-7

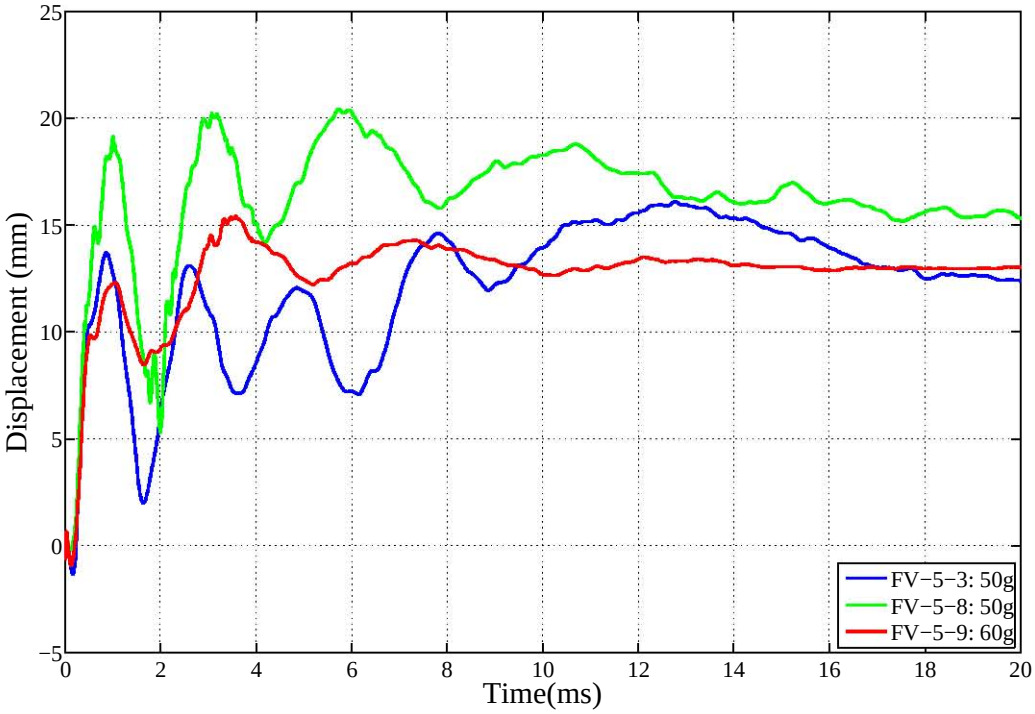

Figure D.17: Transient Deflection Results for FV-5-3, FV-5-8 and FV-5-9

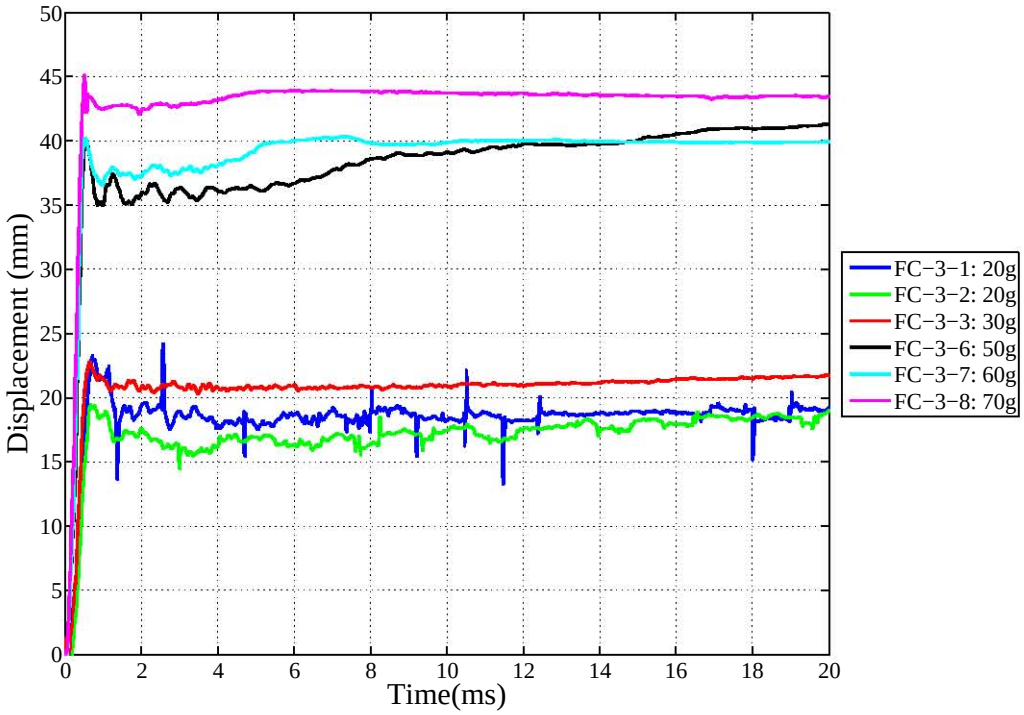

Figure D.18: Transient Deflection Results for FC-3-1, FC-3-2, FC-3-3, FC-3-6, FC-3-7 and FC-3-8

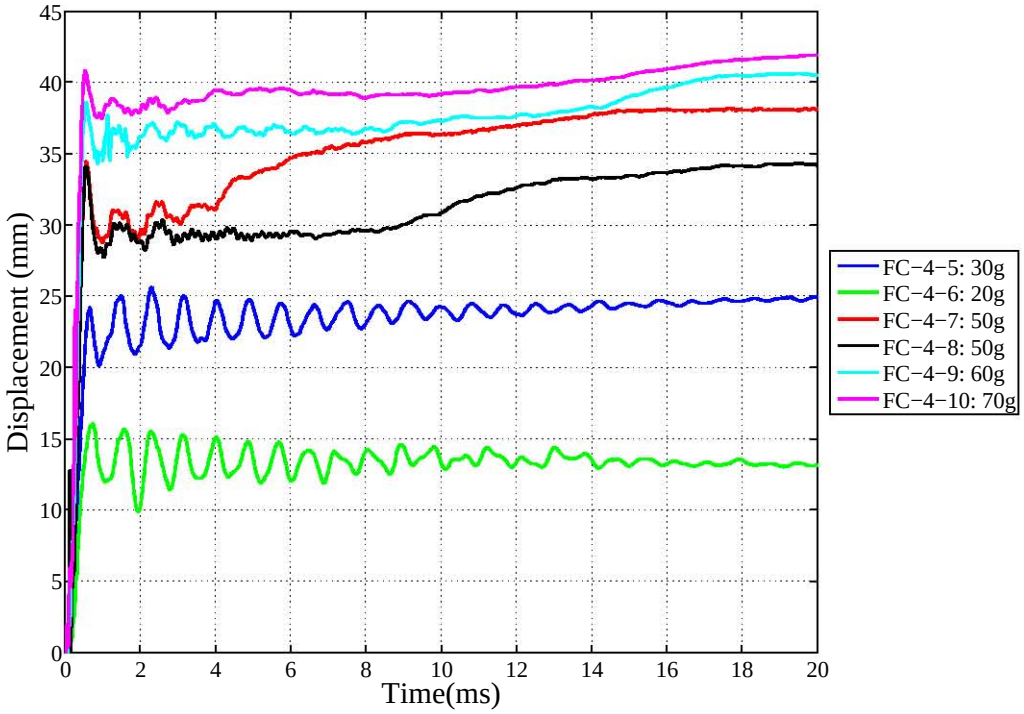

Figure D.19: Transient Deflection Results for FC-4-5, FC-6-3, FC-4-7, FC-4-8, FC-4-9 and FC-4-10

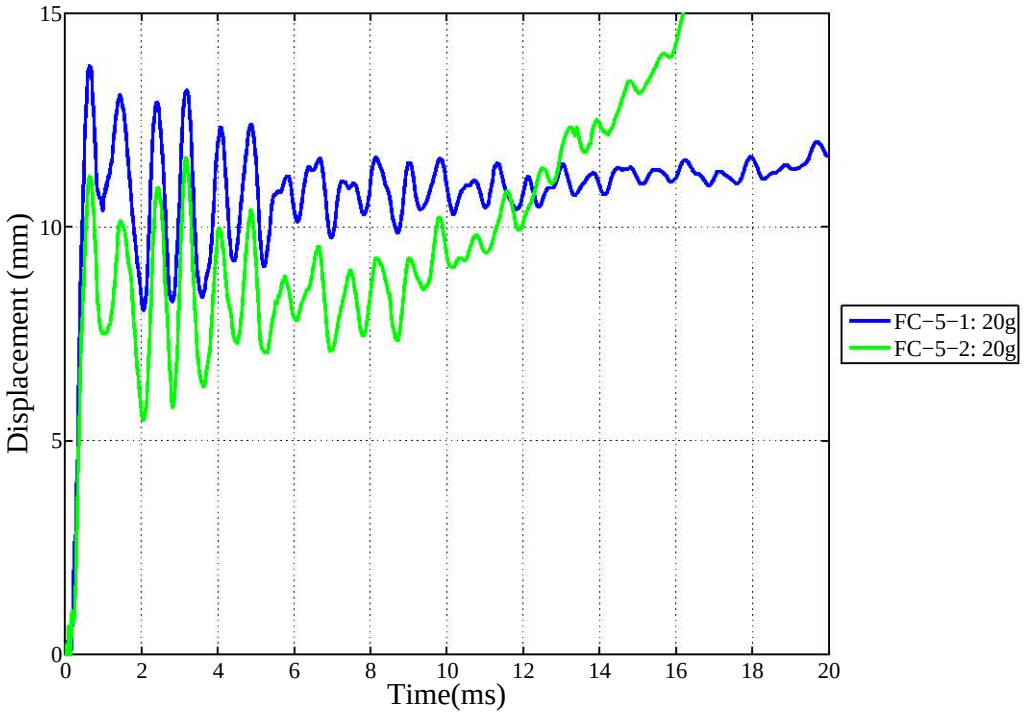

Figure D.20: Transient Deflection Results for FC-5-1 and FC-5-2

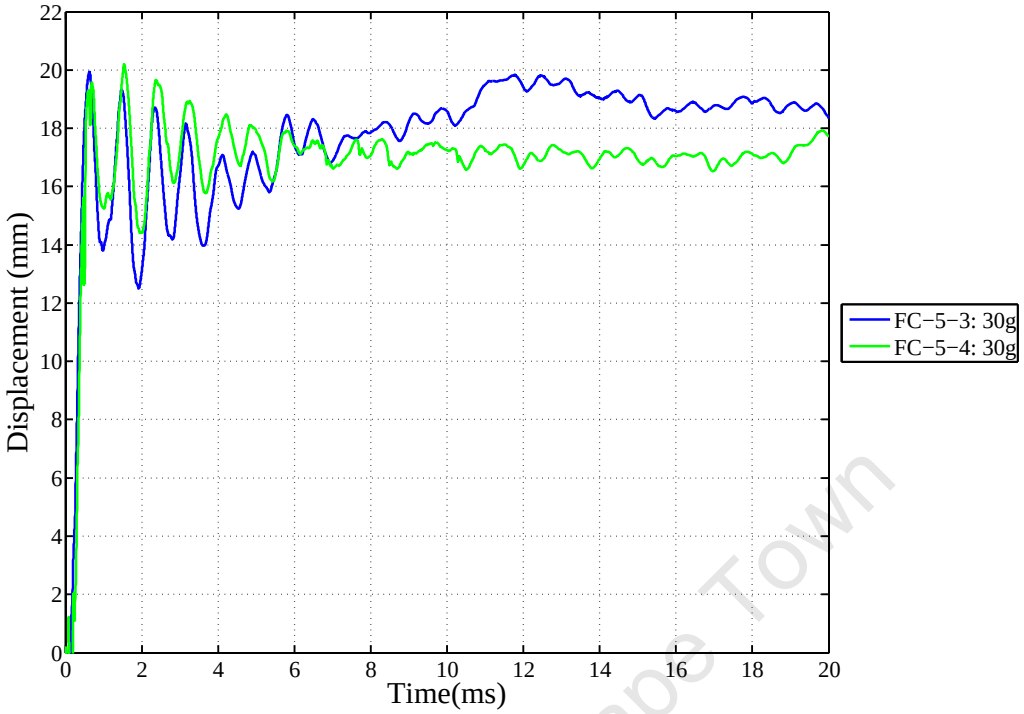

Figure D.21: Transient Deflection Results for FC-5-3 and FC-5-3

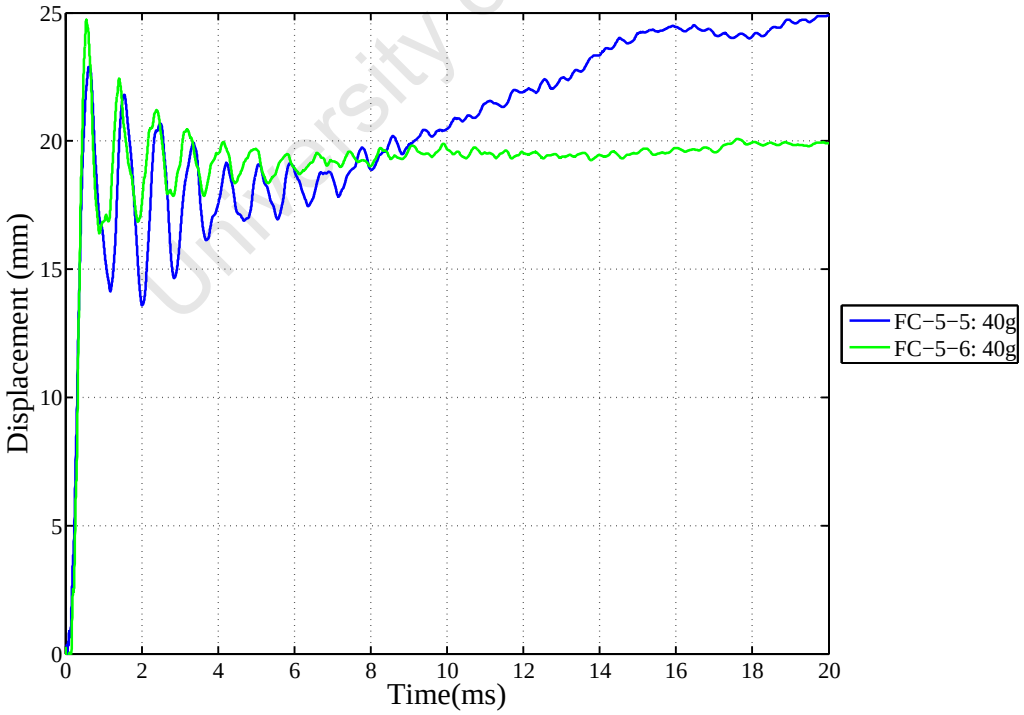

Figure D.22: Transient Deflection Results for FC-5-5 and FC-5-6

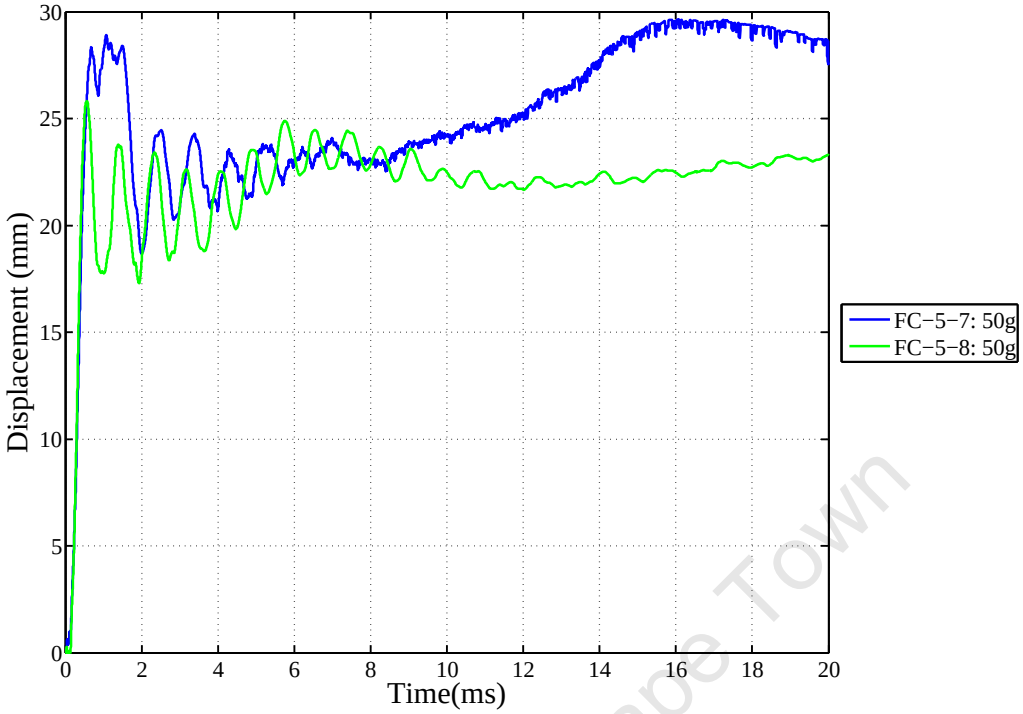

Figure D.23: Transient Deflection Results for FC-5-7 and FC-5-8

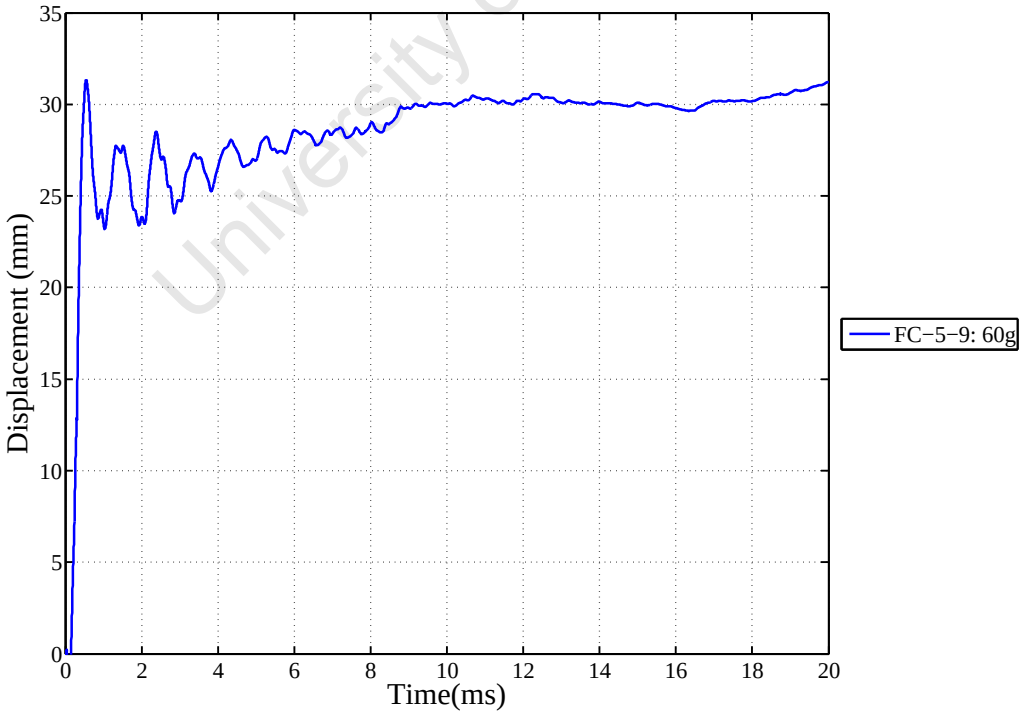

Figure D.24: Transient Deflection Results for FC-5-9

E Results For Experimental Data

Contents

Tables

E.1 Introduction

The calculations for the impulse ratio between the fully vented and unconfined blast experiments (Table E.1), the actual normalised midpoint deflection ratios between the target plate thicknesses (Tables E.2, E.3 and E.4) and the normalised deflection ratios with respects to target plate thickness between the degrees of confinement are presented in this Appendix.

Table E.1: Calculation of Fully Vented to Unconfined Impulse Ratio

Mass of Explosive (g)	Impulse ($I_{FV\ trend}$) (Ns)	Impulse ($I_{UC\ trend}$) (Ns)	$\frac{I_{FV\ trend}}{I_{UC\ trend}}$
10	27.04	8.52	3.17
15	36.48	11.60	3.14
20	45.92	14.69	3.13
25	55.37	17.77	3.12
30	64.81	20.86	3.11
35	74.25	23.94	3.10
40	83.69	27.03	3.10
45	93.14	30.11	3.09
50	102.58	33.20	3.09
55	112.02	36.28	3.09
60	121.47	39.37	3.09
		Average	3.10

Table E.2: Calculation of Actual Normalised Midpoint Deflection Ratio Between the 3 and $4mm$ Thick Target Plates

	Unconfined Trend Deflection		Fully Vented Trend Deflection		Fully Confined Trend Deflection		Ratios		
Mass of Explosive (g)	(δ_{3mmU}) (mm)	(δ_{4mmUC}) (mm)	(δ_{3mmFV}) (mm)	(δ_{4mmFV}) (mm)	(δ_{3mmFC}) (mm)	(δ_{4mmFC}) (mm)	$\frac{\delta_{4mmUC}}{\delta_{3mmUC}}$	$\frac{\delta_{4mmFV}}{\delta_{3mmFV}}$	$\frac{\delta_{4mmFC}}{\delta_{3mmFC}}$
20	3.75	0.70*	9.68	6.35	18.64	13.43	0.19*	0.66	0.72
25	4.94	1.77*	12.48	8.71	21.82	16.36	0.36*	0.70	0.75
30	6.14	2.85*	15.28	11.08	25.00	19.28	0.46*	0.73	0.77
35	7.34	3.92*	18.08	13.44	28.18	22.21	0.53*	0.74	0.79
40	8.53	5.00	20.87	15.81	31.36	25.13	0.59	0.76	0.80
45	9.73	6.07	23.67	18.17	34.54	28.06	0.62	0.77	0.81
50	10.93	7.15	26.47	20.54	37.72	30.99	0.65	0.78	0.82
55	12.12	8.22	29.27	22.90	40.90	33.91	0.68	0.78	0.83
60	13.32	9.30	32.07	25.27	44.07	36.84	0.70	0.79	0.84
						Averages	0.65	0.74	0.79
						Average Ratio 4mm to 3mm	**0.73**		

* not included in calculation as δ_{4mmUC} less than one nominal plate thickness ($4mm$)

Table E.3: Calculation of Actual Normalised Midpoint Deflection Ratio Between the 4 and $5mm$ Thick Target Plates

	Fully Vented Trend Deflection		Fully Confined Trend Deflection		Ratios	
Mass of Explosive (g)	(δ_{4mmFV}) (mm)	(δ_{5mmFV}) (mm)	(δ_{4mmFC}) (mm)	(δ_{5mmFC}) (mm)	$\frac{\delta_{5mmFV}}{\delta_{4mmFV}}$	$\frac{\delta_{5mmFC}}{\delta_{4mmFC}}$
20	6.35	3.95*	13.43	9.78	0.62*	0.73
25	8.71	5.99	16.36	11.82	0.69	0.72
30	11.08	8.02	19.28	13.86	0.72	0.72
35	13.44	10.06	22.21	15.90	0.75	0.72
40	15.81	12.09	25.13	17.94	0.76	0.71
45	18.17	14.13	28.06	19.98	0.78	0.71
50	20.54	16.16	30.99	22.01	0.79	0.71
55	22.90	18.20	33.91	24.05	0.79	0.71
60	25.27	20.23	36.84	26.09	0.80	0.71
				Averages	0.76	0.72
			Average Ratio 5mm to 4mm		**0.74**	

* not included in calculation as δ_{5mmFV} less than one nominal plate thickness ($5mm$)

Table E.4: Calculation of Actual Normalised Midpoint Deflection Ratio Between the 3 and $5mm$ Thick Target Plates

	Fully Vented Trend Deflection		Fully Confined Trend Deflection		Ratios	
Mass of Explosive (g)	(δ_{3mmFV}) (mm)	(δ_{5mmFV}) (mm)	(δ_{3mmFC}) (mm)	(δ_{5mmFC}) (mm)	$\frac{\delta_{5mmFV}}{\delta_{3mmFV}}$	$\frac{\delta_{5mmFC}}{\delta_{3mmFC}}$
20	9.68	3.95	18.64	9.78	0.41	0.52
25	12.48	5.99	21.82	11.82	0.48	0.54
30	15.28	8.02	25.00	13.86	0.53	0.55
35	18.08	10.06	28.18	15.90	0.56	0.56
40	20.87	12.09	31.36	17.94	0.58	0.57
45	23.67	14.13	34.54	19.98	0.60	0.58
50	26.47	16.16	37.72	22.01	0.61	0.58
55	29.27	18.20	40.90	24.05	0.62	0.59
60	32.07	20.23	44.07	26.09	0.63	0.59
				Averages	0.58	0.57
			Average Ratio 5mm to 3mm		**0.57**	

Table E.5: Calculation of Normalised Midpoint Deflection Ratio With Respects to Target Plate Thickness Between the Degrees of Confinement

	3mm Trend Deflection			Ratios		
Mass of Explosive (g)	(δ_{3mmUC}) (mm)	(δ_{3mmFV}) (mm)	(δ_{3mmFC}) (mm)	$\frac{\delta_{3mmFV}}{\delta_{3mmUC}}$	$\frac{\delta_{3mmFC}}{\delta_{3mmUC}}$	$\frac{\delta_{3mmFC}}{\delta_{3mmFV}}$
20	3.75	9.68	18.64	2.58	4.97	1.93
25	4.94	12.48	21.82	2.52	4.41	1.75
30	6.14	15.28	25.00	2.49	4.07	1.64
35	7.34	18.08	28.18	2.46	3.84	1.56
40	8.53	20.87	31.36	2.45	3.68	1.50
45	9.73	23.67	34.54	2.43	3.55	1.46
50	10.93	26.47	37.72	2.42	3.45	1.42
55	12.12	29.27	40.90	2.41	3.37	1.40
60	13.32	32.07	44.07	2.41	3.31	1.37
Average				**2.46**	**3.85**	**1.56**
	4mm Trend Deflection			Ratios		
Mass of Explosive (g)	(δ_{4mmUC}) (mm)	(δ_{4mmFV}) (mm)	(δ_{4mmFC}) (mm)	$\frac{\delta_{4mmFV}}{\delta_{4mmUC}}$	$\frac{\delta_{4mmFC}}{\delta_{4mmUC}}$	$\frac{\delta_{4mmFC}}{\delta_{4mmFV}}$
20	0.70*	6.35	13.43	9.07*	19.19*	2.12
25	1.77*	8.71	16.36	4.91*	9.22*	1.88
30	2.85*	11.08	19.28	3.89*	6.77*	1.74
35	3.92*	13.44	22.21	3.43*	5.66*	1.65
40	5.00	15.81	25.13	3.16	5.03	1.59
45	6.07	18.17	28.06	2.99	4.62	1.54
50	7.15	20.54	30.99	2.87	4.33	1.51
55	8.22	22.90	33.91	2.79	4.12	1.48
60	9.30	25.27	36.84	2.72	3.96	1.46
Average				**2.91**	**4.41**	**1.66**
	5mm Trend Deflection			Ratios		
Mass of Explosive (g)	(δ_{5mmUC}) (mm)	(δ_{5mmFV}) (mm)	(δ_{5mmFC}) (mm)	$\frac{\delta_{5mmFV}}{\delta_{5mmUC}}$	$\frac{\delta_{5mmFC}}{\delta_{5mmUC}}$	$\frac{\delta_{5mmFC}}{\delta_{5mmFV}}$
20	*NA*	3.95*	9.78	*NA*	*NA*	2.47*
25	*NA*	5.99	11.82	*NA*	*NA*	1.97
30	*NA*	8.02	13.86	*NA*	*NA*	1.73
35	*NA*	10.06	15.90	*NA*	*NA*	1.58
40	*NA*	12.09	17.94	*NA*	*NA*	1.48
45	*NA*	14.13	19.98	*NA*	*NA*	1.41
50	*NA*	16.16	22.01	*NA*	*NA*	1.36
55	*NA*	18.20	24.05	*NA*	*NA*	1.32
60	*NA*	20.23	26.09	*NA*	*NA*	1.29
Average						**1.63**
Overall Average				***2.69***	***4.13***	***1.62***

*not included in calculation as Trend Deflection less than one nominal plate thickness

This page has been intentionally left blank.